Ph.D. Thesis July 2024

Circularly Polarized Luminescence Active Crystalline Materials Based on Chiral NHC Au(I) Complexes and Control by Molecular Dynamics

Hokkaido University

Graduate School of Chemical Science and Engineering

Organoelement Chemistry Laboratory

有機元素化学研究室

Pingyu Jiang

姜 平宇

CONTENTS

1. General Introduction

1.1 Circularly polarized luminescence

1.1.1 The basic of circularly polarized luminescence

The word 'chiral' is derived from ancient Greek χείρ (cheir) 'hand', which describes elements that cannot be superimposed onto their mirror images (Figure 1.1a),[1-3] encompasses a broad spectrum of materials and phenomena, revealing the broken mirror symmetry prevalent in the natural world.[4,5] Its profound significance spans multiple disciplines, including chemistry, biology, physics, and materials science, and operates across a range of length scales from the atomic to the macroscopic level.[6-9] From the intricate molecular structures of amino acids and DNA to the vast expanse of galaxies, chirality is woven into the very fabric of existence (Figure 1.1b). Inspired by nature's chiral architectures, a diverse array of synthetic materials exhibiting intriguing chirality has emerged.[2,4,5,10,11]

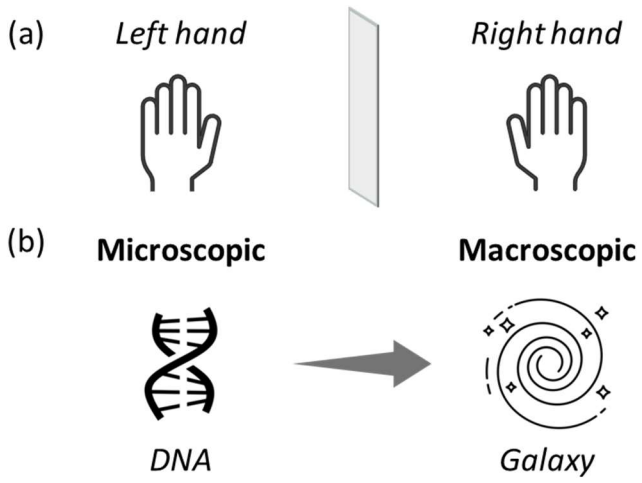

Figure 1.1 Introduction of chirality.

Polarization, an inherent attribute of electromagnetic wave, especially light, refers to the asymmetry between the vibration direction and the propagation direction of the wave.[12] This property is crucial in various fields, including display technology, remote sensing, and information storage.[13] Circularly polarized light (CP-light), generated by combining two linearly polarized lights (LP-light) of identical frequency but perpendicular polarization orientations (Figure 1.2a), offers vast optical insights while retaining angle-independence.[5,14] It has wide application in quantum computing, asymmetric synthesis, and 3D displays because of these distinctive characteristics.[14-17] Notably, there are a lot of research has spotlighted the interplay between chiral materials and their chiral optical properties, leveraging CP-light techniques such as circular dichroism (CD) for diverse CP-light absorption and circularly polarized luminescence (CPL) for selective one-side CP-light emission. CD spectra could provide Chiroptical information in the ground state, which CPL spectra could provide Chiroptical information in the excited state(Figure 1.2b).[14]

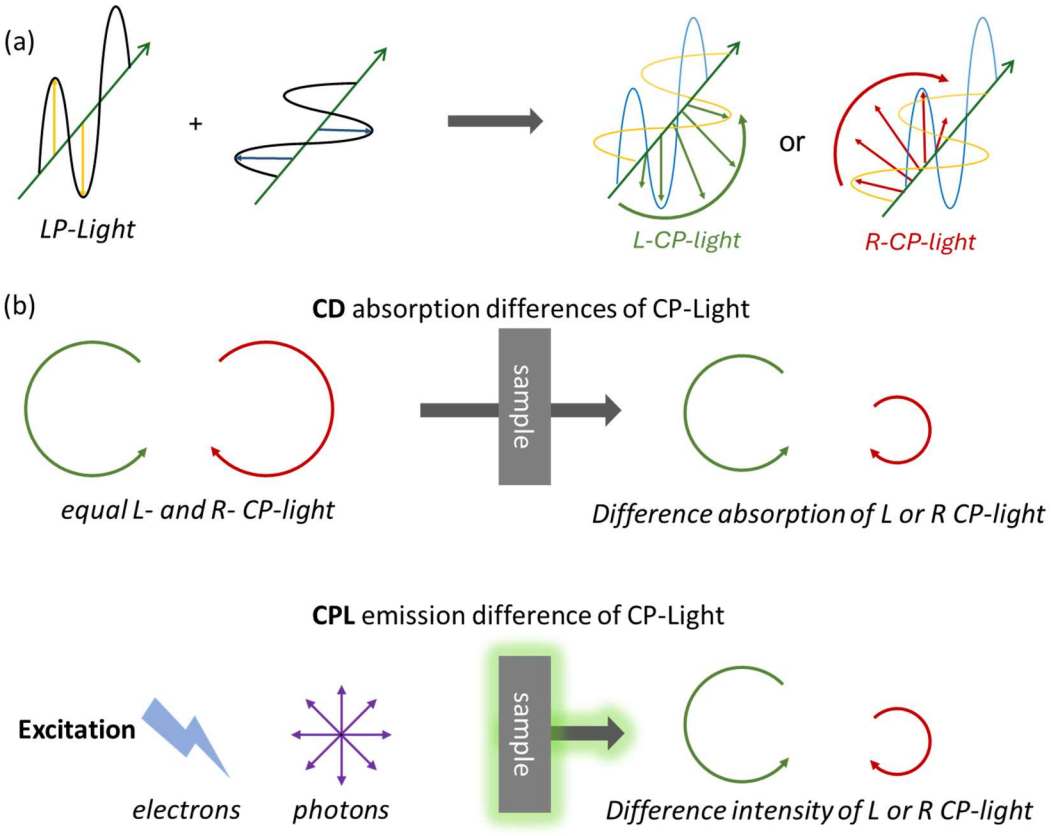

Figure 1.2 Introduction and applications of circularly polarized light in chiroptical research.

Traditionally, circularly polarized light (CP-light) is generated by passing linearly polarized light (LP-light) through a quarter wave plate. Alternatively, chiral luminescent materials can directly emit CP-light, avoiding the energy loss associated with the plate transition process (Figure 1.3).[5,19] Utilizing CPL-active materials provides an efficient method to generate CP-light directly, enhancing efficiency and simplifying device structures. There are several approaches to creating CPL-active materials:[20]

1. Intrinsic CPL: Utilizing single-component chiral chromophores.

2. Chirality Transfer: Assembling chiral structures with achiral emitting molecules.

3. Symmetry Breaking: Inducing chirality and CPL through the symmetry breaking of achiral chromophores.

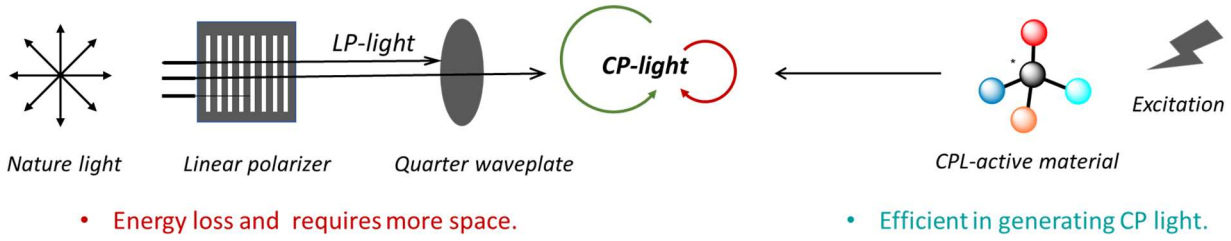

Figure 1.3 Comparison between producing CP-Light via traditional methods and CPL-active materials.

In the experimental analysis of chiral emissive materials, CD and CPL spectral measurements are commonly conducted. CD spectroscopy assesses the material's differential absorption of left-handed CP-Light (L-CP-Light) and right-handed CPL (R-CP-Light). The degree of CD is quantified by the absorption dissymmetry factor, g_{abs}, which is determined by Equation 1.1:

$$g_{abs} = \frac{\varepsilon_L - \varepsilon_R}{\frac{1}{2}(\varepsilon_{L+}\varepsilon_R)} \quad (1.1)$$

where ε_L and ε_R are the molar absorption coefficients of L-CP-Light and R-CP-Light, respectively.

Experimentally, the g_{abs} value can be determined by Equation 1.2:

$$g_{abs} = \frac{\text{ellipticity}}{32980 \times \text{absorbance}} \tag{1.2}$$

where the "ellipticity" and "absorbance" values can be directly obtained from CD spectral measurement.

In contrast to CD spectra, CPL spectra are linked to the excited state characteristics of chiral systems. The CPL property can be assessed through the luminescence dissymmetry factor, g_{lum}, as defined by Equation 1.3:

$$g_{lum} = \frac{I_L - I_R}{\frac{1}{2}(I_L + I_R)} \tag{1.3}$$

where I_L and I_R represent the luminescence intensity of L-CP-Light and R-CP-Light, respectively.

Theoretically, g_{lum} is predicted to be related by Equation 1.4:

$$g_{lum} = 4\cos\theta \frac{|m|\cdot|\mu|}{|m|^2 + |\mu|^2} \tag{1.4}$$

where m and μ denote the magnetic and electric transition dipole moments, respectively, and θ is the angle between them. In this situation, achieving highly emissive materials with a high emission quantum yield (QY) typically necessitates a high $|\mu|$. However, this presents a dilemma as it becomes challenging to attain materials with both high g_{lum} and QY.

According to Equation 1.1 and Equation 1.3, both g_{abs} and g_{lum} values fall within the range from −2 to +2. The absolute values $|g_{abs}|$ and $|g_{lum}|$ indicate the magnitude of the Cotton effect and luminescence polarization, respectively. CPL-active materials ($|g_{lum}| \neq 0$) generally exhibit distinct Cotton effects ($|g_{abs}| \neq 0$). Nonetheless, the observation of Cotton effects does not conclusively indicate CPL activity, as they are associated with the ground-state and excited-state properties of the material, respectively.

1.1.2 CPL-Active materials

Since the initial discovery of CPL-active molecular material, chiral hydrindane, in 1967,[20] significant progress has been achieved in this field. Particularly, CPL-active materials have garnered considerable attention over the past decade and have evolved into a frontier field encompassing various scientific disciplines, including molecular materials, nanoscience and technology, photochemistry, and optoelectronic devices. And researchers focus on using small molecules, metal-ligand coordination materials, polymers, supramolecular assemblies, metal clusters, and other system to build CPL-active materials.[5,14]

Chiral small molecules

In recent, there has been a growing number of studies focusing on CPL-active materials employing versatile chiral small molecules. Specifically, derivatives featuring axially chiral binaphthyls (**1a-1h**),[21-23] helicenes (**1i-1k**),[24-26] and planar chiral structure molecules (**1l-1m**)[27,28] have been subject to extensive investigation (Figure 1.4). Chiral small molecules offer numerous dvantages over chiral polymers, including facile structural modification, high fluorescence efficiency, precise tuning of emission wavelength, a clear structure-performance relationship, and a straightforward manufacturing process.

Metal-ligand coordination materials

The exploration of CPL-active metal-ligand coordination materials, including discrete organic molecular metal complexes (**1n-1p**),[29-31] metal-organic coordination polymers (MOPs, **1q**),[32] and metal-organic frameworks (MOFs, **1r**)[33,34] (Figure 1.5), has garnered increasing interest. These materials are attractive due to their versatile coordination modes, abundant metal-involving excited states, high QY, and high g_{lum} values, and their potential applications in optoelectronic devices. For instance,

lanthanide metal complexes often achieve high g_{lum} values due to strong spin-orbit coupling and the presence of magnetic transition dipole moments.

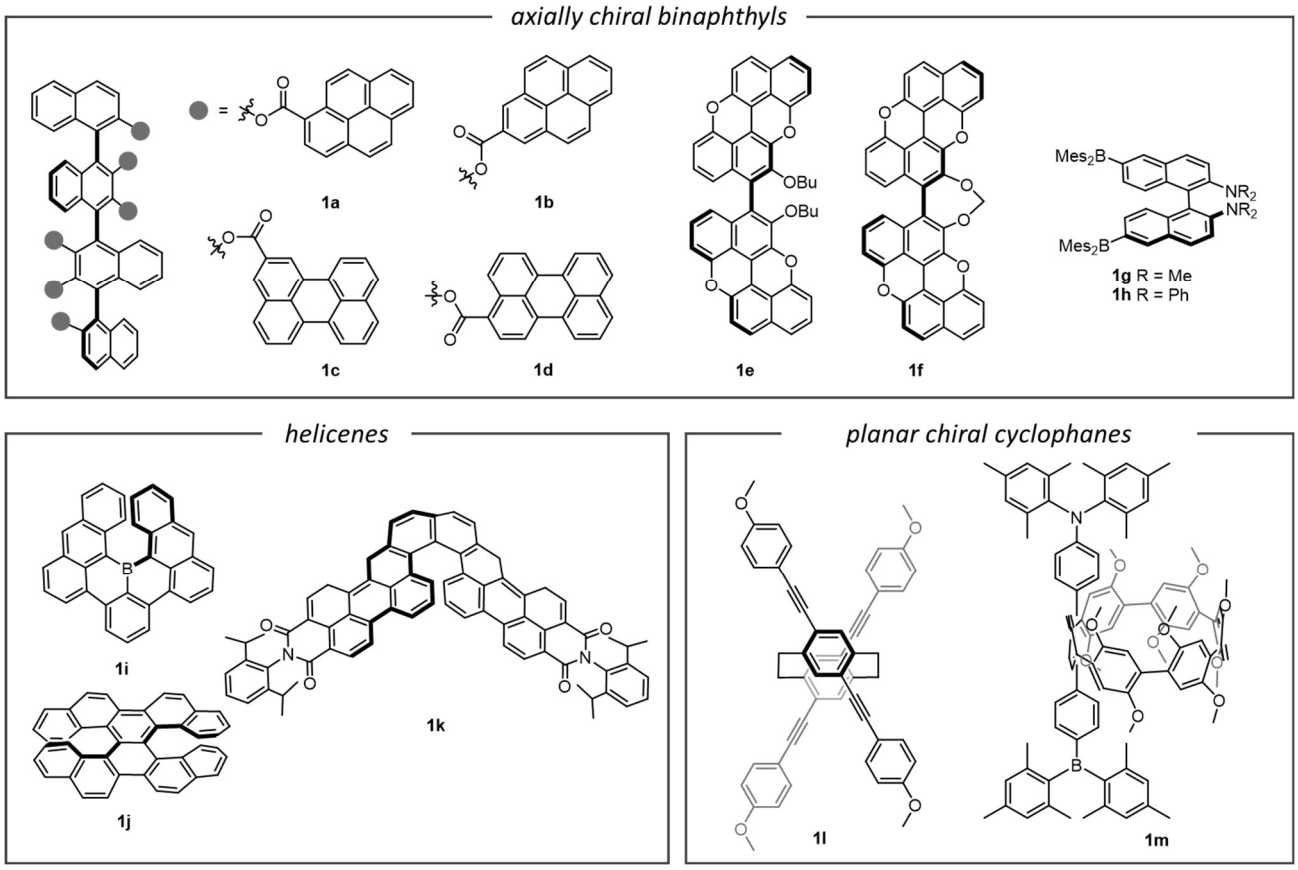

Figure 1.4 Chemical structures of chiral small molecules.

CPL-active polymers

Polymer-based CPL-active materials have garnered increasing interest, in part due to the advantages of polymers, such as high stability and excellent processability. These materials are typically prepared using two strategies based on the combination of chirality and fluorescence (Figure 1.6). First, the covalent bonding method, where the chiral and fluorescent components are chemically bonded at different locations within the polymer chains (**1s**).[35] Alternatively, the physical blending method relies on chirality transfer achieved through non-covalent interactions between the chiral and fluorescent components or by utilizing chiral polymers directly as CPL filters, independent of non-covalent interactions (**1t**).[36]

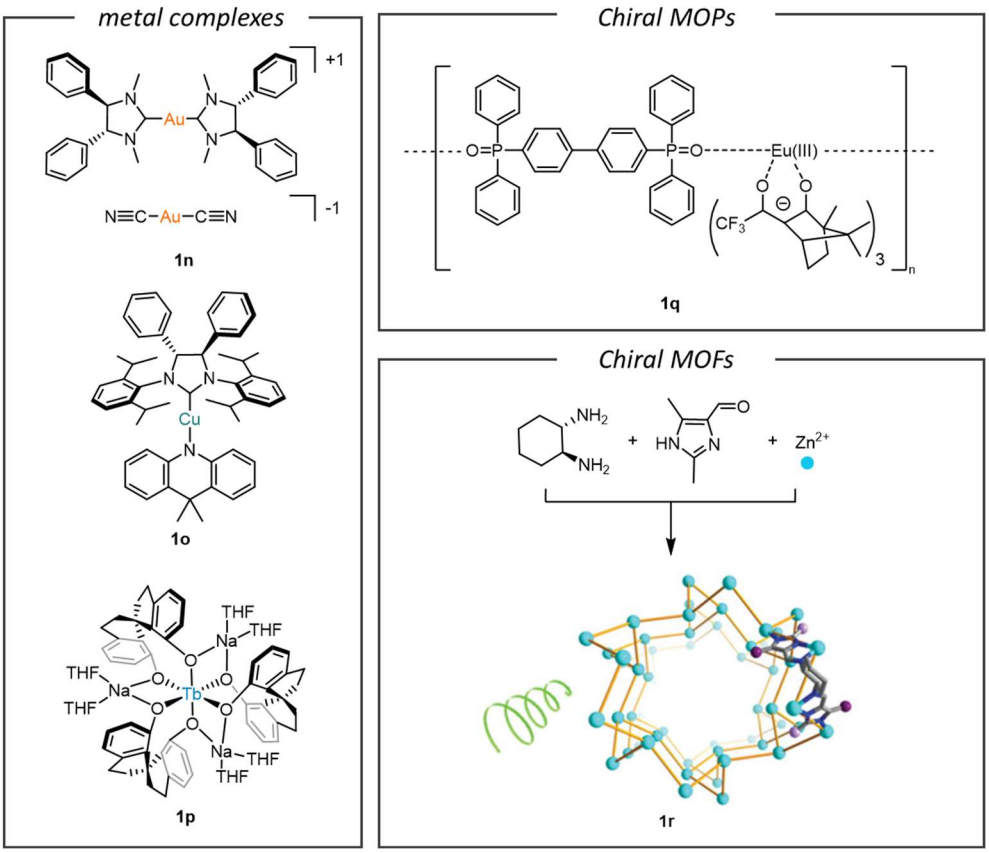

Figure 1.5 Chemical structures of chiral metal-ligand coordination materials. Figure adapted and reproduced from Ref.34 with permission.

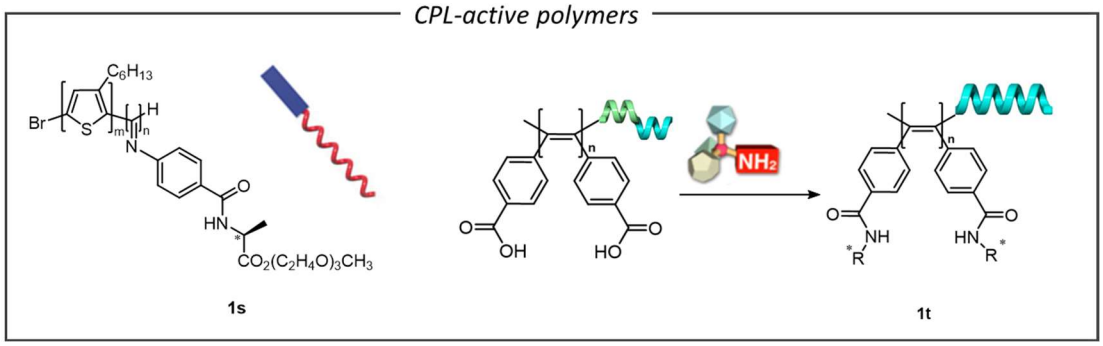

Figure 1.6 Chemical structures of CPL-active polymers. Figure adapted and reproduced from Ref. 35 and 36 with permission.

CPL-active supramolecular assemblies

Over the past few decades, with the rapid advancements in supramolecular chemistry, chiral supramolecular self-assemblies and co-assemblies have emerged as promising candidates for CPL-active materials. These assemblies, with customizable microstructures, offer a potent means to precisely control the arrangement of

building blocks and enhance CPL signals through noncovalent interactions such as π-π stacking, hydrogen bonds, hydrophobic interactions, van der Waals forces, and host-guest interactions.[14] General, the CPL-active supramolecular assemblies could be classified to two main classes (Figure 1.7): amplification of CPL through supramolecular self-assembly of chiral molecules (**1u**)[37] and emergence of CPL from achiral luminophores assembled with chiral matrices (**1v**).[38]

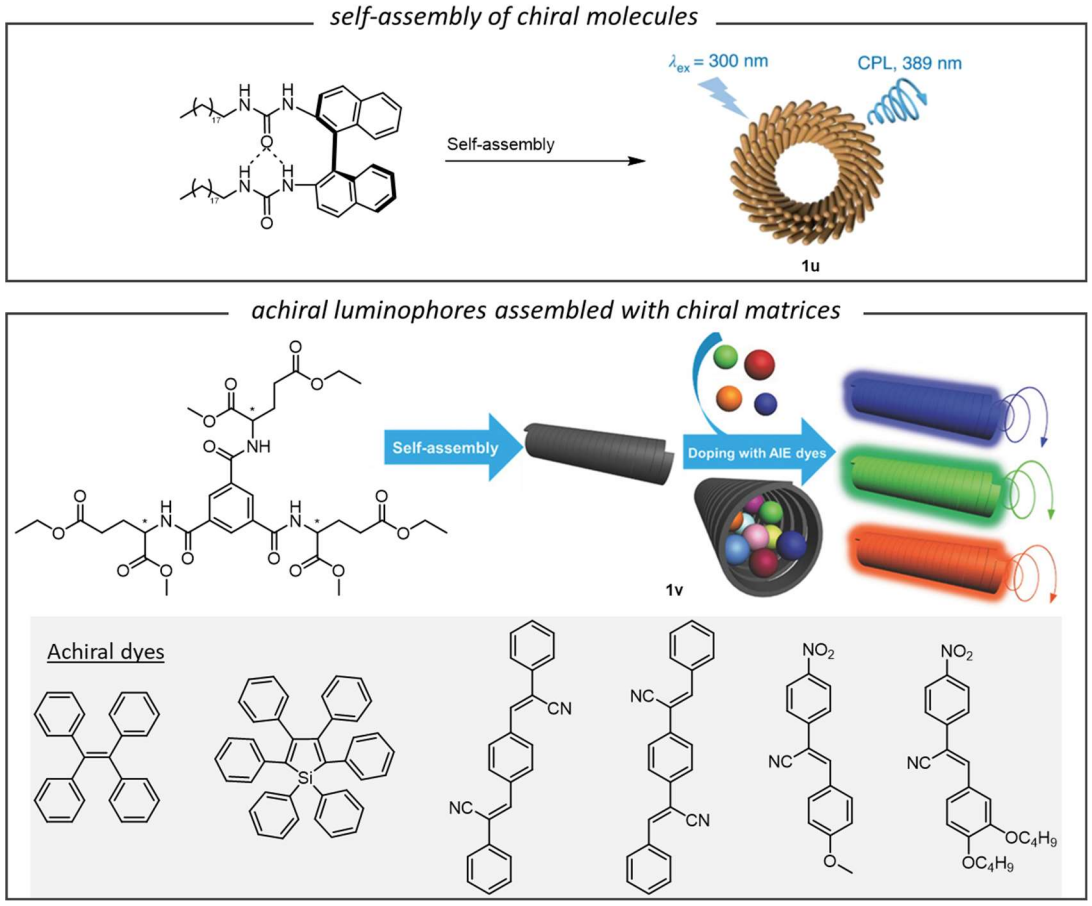

Figure 1.7 Structures of CPL-active supramolecular assemblies. Figure adapted and reproduced from Ref. 37 and 38 with permission.

Other CPL-active materials

To data, there are a number of other types of materials could be used as CPL-active materials: compounds with aggregation-induced emissions (AIEs), liquid crystals (LCs), metal clusters, inorganic nanomaterials, and photon upconversion systems.[5,11]

1.1.3 Control of CPL via external stimuli

The CPL properties depend on the dipole moments of the CPL-active material, which is related to its chirality. By controlling the molecular structure or supramolecular conformation, it is possible to alter the chirality and subsequently manipulate CPL. This process is dynamic and responsive to external stimuli such as solvent, pH value, electric and mechanical forces, and temperature. This sensitivity offers a means to regulate the chirality and CPL signal in CPL-active materials.[39]

Solvent, as the medium of the CPL-active materials, can significantly influence inter-/intra- molecular interactions through specific solute-solvent interactions. Therefore, adjusting the solvent properties can control the supramolecular chirality of assembly structures, such as polarity, concentration, and so on. For instance, Ema, T., and co-workers reported an example where compound **1w** exhibited solvent-dependent inversion of CPL.[40] This inversion was attributed to changes in excimer chirality, which were influenced by the presence or absence of intermolecular hydrogen bonds in the excited state. Additionally, the CPL intensity varied with changes in temperature and concentration. (Figure 1.8a). The pH value also could significantly impact intermolecular interactions, leading to different molecular arrangements and triggering helicity inversion. For example, Liu, M., and colleagues reported a histidine π-gel **1x**,[41,] which achieved dynamic control of CPL by adding acid and base. This control is attributed to the cooperative adjustment of hydrogen bonds and π–π stacking upon histidine protonation and deprotonation, which causes the reorientation of pyrene chromophores (Figure 1.8b). Moreover, the electrical and/or electrochemical control of the CPL is particularly appealing for applications in chiral optical and electronic devices. Yan, Y., and co-workers found that the CPL of self-assembled conducting polyaniline helical microfibers **1y** could be reversibly switched by applying an alternating electrical bias (Figure 1.8c).[42] This electrochemically switchable CPL is derived from the reversible transformation of the chirality of the

polyaniline microfibers, which is probably due to the change in the molecular interchain distance upon doping and dedoping. Furthermore, mechanical force could also switch the CPL activity. Duan, P., and colleagues discovered solid-state CPL-active materials **1z**,[43] which shows reversible mechanochromic CPL under mechanical grinding and recrystallization. This behavior is due to the chiral supramolecular arrangement of chromophores in the crystalline state, where the resulting excimer emission in crystals amplifies chirality and enhances CPL properties. (Figure 1.8d).

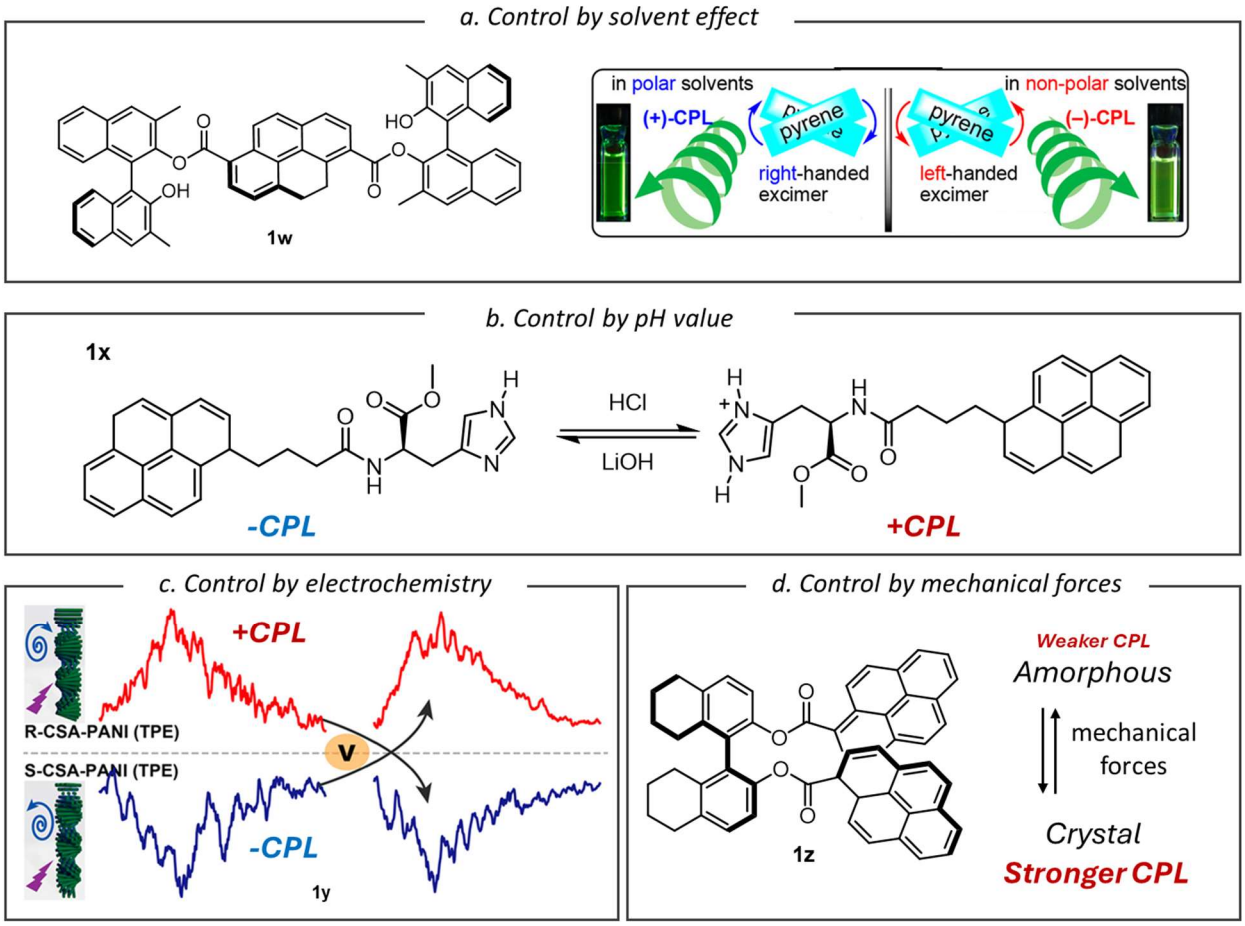

Figure 1.8 Illustrations of CPL regulation through different external stimuli. Figure adapted and reproduced from Ref.40, 42 with permission.

1.2 Molecular dynamic in crystalline solid state

In crystals, molecules are densely packed in close-packed environments, leading to limited atomic and molecular motion.[44-49] This arrangement minimizes empty space and restricts the individual degrees of freedom of the molecules. To understand the relationship between molecular dynamics and the assembled, as illustrated in Figure 1.9.[45]

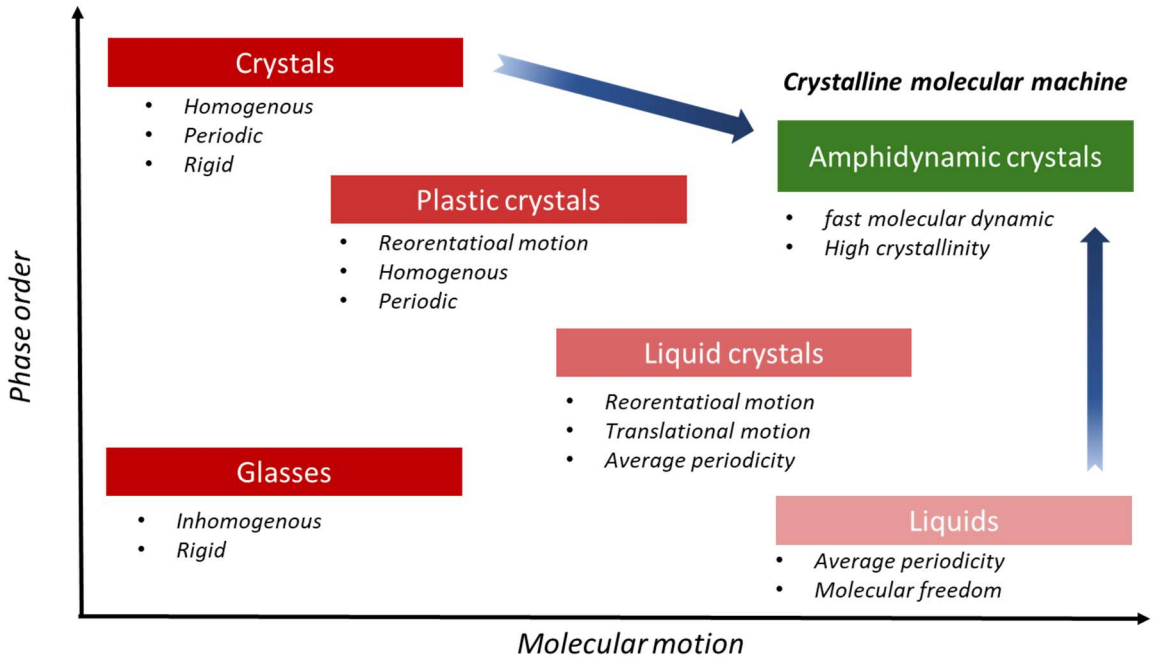

Figurer 1.9 Plot of phase order versus molecular motion with schematic representation of each assembly phase.

In contrast, the liquid phase, located in the bottom right corner of the plot, lacks long-range order. Molecules in liquids exhibit rapid full molecular rotation, resulting in homogeneity on average over time. Crystals, on the other hand, are characterized by homogeneity, periodicity, rigidity, and macroscopic anisotropy. In order to investigate the molecular dynamic in crystalline, the concept of amphidynamic crystal has been proposed by Garcia-Garibay M. A. and co-workers,[44-46] referring to highly ordered structures with fast rotatory dynamics defined at both molecular and macroscopic scales. These crystals show promise as platforms for solid-state

molecular machines and smart materials, as their solid-state functions arise from molecular rotations and reorientations that cause anisotropic changes in physical properties.[47-49]

When investigating the dynamics in these amphidynamic crystals, precise crystal structure information can be obtained from single-crystal X-ray diffraction (SC-XRD). However, SC-XRD analysis does not directly provide information about molecular dynamics in the crystal. Therefore, coupling complementary techniques that span a wider range of frequencies, such as variable-temperature solid-state NMR[44] (including CP-MAS, wide-line analysis of ^{2}H spin echo, and *T1* spin-lattice relaxation), could offer insights into the amplitude and frequency of motion, as well as the energy of activation of dynamic processes within the crystal lattice.[45]

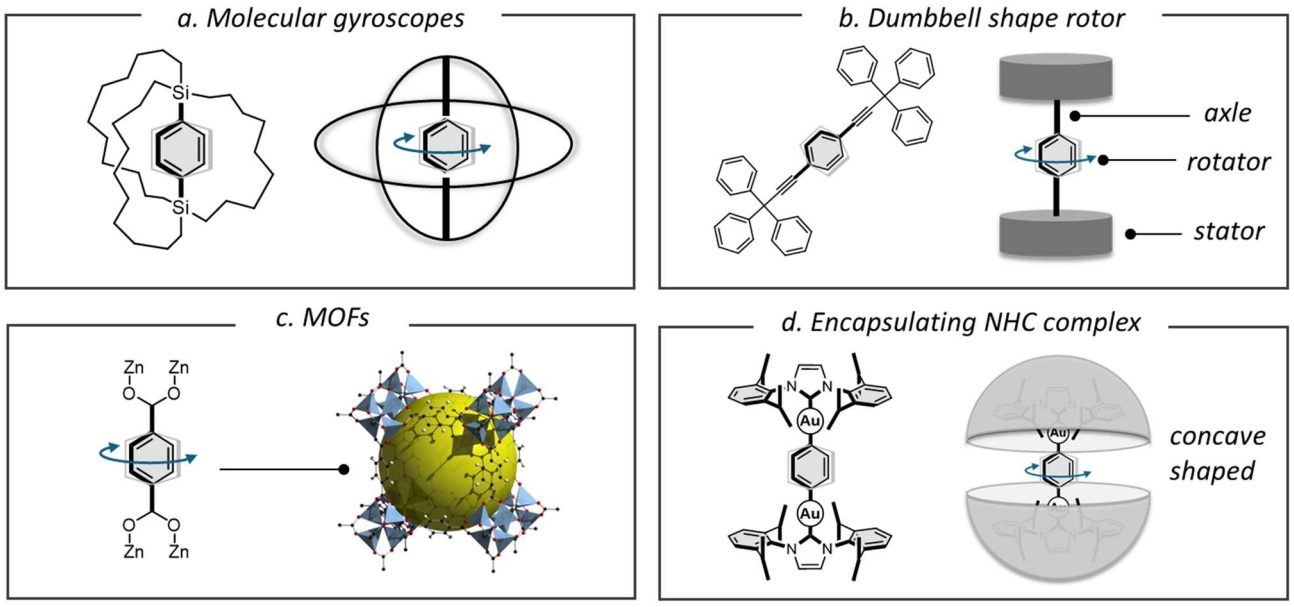

Figure 1.10 Various platforms have been employed for constructing amphidynamic crystals. Figure adapted and reproduced from Ref.53 with permission.

However, designing structural motifs for amphidynamic crystals to control motions in the solid state requires intricate planning to ensure there is sufficient free local space for molecular dynamics. Various platforms have been employed for constructing amphidynamic crystals (Figure 1.10),[50] including gyroscope-like

molecular rotors, dumbbell-shaped molecules, and porous materials such as metal-organic frameworks (MOFs).

Gyroscope-like molecular rotors consist of a functional rotator connected to an enclosing stator by triple bonds serving as the rotation axle. These were first proposed by Garcia-Garibay M. A. and colleagues for constructing crystalline molecular rotors. This was followed by the development of bridged trityl-based molecular gyroscopes, metal complexes with bridgehead diphosphine cages, and phenylene rotors shielded by bridging silyl cages (Figure 1.10a).[51,52] Another efficient access to a wide range of amphidynamic crystals was demonstrated by utilizing dumbbell-shaped structures, as shown by Garcia-Garibay M. A. and colleagues. In this design, trityl stators create a convex shape around the central rotator, preventing intramolecular steric interactions, although intermolecular steric shielding remains largely unpredictable (Figure 1.10b).[44,45] In contrast to gyroscope-like or dumbbell-shaped close-packed molecular rotors, highly porous MOFs can be built with molecular rotors that have minimal steric hindrance(Figure 1.10c).[53,54] For example, arylene dicarboxylates used as building blocks and molecular rotators in zinc-oxide and paddlewheel MOF structures exhibit electronic barriers to rotation resulting from changes in conjugation between the central phenylene rotator and the coordinated carboxylate groups. Recently, Ito, H. and Jin, M. et al. introduced a novel platform for crystalline molecular rotors by encapsulating a central arylene-based rotator with bulky *N*-heterocyclic carbene (NHC) Au(I) or Cu(I) complexes as stators (Figure 1.10d).[50,55,56] The concave-shaped NHC ligands provide steric shielding for the rotator, creating local space near the rotator, and allowing for molecular rotation.

Moreover, molecular dynamics within crystals can profoundly influence not only the crystal structure itself but also the bulk properties of the material. At the molecular level, dynamic motions can alter the orientation and symmetry of the constituent molecules.[57] This structural dynamics can then propagate to the macroscopic scale, affecting structural properties such as thermal expansion[58] and

phase transitions,[59] or functional properties such as electromagnetic behavior[60] and photophysical characteristics.[61] The ability of molecular dynamics to modulate both the structural and functional aspects of crystalline materials have positioned amphidynamic crystals as a promising avenue for developing solid-state molecular machines and stimuli-responsive functional materials. By harnessing the intricate interplay between molecular motion and material properties, researchers can design dynamic systems that respond to external stimuli, undergo controlled structural transformations, or exhibit tunable functionalities. This emerging field holds significant potential for applications in areas such as molecular sensing, data storage, energy conversion, and smart materials, where the ability to dynamically control and manipulate material properties is highly desirable.

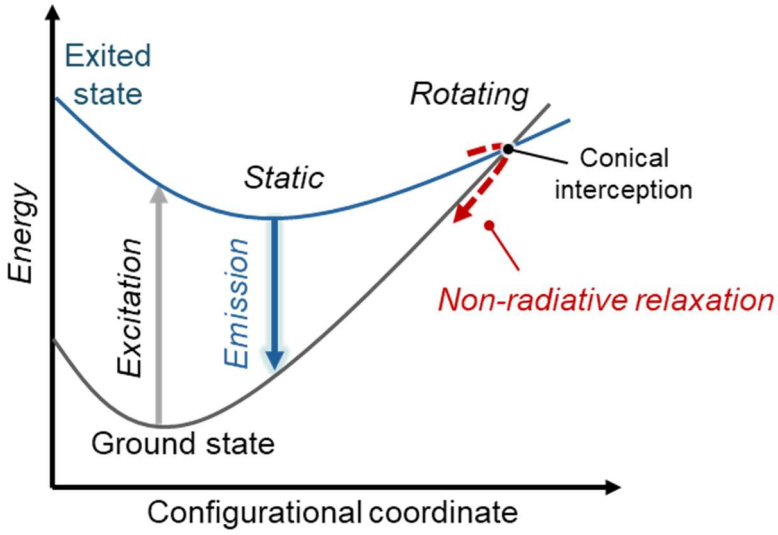

Figure 1.11 Molecular dynamic induce emission quenching and excited state decay through a nonradiative relaxation pathway.

The precise control of luminescent properties in solid-state materials has attracted much attention because of the potential for the development of functional materials such as sensors and external field-responsive devices.[62] Recently, several amphidynamic crystals with emission properties were demonstrated for controlling solid-state phosphorescence and sensing the inclusion of organic vapors or solvents

in solid-state porous materials.[50] The emission properties in these amphidynamic crystals were found to be strongly affected by internal rotational motion. The presence of rotational motion in the crystals can cause reorientation and variation in the conjugation of the luminophore moieties, facilitating access to conical intersections between excited and ground states, causing emission quenching and excited state decay through non-radiative relaxation pathways (Figure 1.1). Conversely, the restriction or inhibition of molecular rotation should enhance the photophysical performance, making this phenomenon akin to aggregation-induced emission. While the presence of thermally-activated molecular motion is usually an unwanted feature for solid-state luminescent materials, in the case of amphidynamic crystals, their rational design allows for fine-tuning and precise control of rotational motion. This results in emerging thermo-responsive luminescent properties, allowing control over luminescence intensity, lifetime, and color through the rate and mode of rotational dynamics.

1.3 Overview of this thesis

In this Ph.D. thesis, I will introduce several novel CPL-active solid-state materials utilizing *N*-heterocyclic carbene (NHC) Au(I) complexes. These materials are designed to control chiroptical and photophysical properties, especially CPL, through molecular dynamics (Figure 1.12).

Chapter 2 is about how the full inhibition of molecular dynamics can "turn on" CPL properties. In this chapter, I introduce a new approach for dynamic chirality stabilization in the conformationally flexible azahelicene species by crystallization-induced intermolecular chirality transfer. By employing shape-tailored chiral NHC ligands, the crystallization of azahelicene Au(I) complexes can lead not only to the suppression of conformational dynamics in the case of the dibenzocarbazole species but also to their homochirality stabilization through the intermolecular conjunction between chiral NHC and dibenzocarbazole ligands. In the case of Au(I) benzocarbazole complexes, the presence of the intermolecular conjunction and chirality transfer in the crystals results in chirality induction of the initially achiral benzocarbazole ligand. Furthermore, the crystallization of the studied complexes also results in the activation of their CPL properties, which were suppressed in solution. Importantly, the presence of chirality transfer within the crystal structure leads to a significant CPL enhancement, with luminescence dissymmetry factors that are 5 to 10 times higher compared to the crystalline complexes without chirality transfer.

In contrast to the full stop of molecular dynamics and active CPL, Chapters 3 and 4 discuss the utilization of molecular dynamics to control CPL properties. Chapter 3 presents a new type of crystalline molecular rotor featuring a neutral *para*-phenylene rotator enclosed by NHC stators and connected by a C-Au-C rotation axis. By using the chiral NHC ligand, the effect of thermal-induced molecular rotation on CPL was investigated. However, because the rotation in the central *para*-phenylene rotator does not change the symmetry of the crystal, the rotation could only quench the

emission intensity but not change the dissymmetry factor of CPL. Based on these results, Chapter 4 demonstrates how molecular dynamics can alter internal molecular symmetry and further modulate not only CPL intensity but also luminescence dissymmetry factors in the crystalline state. In this chapter, I prepared a pair of chiral binuclear NHC Au(I) complexes that exhibit a distinct axially chiral conformation with C_2-symmetry, derived from non-equivalent orientations of phenyl moieties at the chiral centers of NHC ligands. Solid-state NMR studies reveal that these non-equivalent phenyl moieties undergo fast rotational motion, potentially leading to the symmetrization of complexes in the crystal. These complexes display strong CPL in the crystalline state, with emission intensity, lifetime, and, most importantly, luminescence dissymmetry factors showing temperature-dependent behavior controlled by molecular rotation.

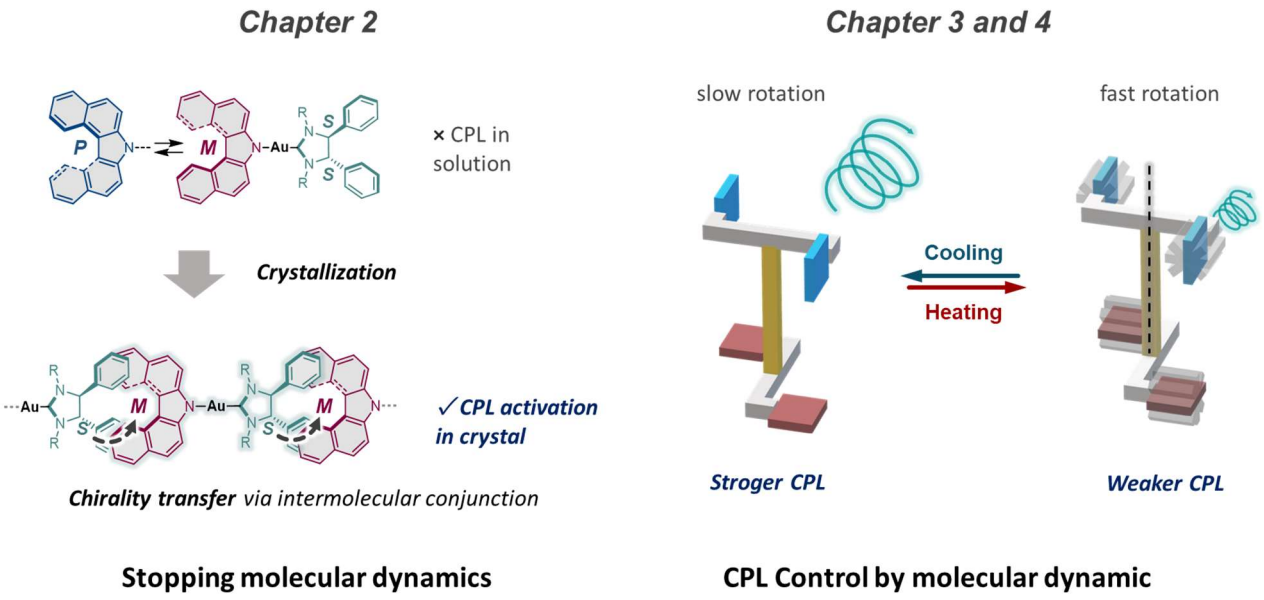

Figure 1.12 Overview of this Ph.D. thesis.

1.4 Reference

1. Thomson, W. *Baltimore Lectures on Molecular Dynamics and the Wave Theory of Light*. **1904**, Appendix H., Sect. 22, Footnote p. 619. Cambridge University Press Warehouse, London.
2. Ma, W.; Xu, L.; De moura, A. F.; Wu, X.; Kuang, H.; Xu, C.; Kotov, N. A. Chiral Inorganic Nanostructures. *Chem. Rev.* **2017**, *117*, 8041–8093.
3. Petitjean, M. Chirality in Metric Spaces. *Optim. Lett.* **2020**, *14*, 329–338.
4. Semnani, B.; Flannery, J.; Al Maruf, R.; Bajcsy, M. Spin-preserving chiral photonic crystal mirror. *Light Sci. Appl.* **2020**, *9*, 23.
5. Deng, Y.; Wang, M.; Zhuang, Y.; Liu, S.; Huang, W.; Zhao, Q. Circularly polarized luminescence from organic micro-/nano-structures. *Light Sci. Appl.* **2021**, *10*, 76.
6. Plum, E.; Zhou, J.; Dong, J.; Fedotov, V. A.; Koschny,T.; Soukoulis, C. M.; Zheludev, N. I. Metamaterial with negative index due to chirality. *Phy. Rev. B* **2009**, 79, 035407.
7. Zhang, S.; Park, Y. S.; Li, J.; Lu, X.; Zhang, W.; Zhang, X. Negative Refractive Index in Chiral Metamaterials. *Phys. Rev. Lett.* **2009***, 102*, 023901.
8. Xiao, W.; Ernst, K.-H.; Palotas, K.; Zhang, Y.; Bruyer, E.; Peng, L.; Greber, T.; Hofer, W. A.; Scott, L. T.; Fasel, R. Microscopic origin of chiral shape induction in achiral crystals. *Nat. Chem.* **2016**, *8*, 326–330.
9. Sanganyado, E.; Lu, Z.; Fu, Q.; Schlenk, D.; Gan, J. Chiral Pharmaceuticals: A Review on Their Environmental Occurrence and Fate Processes. *Water Res.* **2017**, *124*, 527–542.
10. Cahn, R. S.; Ingold, C.; Prelog, V. Specification of Molecular Chirality. *Angew. Chem. Int. Ed*. **1966**, *5*, 385–415.
11. Cahn, R.S.; Ingold, C.K; Prelog, V. The specification of asymmetric configuration in organic chemistry. *Experientia* **1956**, *12*, 81–94.
12. Nicholls, L. H.; Rodríguez-Fortuño, F. J.; Nasir, M. E.; Córdova-Castro, R. M.; Olivier, N.; Wurtz, G. A.; Zayats, A. V. Ultrafast Synthesis and Switching of Light Polarization in Nonlinear Anisotropic Metamaterials. *Nat. Photonics* **2017**, *11*, 628–633.
13. Albano, G.; Pescitelli, G.; Di Bari, L. Chiroptical Properties in Thin Films of Pi-Conjugated Systems. *Chem. Rev.* **2020**, *120*, 10145–10243.
14. Gong, Z.-L.; Zhu, X.; Zhou, Z.; Zhang, S.-W.; Yang, D.; Zhao, B.; Zhang, Y.-P.; Deng, J.; Cheng, Y.; Zheng, Y.-X.; Zang, S.-Q.; Kuang, H.; Duan, P.; Yuan, M.; Chen, C.-F.; Zhao, Y. S.; Zhong, Y.-W.; Tang, B. Z.; Liu, M. Frontiers in Circularly Polarized Luminescence: Molecular Design, Self-Assembly, Nanomaterials, and Applications. *Sci. China Chem.* **2021**, *64*, 2060–2104.
15. Sherson, J. F.; Krauter, H.; Olsson, R. K.; Julsgaard, B.; Hammerer, K.; Cirac, I.; Polzik, E. S. Quantum Teleportation between Light and Matter. *Nature* **2006**, *443*, 557–560.
16. Richardson, R. D.; Baud, M. G. J.; Weston, C. E.; Rzepa, H. S.; Kuimova, M. K.; Fuchter, M. J. Dual Wavelength Asymmetric Photochemical Synthesis with Circularly Polarized Light. *Chem. Sci.* **2015**, *6*, 3853–3862.

17. Han, J.; Guo, S.; Lu, H.; Liu, S.; Zhao, Q.; Huang, W. Recent Progress on Circularly Polarized Luminescent Materials for Organic Optoelectronic Devices. *Adv. Opt. Mater.* **2018**, *6*, 1800538.
18. Baek, K.; Lee, D.-M.; Lee, Y.-J.; Choi, H.; Seo, J.; Kang, I.; Yu, C.-J.; Kim, J.-H. Simultaneous Emission of Orthogonal Handedness in Circular Polarization from a Single Luminophore. *Light: Sci. Appl.* **2019**, *8*, 120.
19. Sang, Y.; Han, J.; Zhao, T.; Duan, P.; Liu, M. Circularly Polarized Luminescence in Nanoassemblies: Generation, Amplification, and Application. *Adv. Mater.* **2020**, *32*, 1900110.
20. Emeis, C. A.; Oosterhoff, L. J. Emission of Circularly-Polarised Radiation by Optically-Active Compounds. *Chem. Phys. Lett.* **1967**, *1*, 129–132.
21. Takaishi, K.; Iwachido, K.; Takehana, R.; Uchiyama, M.; Ema, T. Evolving Fluorophores into Circularly Polarized Luminophores with a Chiral Naphthalene Tetramer: Proposal of Excimer Chirality Rule for Circularly Luminescence. *J. Am. Chem. Soc.* **2019**, *141*, 6185–6190.
22. Takaishi, K.; Hinoide, S.; Matsumoto, T.; Ema, T. Axially Chiral peri-Xanthenoxanthenes as a Circularly Polarized Luminophore. *J. Am. Chem. Soc.* **2019**, *141*, 11852–11857.
23. Sun, Z.-B.; Liu, J.-K.; Yuan, D.-F.; Zhao, Z.-H.; Zhu, X.-Z.; Liu, D.-H.; Peng, Q.; Zhao, C.-H. 2,2′-Diamino-6,6′-diboryl-1,1′-binaphthyl: A Versatile Building Block for Temperature-Dependent Dual Fluorescence and Switchable Circularly Polarized Luminescence. *Angew. Chem., Int. Ed.* **2019**, *58*, 4840–4846.
24. Schnitzlein, M.; Shoyama, K.; Würthner, F. A highly fluorescent bora[6]helicene exhibiting circularly polarized light emission. *Chem. Sci.* **2024**, *15,* 2984–2989.
25. Mori, T. Significance of Vibronic Coupling that Shapes Circularly Polarized Luminescence of Double Helicenes. *Angew. Chem., Int. Ed.* **2024**, *63*, e202319702.
26. Tian, X.; Shoyama, K.; Mahlmeister, B.; Brust, F.; Stolte, M.; Würthner, F. Naphthalimide-Annulated [n]Helicenes: Red Circularly Polarized Light Emitters. *J. Am. Chem. Soc.* **2023**, *145*, 9886–9894.
27. Kikuchi, K.; Nakamura, J.; Nagata, Y.; Tsuchida, H.; Kakuta, T.; Ogoshi, T.; Morisaki, Y. Control of circularly polarized luminescence by orientation of stacked π-electron systems. *Chem. - Asian J.* **2019**, *14*, 1681–1685.
28. Chen, J.-F.; Yin, X.; Wang, B.; Zhang, K.; Meng, G.; Zhang, S.; Shi, Y.; Wang, N.; Wang, S.; Chen, P. Planar Chiral Organoboranes with Thermoresponsive Emission and Circularly Polarized Luminescence: Integration of Pillar[5]arenes with Boron Chemistry. *Angew. Chem., Int. Ed.* **2020**, *59*, 11267–11272.
29. Yang, J. G.; Li, K.; Wang, J.; Sun, S.; Chi, W.; Wang, C.; Chang, X.; Zou, C.; To, W. P.; Li, M. D.; Liu, X.; Lu, W.; Zhang, H. X.; Che, C. M.; Chen, Y. Controlling Metallophilic Interactions in Chiral Gold(I) Double Salts towards Excitation Wavelength-Tunable Circularly Polarized Luminescence. *Angew. Chem., Int. Ed.* **2020**, *59*, 6915–6922.
30. Ying, A.; Ai, Y.; Yang, C.; Gong, S. AggregationDependent Circularly Polarized Luminescence and Thermally Activated Delayed Fluorescence from Chiral CarbeneCu-I-Amide Enantiomers. *Angew. Chem. Int. Ed.* **2022**, *61*, e202210490.

31. Willis, B.-A. N.; Schnable, D.; Schley, N. D.; Ung, G. Spinolate Lanthanide Complexes for High Circularly Polarized Luminescence Metrics in the Visible and Near-Infrared. *J. Am. Chem. Soc.* **2022***, 144 (49)*, 22421–22425.
32. Hasegawa, Y.; Miura, Y.; Kitagawa, Y.; Wada, S.; Nakanishi, T.; Fushimi, K.; Seki, T.; Ito, H.; Iwasa, T.; Taketsugu, T.; Gon, M.; Tanaka, K.; Chujo, Y.; Hattori, S.; Karasawa, M.; Ishii, K.; Spiral Eu (III) coordination polymers with circularly polarized luminescence. *Chem. Commun*. **2018**, *54*: 10695–10697.
33. Hall, L. A.; D'Alessandro, D. M.; Lakhwani, G. Chiral metal–organic frameworks for photonics. *Chem. Soc. Rev.*, **2023**, *52*, 3567–3590.
34. Wang, X.-Z.; Sun, M.-Y.; Huang, Z. J.; Xie, M.; Huang, R. S.; Lu, H. H.; Zhao, Z. J.; Zhou, X.-P.; Li, D. Turn-On Circularly Polarized Luminescence in Metal-Organic Frameworks. *Adv. Opt. Mater.* **2021**, *9 (23)*, 2002096–2002102.
35. Xu, L.; Wang, C.; Li, Y.-X.; Xu, X.-H.; Zhou, L.; Liu, N.; Wu, Z.-Q. Crystallization-Driven Asymmetric Helical Assembly of Conjugated Block Copolymer and the Aggregation Induced White-light Emission and Circularly Polarized Luminescence. *Angew. Chem., Int. Ed.* **2020**, *59*, 16675–16682.
36. Maeda, K.; Nozaki, M.; Hashimoto, K.; Shimomura, K.; Hirose, D.; Nishimura, T.; Watanabe, G.; Yashima, E. Helix-Sense-Selective Synthesis of Right- and Left-Handed Helical Luminescent Poly(Diphenylacetylene)s with Memory of the Macromolecular Helicity and Their Helical Structures. *J. Am. Chem. Soc.* **2020**, *142*, 7668–7682.
37. Han, J.; You, J.; Li, X.; Duan, P.; Liu, M. Full-color tunable circularly polarized luminescent nanoassemblies of achiral AIEgens in confined chiral nanotubes. *Adv. Mater.* **2017**, *29,* 1606503.
38. Du, C.; Li, Z.; Zhu, X.; Ouyang, G.; Liu, M. Hierarchically Self-Assembled Homochiral Helical Microtoroids. *Nat. Nanotechnol.* **2022**, *17*, 1294–1302.
39. Zhang, L.; Wang, H.-X.; Li, S.; Liu, M. Supramolecular chiroptical switches. *Chem. Soc. Rev.* **2020**, *49*, 9095–9120.
40. Takaishi, K.; Iwachido, K.; Ema, T. Solvent-Induced Sign Inversion of Circularly Polarized Luminescence: Control of Excimer Chirality by Hydrogen Bonding. *J. Am. Chem. Soc.* **2020**, *142*, 1774–1779.
41. Niu, D.; Ji, L.; Ouyang, G.; Liu, M. Histidine Proton Shuttle-Initiated Switchable Inversion of Circularly Polarized Luminescence. *ACS Appl. Mater. Interfaces* **2020**, *12*, 18148–18156.
42. Wang, C.; Liu, L.; Wang, J.; Yan, Y. Electrochemically Switchable Circularly Polarized Photoluminescence within Self-Assembled Conducting Polymer Helical Microfibers. *J. Am. Chem. Soc.* **2022**, *144*, 19714–19718.
43. Han, J.; Shi, Y.; Jin, X.; Yang, X.; Duan, P. Regulating the excited state chirality to fabricate high-performance-solid-state circularly polarized luminescence materials. *Chem. Sci.* **2022**, *13*, 6074–6080.
44. Garcia-Garibay, M. A. Nanoscale gadgets. *Nat. Mater.* **2008**, *7*, 431–432.
45. Vogelsberg, C. S.; Garcia-Garibay, M. A. Crystalline molecular machines: function, phase order, dimensionality, and composition. *Chem. Soc. Rev.* **2012**, *41*, 1892–1910.

46. Howe, M. E.; Garcia-Garibay, M. A. The Roles of Intrinsic Barriers and Crystal Fluidity in Determining the Dynamics of Crystalline Molecular Rotors and Molecular Machines. *J. Org. Chem*. **2019**, *84*, 9835–9849.
47. Costil, R.; Holzheimer, M.; Crespi, S.; Simeth, N. A.; Feringa, B. L. Directing coupled motion with light: a key step toward machine-like function*, Chem. Rev.* **2021**, *121*, 13213–13237.
48. Ehnbom, A.; Gladysz, J. A. Gyroscopes and the Chemical Literature, 2002–2020: Approaches to a Nascent Family of Molecular Devices. *Chem. Rev*. **2021**, *121*, 3701–3750.
49. Erbas-Cakmak, S.; Leigh, D. A.; McTernan, C. T.; Nussbaumer, A. L. Artificial molecular machines. *Chem. Rev.* **2015**, *115*, 10081–10206.
50. Jin, M.; Ando, R.; Jellen, M. J.; Garcia-Garibay, M. A.; Ito, H. Encapsulating N-heterocyclic carbene binuclear transition-metal complexes as a new platform for molecular rotation in crystalline solid-state. *J. Am. Chem. Soc.* **2021**, *143*, 1144–1153.
51. Nuñez, J. E.; Natarajan, A.; Khan, S. I.; Garcia-Garibay, M. A. Synthesis of a Triply-Bridged Molecular Gyroscope by a Directed Meridional Cyclization Strategy. *Org. Lett.* **2007**, *9*, 3559–3561.
52. Lang, G. M.; Shima, T.; Wang, L.; Cluff, K. J.; Skopek, K.; Hampel, F.; Blümel, J.; Gladysz, J. A. Gyroscope-like complexes based on dibridgehead diphosphine cages that are accessed by three-fold intramolecular ring-closing metatheses and encase Fe(CO)3, Fe(CO)2 (NO)+, and Fe(CO)3(H)+ rotators. *J. Am. Chem. Soc.* **2016**, *138*, 7649–7663.
53. Gould, S. L.; Tranchemontagne, D.; Yaghi, O. M.; Garcia-Garibay, M. A. Amphidynamic Character of Crystalline MOF-5: Rotational Dynamics of Terephthalate Phenylenes in a Free-Volume, Sterically Unhindered Environment. *J. Am. Chem. Soc.* **2008**, *130*, 3246–3247.
54. Vukotic, V. N.; Harris, K. J.; Zhu, K.; Schurko, R. W.; Loeb, S. J. Metal-organic frameworks with dynamic interlocked components. *Nat. Chem.* **2012**, *4,* 456–460.
55. Jin, M.; Matsuura, S.; Yamamoto, H.; Mizuno, M.; Ito, H. Multidynamic Crystalline Molecular Rotors Comprising an N-Heterocyclic Carbene Binuclear Au(I) Complex Bearing Multiple Rotators*. Eur. J. Org. Chem.* **2023**, e202201468.
56. Ando, R.; Sato-Tomita, A.; Ito, H.; Jin, M. Giant Crystalline Molecular Rotors that Operate in the Solid State*. Angew. Chem. Int. Ed.* **2023**, *62*, e202309694.
57. Yao, Z. S.; Mito, M.; Kamachi, T.; Shiota, Y.; Yoshizawa, K.; Azuma, N.; Miyazaki, Y.; Takahashi, K.; Zhang, K.; Nakanishi, T.; Kang, S.; Kanegawa, S.; Sato, O. Molecular motor-driven abrupt anisotropic shape change in a single crystal of a Ni complex. *Nat. Chem.* **2014**, *6*, 1079–1083.
58. Setaka, W.; Yamaguchi, K. A Molecular Balloon: Exp Jin, M.; Kitsu, R.; Hammyo, N.; Sato-Tomita, A.; Mizuno, M.; Mikherdov, A. S.; Tsitsvero, M.; Lyalin, A.; Taketsugu, T.; Ito, H. A Steric-Repulsion-Driven Clutch Stack of Triaryltriazines: Correlated Molecular Rotations and a Thermoresponsive Gearshift in the Crystalline Solid. *J. Am. Chem. Soc*. **2023**, *145*, 27512–27520.
59. Jin, M.; Kitsu, R.; Hammyo, N.; Sato-Tomita, A.; Mizuno, M.; Mikherdov, A. S.; Tsitsvero, M.; Lyalin, A.; Taketsugu, T.; Ito, H. A Steric-Repulsion-Driven Clutch Stack of Triaryltriazines: Correlated Molecular Rotations and a Thermoresponsive Gearshift in the Crystalline Solid. *J. Am. Chem. Soc*. **2023**, *145*, 27512–27520.

60. Akutagawa, T.; Koshinaka, H.; Sato, D.; Takeda, S.; Noro, S.; Takahashi, H.; Kumai, R.; Tokura, Y.; Nakamura, T. Ferroelectricity and polarity control in solid-state flip-flop supramolecular rotators. *Nat. Mater.* **2009**, *8*, 342–347.
61. Friend, R. H.; Gymer, R. W.; Holmes, A. B.; Burroughes, J. H.; Marks, R. N. Electroluminescence in conjugated polymers. *Nature* **1999**, *397*, 121–128.

2. Crystallization-Induced Chirality Transfer in Conformationally Flexible Azahelicene Au(I) Complexes with Circularly Polarized Luminescence Activation

2.1 Introduction

Angularly annulated polyaromatic compounds such as helicenes,[1] twistacenes,[2] and related twisted polyaromatic systems[3, 4] are currently gaining significant attention due to their ability to exhibit helical chirality (Figure 2.1a). This unique feature makes them promising for applications in chiroptical devices,[5, 6] asymmetric catalysis,[7-9] organic electronics,[10] molecular machines,[11, 12] and medicinal chemistry.[13, 14] Since the helical chirality in these systems originates from a strain-induced twist,[3] low-strain annulated π-systems with low-lying conformational flip barriers can exhibit dynamic chirality, allowing interconversion between enantiomers (Figure 2.1b).[15-17] Although this dynamic chirality can sometimes be exploited to obtain chirality-switchable properties,[18] as well as easy access to different conformers of a polyaromatic species,[19] it often merely results in racemization, which negates most of the valuable properties derived from helical homochirality. Therefore, stabilizing the homochirality of these systems is crucial to preserve their unique properties.

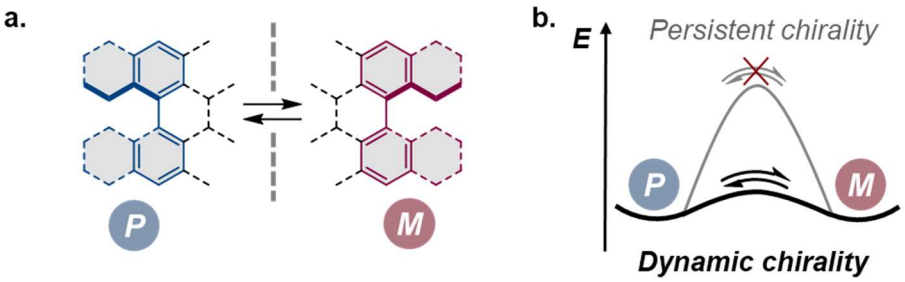

Figure 2.1 The dynamic helical chirality and their energy.

The most common approach to suppress dynamic chirality in polyaromatic species is kinetic stabilization of their conformation by introducing bulky substituents in the polyaromatic scaffold, interlocking the system and dramatically increasing the conformational flip barrier.[20, 21] However, enantioselective reactions during synthesis or subsequent chiral resolution of the formed enantiomeric mixture during isolation is required,[22] which can be laborious and challenging. Another approach involves chirality transfer via the introduction of a chiral auxiliary group to a twisted and flexible polyaromatic system (Figure 2.2).

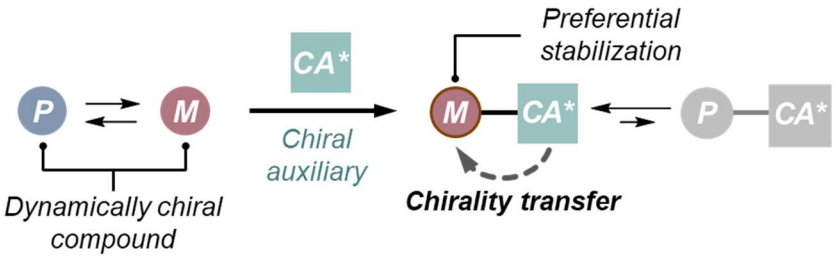

Figure 2.2 Suppress chirality via chirality transfer.

As examples, using perylene diimide-based twistacene species, it has been demonstrated that chirality transfer can occur intramolecularly by introducing chiral auxiliary groups that induce strain in the polyaromatic ribbon (Figure 2.3a),[23] steric repulsion (Figure 2.3b),[24, 25] or attractive through-space interactions between molecule fragments (Figure 2.3c).[26, 27] Additionally, intermolecular chirality transfer from a molecule with persistent chirality to a conformationally flexible perylene-diimide-based cyclophane species resulted in the stabilization of one of the conformational enantiomers of the cyclophane through host-guest interactions in solution (Figure 2.3d).[28] Conversely, the binding of flexible helicene guests exhibiting dynamic chirality by homochiral hosts resulted in the enantiomerization of enantiomerically pure guests[29] or deracemization of racemic guest mixtures[30] due to a reduced enantiomerization barrier (Figure 2.3e).

Moreover, the chirality transfer can also influence the properties of dynamic twistacene systems, such as solvent- and redox-dependent electronic circular dichroism[24, 25], and circularly polarized luminescence.[26] This indicates the potential for utilization of chirality transfer to flexible polyaromatic systems as a promising strategy for constructing new chirality-induced functional systems.

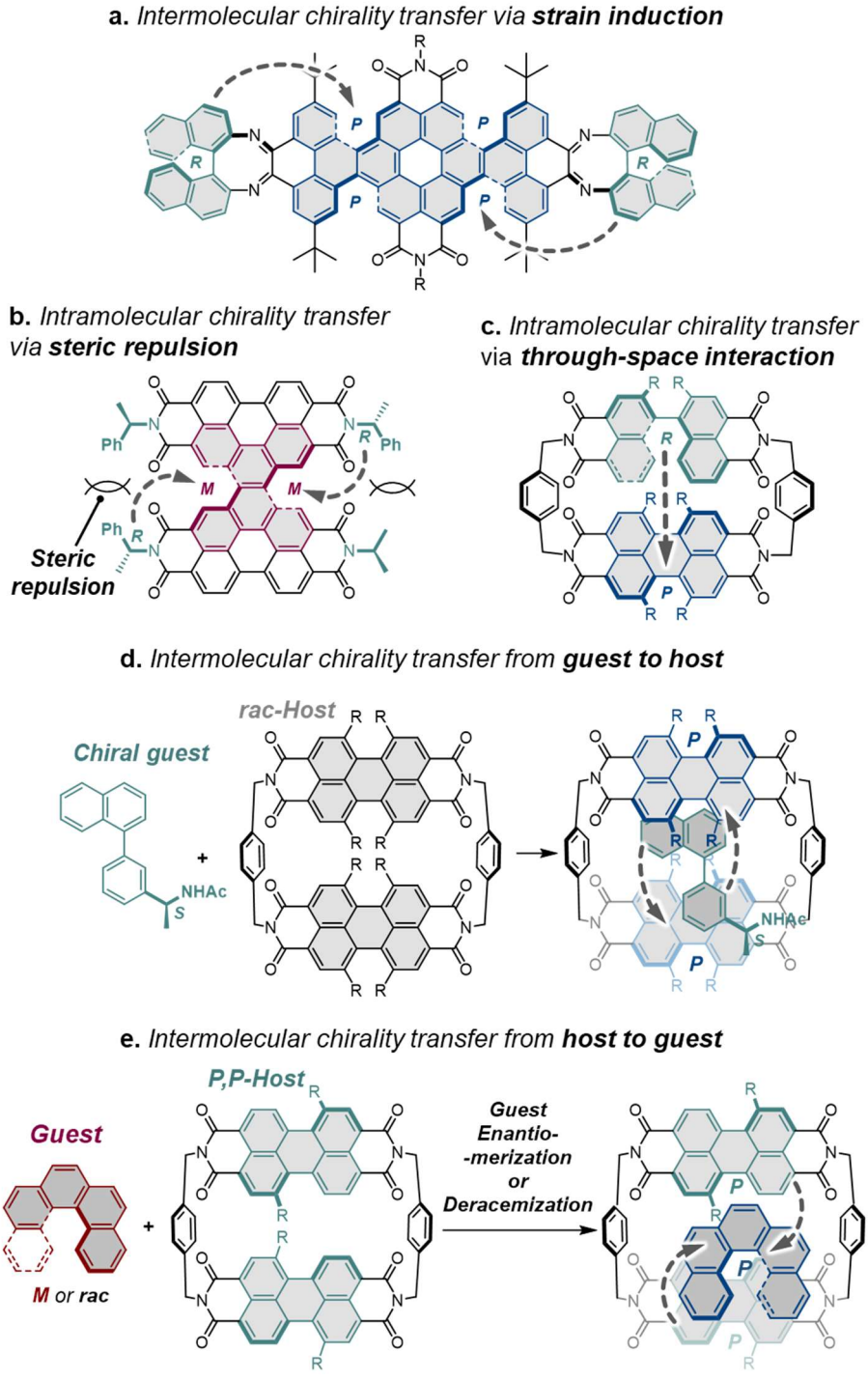

Figure 2.3 Previously report include chirality transfer strategy.

Because the abovementioned examples of dynamic chirality control via chirality transfer operate in solution, in some cases, the effect is limited to preferential thermodynamic stabilization of one of the conformers without complete suppression of dynamic chirality. That is, interconversion between the different forms of the studied species may still occur in solution. In this chapter, I introduce a new approach for dynamic chirality stabilization in azahelicene species via crystallization-induced intermolecular chirality transfer in Au(I) complexes featuring a rigid enantio-pure *N*-heterocyclic carbene (NHC) ligand with persistent chirality and a conformationally flexible azahelicene ligand, namely, dibenzo[*c,g*]carbazole or benzo[*c*]carbazole. In solution, the NHC Au(I) dibenzocarbazole complexes exhibit dynamic chirality with very rapid exchange between the *P*- and *M*-conformers (Figure 2.4). However, when an NHC ligand with a shape tailored for complementary interactions is used, the crystallization of these complexes can not only suppress the dynamic chirality of the dibenzocarbazole moiety but also induce and stabilize homochirality through intermolecular chirality transfer by the intermolecular conjunction between the chiral NHC and dibenzocarbazole ligands in the crystal. In the case of the Au(I) benzocarbazole complexes, the presence of a similar conjunction between the molecules in the crystals induces chirality in the initially achiral benzocarbazole ligand. Furthermore, the crystallization of these complexes activates their circularly polarized luminescence (CPL), which was suppressed in solution due to dynamic chirality. Notably, the complexes exhibiting intermolecular chirality transfer in their crystals display a dramatic 5–10-fold enhancement in their luminescence dissymmetry factor values compared to the structures without direct chirality transfer. I believe that this approach to engineering intermolecular chirality transfer will be useful for the development of new types of solid-state chiral and chiroptical materials.[6, 31-35]

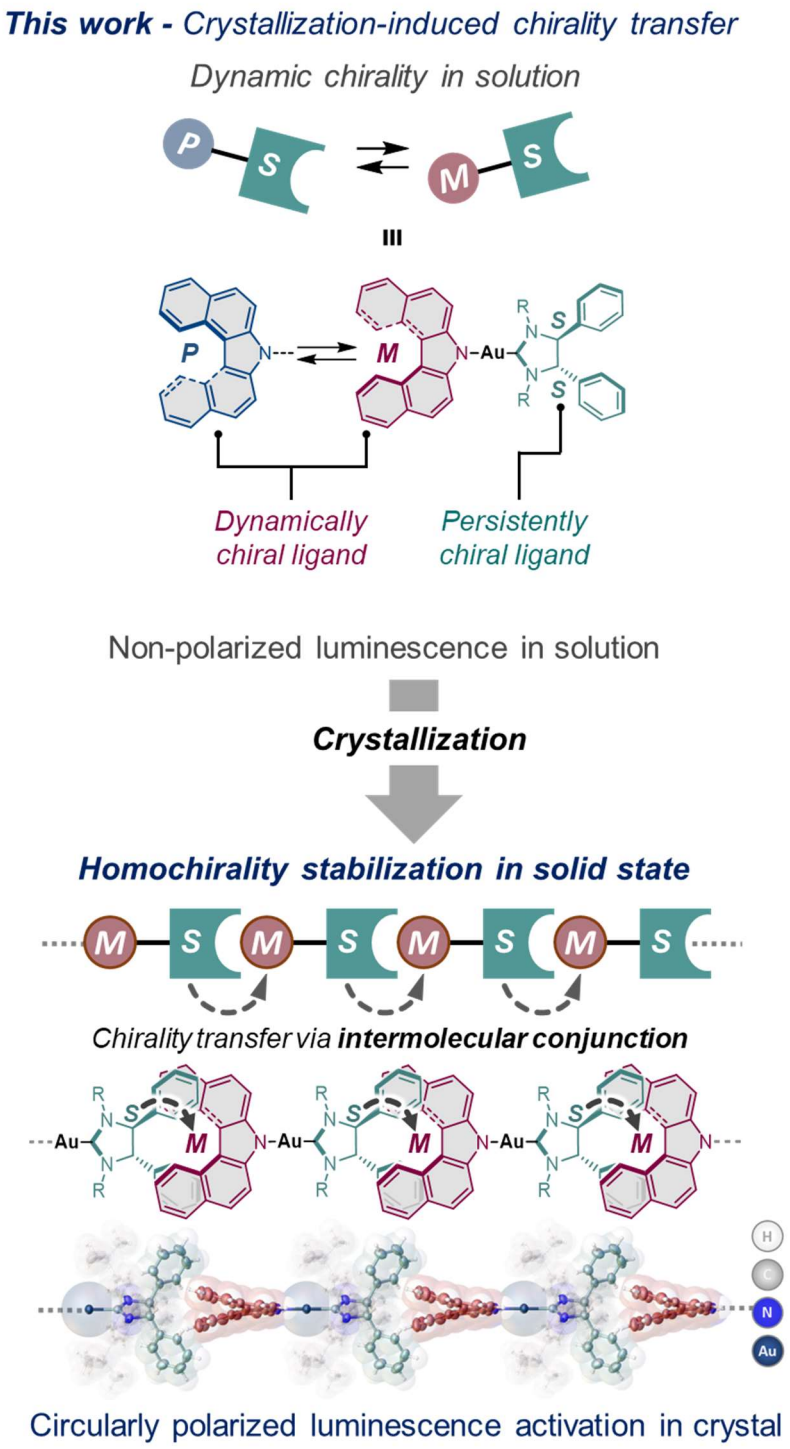

Figure 2.4 Brief introduce of this chapter: crystallization-induced chirality transfer in conformationally flexible azahelicene Au(I) complexes with CPL activation.

2.2 Result and discussion

2.2.1 Synthesis and Characterization of NHC Au(I) Azahelicene Complexes in Solution.

To explore the potential for ligand-to-ligand chirality transfer in NHC Au(I) azahelicene complexes, I investigated a set of NHC and carbazole ligands (Figure 2.5). 1,3-Bis(3,5-di-*tert*-butylbenzyl)-imidazolinium scaffolds with various substituents at the 4- and 5-positions of the imidazolinium backbone were utilized to study the capability NHC ligand of chirality transfer: the unsubstituted achiral NHC (**1**) (as a reference structure), the cyclohexyl-substituted NHC enantiomer pair [**2**-(*S,S*) and **2.2**-(*R,R*)], and the diphenyl-substituted enantiomer pair [**3**-(*S,S*) and **3**-(*R,R*)]. The azahelicene ligands were benzo[*c*]carbazole (**BCz**), which served as a reference structure with no inherent chirality, and dibenzo[*c,g*]carbazole (**DBCz**), which should be capable of displaying dynamic chirality in solution. The target NHC Au(I) azahelicene complexes were obtained in 84–96% yields by reacting the corresponding NHC Au(I) chloride complexes and DBCz or BCz in the presence of potassium *tert*-butoxide in tetrahydrofuran solution at 45 °C. All complexes were characterized using ^{1}H and ^{13}C NMR spectroscopy, high-resolution mass-spectrometry (HRMS), C, H, N elemental analysis, thermogravimetric analysis (TGA), differential scanning calorimetry (DSC), single-crystal and powder X-ray diffraction (SCXRD and PXRD), circular dichroism (CD), photoluminescence, and circularly polarized luminescence (CPL) spectroscopy in solution and the solid state.

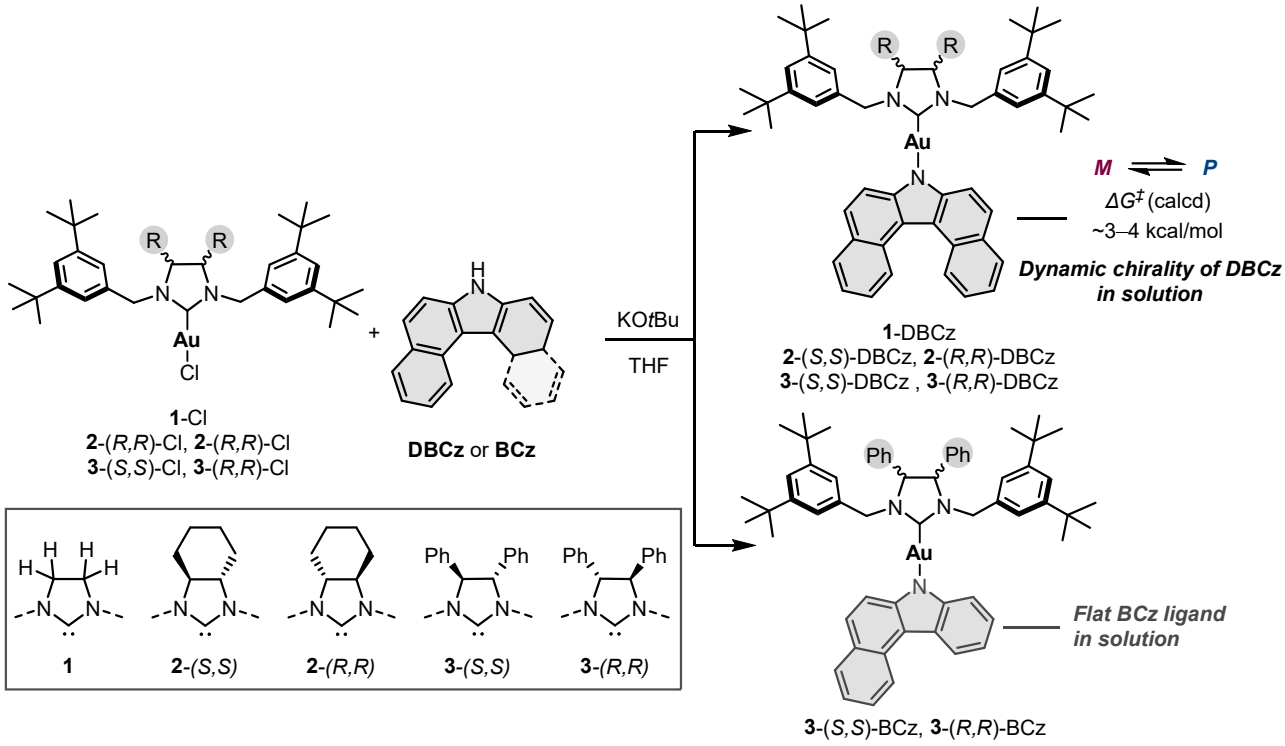

Figure 2.5 Synthesis and dynamic chirality of NHC Au(I) azahelicene complexes.

For all complexes, the solution-state ^{1}H and ^{13}C NMR spectra display only one set of signals, indicating that either only a single species is present or the annulated carbazole ligands undergo *P*/*M*-exchange that is too rapid to be observed on the NMR timescale. For DBCz complexes, even low-temperature ^{1}H NMR measurements (–80 °C in CD_2Cl_2) have not shown any noticeable signal splitting that could indicate stabilization of two distinct forms of the DBCz ligand in solution (Figures S2.2 and S2.3). Therefore, to investigate the potential dynamic chirality and intramolecular chirality transfer for the obtained complexes in solution, I conducted a theoretical investigation of the energy barriers for interconversion and the relative stability of the two possible *P*-/*M*-conformers of the **3**-(*S*,*S*)-DBCz complex, as well as of the structure of **3**-(*S*,*S*)-BCz in CH_2Cl_2 (using the PBE0-D3(BJ) /def2TZVP+MDF60/SMD(CH_2Cl_2) level of theory[36-42]). The optimization of **3**-(*S*,*S*)-BCz yields a structure featuring an overall flat BCz moiety; therefore, the BCz ligand should not possess any chirality and should exist in a single form in solution (Figure S2.5). In contrast, for the **3**-(*S*,*S*)-DBCz complexes, two structures featuring the *P*- and

M-conformation of DBCz moiety could be present in solution with an energy difference (ΔG_{298}) of 0.5 kcal/mol and a DBCz conformation flip energy barrier ($\Delta G^{\ddagger}$) of 3–4 kcal/mol (Table S2.3, Figure S2.4). The obtained energy values support the presence of a very fast exchange process between the *P*- and *M*-conformers with the expected enantiomer half-life in the microsecond range.[43] The enantiomerization barriers of DBCz complexes are comparable to the reported one for the dibenzo[*c,g*]fluorenide anion ($\Delta E^{\ddagger}_{calcd}$ = 4.3 kcal/mol)[44] which is isoelectronic to free DBCz. Considering "conventional" helicene species, the enantiomerization barrier of DBCz is even closer to carbo[4]- and monoaza[4]helicenes ($\Delta E^{\ddagger}_{calcd}$ ~ 4 kcal/mol)[45, 46] than to relevant carbo[4]helicenes and pyridine-based monoaza[5]helicene species ($\Delta G^{\ddagger}_{exp}$ = 20–23 kcal/mol).[47] The reason for that is the presence of the five-membered pyrrole core in DBCz instead of a six-membered pyridine or benzene one in similar [5]helicene species, which results in a significantly lower strain of DBCz π-system. In summary, the presence of a small conformation flip barrier as well as a small energy difference between the conformers, imply the absence of any significant intramolecular chirality transfer from the NHC to the DBCz ligands.

2.2.2 Crystal Structures and Chirality Transfer.

Crystallization of the obtained complexes yielded crystalline samples with no solvent inclusion. The obtained single crystals were characterized by SCXRD at 293 K. The composition of the bulk crystalline samples was confirmed by PXRD at room temperature and elemental analysis. The obtained crystalline samples display good thermal stability (see Section S3 for the TGA/DSC data) and can be stored in air for at least several months. The crystal structures of all the complexes are presented in Figures 2.6–2.10, while the crystal data parameters are listed in Tables S2.4–2.6 in the Supporting Information.

The crystal structure of **1**-DBCz with an achiral NHC ligand features the centrosymmetric *Pbca* space group. The asymmetric unit consists of only one

molecule of the complex, while the unit cell contains four pairs of molecules featuring both *P*- and *M*-curved DBCz moieties. Therefore, the crystal of **1**-DBCz can be considered a true racemate (Figure 2.6).

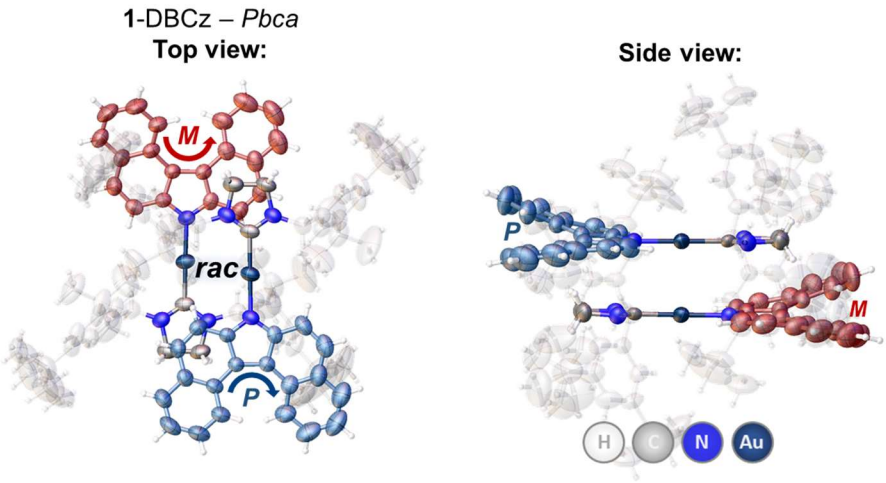

Figure 2.6 Views of crystal structures of **1**-DCBz.

The crystal structures of **2**-(*S,S*)- and **2**-(*R,R)*-DBCz display a similar packing pattern to that observed for **1**-DBCz (Figures S2.11–S2.12). Although the crystal structures of the **2**-(*S,S*)- and **2**-(*R,R*)-DBCz complexes feature a non-centrosymmetric *P*1 space group, they contain both *P*- and *M*-curved DBCz ligands in a 1:1 ratio, forming a diastereomeric mixture in the crystal (Figure 2.7a). Thus, the introduction of the chiral *S,S*- or *R,R*-cyclohexyl moiety in the NHC backbone does not cause direct chirality transfer from the NHC to the DBCz ligand in either solution or the solid state. However, it should be mentioned that the *P*- and *M*-curved DBCz ligands of **2**-(*S,S*)- and **2**-(*R,R*)-DBCz have different packing environments and exhibit different non-covalent interactions with the NHC ligand. For example, for **2**-(*S,S*)-DBCz, the *M*-curved DBCz ligand is involved in only one short C–H···π contact with each of the neighboring *S,S*-cyclohexyl fragments in the NHC ligands, while the *P*-DBCz forms two C–H···π interactions with each NHC fragment (Figure 2.7b). The opposite pattern was observed for **2**-(*R,R*)-DBCz.

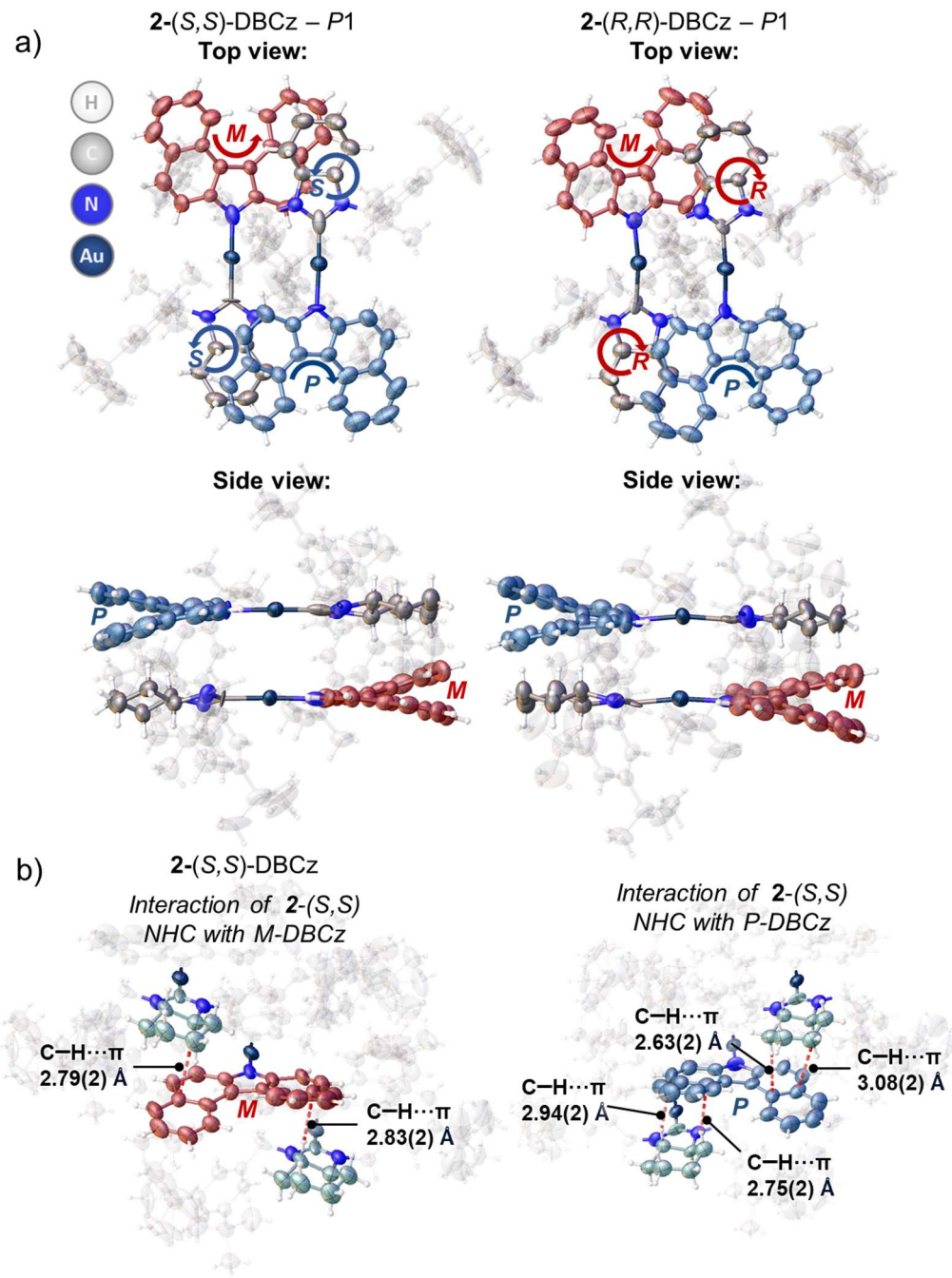

Figure 2.7 (a) Views of crystal structures of **2**-(*S,S*)-DCBz and **2**-(*R,R*)-DCBz; (b)) C–H···π interactions (red stripes) between **2**-(*S,S*)-NHC ligand and *P*- or *M*-DBCz ligands in structure of **2**-(*S,S)*-DBCz.

Unlike the previous examples, the **3**-(*S,S*)- and **3**-(*R,R*)-DBCz complexes, which contain a chiral diphenyl moiety in the NHC backbone, crystallize in an enantiomorphic (chiral) space group pair: $P4_12_12$ and $P4_32_12$, respectively. Each complex features only one type of curved DBCz ligand, i.e., the *M*-conformation in **3**-(*S,S*)-DBCz and the *P*- one in **3**-(*R,R*)-DBCz (Figure 2.8). The fixation of the homochiral

conformation of the DBCz ligand suggests that the “hinge”-shaped chiral **3**-(*S,S*)- and **3**-(*R,R*)-NHC ligands are capable of transferring chirality to the DBCz ligand. In the latter case, the transfer occurs through an intermolecular head-to-tail conjunction between the NHC diphenyl moiety and the DBCz ligand assisted by intermolecular C–H···π interactions (Figure S2.6). Additionally, in both crystal structures, the molecules of the complex form a helical supramolecular arrangement defined by the presence of a 4-fold screw axis in the unit cell: an *M*-helical packing for **3**-(*S,S*)-DBCz and a *P*-one for **3**-(*R,R*)-DBCz (Figure S2.13).

Surprisingly, the complexes **3**-(*S,S*)- and **3**-(*R,R*)-BCz, which featured achiral benzo[*c*]carbazole (BCz), resulted in crystal structures almost identical to those of the **3**-(*S,S*)- and **3**-(*R,R*)-DBCz pair: both the ***3***-(*S,S*)-BCz and **3**-(*R,R*)-BCz crystal structures also have the $P4_12_12$ and $P4_32_12$ chiral space groups, as well as nearly the same unit cell parameters as **3**-(*S,S*)- and **3**-(*R,R*)-DBCz (Tables S2.5–S2.6). The observed similarity in the crystal packing of the **3**-(*S,S*)-/ **3**-(*R,R*)-DBCz and **3**-(*S,S*)-/ **3**-(*R,R*)-BCz crystals is possibly due to the disorder of the BCz moiety in two positions in the crystals (Figure S2.14), which “mimics” the shape of the DBCz ligand in the structures of **3**-(*S,S*)- and **3**-(*R,R*)-DBCz. Furthermore, the similar crystal packing effects and the presence of intermolecular head-to-tail conjunction between the NHC and BCz ligands also cause the BCz moiety, which is initially achiral and planar in solution (according to DFT calculations), to adopt a chiral curvature in the solid state due to chirality transfer from the NHC ligand (Figure 2.9). As a result, the obtained structures can be described as **3**-(*S,S*)-BCz-(*M*) and **3**-(*R,R*)-BCz-(*P*). The key structural difference between the DBCz- and BCz-derived structures is the degree of curvature of the DBCz- and BCz moieties. The torsion angles (Table S2.7) between the aryl planes demonstrate that the DBCz ligand in **3-**(*S,S*)- and **3**-(*R,R*)-DBCz is almost twice as curved as the BCz in **3**-(*S,S*)- and **3**-(*R,R*)-BCz.

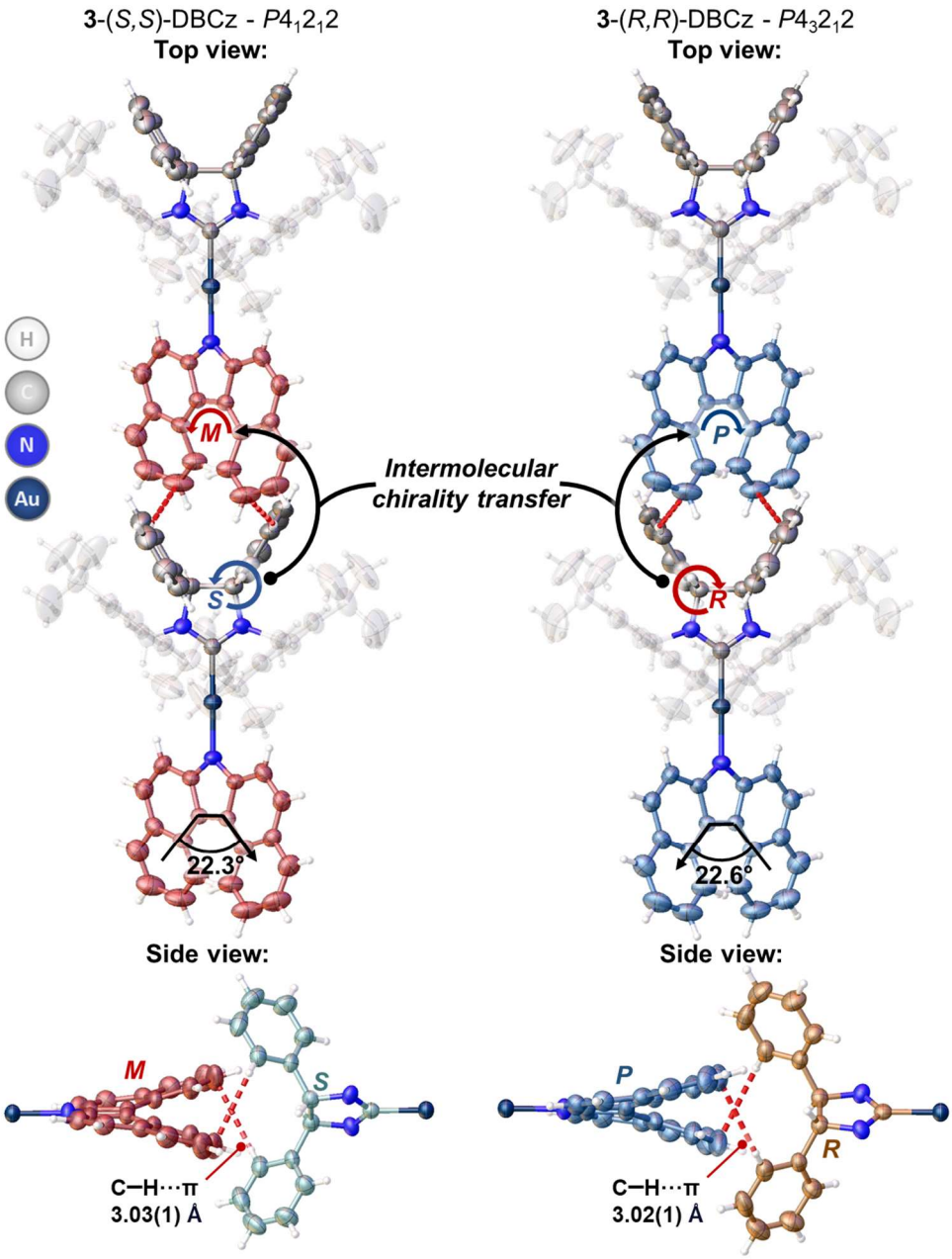

Figure 2.8 Views of crystal structures of **3**-(*S,S*)-DBCz, **3**-(*R,R*)-DBCz. On the side views, the fragments not participating in chirality transfer are omitted for clarity. Blue (*P*) and red (*M*) colors of DBCz ligands indicate the configuration, while blue (*S*) and red (*R*) circular arrows indicate the configuration of chiral center in the NHC ligand. C–H···π interactions indicated by the red stripes.

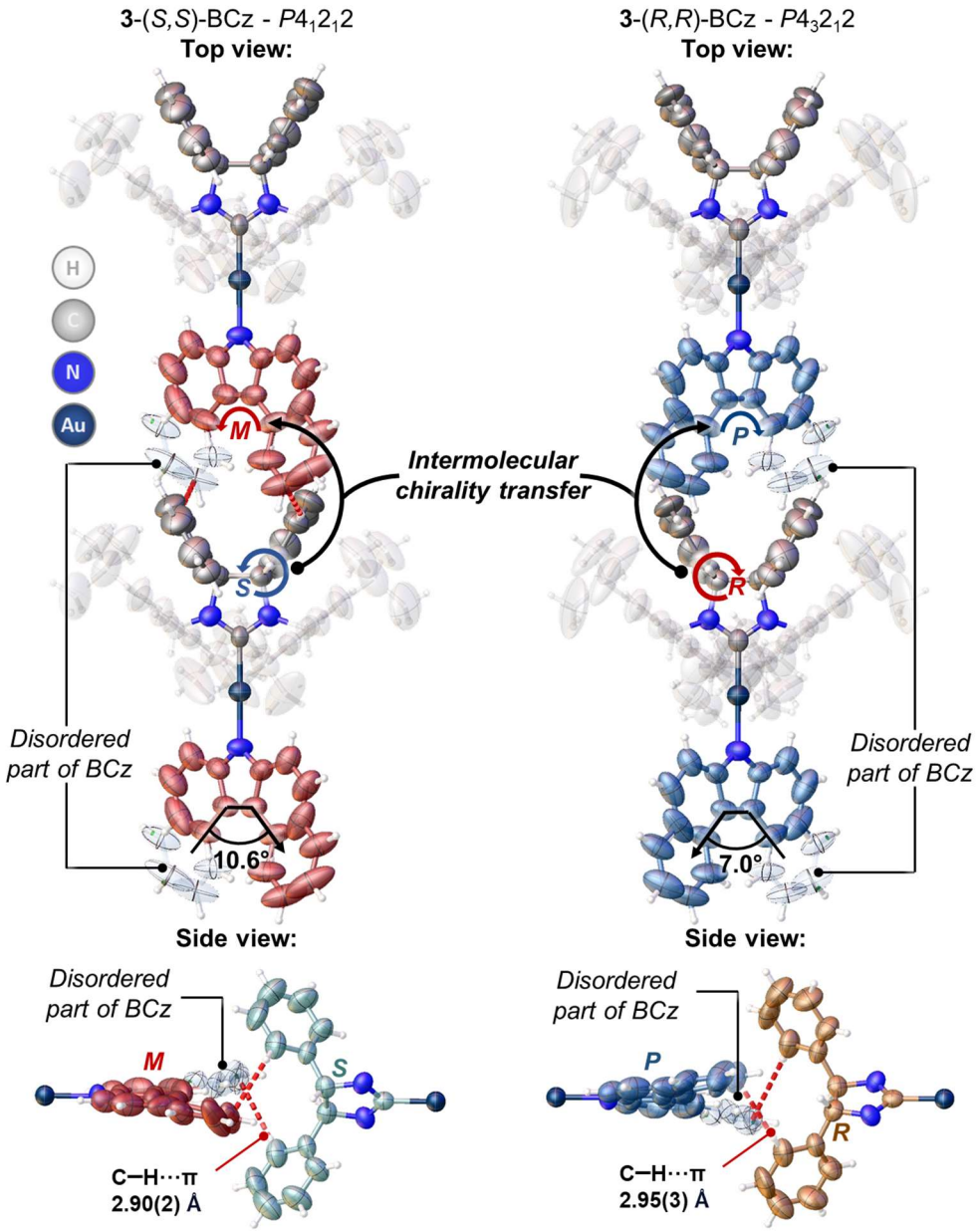

Figure 2.9 Views of crystal structures of **3**-(*S,S*)-BCz, **3**-(*R,R*)-BCz. On the side views, the fragments not participating in chirality transfer are omitted for clarity. Blue (*P*) and red (*M*) colors of DBCz ligands indicate the configuration, while blue (*S*) and red (*R*) circular arrows indicate the configuration of chiral center in the NHC ligand. C–H···π interactions indicated by the red stripes. Transparent ellipsoids depict one of disordered parts of benzo moiety in BCz.

From the obtained structural data, It can be concluded that the structure and shape of the NHC ligand play a crucial role in the chirality transfer to azahelicene

ligands in the solid state. The obtained structures can be categorized into three cases (Figure 2.10):

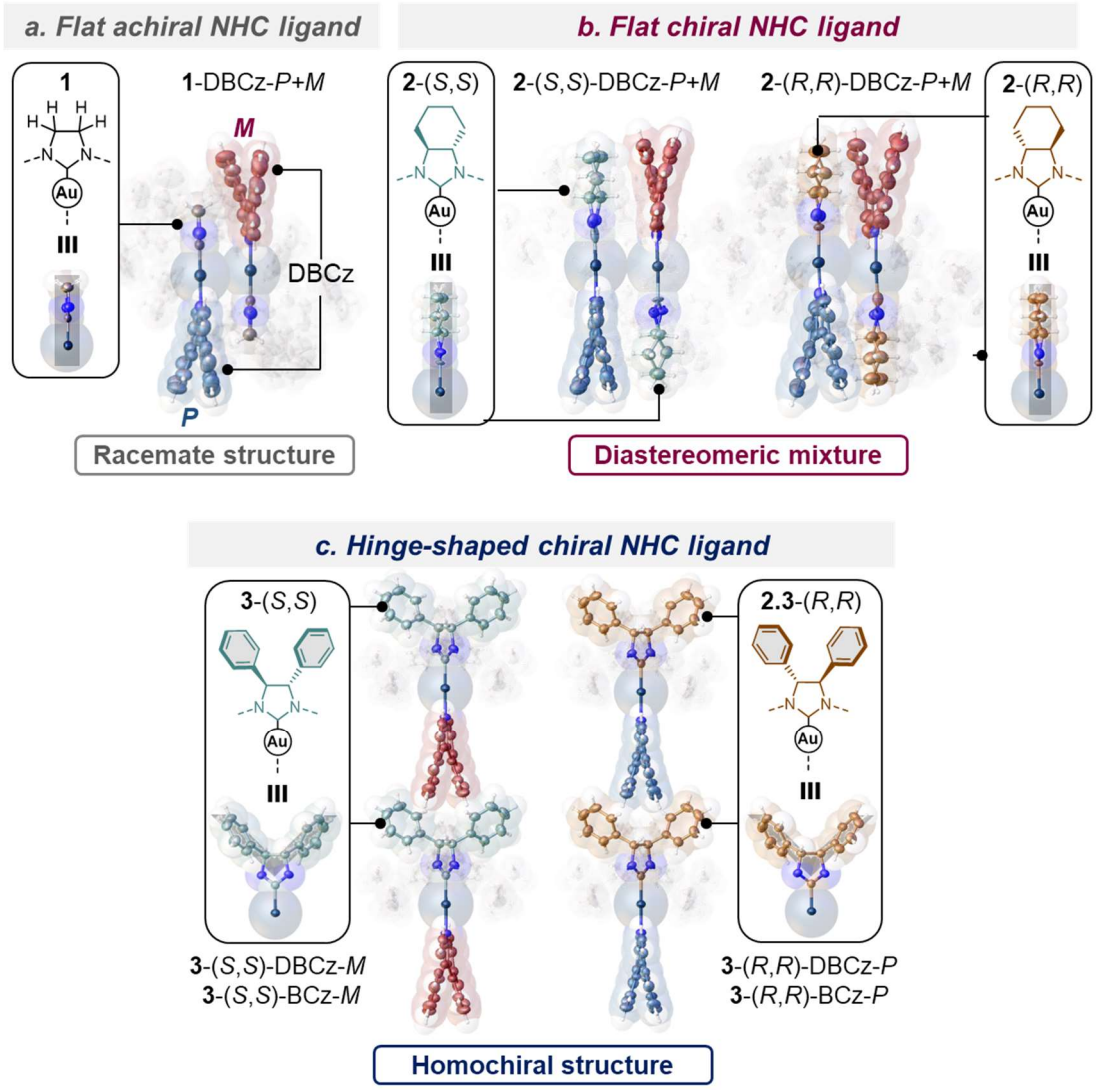

Figure 2.10. (a)The **1**-DBCz complex, in which an achiral NHC ligand forms racemate crystals containing both *P*- and *M*-DBCz moieties; (b) The **2**-(*S,S*)- and **2**-(*R,R*)-DBCz complexes, which have flat chiral NHC ligands that are not capable of chirality transfer, resulting in a diastereomeric mixture with both *P*- and *M*-DBCz moieties in the crystals; (c) The **3**-(*S,S*)- and **3**-(*R,R*)-DBCz/BCz complexes, featuring "hinge"-shaped chiral NHC ligands capable of direct chirality transfer, form homochiral crystal structures with either *P*- or *M*-DBCz/BCz moieties.

This indicates that the mere presence of an additional chiral moiety in the molecule is not sufficient to induce direct chirality transfer and the exclusive

stabilization of either the *M*- or *P*-DBCz conformation. In the case of the **2**-(*S,S*)- and **2**-(*R,R*)-DBCz crystals, the flat shape of the cyclohexyl moiety in the NHC ligand and its inability to form a conjunction with the DBCz ligand results in the coexistence of both *P*- and *M*-DBCz moieties in the crystal, along with a crystal packing similar to the racemate crystal of **1**-DBCz. On the contrary, the bulkier and hinge-shaped diphenyl moiety in **3**-(*S,S*)- and **3**-(*R,R*)-DBCz/BCz is capable of forming a "complimentary pair" with the DBCz/BCz ligands. This leads not only to the stabilization of one form of the DBCz ligand through direct chirality transfer but also to the induction of chirality in the initially achiral BCz ligand.

2.2.3 Chiroptical and Emission Properties of NHC Au(I) Azahelicene Complexes.

The coordination of DBCz and BCz ligands to the Au(I) center leads to a ca. 30 nm red-shift of their absorption in dichloromethane (CH_2Cl_2) solution, while the overall absorption profile remains mostly unchanged (Figure 2.11 for 2.1-DBCz and Figures S2.20–2.21 for the other complexes). Additionally, the absorption within 250–280 nm range should also correspond to the NHC Au(I) fragment, similar to the NHC Au(I) chloride precursor complexes. In the solid state, all complexes exhibit a slightly red-shifted absorption profile that is nearly identical in shape to that in CH_2Cl_2 solution.

Based on an analysis of the experimental spectra and the conducted TD-DFT calculations (Figure 2.11b and Figures S2.7–S2.10), the absorption spectrum of the obtained NHC Au(I) azahelicene complexes can be divided into three regions. From the higher wavelengths down to 350 nm, the absorption is mainly attributed to states involving only DBCz/BCz intra-ligand charge transfer (ILCT) with a slight admixture of Au(I)-to-DBCz/BCz metal-to-ligand charge transfer (MLCT). Below 350 nm, there is a noticeable contribution from ligand-to-ligand (LLCT) charge transfer involving both the NHC and DBCz/BCz moieties. Lastly, from 300 nm to 250 nm, in addition to the absorption from the DBCz ligand, there are ILCT/MLCT bands involving the NHC ligand.

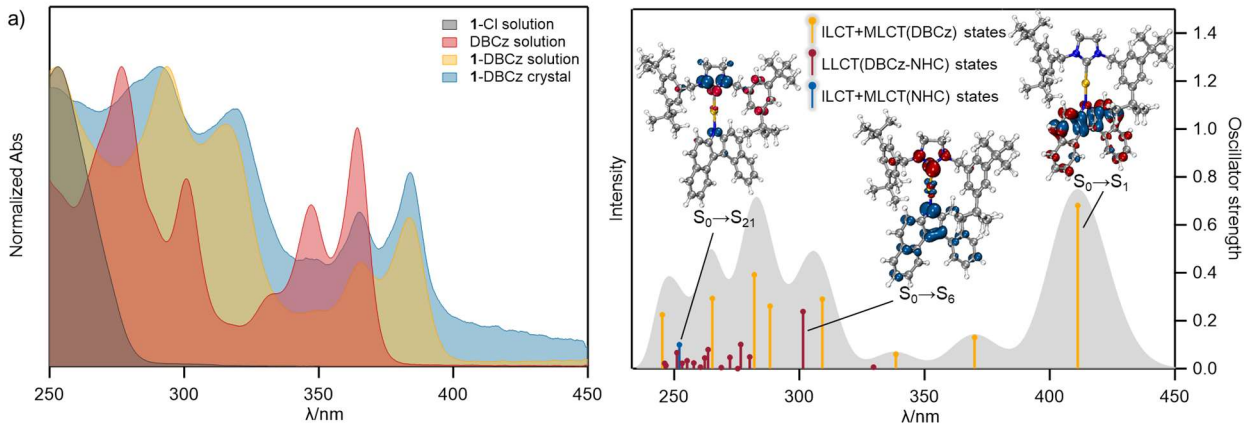

Figure 2.11 . (a) Absorption spectra of **1**-Cl (gray, 1.2×10^{-4} M), DBCz (red, 2×10^{-5} M), **1**-DBCz (yellow, 2×10^{-5} M) in DCM solution, and **1**-DBCz in solid state (blue, 2% w/w in paraffin oil). b) Calculated TD-DFT absorption spectrum and oscillator strengths of **1**-DBCz with the hole-electron distribution maps[38] (isovalue 0.003) for the selected transitions: hole distribution is indicated in blue and electron distribution in red.

As expected, **1**-DBCz does not exhibit any circular dichroism (CD) signal in the CH_2Cl_2 solution due to the absence of a chiral moiety in the NHC ligand and the fast *P/M*-exchange of the DBCz ligand (Figure S2.22). The absence of a CD response was also observed for the crystalline sample of **1**-DBCz due to the presence of two equivalent *P*- and *M*-DBCz moieties in the racemate crystal structure.

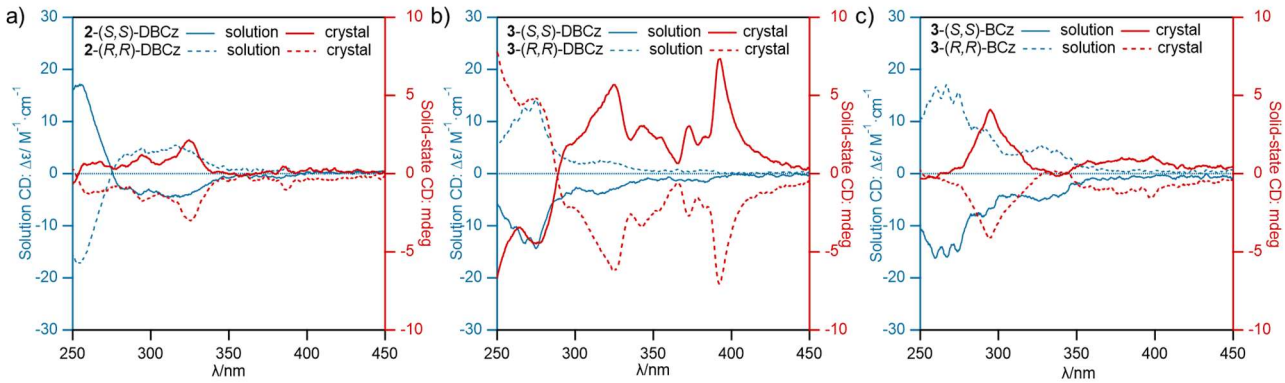

Figure2.12 CD spectra of (a) **2**-(*S,S*)- and **2**-(*R,R*)-DBCz, (b) **3**-(*S,S*)- and **3**-(*R,R*)-DBCz, (c) **3**-(*S,S*)- and **3**-(*R,R*)-BCz complexes in CH_2Cl_2 solution (blue lines, left CD axis, 2×10^{-5} M) and the solid state (red lines, right CD axis, 2% *w*/*w* in paraffin oil).

In contrast, upon introducing the chiral cyclohexyl moiety in the NHC backbone, the **2**-(*S,S*)- and **2**-(*R,R*)-DBCz complexes exhibit a distinct mirrored CD profile in CH_2Cl_2 solution (Figure 2.11a; blue lines). Almost no CD signal was observed in the range of 350–400 nm corresponding to DBCz absorption. However, in the lower wavelength region, two CD areas with opposite Cotton effects are observed, with CD maxima at 330 nm and 256 nm and absorption dissymmetry factor ($|g_{abs}|$) values of 1.4–1.8 × 10^{-4} and 4.5–4.7 × 10^{-4}, respectively. The emergence of CD signal in the 330nm region can be attributed to the LLCT from the chiral NHC ligand to the carbazole fragment of DBCz (Figure S2.8) and should not be significantly affected by DBCz conformation. The Cotton effect maxima at 256 nm can be attributed to the absorption of the chiral NHC Au(I) fragment, and the sign of the Cotton effect in this region is the same as that of the precursor **2**-(*S,S*)- and **2**-(*R,R*)-Cl complexes **(Figure S2.23).** In the crystalline state, the **2**-(*S,S*)- and **2**-(*R,R*)-DBCz complexes exhibit an inversion of the CD signal in the region from 280 nm to 425 nm compared to that in solution (Figure 2.11a; red lines). Additionally, a weak CD signal emerges at ca. 387 nm ($|g_{abs}|$ = 0.3–0.6 × 10^{-3}), and the CD signal at 327 nm is amplified, with $|g_{abs}|$ values of 1.2–1.3 × 10^{-3}. These regions correspond to the DBCz ligand, and the transition from the solution to crystalline state leads to an almost one order of magnitude increase in their $|g_{abs}|$ values. This could be caused by the elimination of the *P*-/*M*-exchange of the DBCz ligand and the confirmational fixation in the solid state. At the same time, in the absence of direct chirality transfer in the crystal, the appearance and increase of the CD response in these regions can be attributed to the presence of asymmetry in the packing environment of the *P*- and *M*-DBCz ligands observed in the crystals.

While the complexes **3**-(*S,S*)- and **3**-(*R,R*)-DBCz and -BCz show similar CD response levels to **2**-(*S,S*)- and **2**-(*R,R*)-DBCz in CH_2Cl_2 solution, more significant changes in the CD profiles were observed after crystallization. In CH_2Cl_2 solution, all the **3**-(*S,S*)-/ **3**-(*R,R*)-DBCz and -BCz complexes exhibit quite similar CD profiles (Figure 2.11b,c; blue

lines). The CD maxima at 275 nm ($|g_{abs}|$ = 5.6–5.8 × 10^{-4}) for **3**-(*S,S*)- and **3**-(*R,R*)-DBCz and at 267 nm ($|g_{abs}|$ = 3.8–4.2 × 10^{-4}) for **3**-(*S,S*)- and **3**-(*R,R*)-BCz correspond mostly to the absorption of the chiral NHC Au(I) fragment with the same sign as parent **2**-(*S,S*)- and **2**-(*R,R*)-Cl complexes (Figure S2.23). At the same time, in the DBCz and BCz absorption regions, the CD response is noticeably weaker: the CD maxima were observed at 316 nm for **3**-(*S,S*)- and **3**-(*R,R*)-DBCz ($|g_{abs}|$ = 0.9–1.2 × 10^{-4}) and at 297 nm for **3**-(*S,S*)- and **3**-(*R,R*)-BCz ($|g_{abs}|$ = 2.0–2.1 × 10^{-4}) and can be attributed to NHC-carbazole LLCT bands (Figures S2.9-S2.10). Conversely, after crystallization, a strong increase in the CD signals in the DBCz and BCz absorption regions was observed. The complexes **3-**(*S,S*)- and **3**-(*R,R*)-DBCz display two main CD maxima at 324 nm and 392 nm with $|g_{abs}|$ values of 2.45–3.22 × 10^{-3} and 4.45–4.46 × 10^{-3}, respectively. In the case of **3**-(*S,S*)- and **3**-(*R,R*)-BCz, the maximum CD response was observed at 295 nm with a $|g_{abs}|$ value of 2.04–2.45 × 10^{-3} which also corresponds to its absorption maximum. Noteworthily, similarly to the **2**-(*S,S*)- and **2**-(*R,R*)-DBCz complexes, the crystallization of the **3**-(*S,S*)- and **3**-(*R,R*)-DBCz complexes, as well as the **3**-(*S,S*)- and **3**-(*R,R*)-BCz complexes, also leads to the inversion of the CD signal above 280 nm for **3**-(*S,S*)- and **3**-(*R,R*)-DBCz and above 255 nm for **3**-(*S,S*)- and **3**-(*R,R*)-BCz relative to their solution spectra. In the case of the **3**-(*S,S*)-/ **3**-(*R,R*)-DBCz complexes, the obtained CD spectral profiles in the solid state correspond well with previously reported CD solution data for relevant aza[7]helicene (dinaphtho[2,3-*c*:2',3'-*g*]carbazoles) species[49] and Au(I) complexes that feature a functionalized dibenzo[*c,g*]fluorene moiety,[50] which are conformationally stable and do not exhibit dynamic chirality in a solution.

Based on the obtained CD data, it can be seen that the **3**-(*S,S*)-/ **3**-(*R,R*)-complexes of -DBCz and -BCz, which feature direct chirality transfer from the NHC to the DBCz/BCz ligands, display a stronger CD response in the DBCz/BCz absorption regions than the **2**-(*S,S*)- and **2**-(*R,R*)-DBCz complexes in the solid state.

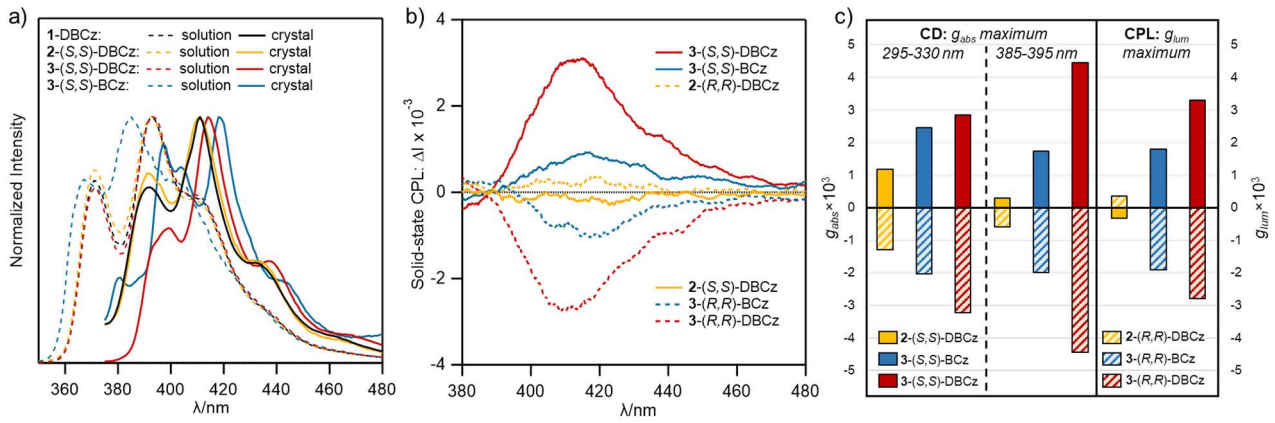

Figure 2.13 (a) Normalized emission spectra of **1**-DBCz, **2**-(*S,S*)-DBCz, **3**-(*S,S*)-DBCz, and **3**-(*S,S*)-BCz complexes in CH_2Cl_2 solution (dashed lines; 2×10^{-5} M) and the solid state (solid lines; 10% *w*/*w* in paraffin oil). (b) CPL spectra of NHC Au(I) azahelicene complexes in the solid state (10% *w*/*w* in paraffin oil). (c) Bar chart of absorption and luminescence dissymmetry factor maximum values (g_{abs} and g_{lum}) of NHC Au(I) azahelicene complexes in the solid state; the data was taken from **Table S2.10**.

In CH_2Cl_2 solution, all complexes with a DBCz ligand exhibit similar photoluminescence emission bands with maximum wavelengths in the range of 390–400 nm, indicating the minor effect of the substituent structure of the NHC ligand on the emission profile (Figure 2.13a). Notably, the emission of **3**-(*S,S*)- and **3**-(*R,R*)-BCz is blue-shifted compared to those of the other complexes, with an emission maximum at 386 nm. At the same time, in the crystalline state, a general emission red-shift of ca. 25–35 nm was observed for all complexes. In addition, a weaker side band in the 450–600 nm region was observed for crystalline samples (Figure S2.26).

None of the obtained complexes display CPL properties in CH_2Cl_2 solution, regardless of the excitation wavelength (Figure S2.27). This can be explained by the dynamic chirality of the DBCz moiety in solution and the absence of chirality transfer from the NHC ligand to the DBCz/BCz ligand. In contrast, in the solid state, all complexes except the racemic **1**-DBCz display a noticeable CPL response in the 390–470 nm region (Figure 2.13b). The weakest CPL performance was observed for the

complexes **2**-(*S,S*)- and **2**-(*R,R*)-DBCz, with luminescence dissymmetry factor $|g_{lum}|$ values of only 3.2–3.6 × 10^{-4} (Figure S2.29). Remarkably, these complexes display inverted CPL signals in comparison to their CD signals (the 320 nm band was used for excitation), as well as to the CPL signals of the other complexes. This may relate to the presence of both *P*- and *M*-DBCz ligands in their crystal structures. In contrast, the complexes **3**-(*S,S*)- and **3**-(*R,R*)-DBCz, which feature direct chirality transfer from the NHC to the DBCz ligand and only one type of DBCz ligand, display an almost 10-fold increase in their $|g_{lum}|$ values (2.8–3.3 × 10^{-3}) compared to **2**-(*S,S*)- and **2**-(*R,R*)-DBCz (Figure 2.13b,c). Additionally, the complexes **3**-(*S,S*)- and **3**-(*R,R*)-BCz, which have almost the same crystal structure as their DBCz-derived analogs, show inferior CPL with $|g_{lum}|$ values of 1.8–1.9 × 10^{-3}. The obtained $|g_{lum}|$ values for NHC Au(I) azahelicene complexes are comparable to those of recently reported crystalline chiral amino carbene Au(I) complexes (0.1–5.8 × 10^{-3})[51-53] as well as those of small organic molecules that contain a single [4]helicene (0.1–2.5 × 10^{-3})[54] or [5]helicene fragment (0.25–6.6 × 10^{-3}).[54]

To summarize the obtained CD and CPL results, a consistent trend emerges across the obtained complexes. In solution, none of the complexes featuring chiral NHC ligands show any CPL signal, and they have a weak CD response in the DBCz/BCz absorption regions, mainly due to the flexibility of DBCz and the lack of chirality transfer. Conversely, in the solid state, a clear connection was observed between the crystal structure and both the CPL and CD response levels (Figure 2.13c). The crystals of **2**-(*S,S*)- and **2**-(*R,R*)-DBCz, which include both *P*- and *M*-DBCz moieties that are not involved in direct chirality transfer, demonstrate the lowest luminescence and absorption dissymmetry factor values in the series. The **3**-(*S,S*)- and **3**-(*R,R*)-DBCz/BCz complexes, which feature a “hinge”-shaped diphenyl moiety capable of chirality transfer, exhibit much better CPL performance and stronger CD responses. Despite the almost identical crystal packing of these DBCz- and BCz-derived complexes, their luminescence and absorption dissymmetry factors differ, which can be attributed to

the difference in the structure and degree of curvature of the annulated carbazole ligands. This is similar to previously reported observations for other helicene systems, in which extending the helicene backbone increases the degree of curvature of the system and enhances both CPL and CD responses in solution.[55, 56] Likewise, in the case of the complexes **3**-(*S,S*)- and **3**-(*R,R*)-DBCz/BCz, the change from BCz to DBCz also leads to an increased degree of curvature in the carbazole ligand and enhanced CPL performance as well as CD response. It is noteworthy that, similar to previously reported helicene species,[54] of the obtained complexes also exhibit a correlation between the g_{abs} and g_{lum} values (Figure S2.30). The deviation from the trend is observed for the **3**-(*S,S*)- and **2**-(*R,R*)-DBCz complexes, which display an inverted CPL signal, presumably due to the presence of a second diastereomer in the crystals.

2.3 Conclusion

In this work, using a series of chiral *N*-heterocyclic carbene Au(I) dibenzo[*c,g*]carbazole and benzo[*c*]carbazole complexes, I have demonstrated how the shape of the chiral NHC ligand can enable chirality transfer in the crystal through intermolecular conjunction to stabilize the homochirality of the conformationally flexible azahelicene species. The presence of the "hinge"-shaped chiral diphenyl moiety in the NHC backbone of **3**-(*S,S*)- and **3**-(*R,R*)-DBCz/BCz resulted in the formation of intermolecular head-to-tail conjunction and chirality transfer between the chiral NHC and DBCz/BCz ligands, assisted by intermolecular C–H···π interactions. The complementary shape of the NHC backbone leads not only to selective fixation of one conformation of the dynamically chiral DBCz ligand in the crystal but also to the induction of chirality in the initially achiral BCz ligand. Conversely, the smaller, flat cyclohexyl moiety in the NHC ligand of **2**-(*S*,*S*)- and **2**-(*R*,*R*)-DBCz does not induce chirality transfer in the crystals. Instead, it leads to the formation of a diastereomeric mixture within the crystal and the coexistence of both *P*- and *M*-DBCz moieties. Moreover, crystallization activates the valuable CPL properties of the studied systems, which were suppressed in solution by the presence of dynamic chirality and absence of chirality transfer. In the crystalline state, a clear connection between the crystal structure and CPL properties was observed. Crystalline samples of the complexes **3**-(*S,S*)- and **3**-(*R,R*)-DBCz/BCz featuring direct chirality transfer and a single conformation of the DBCz/BCz ligand display ca. 5–10-fold enhancement in the g_{lum} value in comparison to **2**-(*S,S*)- and **2**-(*R,R*)-DBCz, which contain both *P*- and *M*-DBCz ligands in their crystal structure.

This approach of intermolecular chirality transfer allows the selective isolation of a homochiral form of very flexible helicene systems such as DBCz in the solid state, which cannot be achieved by conventional solution methods due to the extremely low enantiomerization barrier and short half-life. In the future, this strategy for the stabilization of homochirality in species with dynamic chirality could be expanded to

other types of twisted organic and organometallic systems. This should prove useful for the design of a new generation of crystalline and supramolecular chiral and chiroptical materials.

2.4 Experimental details and support information

2.4.1 General information for experience

All commercially available reagents and solvents were reagent grade and used without further purification unless otherwise noted. These reagents were purchased from TCI, Aldrich, Cica, and Wako. Solvents used for synthesis were additionally dried with 4Å molecular sieves. Abbreviations for reagents are as follows: NHC (*N*-heterocyclic carbene), EtOAc (ethyl acetate), Hex (*n*-hexane), THF (tetrahydrofuran). NMR spectra were recorded on a JEOL JNM-ECZ400S (^{1}H: 400 MHz; ^{13}C: 100 MHz), using TMS and solvent residual signals as internal standards. NMR data are presented as follows: singlet (s), doublet (d), triplet (t), doublet of doublets (dd), multiplet (m), coupling constant in Hertz (Hz), and integration. High-resolution mass spectra (HRMS) and elemental analysis (Elem. Anal.) were recorded at the Instrumental Analysis Division, Global Facility Center, Hokkaido University. Using a Thermo Scientific Exactive plus for ESI-HRMS and an Exeter Analytical CE440 CHN analyzer for Elem. Anal.. Details of the thermogravimetric analysis (TGA), differential scanning calorimetry (DSC), theoretical calculations, single-crystal (SCXRD) and powder (PXRD) X-Ray diffraction experiments, as well as the optical analyses (circular dichroism (CD), photoluminescence (PL), and circularly polarized luminescence (CPL)) are given below. The raw data was plotted using Igor Pro version 9.0.5.1.

2.4.2 Synthesis and characterization

Synthesis and characterization of NHC salts

***1**-NHC salt and **2**-NHC salts*

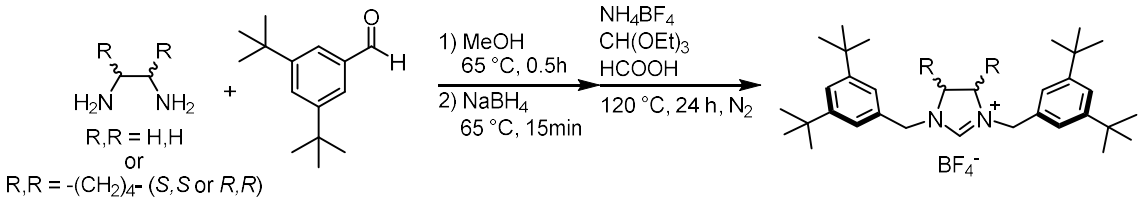

The synthesis of **1**-NHC and **2**-NHC salts was conducted following a modified literature procedure.[54] A corresponding diamine (1.0 equiv., 1.0 mmol), 3,5-di-*tert*-butylbenzaldehyde (2.0 equiv., 2.0 mmol, 437 mg), and MeOH (2.0 mL) were combined in an oven-dried reaction vessel (10 mL capacity). The vessel was sealed with a septum and stirred in an oil bath at 65°C for 0.5 hours. Upon cooling to room temperature, solid $NaBH_4$ (2.0 equiv., 2.0 mmol, 76 mg) was added in portions. Once the bubbles dissipated, the reaction vessel was resealed and subjected to stirring at 65°C for an additional 15 minutes. The reaction was quenched with H_2O (2.0 mL), and the mixture was extracted with CH_2Cl_2 (3 x 10 mL). The combined organic layers were dried over $MgSO_4$, and CH_2Cl_2 was evaporated under vacuum. The residual white solid was transferred to another oven-dried reaction vessel (10 mL capacity), and ammonium tetrafluoroborate (NH_4BF_4, 1.1 equiv., 1.1 mmol), triethyl orthoformate ($CH(OEt)_3$, 3.0 mL), and formic acid (HCOOH, 3 drops) were added. The reaction vessel was purged with nitrogen flow, sealed with a septum, and then stirred in an oil bath at 120°C for 24 hours. Following this, the reaction mixture was filtered through Celite, and the target product was isolated via flash chromatography on silica gel (CH_2Cl_2/EtOAc = 5/1-1/1).

1-NHC BF_4^- salt

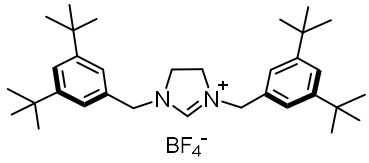

Yield: 85% over two steps, 480 mg, pale yellow powder. ^{1}H NMR (400 MHz, $CDCl_3$, δ): 1.32 (s, 36H, H-^{t}Bu), 3.83 (s, 4H, H-NHC), 4.66 (s, 4H, CH_2), 7.13 (d, *J* = 1.8 Hz, 4H, H-C_{Ar}), 7.42 (t, *J* = 1.8 Hz, 2H, H-C_{Ar}), 8.36 (s, 1H, H-NHC). The NMR spectra was confirmed with the previous report.[54]

2-(*S,S*)-NHC BF_4^- salt

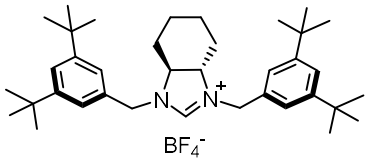

Yield: 81% over two steps, 500 mg, pale yellow powder. ^{1}H NMR (400 MHz, $CDCl_3$, δ): 1.30-1.46 (m, 40H, H-^{t}Bu and H-Cy), 1.85 (d, *J* = 9.2 Hz, 2H, H-Cy), 2.11 (d, *J* = 11.6 Hz, 2H, H-Cy), 3.30-3.39 (m, 2H, H-Cy), 4.72 (dd, *J* = 14.8 Hz, 35.6 Hz, 4H, CH_2), 7.11 (d, *J* = 2.0 Hz, 4H, H-C_{Ar}), 7.39 (m, 2H, H-C_{Ar}), 8.53 (s, 1H, H-NHC). ^{13}C NMR (100 MHz, $CDCl_3$, δ): 23.66 (CH_2), 27.74 (CH_2), 31.38 (CH_3), 34.88 (CH), 51.69 (CH), 67.59 (CH_2), 122.64 (C_{Ar}), 122.68 (C_{Ar}), 132.09 (C_{Ar}), 151.95 (C_{Ar}), 160.63 (C_{NHC}). HRMS (ESI) m/z: $[M\text{-}BF_4^-]^+$ calcd for $[C_{37}H_{57}N_2]^+$: 529.4517. Found: 529.4514.

2-(*R,R*)-NHC BF_4^- salt

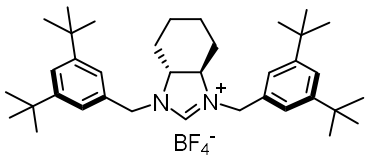

Yield: 87% over two steps, 537 mg, pale yellow powder. ^{1}H NMR (400 MHz, $CDCl_3$, δ): 1.31-1.46 (m, 40H, H-^{t}Bu and H-Cy), 1.85 (d, *J* = 9.6 Hz, 2H, H-Cy), 2.12 (d, *J* = 12.0 Hz, 2H, H-Cy), 3.30-3.39 (m, 2H, H-Cy), 4.71 (dd, *J* = 14.8 Hz, 37.6 Hz, 4H, CH_2), 7.11 (d, *J* = 1.2 Hz, 4H, H-C_{Ar}), 7.40 (m, 2H, H-C_{Ar}), 8.52 (s, 1H, H-NHC). ^{13}C NMR (100 MHz, $CDCl_3$, δ): 23.63 (CH_2), 27.71 (CH_2), 31.35 (CH_3), 34.86 (CH), 51.66 (CH), 67.57 (CH_2), 122.60 (C_{Ar}), 122.66 (C_{Ar}), 132.07 (C_{Ar}), 151.91 (C_{Ar}), 160.60 (C_{NHC}). HRMS (ESI) m/z: $[M\text{-}BF_4^-]^+$ calcd for $[C_{37}H_{57}N_2]^+$: 529.4517. Found: 529.4515.

***3**-NHC salts*

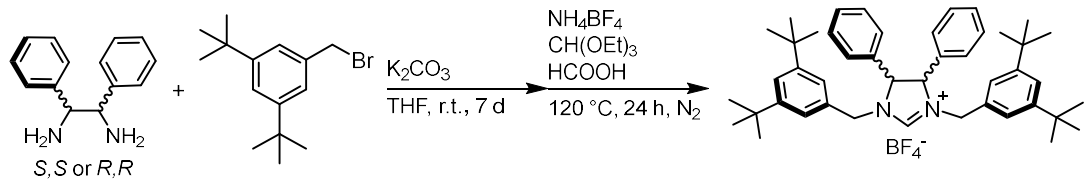

The synthesis of **3**-NHC salts was conducted following a modified literature procedure.[55] (*1S,2S*)-1,2-diphenylethane-1,2-diamine or (*1R,2R*)-1,2-diphenylethane-1,2-diamine (1.0 equiv., 1.0 mmol, 212 mg), 1-(bromomethyl)-3,5-di-*tert*-butylbenzene (2.0 equiv., 2.0 mmol, 567 mg), potassium carbonate (K_2CO_3, 2.5 equiv., 2.5 mmol, 553 mg), and THF (8.0 mL) were combined in an oven-dried round-bottom flask (50 mL capacity). The flask was sealed with a septum and stirred at room temperature for one week. Following this, H_2O (10 mL) was added to the flask, and the mixture was extracted with CH_2Cl_2 (3 x 10 mL). The combined organic layers were dried over $MgSO_4$, and the organic solvent was evaporated under vacuum. The residual white solid was transferred to another oven-dried reaction vessel (10 mL capacity), and ammonium tetrafluoroborate (NH_4BF_4, 1.1 equiv., 1.1 mmol), triethyl orthoformate ($CH(OEt)_3$, 3.0 mL), and formic acid (HCOOH, 3 drops) were added. The reaction vessel was purged with nitrogen flow, sealed with a septum, and then stirred in an oil bath at 120°C for 24 hours. Subsequently, the reaction mixture was filtered through Celite, and the target product was isolated via flash chromatography on silica gel (CH_2Cl_2/EtOAc = 5/1-1/1).

3-(*S,S*)-NHC BF_4^- salt

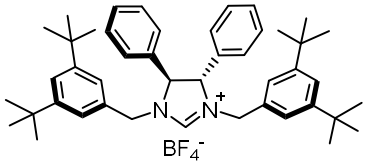

Yield: 73% over two steps, 522 mg, pale yellow solid.^{1}H NMR (400 MHz, $CDCl_3$, δ): 1.28 (s, 36H, ^{t}Bu), 4.10 (d, *J* = 14.4 Hz, 2H, CH_2), 4.48 (s, 2H, H-NHC), 5.18 (d, *J* = 14.4 Hz, 2H, CH_2), 7.02-7.05 (m, 8H, H-C_{Ar}), 7.34-7.43 (m, 8H, H-C_{Ar}), 9.26 (s, 1H, H-NHC). ^{13}C NMR (100 MHz, $CDCl_3$, δ): 31.34 (CH_3), 34.86 (CH), 51.17 (CH_2), 71.37 (C_{NHC}), 122.66 (C_{Ar}), 123.51 (C_{Ar}), 127.30 (C_{Ar}), 129.68 (C_{Ar}), 129.97 (C_{Ar}), 130.97 (C_{Ar}), 135.40 (C_{Ar}),

151.82 (C_{Ar}), 157.21 (C_{NHC}). HRMS (ESI) m/z: $[M\text{-}BF_4^-]^+$ calcd for $[C_{45}H_{59}N_2]^+$: 627.4673. Found: 627.4664.

3-(*R,R*)-NHC BF_4^- salt

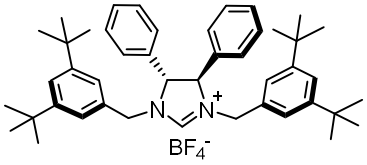

Yield: 73% over two steps, 520 mg, pale yellow powder.^{1}H NMR (400 MHz, $CDCl_3$, δ): 1.30 (s, 36H, H-^{t}Bu), 4.07 (d, *J* = 14.4 Hz, 2H, CH_2), 4.50 (s, 2H, H-NHC), 5.14 (d, *J* = 14.4 Hz, 2H, CH_2), 7.00-7.02 (m, 8H, H-C_{Ar}), 7.35-7.44 (m, 8H, H-C_{Ar}), 9.22 (s, 1H, H-NHC). ^{13}C NMR (100 MHz, $CDCl_3$, δ): 31.34 (CH_3), 34.86 (CH), 51.17 (CH_2), 71.37 (C_{NHC}), 122.67 (C_{Ar}), 123.50 (C_{Ar}), 127.29 (C_{Ar}), 129.69 (C_{Ar}), 129.98 (C_{Ar}), 130.95 (C_{Ar}), 135.39 (C_{Ar}), 151.83 (C_{Ar}), 157.19 (C_{NHC}). HRMS (ESI) m/z: $[M\text{-}BF_4^-]^+$ calcd for $[C_{45}H_{59}N_2]^+$: 627.4673. Found: 627.4661.

Synthesis and characterization of 1-Cl, 2-Cl, and 3-Cl

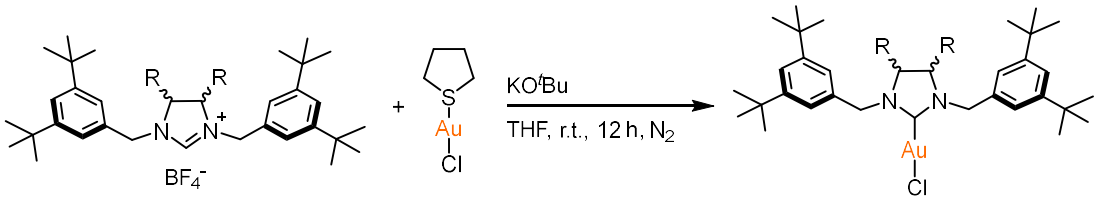

NHC Au(I) chloride complexes **1**-Cl, **2**-Cl, and **3**-Cl were synthesized following a modified literature procedure.[56] Corresponding NHC salt (1.0 equiv., 100 mg) and [Au(THT)Cl] (1.0 equiv.) were combined in an oven-dried reaction vessel (15 mL capacity). The vessel was sealed with a septum and connected to a vacuum/nitrogen Schlenk line. It underwent evacuation and subsequent nitrogen backfilling three times. Dry THF (5.0 mL) was then added using a syringe under a nitrogen atmosphere. After stirring at room temperature for 5 minutes, a solution of potassium *tert*-butoxide (KO^{t}Bu, 1M in THF, 1.2 equiv.) was added via a syringe, resulting in a rapid darkening of the mixture. Following stirring at room temperature for 12 hours, the reaction mixture was filtered through Celite, isolated via flash chromatography on silica gel (CH_2Cl_2), and subsequently recrystallized in a mixture of CH_2Cl_2 and Hex (v:v

= 1:10) at -20°C to obtain a powder. The powder was washed with Hex (in three 3-mL portions) and dried under vacuum.

1-Cl

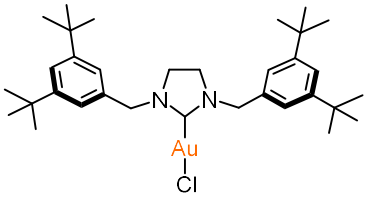

Yield: 60%, 75 mg, white powder.^{1}H NMR (400 MHz, $CDCl_3$, δ): 1.32 (s, 36H, H-^{t}Bu), 3.50 (s, 4H, H-NHC), 4.84 (s, 4H, CH_2), 7.18 (d, *J* = 1.8 Hz, 4H, H-C_{Ar}), 7.38 (t, *J* = 1.8 Hz, 2H, H-C_{Ar}).^{13}C NMR (100 MHz, $CDCl_3$, δ): 31.36 (CH_3), 34.88 (CH), 48.07 (CH_2), 55.37 (C_{NHC}), 122.32 (C_{Ar}), 122.37 (C_{Ar}), 133.92 (C_{Ar}), 151.56 (C_{Ar}), 192.24 (C_{NHC}).HRMS (ESI) m/z: $[M+Na]^+$: Calcd for $[C_{33}H_{50}AuClN_2Na]^+$: 729.3221. Found: 729.3215.Elem. Anal. Calcd for $C_{33}H_{50}AuClN_2$: C, 56.05; H, 7.13; N, 3.96. Found: C, 55.59; H, 7.06; N, 3.76.

2-(*S,S*)-Cl

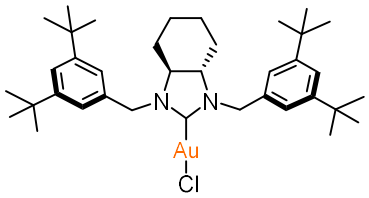

Yield: 75%, 92 mg, white powder.^{1}H NMR (400 MHz, $CDCl_3$, δ): 1.11-1.16 (m, 2H, H-Cy), 1.26-1.28 (m, 2H, H-Cy), 1.31 (s, 36H, H-^{t}Bu), 1.79 (d, *J* = 9.2 Hz, 2H, H-Cy), 2.06 (d, *J* = 10.8 Hz, 2H, H-Cy), 2.91-2.93 (m, 2H, H-Cy), 4.70 (d, *J* = 14.8 Hz, 4H, CH_2), 5.10 (d, *J* = 14.8 Hz, 4H, CH_2), 7.25 (d, *J* = 2.0 Hz, 4H, H-C_{Ar}), 7.35 (t, *J* = 1.6 Hz, 2H, H-C_{Ar}). ^{13}C NMR (100 MHz, $CDCl_3$, δ): 23.94 (CH_2), 28.33 (CH_2), 31.47 (CH_3), 34.86 (CH), 53.31 (CH), 66.30 (CH_2), 121.87 (C_{Ar}), 122.24 (C_{Ar}), 134.16 (C_{Ar}), 151.30 (C_{Ar}), 197.04 (C_{NHC}). HRMS (ESI) m/z: $[M+Na]^+$: Calcd for $[C_{37}H_{56}AuClN_2Na]^+$:783.3690, found: 783.3672. Elem. Anal. Calcd for $C_{37}H_{56}AuClN_2$: C, 58.38; H, 7.41; N, 3.68. Found: C, 58.36; H, 7.49; N, 3.60.

2-(*R,R*)-Cl

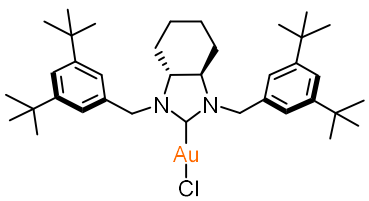

Yield: 82%, 100 mg, white powder. ^{1}H NMR (400 MHz, $CDCl_3$, δ): 1.11-1.16 (m, 2H, H-Cy), 1.27 (m, 2H, H-Cy), 1.32 (s, 36H, H-^{t}Bu), 1.79 (d, *J* = 8.8 Hz, 2H, H-Cy), 2.07 (d, *J* =

10.8 Hz, 2H, H-Cy), 2.91-2.93 (m, 2H, H-Cy), 4.70 (d, *J* = 14.8 Hz, 4H, CH_2), 5.10 (d, *J* = 14.8 Hz, 4H, CH_2), 7.25 (m, 4H, H-C_{Ar}), 7.35 (m, 2H, H-C_{Ar}). ^{13}C NMR (100 MHz, $CDCl_3$, δ): 23.93 (CH_2), 28.33 (CH_2), 31.47 (CH_3), 34.86 (CH), 53.30 (CH), 66.29 (CH_2), 121.87 (C_{Ar}), 122.23 (C_{Ar}), 134.15 (C_{Ar}), 151.30 (C_{Ar}), 197.04 (C_{NHC}). HRMS (ESI) m/z: $[M+Na]^+$: Calcd for $[C_{37}H_{56}AuClN_2Na]^+$:783.3690, found: 783.3672. Elem. Anal. Calcd for $C_{37}H_{56}AuClN_2$: C, 58.38; H, 7.41; N, 3.68. Found: C, 58.38; H, 7.52; N, 3.60.

3-(*S,S*)-Cl

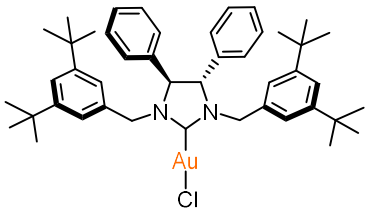

Yield: 72%, 87 mg, white powder. ^{1}H NMR (400 MHz, $CDCl_3$, δ): 1.30 (s, 36H, H-^{t}Bu), 3.85 (d, *J* = 14.4 Hz, 2H, CH_2), 4.32 (s, 2H, H-NHC), 5.61 (d, *J* = 14.4 Hz, 2H, CH_2), 6.95-6.96 (m, 4H, H-C_{Ar}), 7.03 (d, *J* = 1.8 Hz, 4H, H-C_{Ar}), 7.29-7.37 (m, 8H, H-C_{Ar}). ^{13}C NMR (100 MHz, $CDCl_3$, δ): 31.43 (CH_3), 34.84 (CH), 53.30 (CH_2), 71.86 (C_{NHC}), 122.20 (C_{Ar}), 122.62 (C_{Ar}), 126.95 (C_{Ar}), 129.17 (C_{Ar}), 129.34 (C_{Ar}), 133.35 (C_{Ar}), 137.72 (C_{Ar}), 151.40 (C_{Ar}), 190.95 (C_{NHC}). HRMS (ESI) m/z: $[M+Na]^+$: Calcd for $[C_{45}H_{58}AuClN_2Na]^+$: 881.3847, found: 881.3841. Elem. Anal. Calcd for $C_{45}H_{58}AuClN_2$: C, 62.89; H, 6.80; N, 3.26. Found: C, 63.01; H, 6.91; N, 3.16.

3-(*R,R*)-Cl

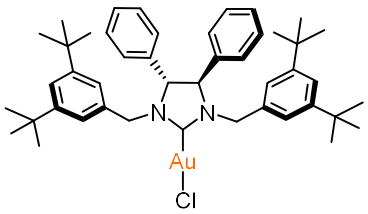

Yield: 71%, 85 mg, white powder. ^{1}H NMR (400 MHz, $CDCl_3$, δ): 1.30 (s, 36H, H-^{t}Bu), 3.85(d, *J* = 14.4 Hz, 2H, CH_2), 4.32 (s, 2H, H-NHC), 5.61 (d, *J* = 14.4 Hz, 2H, CH_2), 6.94-6.97 (m, 4H, H-C_{Ar}), 7.04 (d, *J* = 1.8 Hz, 4H, H-C_{Ar}), 7.30-7.37 (m, 8H, H-C_{Ar}). ^{13}C NMR (100 MHz, $CDCl_3$, δ): 31.43 (CH_3), 34.84 (CH), 53.30 (CH_2), 71.86 (C_{NHC}), 122.20 (C_{Ar}), 122.61 (C_{Ar}), 126.94 (C_{Ar}), 129.16 (C_{Ar}), 129.34 (C_{Ar}), 133.34 (C_{Ar}), 137.71 (C_{Ar}), 151.40 (C_{Ar}), 190.95 (C_{NHC}). HRMS (ESI) m/z: $[M+Na]^+$: Calcd for $[C_{45}H_{58}AuClN_2Na]^+$: 881.3847, found: 881.3831. Elem. Anal. Calcd for $C_{45}H_{58}AuClN_2$: C, 62.89; H, 6.80; N, 3.26. Found: C, 62.61; H, 6.86; N, 3.15.

Synthesis of NHC Au(I) carbazole complexes

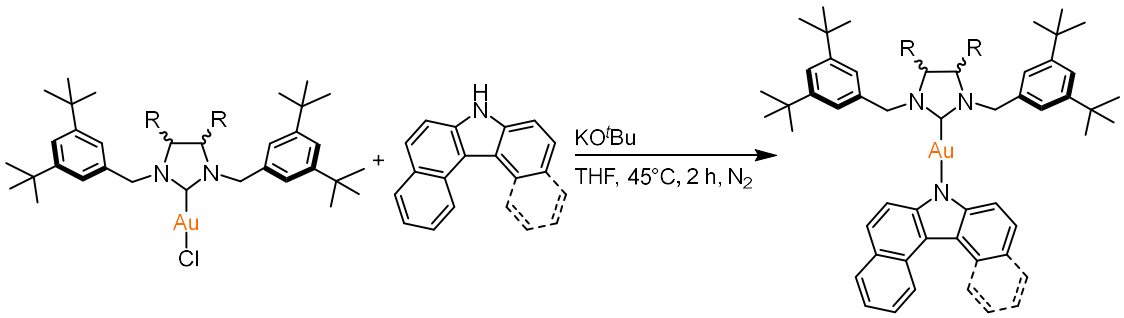

The NHC Au(I) azahelicene complexes were synthesized following a modified literature procedure.[57] The corresponding NHC Au(I) chloride complex (1.0 equiv., 20 mg) and corresponding carbazole (1.0 equiv.) were combined in an oven-dried reaction vessel (10 mL capacity). The vessel was sealed with a septum and connected to a vacuum/nitrogen Schlenk line, undergoing evacuation and nitrogen backfilling cycles three times. Dry THF (0.5 mL) was added using a syringe under a nitrogen atmosphere. Subsequently, a solution of potassium *tert*-butoxide (KO^{t}Bu, 1M in THF, 1.2 equiv.) was introduced into the vessel via a syringe, and the mixture was stirred in an oil bath at 45°C for 2 hours. Following this, the solvent was removed under vacuum, and CH_2Cl_2 (3.0 mL) was added. The mixture was filtered through Celite with CH_2Cl_2 (10 mL). After evaporating the solvent under vacuum, the resulting solid was washed with Hex (in three 3-mL portions) and dried under vacuum.

1-DBCz

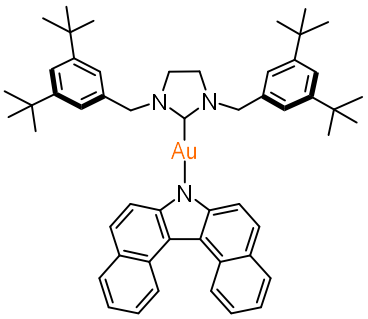

Yield: 84%, 22 mg, pale yellow powder. ^{1}H NMR (400 MHz, $CDCl_3$, δ): 1.21 (s, 36H, H-^{t}Bu), 2.56 (s, 4H, H-NHC), 4.36 (s, 4H, CH_2), 7.00 (s, 4H, H-C_{Ar}), 7.30 (s, 2H, H-C_{Ar}), 7.44 (t, *J* = 7.6 Hz, 2H, H-C_{Ar}), 7.65 (t, *J* = 8.4 Hz, 2H, H-C_{Ar}), 7.78 (d, *J* = 8.8 Hz, 2H, H-C_{Ar}), 8.04 (d, *J* = 8.0 Hz, 2H, H-C_{Ar}), 8.20 (d, *J* = 8.8 Hz, 2H, H-C_{Ar}), 9.30 (d, *J* = 8.0 Hz, 2H, H-C_{Ar}). ^{13}C NMR (100 MHz, $CDCl_3$, δ): 31.39 (CH_3), 34.76 (CH), 47.15 (CH_2), 54.50 (C_{NHC}), 117.92 (C_{Ar}), 118.52 (C_{Ar}), 121.70 (C_{Ar}), 122.01 (C_{Ar}), 122.37 (C_{Ar}), 124.10 (C_{Ar}), 124.33

(C_{Ar}), 124.71 (C_{Ar}), 128.94 (C_{Ar}), 129.74 (C_{Ar}), 129.95 (C_{Ar}), 134.46 (C_{Ar}), 146.67 (C_{Ar}), 151.37 (C_{Ar}), 193.08(C_{NHC}). HRMS (ESI) m/z: $[M+Na]^+$: Calcd for $[C_{53}H_{62}AuN_3Na]^+$: 960.4502. Found:960.4489. Elem. Anal. Calcd for $C_{53}H_{62}AuN_3$: C, 67.86; H, 6.66; N, 4.47. Found: C, 67.84; H, 6.59; N, 4.37.

2-(*S,S*)-DBCz

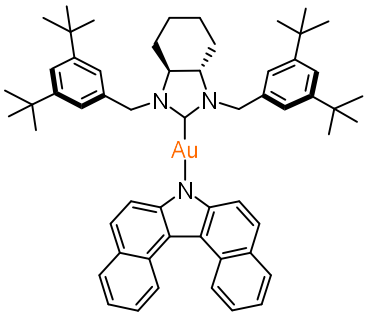

Yield: 80%, 20 mg, pale yellow powder. ^{1}H NMR (400 MHz, $CDCl_3$, δ): 0.65-0.66 (m, 4H, H-Cy), 1.24 (s, 36H, H-^{t}Bu), 1.39-1.41 (m, 2H, H-Cy), 1.57-1.58 (m, 2H, H-Cy), 2.28 (m, 2H, H-Cy), 4.62 (m, 4H, CH_2), 7.13 (d, *J* = 1.2 Hz, 4H, H-C_{Ar}), 7.31 (m, 2H, H-C_{Ar}), 7.42 (t, *J* = 7.2 Hz, 2H, H-C_{Ar}), 7.61 (t, *J* = 6.8 Hz, 2H, H-C_{Ar}), 7.72 (d, *J* = 8.8 Hz, 2H, H-C_{Ar}), 8.00 (d, *J* = 8.0 Hz, 2H, H-C_{Ar}), 8.07 (d, *J* = 8.8 Hz, 2H, H-C_{Ar}), 9.25 (d, *J* = 8.4 Hz, 2H, H-C_{Ar}). ^{13}C NMR (100 MHz, $CDCl_3$, δ): 23.37 (CH_2), 27.60 (CH_2), 31.44 (CH_3), 34.80 (CH), 52.64 (CH), 65.78 (CH_2), 117.92 (C_{Ar}), 118.60 (C_{Ar}), 121.48 (C_{Ar}), 121.57 (C_{Ar}), 121.86 (C_{Ar}), 124.09 (C_{Ar}), 124.14 (C_{Ar}), 124.74 (C_{Ar}), 128.84 (C_{Ar}), 129.56 (C_{Ar}), 130.03 (C_{Ar}), 135.11 (C_{Ar}), 146.66 (C_{Ar}), 151.15 (C_{Ar}), 199.11(C_{NHC}). HRMS (ESI) m/z: $[M+Na]^+$: Calcd for $[C_{57}H_{68}AuN_3Na]^+$: 1014.4971, found: 1014.4959. Elem. Anal. Calcd for $C_{57}H_{68}AuN_3$: C, 69.00; H, 6.91; N, 4.24, found: C, 68.90; H, 6.88; N, 4.21.

2-(*R,R*)-DBCz

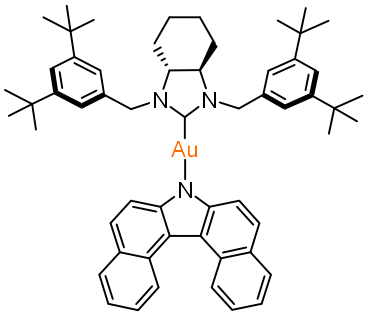

Yield: 80%, 20 mg, pale yellow powder. ^{1}H NMR (400 MHz, $CDCl_3$, δ): 0.74-0.75 (m, 4H, H-Cy), 1.25 (s, 36H, H-^{t}Bu), 1.46-1.48 (m, 2H, H-Cy), 1.65-1.67 (m, 2H, H-Cy), 2.39 (m, 2H, H-Cy), 4.63-4.76 (m, 4H, CH_2), 7.17 (m, 4H, H-C_{Ar}), 7.32 (m, 2H, H-C_{Ar}), 7.40 (t, *J* = 7.2 Hz, 2H, H-C_{Ar}), 7.60 (t, *J* = 7.6 Hz, 2H, H-C_{Ar}), 7.70 (d, *J* = 8.8 Hz, 2H, H-C_{Ar}), 7.99 (d, *J* = 8.0 Hz, 2H, H-C_{Ar}), 8.05 (d, *J* = 8.4 Hz, 2H, H-C_{Ar}), 9.25 (d, *J* = 8.4 Hz, 2H, H-C_{Ar}). ^{13}C NMR (100 MHz, $CDCl_3$, δ): 23.31 (CH_2), 27.52 (CH_2), 31.44 (CH_3), 34.78 (CH), 52.71 (CH), 65.71 (CH_2), 117.91 (C_{Ar}),

118.67 (C_{Ar}), 121.42 (C_{Ar}), 121.59 (C_{Ar}), 121.83 (C_{Ar}), 124.11 (C_{Ar}), 124.16 (C_{Ar}), 124.71 (C_{Ar}), 128.86 (C_{Ar}), 129.58 (C_{Ar}), 130.03 (C_{Ar}), 135.19 (C_{Ar}), 146.68 (C_{Ar}), 151.10 (C_{Ar}), 199.01(C_{NHC}). HRMS (ESI) m/z: $[M+H]^+$: Calcd for $[C_{57}H_{69}AuN_3]^+$: 992.5152, found: 992.5142. Elem. Anal. Calcd for $C_{57}H_{68}AuN_3$: C, 69.00; H, 6.91; N, 4.24, found: C, 68.92; H, 6.90; N, 4.21.

3-(*S,S*)-DBCz

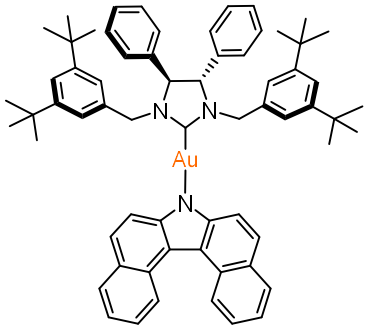

Yield: 88%, 22 mg, pale yellow powder. ^{1}H NMR (400 MHz, $CDCl_3$, δ): 1.35 (s, 36H, H-^{t}Bu), 4.05 (d, *J* = 14.4 Hz, 2H, CH_2), 4.46 (s, 2H, H-NHC), 5.88 (d, *J* = 14.4 Hz, 2H, CH_2), 7.05-7.07 (m, 4H, H-C_{Ar}), 7.25 (m, 4H, H-C_{Ar}), 7.36-7.42 (m, 10H, H-C_{Ar}), 7.60 (t, *J* = 6.8 Hz, 2H, H-C_{Ar}), 7.67 (d, *J* = 8.4 Hz, 2H, H-C_{Ar}), 7.96 (d, *J* = 8.0 Hz, 2H, H-C_{Ar}), 8.09 (d, *J* = 8.4 Hz, 2H, H-C_{Ar}), 9.25 (d, *J* = 8.4 Hz, 2H, H-C_{Ar}). ^{13}C NMR (100 MHz, $CDCl_3$, δ): 31.50 (CH_3), 34.94 (CH), 55.29 (CH_2), 72.32 (C_{NHC}), 117.75 (C_{Ar}), 118.06 (C_{Ar}), 121.51 (C_{Ar}), 122.38 (C_{Ar}), 122.60 (C_{Ar}), 124.08 (C_{Ar}), 124.98 (C_{Ar}), 127.12 (C_{Ar}), 128.63 (C_{Ar}), 129.26 (C_{Ar}), 129.40 (C_{Ar}), 129.43 (C_{Ar}), 129.95 (C_{Ar}), 133.66 (C_{Ar}), 137.75 (C_{Ar}), 146.40 (C_{Ar}), 151.70 (C_{Ar}), 194.07(C_{NHC}). HRMS (ESI) m/z: $[M+H]^+$: Calcd for $[C_{65}H_{71}AuN_3]^+$: 1090.5309. Found: 1090.5306. Elem. Anal. Calcd for $C_{65}H_{70}AuN_3$: C, 71.61; H, 6.47; N, 3.85. Found: C, 70.98; H, 6.40; N, 3.77.

3-(*R,R*)-DBCz

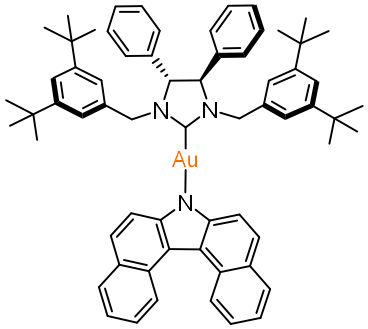

Yield: 88%, 22 mg, pale yellow powder. ^{1}H NMR (400 MHz, $CDCl_3$, δ): 1.35 (s, 36H, H-^{t}Bu), 4.05 (d, *J* = 14.4 Hz, 2H, CH_2), 4.47 (s, 2H, H-NHC), 5.88 (d, *J* = 14.4 Hz, 2H, CH_2), 7.05-7.07 (m, 4H, H-C_{Ar}), 7.26 (m, 4H, H-C_{Ar}), 7.36-7.42 (m, 10H, H-C_{Ar}), 7.60 (t, *J* = 7.2 Hz, 2H, H-C_{Ar}), 7.67 (d, *J* = 9.2 Hz, 2H, H-C_{Ar}), 7.96 (d, *J* = 8.0 Hz, 2H, H-C_{Ar}), 8.09 (d, *J* = 8.4 Hz, 2H, H-C_{Ar}), 9.25 (d, *J* = 8.4 Hz, 2H, H-C_{Ar}). ^{13}C NMR (100 MHz, $CDCl_3$, δ): 31.50 (CH_3),

34.94 (CH), 55.29 (CH_2), 72.32 (C_{NHC}), 117.75 (C_{Ar}), 118.06 (C_{Ar}), 121.51 (C_{Ar}), 122.38 (C_{Ar}), 122.60 (C_{Ar}), 124.08 (C_{Ar}), 124.98 (C_{Ar}), 127.12 (C_{Ar}), 128.63 (C_{Ar}), 129.26 (C_{Ar}), 129.40 (C_{Ar}), 129.43 (C_{Ar}), 129.95 (C_{Ar}), 133.66 (C_{Ar}), 137.75 (C_{Ar}), 146.40 (C_{Ar}), 151.70 (C_{Ar}), 194.07(C_{NHC}). HRMS (ESI) m/z: $[M+H]^+$: Calcd for $[C_{65}H_{71}AuN_3]^+$: 1090.5309. Found: 1090.5310. Elem. Anal. Calcd for $C_{65}H_{70}AuN_3$: C, 71.61; H, 6.47; N, 3.85. Found: C, 71.22; H, 6.45; N, 3.83.

3-(*S,S*)-BCz

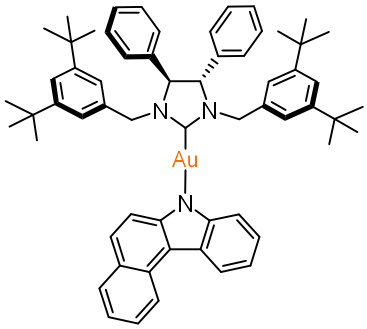

Yield: 96%, 23 mg, pale yellow powder. ^{1}H NMR (400 MHz, $CDCl_3$, δ): 1.34 (s, 36H, H-^{t}Bu), 4.03 (d, *J* = 14.8 Hz, 2H, CH_2), 4.45 (s, 2H, H-NHC), 5.87 (d, *J* = 14.8 Hz, 2H, CH_2), 7.04 (m, 4H, H-C_{Ar}), 7.20-7.24 (m, 5H, H-C_{Ar}), 7.27-7.41 (m, 10H, H-C_{Ar}), 7.60-7.64 (m, 2H, H-C_{Ar}), 7.66 (d, *J* = 8.8 Hz, 2H, H-C_{Ar}), 7.93 (t, *J* = 8.8 Hz, 2H, H-C_{Ar}), 7.97 (d, *J* =12.0 Hz, 2H, H-C_{Ar}), 8.59 (d, *J* = 7.6 Hz, 2H, H-C_{Ar}), 8.78 (d, *J* = 8.4 Hz, 2H, H-C_{Ar}). ^{13}C NMR (100 MHz, $CDCl_3$, δ): 31.47 (CH_3), 34.92 (CH), 55.26 (CH_2), 72.29 (C_{NHC}), 114.60 (C_{Ar}), 115.49 (C_{Ar}), 117.43 (C_{Ar}), 117.52 (C_{Ar}), 120.94 (C_{Ar}), 121.29 (C_{Ar}), 121.96 (C_{Ar}), 122.33 (C_{Ar}), 122.63 (C_{Ar}), 123.06 (C_{Ar}), 124.92 (C_{Ar}), 124.98 (C_{Ar}), 125.58 (C_{Ar}), 127.10 (C_{Ar}), 128.48 (C_{Ar}), 128.47 (C_{Ar}), 129.22 (C_{Ar}), 129.40 (C_{Ar}), 130.82 (C_{Ar}), 133.70 (C_{Ar}), 137.79 (C_{Ar}), 147.42 (C_{Ar}), 148.52 (C_{Ar}), 151.66 (C_{Ar}), 194.43(C_{NHC}). HRMS (ESI) m/z: $[M+Na]^+$: Calcd for $[C_{61}H_{68}AuN_2Na]^+$: 1062.4971, found: 1062.4955.Elem. Anal. Calcd for $C_{61}H_{68}AuN_3$: C, 70.44; H, 6.59; N, 4.04, found: C, 70.16; H, 6.68; N, 3.95.

3-(*R,R*)-BCz

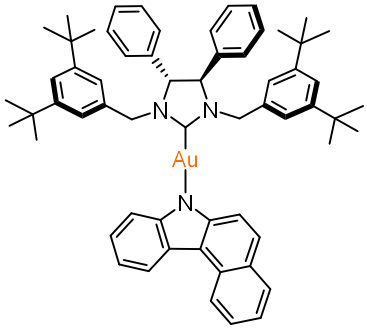

Yield: 92%, 22 mg, pale yellow powder. ^{1}H NMR (400 MHz, $CDCl_3$, δ): 1.34 (s, 36H, H-^{t}Bu), 4.03 (d, *J* = 14.8 Hz, 2H, CH_2), 4.45 (s, 2H, H-NHC), 5.88 (d, *J* = 14.8 Hz, 2H, CH_2), 7.04-7.06 (m, 4H, H-C_{Ar}), 7.20-7.24 (m, 5H, H-C_{Ar}), 7.27-7.41 (m, 10H, H-C_{Ar}), 7.60-7.64 (m, 2H, H-C_{Ar}), 7.66 (d, *J* =

8.8 Hz, 2H, H-C_{Ar}), 7.96 (t, *J* = 8.8 Hz, 2H, H-C_{Ar}), 8.00 (d, *J* = 8.4 Hz, 2H, H-C_{Ar}), 8.59 (d, *J* = 8.0 Hz, 2H, H-C_{Ar}), 8.79 (d, *J* = 8.4 Hz, 2H, H-C_{Ar}). ^{13}C NMR (100 MHz, $CDCl_3$, δ): 31.47 (CH_3), 34.92 (CH), 55.25 (CH_2), 72.28 (C_{NHC}), 114.60 (C_{Ar}), 115.48 (C_{Ar}), 117.44 (C_{Ar}), 117.52 (C_{Ar}), 120.94 (C_{Ar}), 121.29 (C_{Ar}), 121.97 (C_{Ar}), 122.33 (C_{Ar}), 122.63 (C_{Ar}), 123.05 (C_{Ar}), 124.92 (C_{Ar}), 124.98 (C_{Ar}), 125.58 (C_{Ar}), 127.10 (C_{Ar}), 128.48 (C_{Ar}), 128.47 (C_{Ar}), 129.21 (C_{Ar}), 129.40 (C_{Ar}), 130.82 (C_{Ar}), 133.70 (C_{Ar}), 137.78 (C_{Ar}), 147.42 (C_{Ar}), 148.51 (C_{Ar}), 151.66 (C_{Ar}), 194.42(C_{NHC}). HRMS (ESI) m/z: $[M+Na]^+$: Calcd for $[C_{61}H_{68}AuN_2Na]^+$: 1062.4971, found: 1062.4968. Elem. Anal. Calcd for $C_{61}H_{68}AuN_3$: C, 70.44; H, 6.59; N, 4.04, found: C, 70.27; H, 6.74; N, 3.93.

Preparation of crystalline samples

The crystalline samples for TGA, DSC, SCXRD, PXRD, elemental, and solid-state optical analyses were obtained using the following methods:

1-DBCz, **2**-(*S,S*)-DBCz, and **2**-(*R,R*)-DBCz crystals: Approximately 20 mg of the corresponding Au(I) complex powder was placed in a 10 mL flat-bottom vial. The powder was dissolved in 2.0 mL of CH_2Cl_2, and then 0.5 mL of EtOAc was added. The mixture was left at room temperature under ambient air conditions until complete evaporation. After a few hours, white needle-shaped crystals were obtained.

3-(*S,S*)-DBCz and **2**-(*R,R*)-DBCz: About 20 mg of **3**-(*S,S*)-DBCz or **3**-(*R,R*)-DBCz powder was placed in a 10 mL flat-bottom vial. The powder was dissolved in 2.0 mL of CH_2Cl_2, and then 2.0 mL of EtOAc was added. The mixture was left at room temperature under ambient air conditions until complete evaporation. After 1-day, white rectangular-shaped crystals were obtained.

3-(*S,S*)-BCz and **3**-(*R,R*)-BCz: Around 20 mg of **3**-(*S,S*)-BCz or **3**-(*R,R*)-BCz powder was placed in a 10 mL flat-bottom vial. The powder was dissolved in 2.0 mL of CH_2Cl_2, and then 2.0 mL of Hex was added. The mixture was left at room temperature under ambient air conditions until complete evaporation. After 1-day, white rectangular-shaped crystals were obtained.

2.4.4 TGA and DSC analyses

TGA profiles of the crystalline samples were recorded on a Rigaku TG-DTA8122/S using a heating rate of 20 °C/min. DSC profiles of the crystalline samples were measured on a HITACHI DSC7020 using a heating rate of 20 °C/min. The TGA results indicated that weight loss due to decomposition of the complexes occurs only above ~290°C (**Figure S2.1**). Concurrently, the DSC measurements showed two consecutive endothermic and exothermic peaks (**Figure S2.1**), which can be attributed to crystal melting and decomposition of the complexes, respectively.

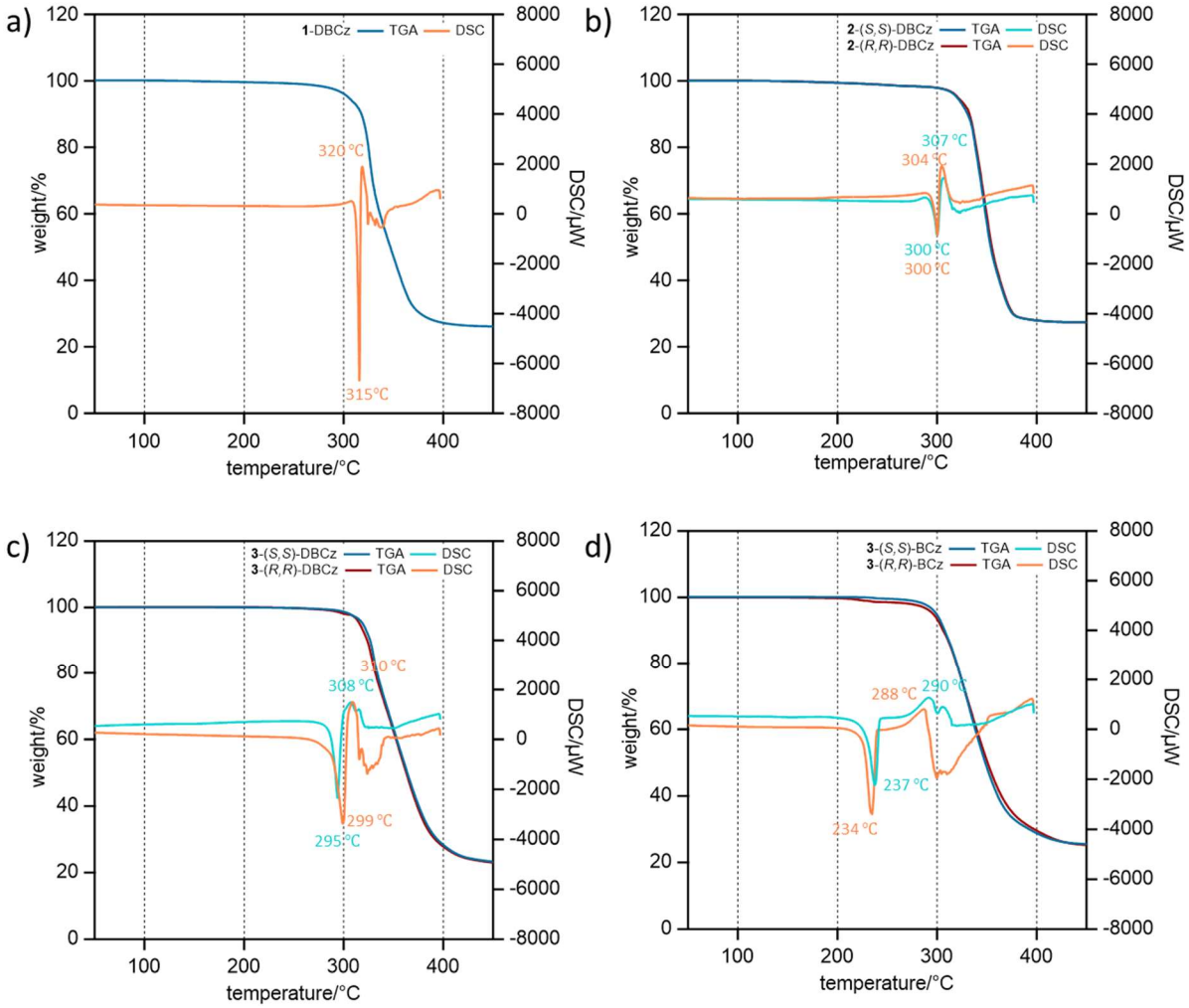

Figure S2.1. TGA/DSC profiles of crystalline sample of (a) **1**-DBCz, (b) **2**-(*S,S*)-DBCz and **2**-(*R,R*)-DBCz, (c) **3**-(*S,S*)-DBCz and **3**-(*R,R*)-DBCz, (d)**3**-(*S,S*)-BCz and **3**-(*R,R*)-BCz.

2.4.5 Variable-temperature solution NMR study

To study the possible *P*/*M*-exchange of the DBCz ligand in solution, ^{1}H NMR measurements at temperatures down to -80 °C in CD_2Cl_2 were performed for **3**-(*S,S*)-DBCz and **2**-(*R,R*)-DBCz. However, even at -80 °C, no clear splitting of the DBCz signals was observed for either complex, which discards the notion of a possible stabilization of two distinct forms of DBCz in solution. For **3**-(*S,S*)-DBCz, cooling resulted in a slight shift of the DBCz proton signal and broadening of some NHC signals in the ^{1}H NMR spectrum in CD_2Cl_2 (**Figure S2.2**).

At the same time, the **2**-(*R,R*)-DBCz complex presents a more complex scenario. The cyclohexyl moiety in the **2**-(*R,R*)-NHC backbone is significantly less bulky than the diphenyl moiety in **3**-(*S,S*)-NHC. This reduced steric hindrance may allow the free rotational motion of the 1,3-bis(3,5-di-*tert*-butylbenzyl) substituents at the nitrogen atoms of the NHC ligand, potentially resulting in an equilibrium between four possible conformers in solution (**Figure S2.3a**). Upon cooling **2**-(*R,R*)-DBCz in CD_2Cl_2, observed a noticeable shift and broadening of all signals corresponding to the NHC ligand in the ^{1}H NMR spectra, whereas some broadening in the DBCz signal region was only noted at -60 °C and -80 °C (**Figure S2.3b**). However, almost no change was detected for the DBCz proton in the “cove” region of DBCz (marked as “a”). Considering the results obtained for **3**-(*S,S*)-DBCz, presume that the observed broadening in the DBCz signal region at -80 °C for **2**-(*R,R*)-DBCz is primarily the result of exchange between different NHC conformers, which likely exert varying shielding effects on the DBCz ligand.

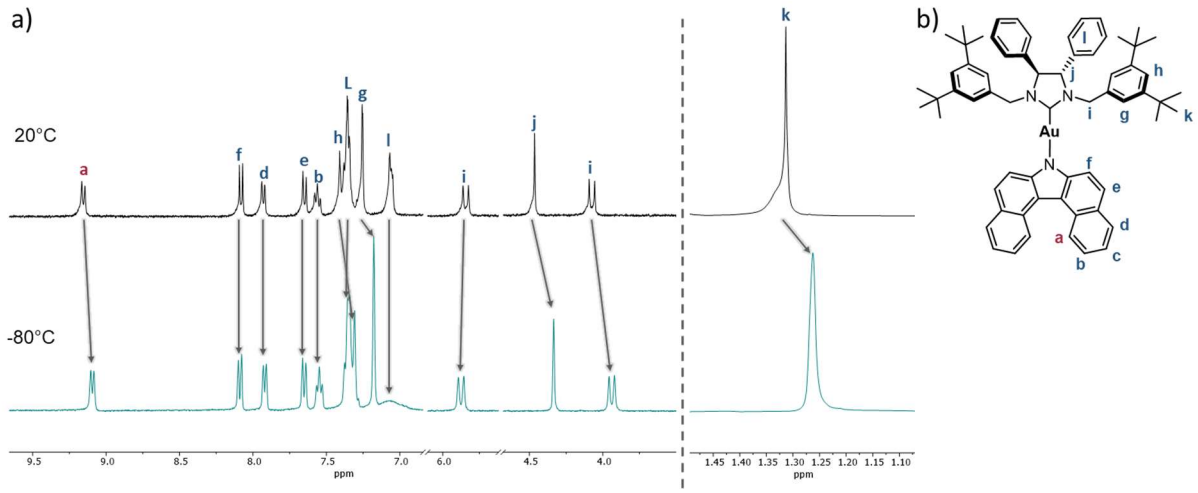

Figure S2.2. (a) ^{1}H NMR spectra of **3**-(*S,S*)-DBCz at 20 °C and -80 °C in CD_2Cl_2. (b) Chemical structure and hydrogen-atom labelling in **3**-(*S,S*)-DBCz. The ^{1}H NMR signal assignment was accomplished with the help of ^{1}H-^{1}H COSY and ^{1}H-^{1}H NOESY techniques.

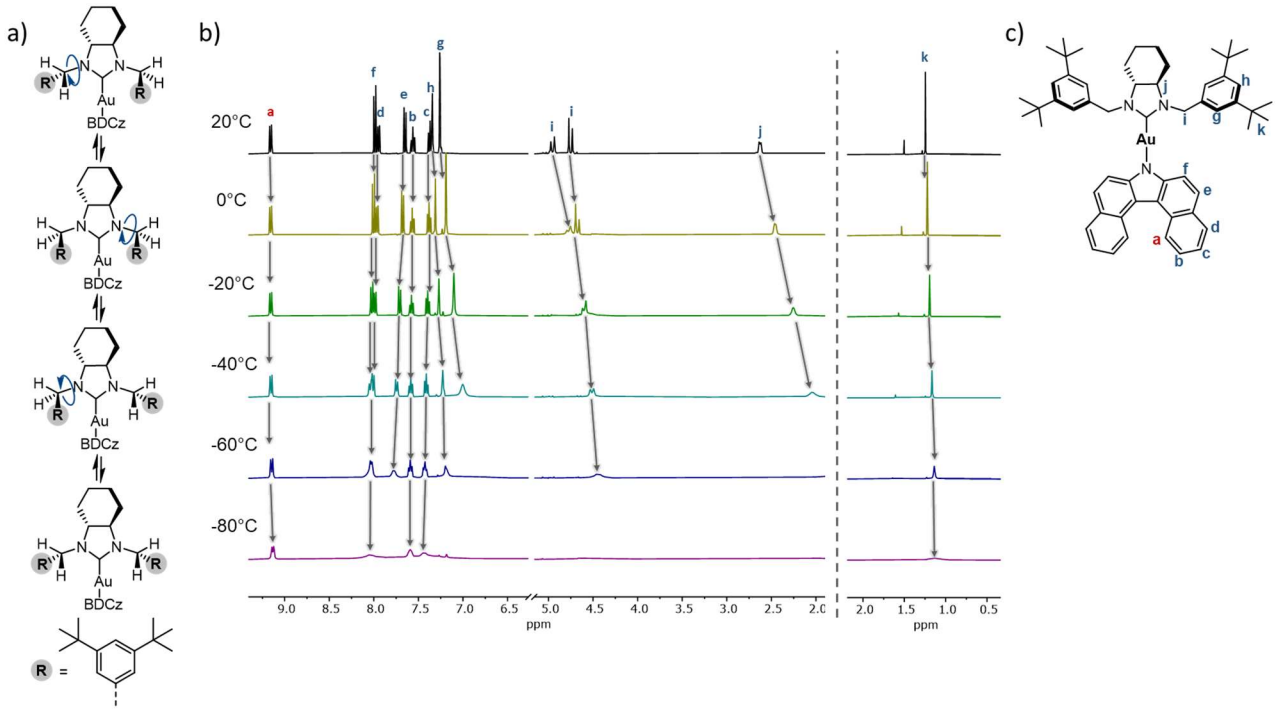

Figure S2.3. (a) Possible NHC ligand conformations of **2**-(*R,R*)-DBCz in solution. (b) Variable-temperature ^{1}H NMR spectra of **2**-(*R,R*)-DBCz in CD_2Cl_2. (c) Chemical structure and hydrogen-atom labelling in **2**-(*R,R*)-DBCz. The ^{1}H NMR signal assignment was accomplished with the help of ^{1}H-^{1}H COSY and ^{1}H-^{1}H NOESY techniques.

2.4.6 DFT and TD-DFT calculations

Structures optimization and thermodynamic parameters

All geometry optimization and single-point calculations were performed using the Gaussian 16 (revision C.01) program package.[58] The full geometry optimization of complexes has been carried out starting from experimental XRD structures using the PBE[59]-D3[60](BJ)[61] functional and mixed basis set: relativistic pseudopotentials ECP60MDF with corresponding Stuttgart–Köln basis sets for Au[62] atom and def2-TZVP[63, 64] basis set for other atoms. The solvent effects were taken into account using the SMD continuum solvation model with CH_2Cl_2 as solvent[65]. No symmetry restrictions have been applied during the geometry optimization procedure. In all cases, the frequency analyses were carried out to ensure that the optimized geometries belong to minima on the potential energy surface (no imaginary frequencies were found for the stationary state structures, and one imaginary frequency was found for TS structures) and to obtain thermodynamic parameters. The theoretically calculated thermodynamic parameters at 298K for the different structures are given in **Tables S2.1**–2.**S3** and **Figure S2.4**.

Table S2.1. Calculated total energies, enthalpies, Gibbs free energies (in Hartree) for optimized structures.

Structure	**3**-(*S,S*)-DBCz-(*M*)	**3**-(*S,S*)-DBCz-(*P*)	**3**-(*S,S*)-DBCz-(*TS*)	**1**-DBCz-(*M*)	**1**-DBCz-(*TS*)
E, Hartree	-2815.947921	-2815.947979	-2815.943969	-2354.355827	-2354.352230
H, Hartree	-2815.946977	-2815.947035	-2815.943024	-2354.354882	-2354.351286
G, Hartree	-2816.123399	-2816.122632	-2816.118014	-2354.508171	-2354.501221

Table S2.2. Calculated differences in total energies, enthalpies, Gibbs free energies, and entropies at 298K between the optimized structures of **3**-(*S,S*)-DBCz.

ΔE(**3**-(*S,S*)-DBCz-(*M*) –**3**-(*S,S*)-DBCz-(*P*))	0.0 kcal/mol
ΔH(**3**-(*S,S*)-DBCz-(*M*) –**3**-(*S,S*)-DBCz-(*P*))	0.0 kcal/mol
ΔG(**3**-(*S,S*)-DBCz-(*M*) –**3**-(*S,S*)-DBCz-(*P*))	0.5 kcal/mol
ΔS(**3**-(*S,S*)-DBCz-(*M*) –**3**-(*S,S*)-DBCz-(*P*))	-1.7 cal/mol•K

Table S2.3. Calculated total energies, enthalpies, Gibbs free energies and entropies of activation at 298K for the optimized structures of **3**-(*S,S*)-DBCz and **1**-DBCz.

Transition	**3**-(*S,S*)-DBCz-(*M*)	**1**-DBCz-(*M*)
$\Delta E^{‡}$, kcal/mol	2.5	2.3
$\Delta H^{‡}$, kcal/mol	2.5	2.3
$\Delta G^{‡}$, kcal/mol	3.4	4.4
$\Delta S^{‡}$, cal/mol•K	-3.0	-7.1

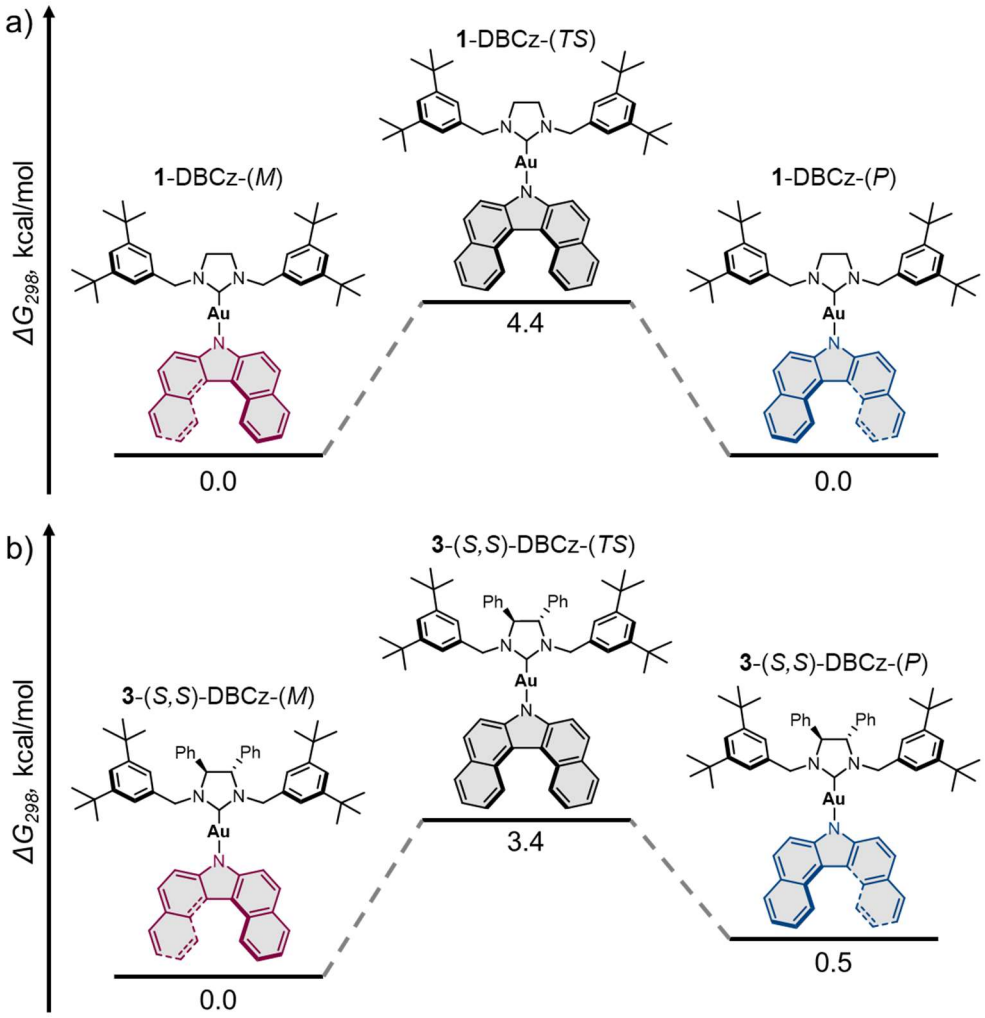

Figure S2.4. Thermodynamic parameters calculated at the PBE0-D3(BJ)/def2TZVP +MDF60/SMD(CH_2Cl_2) level and reaction paths for the enantiomerization of the **1**-DBCz and **3**-(*S,S*)-DBCz complexes

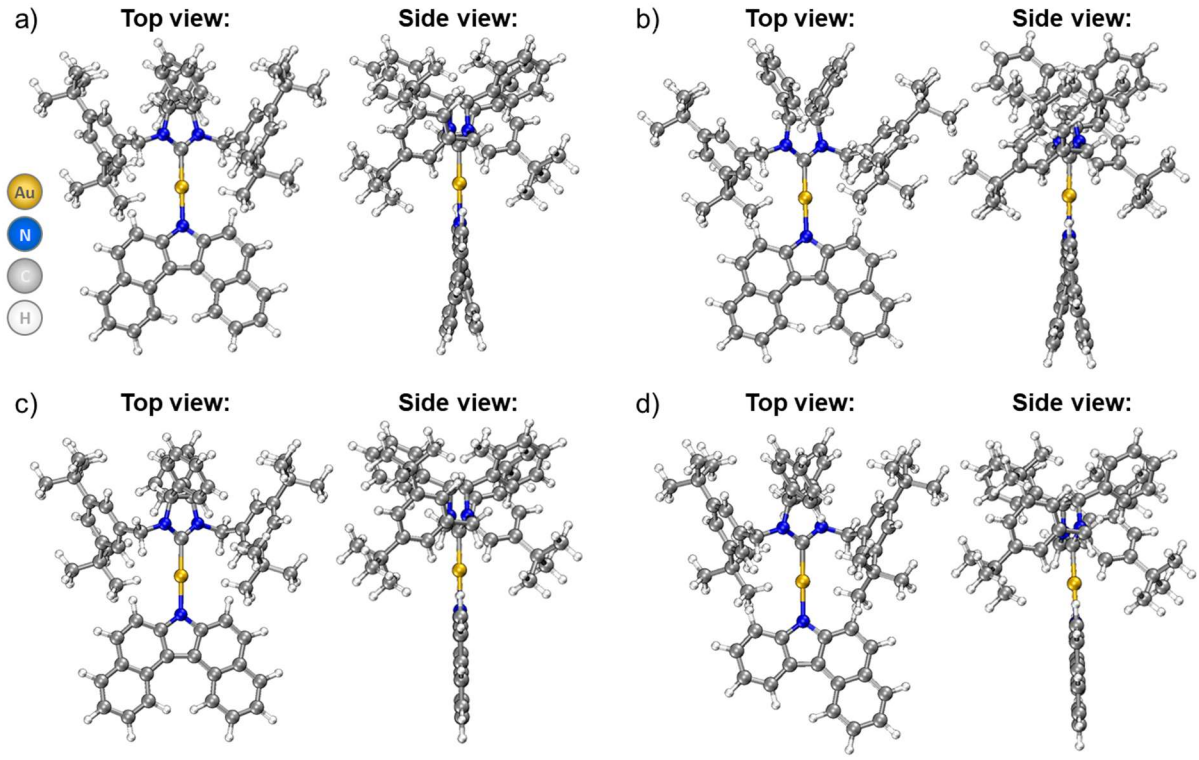

Figure S2.5. Views of PBE0-D3(BJ)/def2TZVP+MDF60/SMD(CH_2Cl_2) optimized structures of (a) **3**-(*S,S*)-DBCz-(*M*), (b) **3**-(*S,S*)-DBCz-(*P*), (c) **3**-(*S,S*)-DBCz-(TS), and (d) **3**-(*S,S*)-BCz. Structures are visualized by VMD software.[17]

Theoretical analysis of non-covalent interactions

In order to analyze theoretically non-covalent interactions assisting the chirality transfer in crystal structre of **3**-(*S,S*)-DBCz, DFT calculations along with Atoms-in-Molecules (QTAIM)[66] and Independent Gradient Model (IGMH)[67] analyses were performed for the experimental XRD geometries of **3**-(*S,S*)-DBCz dimeric associate (**Figure S2.6**). For the experimental geometry, only the positions of H atoms were optimized using the DFT calculations at PBE0[59]-D3[60](BJ)[61]/def2-SVP[63, 64] level, while the positions of all other atoms were fixed to preserve the XRD geometrey. The single-point calculations for further theoretical studies were carried out using the PBE0[59]-D3[60](BJ)[61] functional and mixed basis set: relativistic pseudopotentials ECP60MDF with corresponding Stuttgart–Köln basis sets for Au[62] atom and def2-

TZVP[63, 64] bass set for other atoms. The basis set superposition error for the calculation of interaction energies for the studied dimeric associate has been corrected using the counterpoise method. The QTAIM and IGMH analyses were carried out using the Multiwfn 3.83[69] and were visualized by VMD software.[70] The Cartesian atomic coordinates for dimer structure are given as XYZ-file in Supplementary Files. Both QTAIM and IGMH analyses have confirmed the presence of the C–H···π interactions between the phenyl moieties of NHC ligand and DBCz ligand.

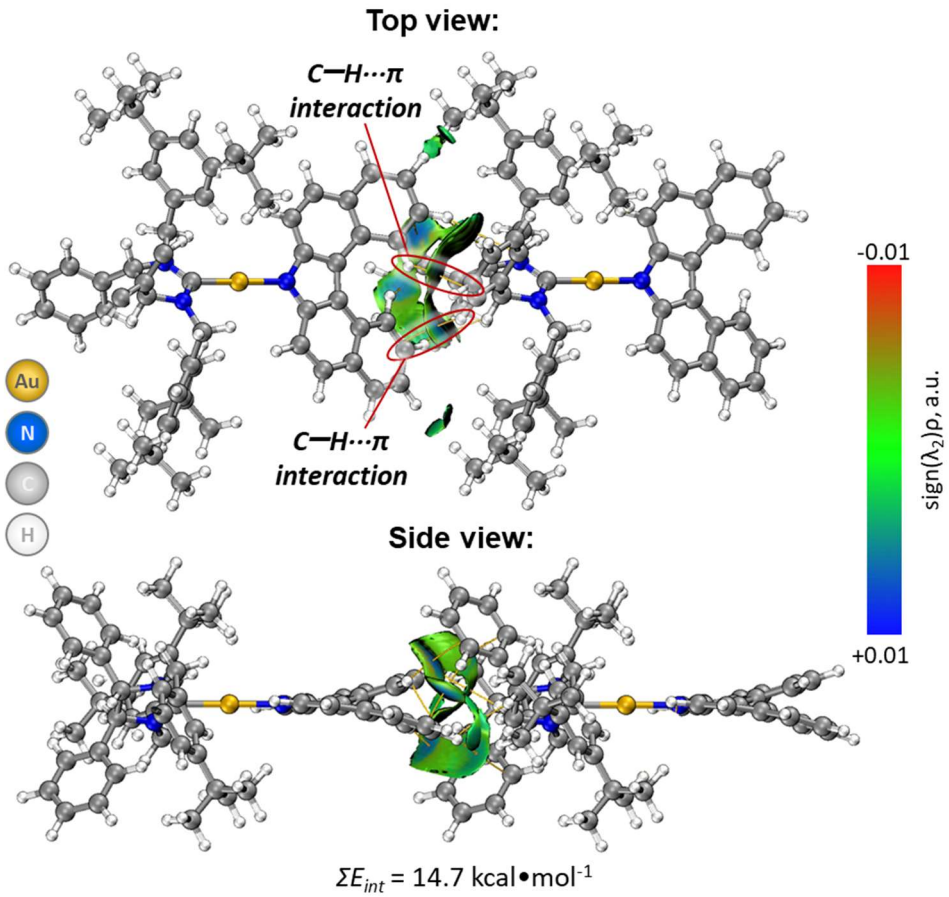

Figure S2.6. Visualization of IGMH analysis (sign(λ_2)ρ colored isosurfaces of δg_{inter}, isovalue = 0.0025 a.u.) and QTAIM bond critical points [3;-1], and bond paths for the C–H···π interactions between the phenyl moieties of NHC ligand and DBCz ligand (all other BCPs and paths are omitted for clarity) in dimeric associates of **3**-(*S,S*)-DBCz.

TD-DFT calculations

The PBE0[59]-D3[60](BJ)[61]/def2SVP[63,64]+MDF60[62]/SMD(CH_2Cl_2) level of theory was used for TD-DFT for the optimization of the lowest singlet exited state (S_1) and the calculation of the first singlet 25 excited states of **1**-DBCz-(*M*), **2**-(*S,S*)-DBCz-(*M*), **3**-(*S,S*)-DBCz-(*M*) and **3**-(*S,S*)-BCz complexes. To study the nature of single-electron excitation transitions and associated with them charge transfers, the hole-electron distribution analysis[68] was performed using Multiwfn 3.8 software[69] and visualized by VMD software.[70] The latter method describes where the excited electron leaves as "hole" and arrives as "electron". Based on this information, the classification of the exited states was made according to participation of different fragments of complexes in the charge transfer. The Cartesian atomic coordinates for model structures are given as XYZ-files in Supplementary Files. The results are shown in **Figures S2.7–S2.10.**

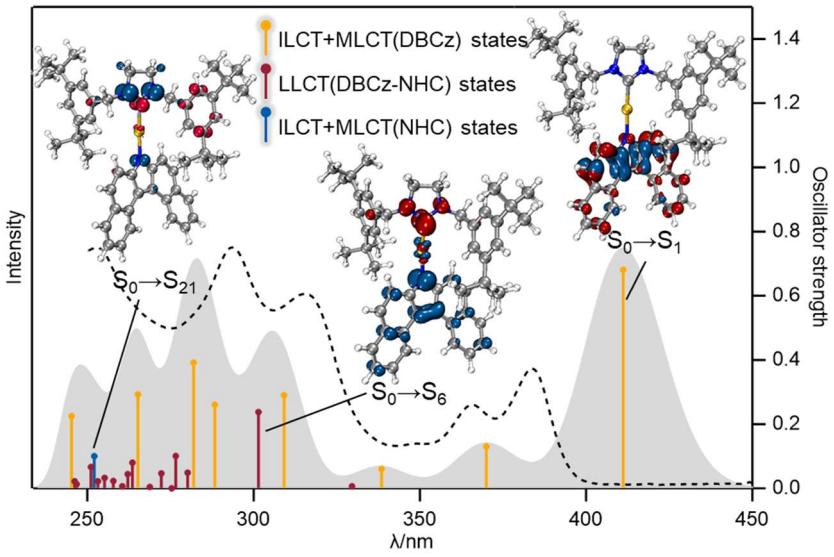

Figure S2.7. Experimental (black dashed line) and calculated (grey area) absorption spectrum, and oscillator strengths of **1**-DBCz-(*M*) together with the hole-electron distribution isosurfaces (isovalue 0.003) for the selected transitions (hole distribution: blue; electron distribution: red).

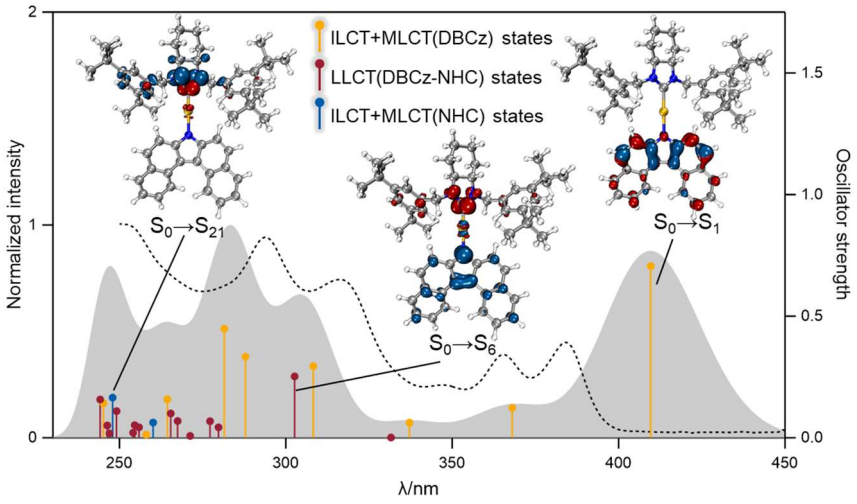

Figure S2.8. Experimental (black dashed line) and calculated (grey area) absorption spectrum, and oscillator strengths of **2**-(*S,S*)-DBCz-(*M*) together with the hole-electron distribution isosurfaces (isovalue 0.003) for the selected transitions (hole distribution: blue; electron distribution: red).

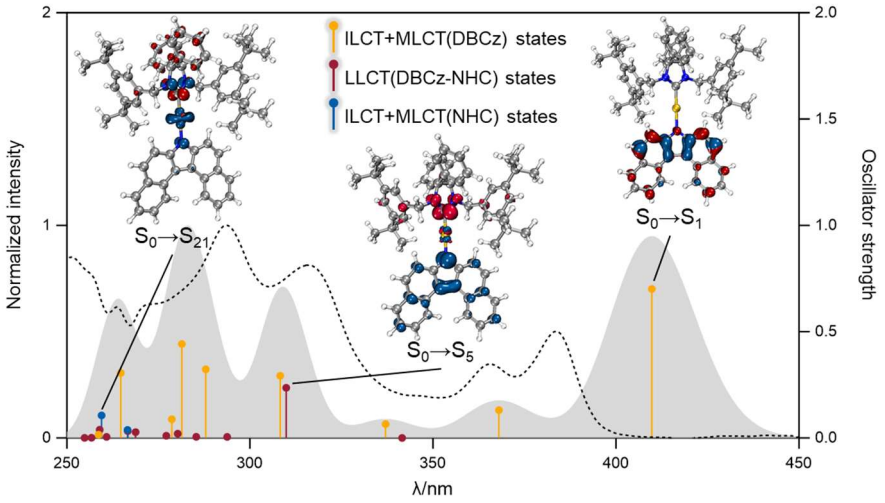

Figure S2.9. Experimental (black dashed line) and calculated (grey area) absorption spectrum, and oscillator strengths of **3**-(*S,S*)-DBCz-(*M*) together with the hole-electron distribution isosurfaces (isovalue 0.003) for the selected transitions (hole distribution: blue; electron distribution: red)**.**

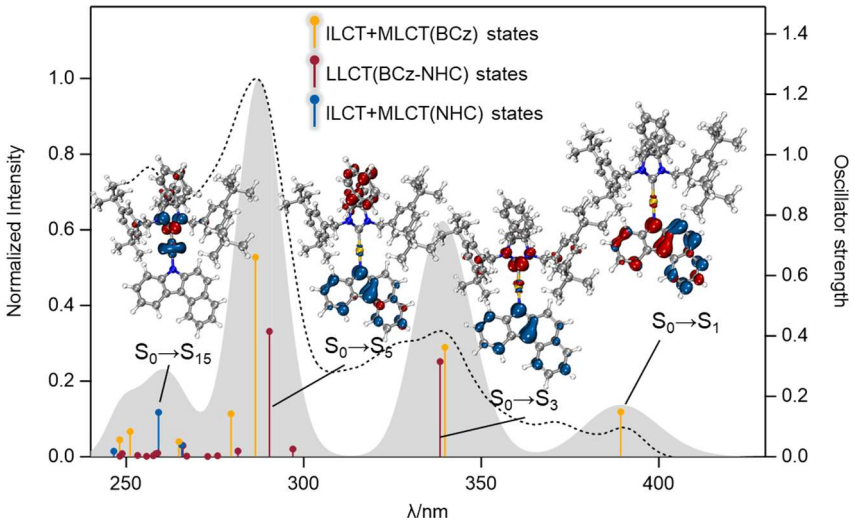

Figure S2.10. Experimental (black dashed line) and calculated (grey area) absorption spectrum, and oscillator strengths of **3**-(*S,S*)-BCz together with the hole-electron distribution isosurfaces (isovalue 0.003) for the selected transitions (hole distribution: blue; electron distribution: red).

2.4.7 Single-crystal X-ray diffraction analysis

Single-crystal X-ray diffraction (SCXRD) analyses were carried out on a Rigaku XtaLAB Synergy diffractometer using graphite monochromated Cu-Kα radiation. The structures were solved with the SHELXT structure solution program using Intrinsic Phasing incorporated in the OLEX2 program package[71] and refined with the SHELXL package[72] and olex2.refine refinement package[73] using Levenberg-Marquardt minimization. Hydrogen atoms were refined using the riding model. The crystal data parameters are given in **Tables S2.4–S2.6,** while the crystal structure views of complexes are shown in **Figures S2.11–S2.14.**

Table S2.4. Crystal data and structure refinement for **1**_DBCz_293K, **2**_SS_DBCz_123K, **2**_SS_DBCz_293K crystal structures.

Identification code	**1**_DBCz _293K	**2**_SS_DBCz _123K*	**2**_SS_DBCz _293K*
CCDC code	2321139	2321136	2321134
Empirical formula	$C_{53}H_{62}AuN_3$	$C_{57}H_{68}AuN_3$	$C_{57}H_{68}AuN_3$
Formula weight	938.02	992.11	992.11
Temperature/K	293	123	293
Crystal system	orthorhombic	triclinic	triclinic
Space group	Pbca	P1	P1
a/Å	29.9308(3)	9.59749(8)	9.77490(10)
b/Å	9.48390(10)	16.87313(14)	17.1688(2)
c/Å	34.3545(4)	17.34030(15)	17.2868(2)
α/°	90	118.5208(9)	118.6930(10)
β/°	90	90.6409(7)	90.3220(10)
γ/°	90	92.1614(7)	93.0050(10)
Volume/Å^3	9751.89(18)	2464.18(4)	2539.81(5)
Z	8	2	2
ρ_{calc}g/cm^3	1.278	1.337	1.297
μ/mm^{-1}	5.925	5.891	5.716
F(000)	3840.0	1020.0	1020.0
Crystal size/mm^3	0.1 × 0.01 × 0.01	0.2 × 0.01 × 0.01	0.2 × 0.01 × 0.01
Radiation	Cu Kα (λ = 1.54184)	Cu Kα (λ = 1.54184)	Cu Kα (λ = 1.54184)
2Θ range for data collection/°	5.144 to 152.68	5.804 to 133.2	5.832 to 153.062
Index ranges	-37 ≤ h ≤ 36, -11 ≤ k ≤ 9, -38 ≤ l ≤ 43	-10 ≤ h ≤ 11, -20 ≤ k ≤ 20, -20 ≤ l ≤ 20	-10 ≤ h ≤ 11, -21 ≤ k ≤ 21, -21 ≤ l ≤ 21
Reflections collected	78013	88081	94381
Independent reflections	9926 [R_{int} = 0.0594, R_{sigma} = 0.0221]	16974 [R_{int} = 0.0580, R_{sigma} = 0.0377]	19273 [R_{int} = 0.0583, R_{sigma} = 0.0373]
Data/restraints/parameters	9926/154/556	16974/3/1123	19273/525/1256
Goodness-of-fit on F^2	1.291	1.044	1.072
Final R indexes [I>=2σ (I)]	R_1 = 0.0917, wR_2 = 0.1937	R_1 = 0.0341, wR_2 = 0.0860	R_1 = 0.0455, wR_2 = 0.1283
Final R indexes [all data]	R_1 = 0.1132, wR_2 = 0.2049	R_1 = 0.0374, wR_2 = 0.0887	R_1 = 0.0505, wR_2 = 0.1329
Largest diff. peak/hole / e Å^{-3}	1.87/-0.93	1.52/-0.79	1.10/-1.10
Flack parameter	-	0.018(15)	0.063(17)
* – the same single crystal was used for 123K and 293K measurements			

Table S2.5. Crystal data and structure refinement for **2**_RR_DBCz_123K, **2**_RR_DBCz_293K, **3**_SS_DBCz_293K crystal structures.

Identification code	**2**_RR_DBCz _123K*	**2**_RR_DBCz _293K*	**3**_SS_DBCz _293K
CCDC code	2321138	2321133	2321140
Empirical formula	$C_{57}H_{68}AuN_3$	$C_{57}H_{68}AuN_3$	$C_{65}H_{70}AuN_3$
Formula weight	992.11	992.11	1090.20
Temperature/K	123	293	293
Crystal system	triclinic	triclinic	tetragonal
Space group	P1	P1	$P4_12_12$
a/Å	9.5868(2)	9.78045(11)	10.70425(4)
b/Å	16.8650(2)	17.19108(19)	10.70425(4)
c/Å	17.3535(3)	17.27739(15)	48.7415(3)
α/°	118.5550(10)	118.7677(11)	90
β/°	90.608(2)	90.2485(9)	90
γ/°	92.1700(10)	93.0863(9)	90
Volume/Å^3	2461.36(8)	2541.21(5)	5584.84(5)
Z	2	2	4
ρ_{calc}g/cm^3	1.339	1.297	1.297
μ/mm^{-1}	5.898	5.713	5.251
F(000)	1020.0	1020.0	2240.0
Crystal size/mm^3	0.2 × 0.01 × 0.01	0.2 × 0.01 × 0.01	0.1 × 0.1 × 0.05
Radiation	Cu Kα (λ = 1.54184)	Cu Kα (λ = 1.54184)	Cu Kα (λ = 1.54184)
2Θ range for data collection/°	5.802 to 134.152	5.84 to 152.862	8.458 to 152.726
Index ranges	-11 ≤ h ≤ 11, -20 ≤ k ≤ 20, -20 ≤ l ≤ 20	-12 ≤ h ≤ 11, -21 ≤ k ≤ 21, -21 ≤ l ≤ 21	-13 ≤ h ≤ 13, -8 ≤ k ≤ 13, -61 ≤ l ≤ 61
Reflections collected	81503	92663	54508
Independent reflections	17134 [R_{int} = 0.0597, R_{sigma} = 0.0355]	19290 [R_{int} = 0.0533, R_{sigma} = 0.0323]	5804 [R_{int} = 0.0492, R_{sigma} = 0.0203]
Data/restraints/parameters	17134/149/1123	19290/542/1246	5804/96/319
Goodness-of-fit on F^2	1.072	1.122	1.152
Final R indexes [I>=2σ (I)]	R_1 = 0.0455, wR_2 = 0.1168	R_1 = 0.0678, wR_2 = 0.1811	R_1 = 0.0323, wR_2 = 0.0641
Final R indexes [all data]	R_1 = 0.0491, wR_2 = 0.1192	R_1 = 0.0748, wR_2 = 0.1862	R_1 = 0.0335, wR_2 = 0.0646
Largest diff. peak/hole / e Å^{-3}	1.61/-0.64	1.14/-1.67	0.41/-0.64
Flack parameter	0.04(2)	0.12(3)	-0.012(5)
* – the same single crystal was used for 123K and 293K measurements			

Table S2.6. Crystal data and structure refinement for **3**_SS_BCz_293K, **3**_RR_DBCz_293K, **2**_RR_BCz_293K crystal structures.

Identification code	**3**_SS_BCz _293K	**3**_RR_DBCz _293K	**3**_RR_BCz _293K
CCDC code	2321137	2321135	2321141
Empirical formula	$C_{61}H_{68}AuN_3$	$C_{65}H_{70}AuN_3$	$C_{61}H_{68}AuN_3$
Formula weight	1040.15	1090.20	1040.15
Temperature/K	293	293	293
Crystal system	tetragonal	tetragonal	tetragonal
Space group	$P4_12_12$	$P4_32_12$	$P4_32_12$
a/Å	10.61070(10)	10.70641(5)	10.62127(6)
b/Å	10.61070(10)	10.70641(5)	10.62127(6)
c/Å	49.0089(4)	48.6727(4)	49.0259(4)
α/°	90	90	90
β/°	90	90	90
γ/°	90	90	90
Volume/Å^3	5517.76(11)	5579.22(7)	5530.68(8)
Z	4	4	4
ρ_{calc}g/cm^3	1.252	1.298	1.249
μ/mm^{-1}	5.288	5.256	5.276
F(000)	2136.0	2240.0	2136.0
Crystal size/mm^3	0.1 × 0.1 × 0.1	0.1 × 0.1 × 0.05	0.2 × 0.1 × 0.1
Radiation	Cu Kα (λ = 1.54184)	Cu Kα (λ = 1.54184)	Cu Kα (λ = 1.54184)
2Θ range for data collection/°	7.214 to 153.074	7.264 to 153.012	7.212 to 153.118
Index ranges	-12 ≤ h ≤ 13, -13 ≤ k ≤ 12, -61 ≤ l ≤ 61	-13 ≤ h ≤ 13, -12 ≤ k ≤ 10, -61 ≤ l ≤ 61	-13 ≤ h ≤ 13, -9 ≤ k ≤ 13, -59 ≤ l ≤ 61
Reflections collected	54218	53840	54475
Independent reflections	5739 [R_{int} = 0.0511, R_{sigma} = 0.0176]	5737 [R_{int} = 0.0383, R_{sigma} = 0.0166]	5718 [R_{int} = 0.0866, R_{sigma} = 0.0293]
Data/restraints/parameters	5739/155/350	5737/24/319	5718/478/359
Goodness-of-fit on F^2	1.189	1.099	1.161
Final R indexes [I>=2σ (I)]	R_1 = 0.0352, wR_2 = 0.0817	R_1 = 0.0243, wR_2 = 0.0535	R_1 = 0.0434, wR_2 = 0.0950
Final R indexes [all data]	R_1 = 0.0365, wR_2 = 0.0824	R_1 = 0.0251, wR_2 = 0.0539	R_1 = 0.0465, wR_2 = 0.0967
Largest diff. peak/hole / e Å^{-3}	0.67/-0.71	0.47/-0.43	0.65/-1.01
Flack parameter	0.008(6)	-0.020(3)	0.001(10)

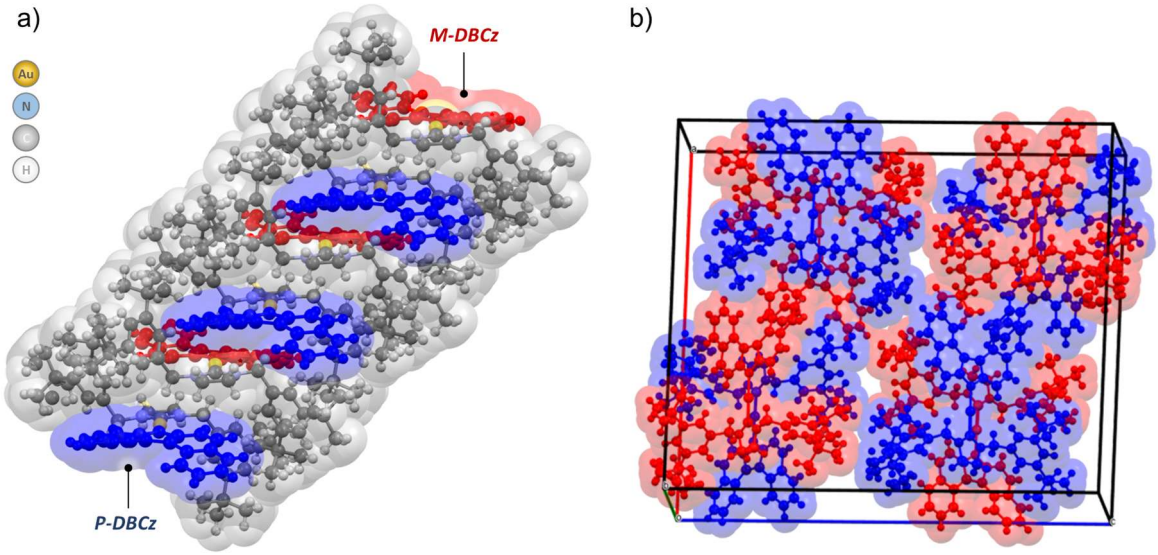

Figure S2.11. View of (a) crystal packing and (b) unit cell of **1**-DBCz. On frame "b" blue and red colors depict the complexes with *P*- and *M*-DBCz moieties, correspondingly.

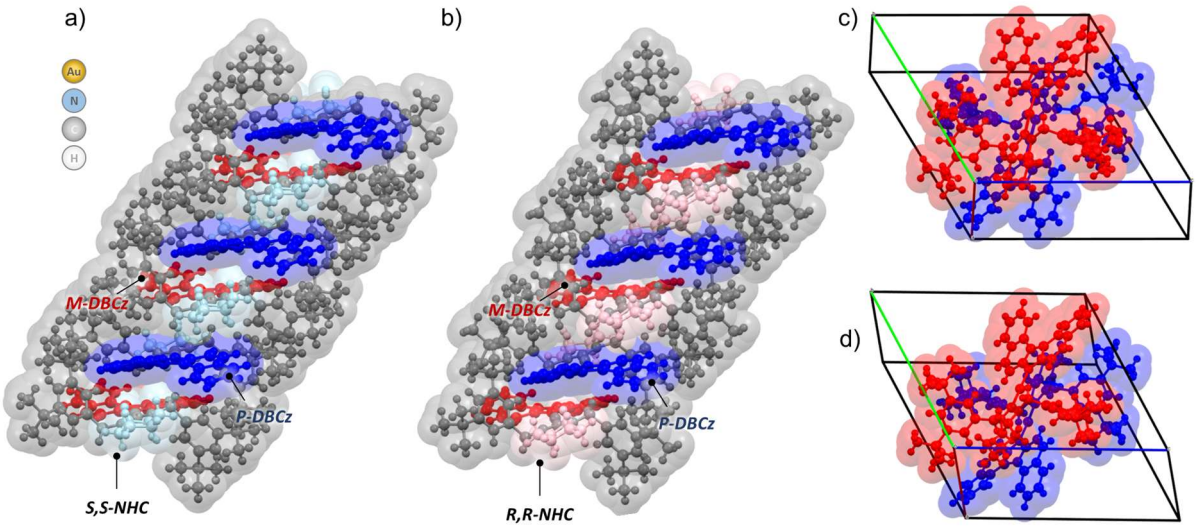

Figure S2.12. View of crystal packing and unit cell of (a,c) **2**-(*S,S*)-DBCz and (b,d) **2**-(*R,R*)-DBCz. On frames "c,d" blue and red colors depict the complexes with *P*- and *M*-DBCz moieties, correspondingly.

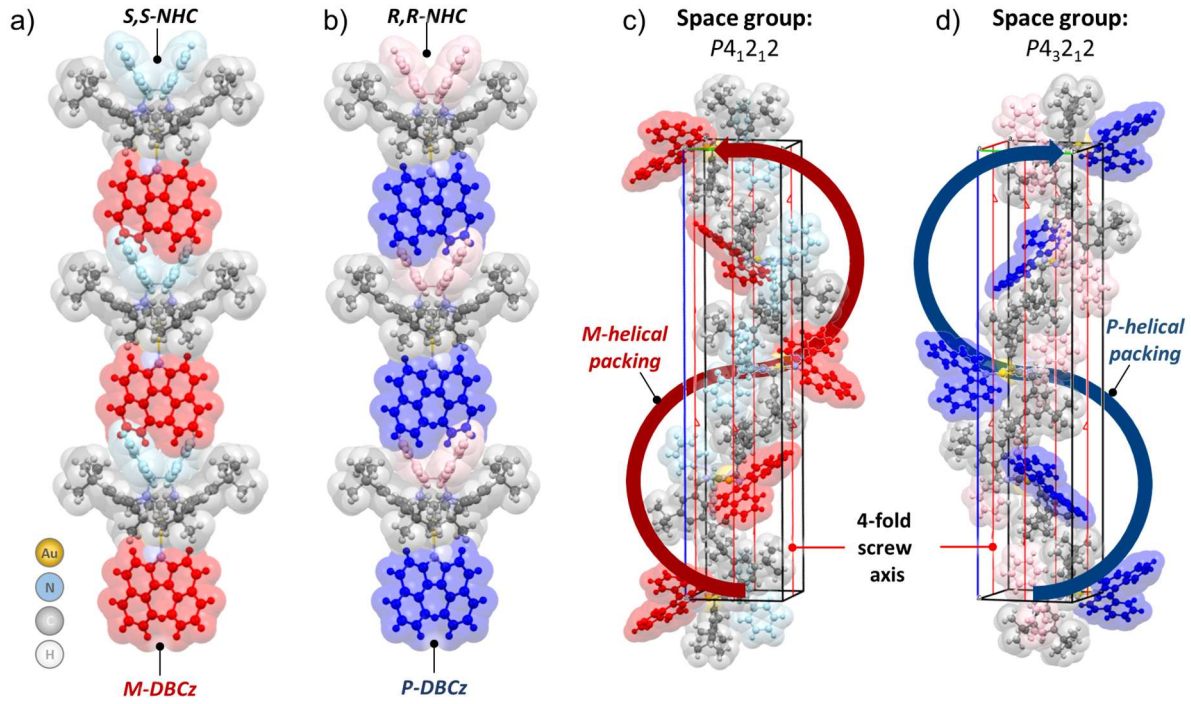

Figure S2.13. View of crystal packing and unit cell of (a,c) **3**-(*S,S*)-DBCz and (b,d) **3**-(*R,R*)-DBCz.

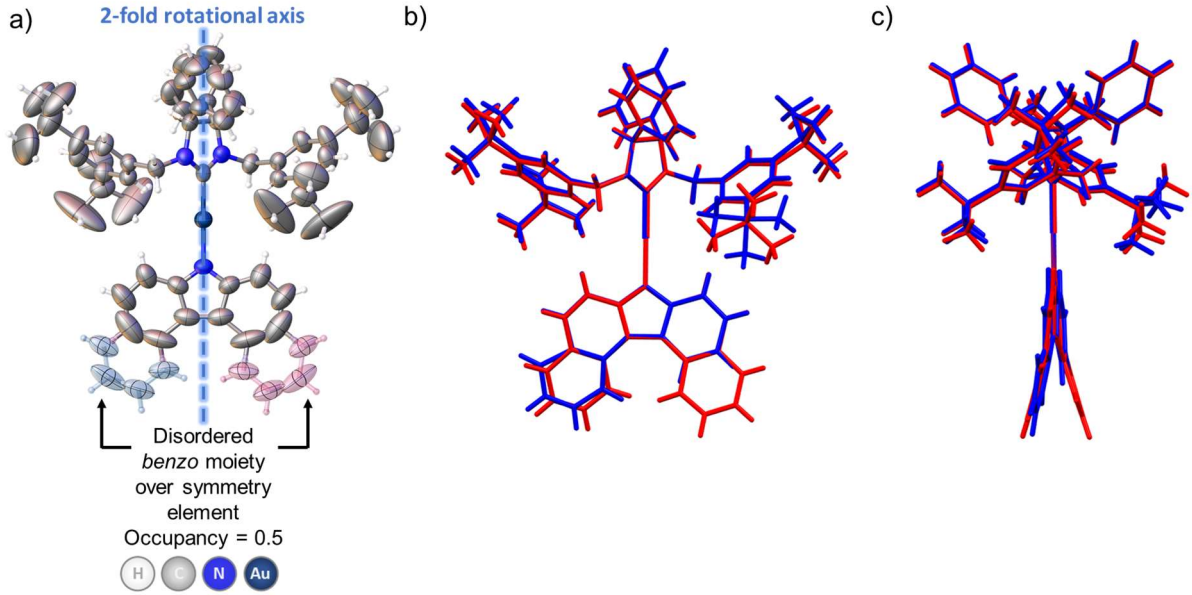

Figure S2.14. (a) View of the crystal structure of **3**-(*S,S*)-BCz with disordered benzo moiety over a symmetry element. Overlap of structures of **3**-(*S,S*)-DBCz (red) and **3**-(*S,S*)-BCz (blue) from the crystal structures: (b) front view and (c) side view.

Table S2.7. The geometrical parameters of curvature of DBCz and BCz moieties in XRD structures.

Complex	T	Type	θ_1, deg	θ_2, deg	θ_3, deg
1-DBCz	293K	*M/P*	19.1(17)	9.6(16)	10.8(15)
2-(*S,S*)-DBCz	293K	*M*	15(3)	15(3)	10(3)
		P	19(3)	13(3)	4(3)
	123K	*M*	18(2)	12(2)	11(2)
		P	17(3)	11(3)	9(2)
2-(*R,R*)-DBCz	293K	*M*	14(6)	9(5)	16(4)
		P	20(4)	8(4)	11(4)
	123K	*M*	18(3)	7(3)	13(3)
		P	16(3)	9(3)	16(3)
3-(*S,S*)-DBCz	293K	*M*	22.3(8)	8.7(10)	-
3-(*R,R*)-DBCz	293K	*P*	22.6(7)	8.3(8)	-
3-(*S,S*)-BCz	293K	*M*	10.6(12)	10(2)	-
3-(*S,S*)-BCz	293K	*P*	7.0(15)	11(2)	-

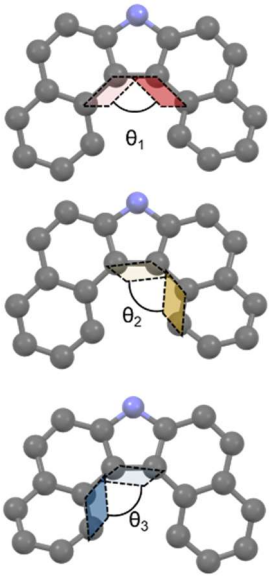

4.4.8 Powder X-ray diffraction analysis

Powder X-ray diffraction (PXRD) data of the crystalline samples were collected on a Rigaku SmartLab diffractometer with Cu-Kα radiation and D/teX Ultra detector covering a 5-50° (2θ) range at room temperature. The ground crystal samples were prepared by grinding the crystals in an agate mortar for one minute. For the crystalline samples air stability test, the crystals were stored under ambient air conditions at room temperature for approximately five months. Simulated PXRD patterns were generated with Mercury 2022.2.0[74] from the structures determined by the SCXRD at 293K (**Figures S2.15–S2.18**).

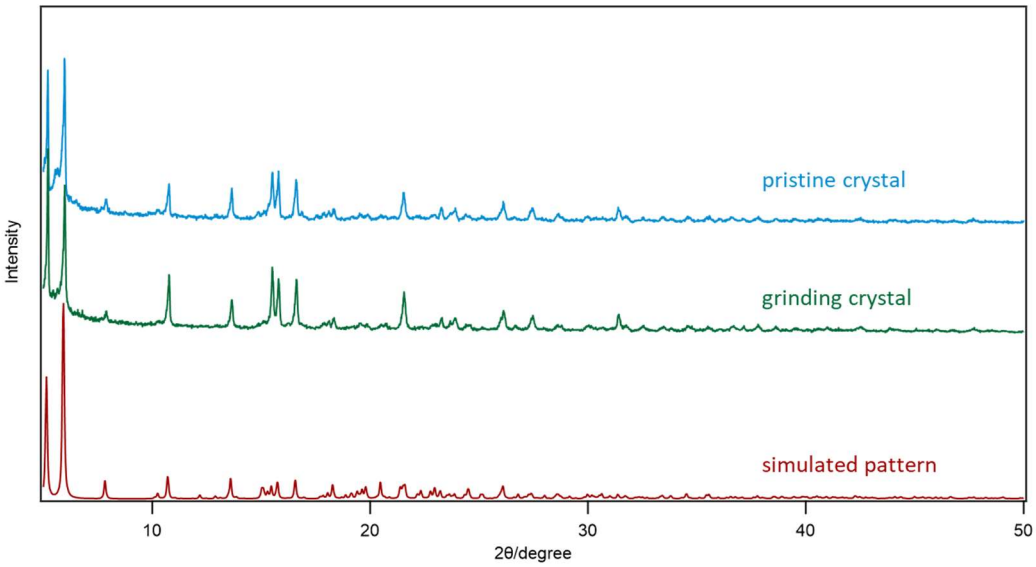

Figure S2.15. Experimental (for pristine and ground crystals) and simulated PXRD patterns of crystalline samples of **1**-DBCz.

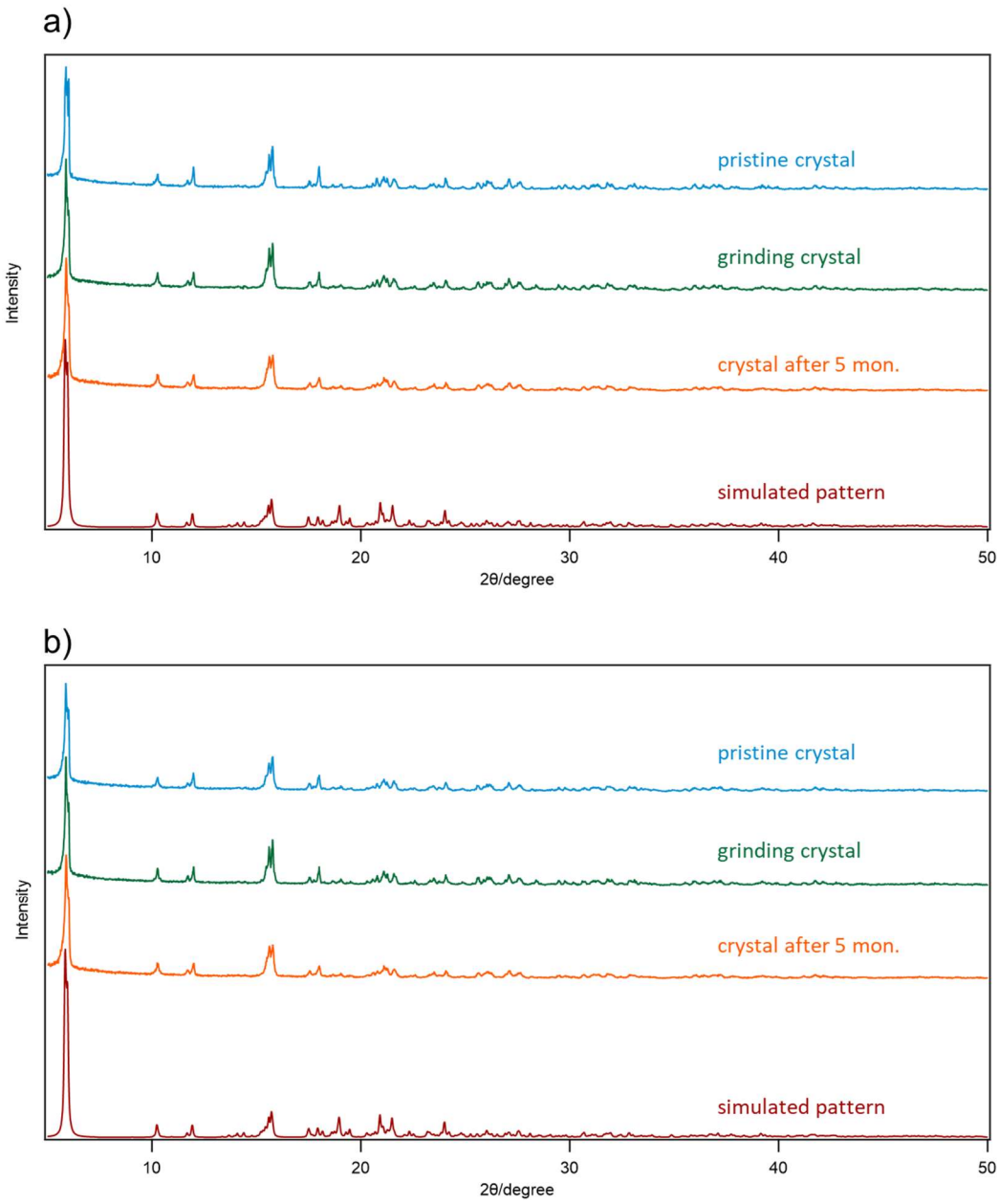

Figure S2.16. Experimental (for pristine and ground crystals, as well as pristine crystals after five months of storage under air) and simulated PXRD patterns of crystalline samples of (a) **2.2**-(*S,S*)-DBCz and (b) **2**-(*R,R*)-DBCz.

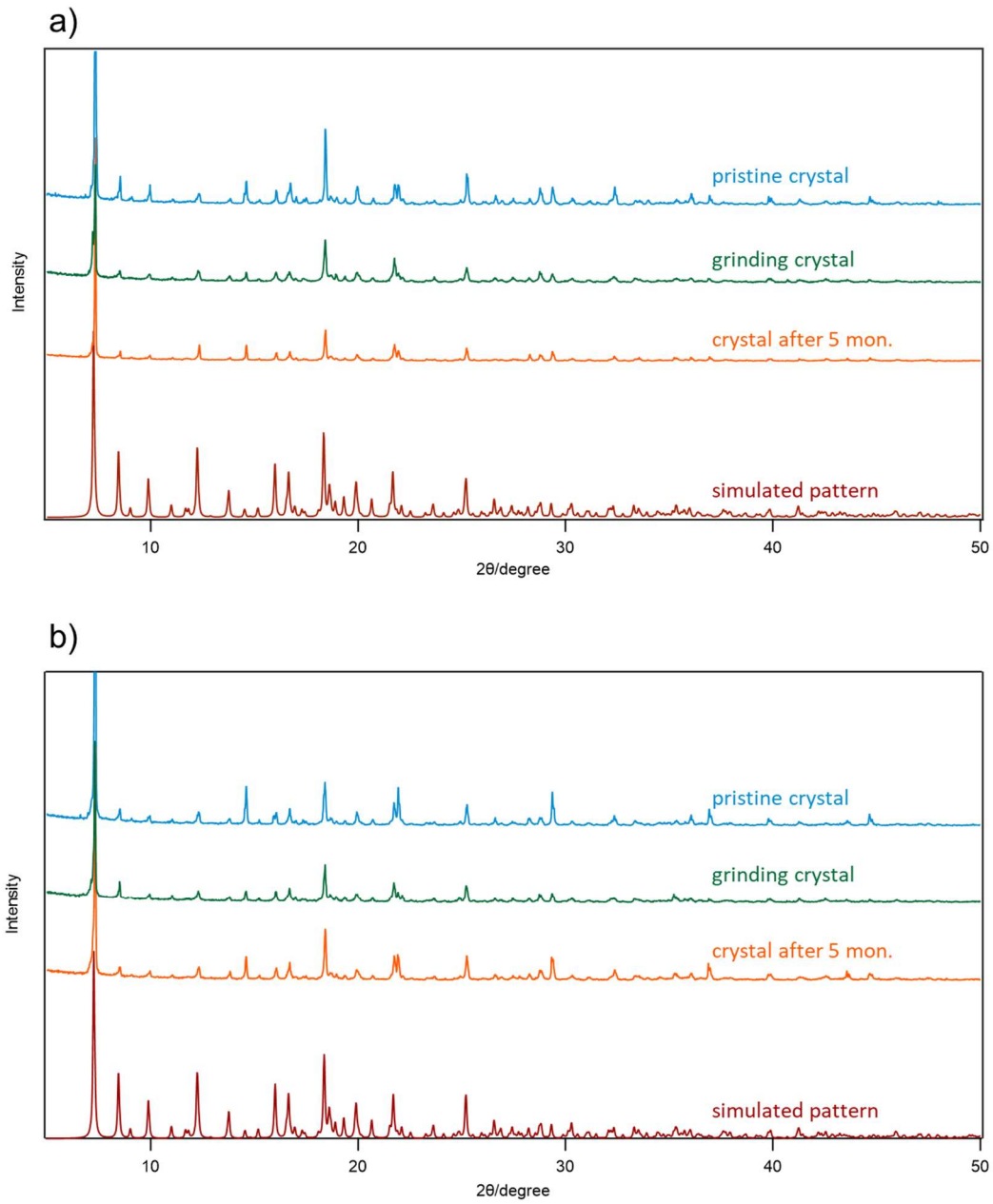

Figure S2.17. Experimental (for pristine and ground crystals, as well as pristine crystals after five months of storage under air) and simulated PXRD patterns of crystalline samples of (a) **3**-(*S,S*)-DBCz and (b) **3**-(*R,R*)-DBCz.

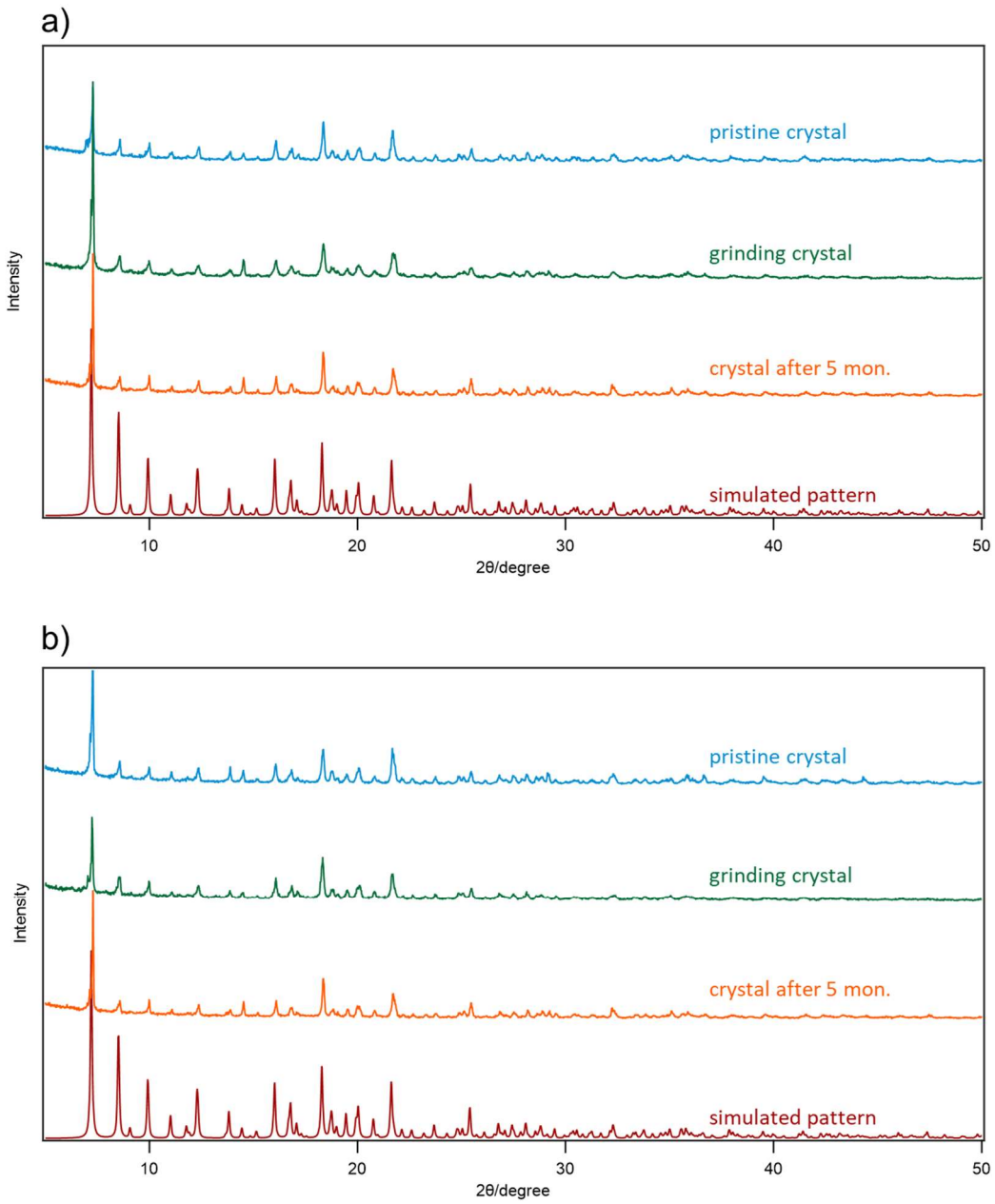

Figure S2.18. Experimental (for pristine and ground crystals, as well as pristine crystals after five months of storage under air) and simulated PXRD patterns of crystalline samples of (a) **3**-(*S,S*)-DBCz and (b) **3**-(*R,R*)-DBCz.

4.4.9 Optical analysis

The solution samples for CD, CPL, and PL measurements were prepared by dissolution of the crystalline complexes in CH_2Cl_2. 1.2×10^{-4} mol·L^{-1} concentration was used for the measurements of **1**-Cl, **2**-Cl, and **3**-Cl complexes, while 2.0×10^{-5} mol·L^{-1} concentration was used for the measurements of DBCz, BCz, **1**-DBCz, **2**-DBCz,.**3**-DBCz, and **3**-BCz species.

The samples for solid-state measurements of CD, CPL, and PL were prepared by the Nujol mull method [75-76] (see **Figure S2.19** for the procedure). The sample crystallinity after the neat grinding was insured by the PXRD method (see Section S7). For CD measurements, the samples were prepared by mixing 2.0 mg of the ground complex with 100 mg mineral (paraffin) oil (2% w/w of the Au(I) complex). For CPL and PL measurements, the samples were prepared by mixing 2.0 mg of ground complex with 20 mg mineral oil (10% w/w of the Au(I) complex).

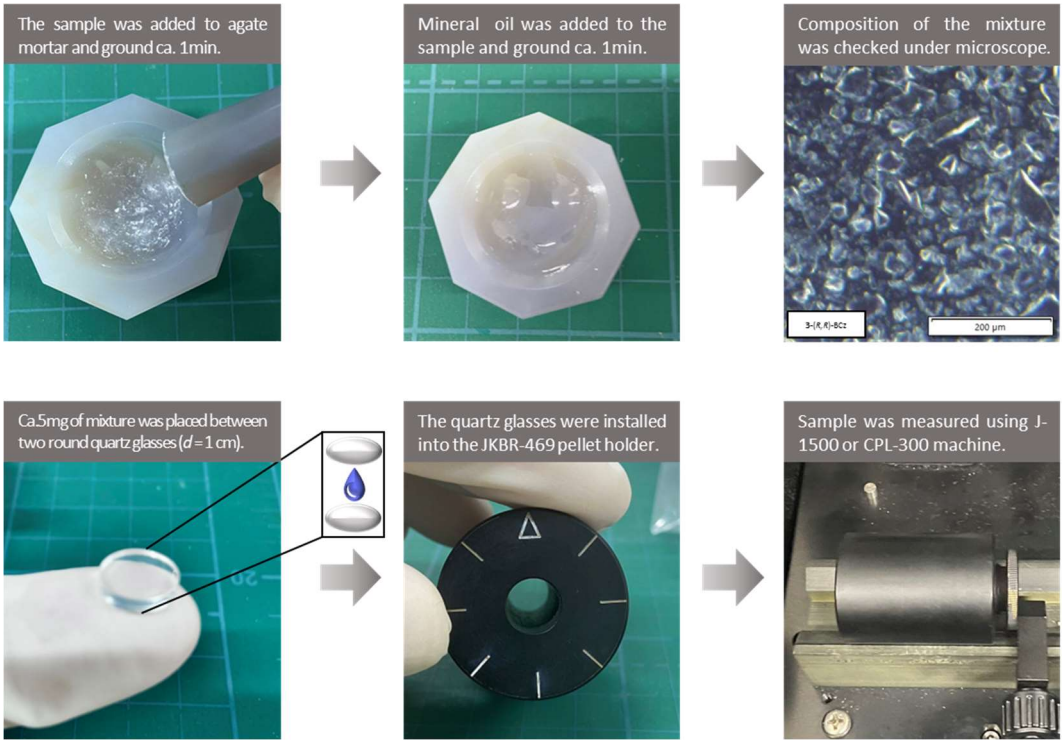

Figure S2.19. The procedure for sample preparation for solid-state CD and CPL measurements by Nujol mull method.

Absorption and circular dichroism

Absorption and circular dichroism (CD) spectra were measured on a JASCO J-1500 Circular Dichroism Spectrophotometer at room temperature. The cell for solution sample was 10 mm in size. 2 sec D.I.T. with 1.0 nm bandwidth, 200 nm/min scanning speed, and four accumulations were used for both solution and crystalline sample (**Figures S2.20–S2.23**). All data underwent background subtraction (CH_2Cl_2 for solution measurements and mineral oil for solid-state measurements). The absorption dissymmetry factors (g_{abs}) (**Figure S2.24**) were calculated using JASCO Spectra Manager software.

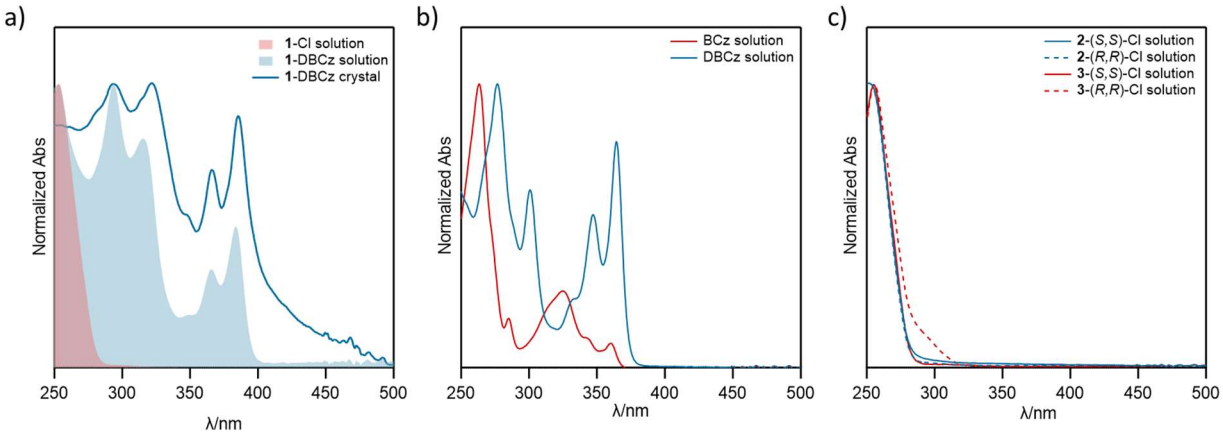

Figure S2.20. (a) Absorption spectra of **1**-Cl and **1**-DBCz in CH_2Cl_2 solution and **1**-DBCz in solid state; (b) Absorption spectra of BCz and DBCz in CH_2Cl_2 solution; (c) Absorption spectra of **2**-(*S,S*)-Cl, **2**-(*R,R*)-Cl, **3**-(*S,S*)-Cl, and **3**-(*R,R*)-Cl in CH_2Cl_2 solution.

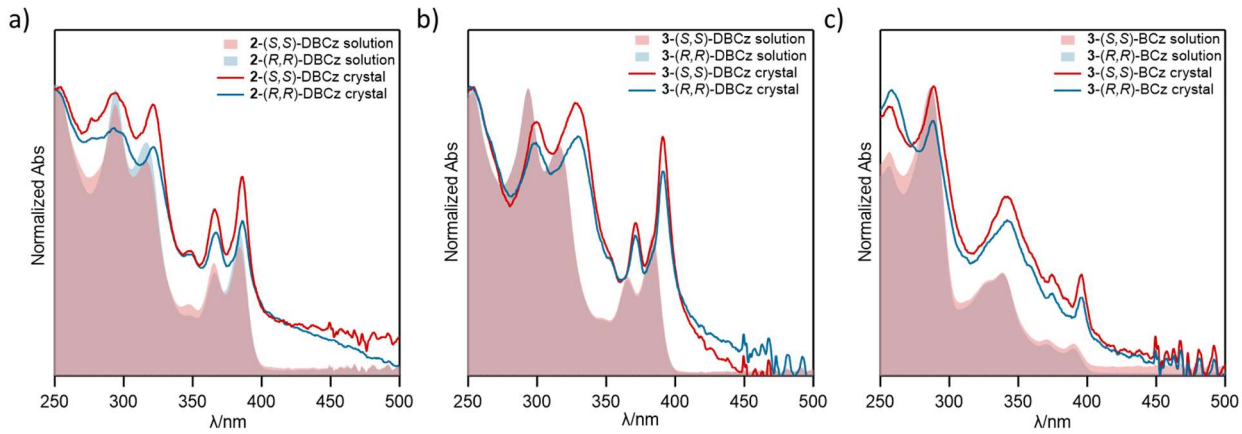

Figure S2.21. (a) Absorption spectra of **2**-(*S,S*)-DBCz and **2**-(*R,R*)-DBCz in CH_2Cl_2 solution and solid state; (b) Absorption spectra of **3**-(*S,S*)-DBCz and **3**-(*R,R*)-DBCz in CH_2Cl_2 solution and solid state; (c) Absorption spectra of **3**-(*S,S*)-BCz and **3**-(*R,R*)-BCz in CH_2Cl_2 solution and solid state.

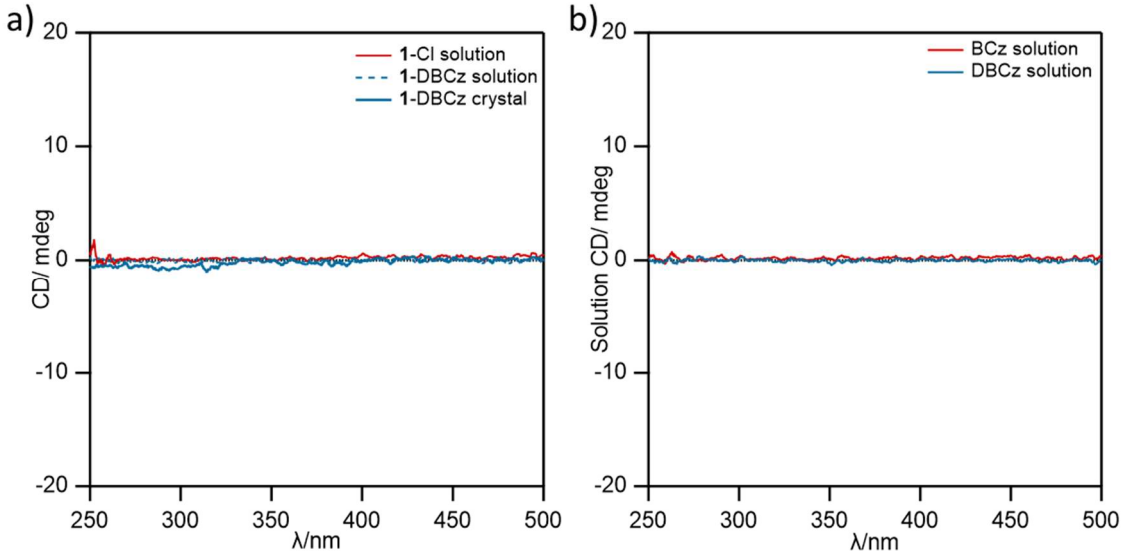

Figure S2.22. (a) CD spectra of **1**-Cl, **1**-DBCz in CH_2Cl_2 solution and **1**-DBCz in solid state; (b) CD spectra of BCz and DBCz in CH_2Cl_2 solution.

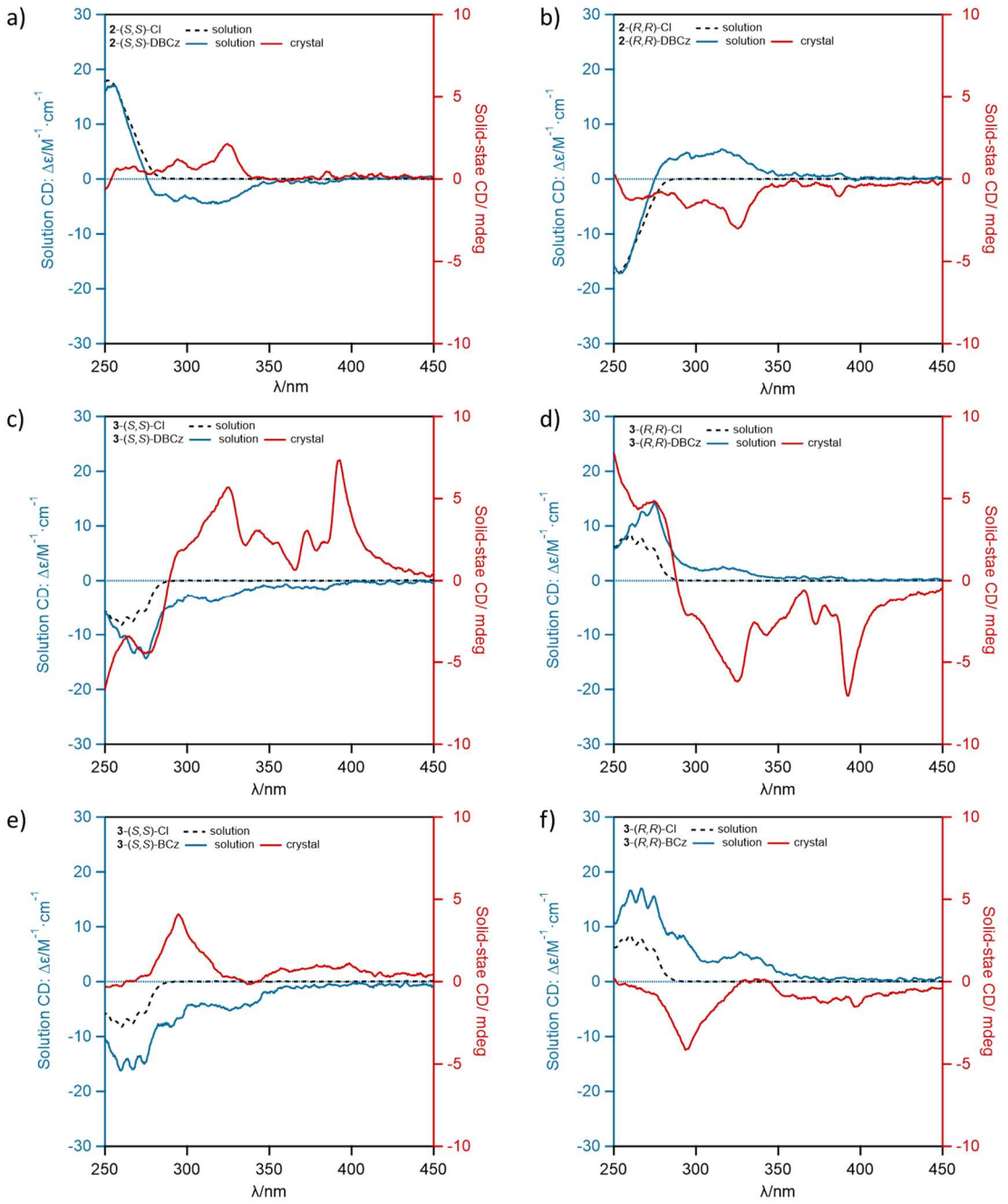

Figure S2.23. Grouped CD spectra of: (a) **2**-(*S,S*)-Cl (solution, black dashed line)**,** **2**-(*S,S*)-DBCz (solution, blue solid line), **2**-(*S,S*)-DBCz (crystal, red solid line); (b) **2**-(*R,R*)-Cl (solution, black dashed line)**,** **2**-(*R,R*)-DBCz (solution, blue solid line), **2**-(*R,R*)-DBCz (crystal, red solid line); (c) **3**-(*S,S*)-Cl (solution, black dashed line)**,.3**-(*S,S*)-DBCz (solution, blue solid line), **3**-(*S,S*)-DBCz (crystal, red solid line); (d) **3**-(*R,R*)-Cl (solution, black dashed line)**,** **3**-(*R,R*)-DBCz (solution, blue solid line), **3**-(*R,R*)-DBCz (crystal, red solid line); (e) **3**-(*S,S*)-Cl (solution, black dashed line)**,** **3**-(*S,S*)-BCz (solution, blue solid line), **3**-(*S,S*)-BCz (crystal, red solid line); (f) **3**-(*R,R*)-Cl (solution, black dashed line)**,** **3**-(*R,R*)-BCz (solution, blue solid line), **3**-(*R,R*)-BCz (crystal, red solid line).

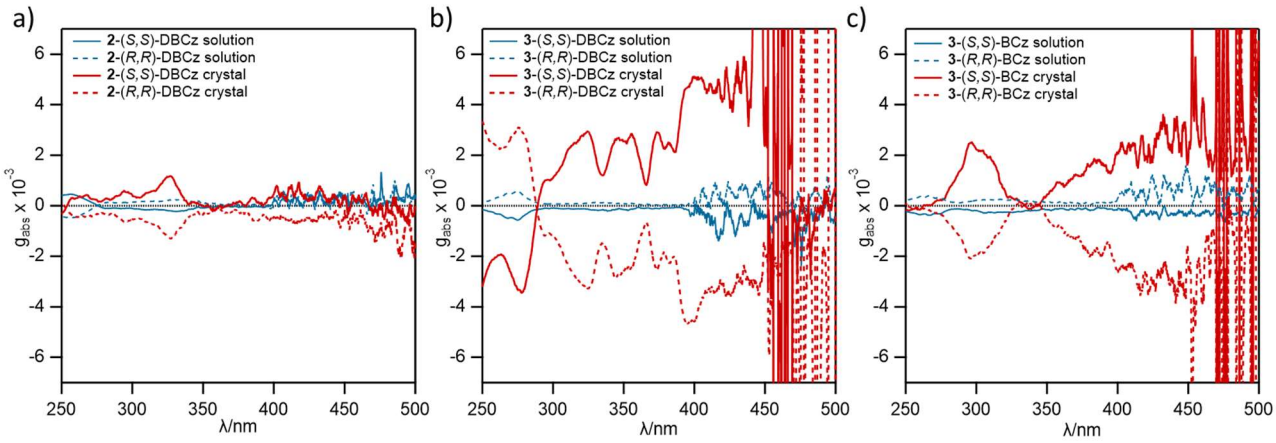

Figure S2.24. (a) g_{abs} plots of **2**-(S,S)-DBCz and **2**-(R,R)-DBCz in CH_2Cl_2 solution and solid state; (b) g_{abs} plots of **3**-(S,S)-DBCz and **3**-(R,R)-DBCz in CH_2Cl_2 solution and solid state; (c) g_{abs} plots of **3**-(S,S)-BCz and **3**-(R,R)-BCz in CH_2Cl_2 solution and solid-state (the noise after 450 nm is due to very low absorption).

Photoluminescence (PL) and circularly polarized luminescence (CPL)

PL emission and excitation spectra (**Figures S2.25–S2.26**) were recorded on an Edinburgh Instruments FLS1000 Photoluminescence Spectrometer. 1.5 nm excitation/emission bandwidth and 0.1 dwell time were used; the data were accumulated 10 times. Emission decay profiles (**Figure S2.27, Tables S2.8–S2.9**) were obtained using an Edinburgh Instruments FLS1000 Photoluminescence Spectrometer with the microsecond halogen flash lamp (μF). The PL quantum yields for solution and solid-state samples (**Tables S2.8–S2.9**) were acquired on a Hamamatsu Quantaurus-QY absolute PL quantum yield spectrometer with an integrating sphere.

Circularly Polarized Luminescence (CPL) data (**Figures S2.28–S2.29**) were recorded on a JASCO CPL-300 Circularly Polarized Luminescence Spectrophotometer at room temperature. For the solution samples, the cell was 10 mm in size. 2 sec D.I.T. with 15.0 nm excitation/emission bandwidth and 200 nm/min scanning speed was set, and the data were accumulated 10 times. For the crystalline samples, 4 sec D.I.T. with 15.0 nm excitation bandwidth, 20.0 nm emission bandwidth, and 100 nm/min scanning speed were set, the data were accumulated 20 times. For the excitation, the region from 250–350 nm was chosen, while 350–400 nm region cannot be utilized due to proximity to the emission wavelengths. Luminescent dissymmetry factors (g_{lum}) (**Figure S2.29c**) were calculated by JASCO Spectra Manager software.

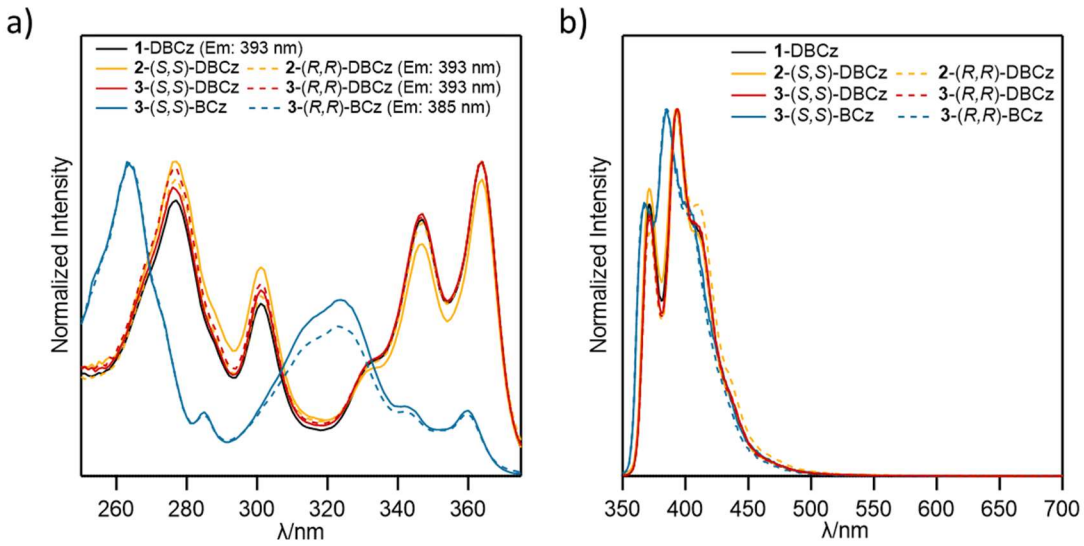

Figure S2.25. (a) Excitation spectra of **1**-DBCz, **2.2**-(*S,S*)-DBCz, **2.2**-(*R,R*)-DBCz, **2.3**-(*S,S*)-DBCz, **2.3**-(*R,R*)-DBCz, **3**-(*S,S*)-BCz, and **3**-(*R,R*)-BCz in CH_2Cl_2 solution; (b) Emission spectra of **1**-DBCz (λ_{ex}=276 nm), **2**-DBCz (λ_{ex}=276 nm), **3**-DBCz (λ_{ex}=276 nm), and **3**-BCz (λ_{ex}=264 nm) in CH_2Cl_2 solution.

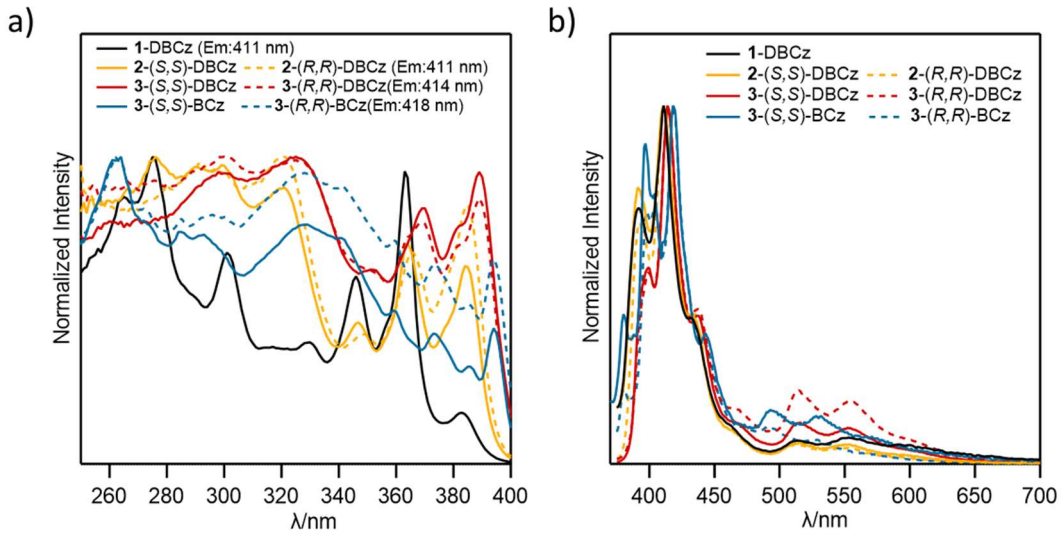

Figure S2.26. (a) Excitation spectra of **1**-DBCz, **2**-(*S,S*)-DBCz, **2**-(*R,R*)-DBCz, **3**-(*S,S*)-DBCz, **3**-(*R,R*)-DBCz, **3**-(*S,S*)-BCz, and **3**-(*R,R*)-BCz in solid state; (b) Emission spectra of **1**-DBCz, **2**-(*S,S*)-DBCz, **2**-(*R,R*)-DBCz (λ_{ex}=320nm), **3**-(*S,S*)-DBCz, **3**-(*R,R*)-DBCz (λ_{ex}=326nm), and **3**-(*S,S*)-BCz, **3**-(*R,R*)-BCz (λ_{ex}=302nm) in solid state.

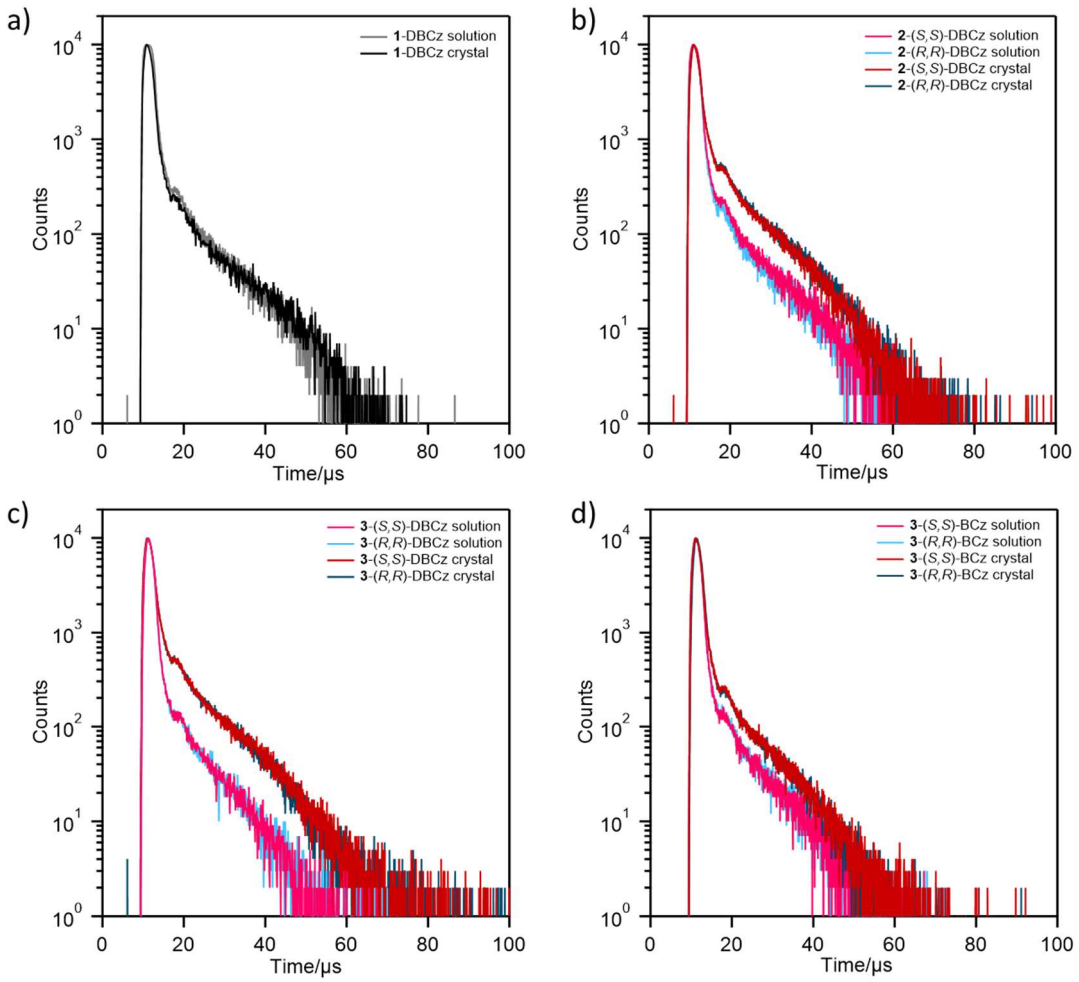

Figure S2.27. (a) Emission decay profiles of **1**-DBCz in CH_2Cl_2 solution (λ_{ex}=276nm, λ_{em}=393nm) and solid state(λ_{ex}=300nm, λ_{em}=418nm); (b) Emission decay profiles of **2**-DBCz in CH_2Cl_2 solution (λ_{ex}=276nm, λ_{em}=393nm) and solid state (λ_{ex}=320nm, λ_{em}=411nm); (c) Emission decay profiles of **3**-DBCz in CH_2Cl_2 solution (λ_{ex}=276nm, λ_{em}=392nm) and solid state (λ_{ex}=326nm, λ_{em}=414nm); (d) Emission decay profiles of **3**-BCz in CH_2Cl_2 solution (λ_{ex}=264nm, λ_{em}=385nm) and solid state (λ_{ex}=302nm, λ_{em}=418nm).

Table S2.8. Emission lifetime fitted from the emission decays and emission quantum yields in CH_2Cl_2 solution.

Complex	λ_{ex}/nm	λ_{em}/nm	t_1/μs	r_1, %	t_2/μs	r_2, %	t_{av}/μs	CHI	QY/%
1-DBCz	276	393	0.717	38.3	8.179	61.7	5.318	1.14	3.1
2-(*S,S*)-DBCz	276	393	0.687	62.0	8.168	38.0	3.530	1.11	1.5
2-(*R,R*)-DBCz	276	393	0.690	64.6	8.314	35.4	3.386	1.10	1.4
3-(*S,S*)-DBCz	276	392	0.808	81.3	7.835	18.7	2.119	1.03	1.6
3-(*R,R*)-DBCz	276	392	0.809	82.8	8.083	17.2	2.061	1.13	2.0
3-(*S,S*)-BCz	264	385	0.681	71.9	7.937	28.1	2.718	1.02	1.2
3-(*R,R*)-BCz	264	385	0.677	69.1	7.809	30.9	2.881	1.06	1.3

Table S2.9. Emission lifetime fitted from the emission decays and emission quantum yields in solid state.

Complex	λ_{ex}/nm	λ_{em}/nm	t_1/μs	r_1, %	t_2/μs	r_2, %	t_{av}/μs	CHI	QY/%
1-DBCz	300	418	0.885	72.0	9.604	28.0	3.326	1.07	2.0
2-(*S,S*)-DBCz	320	411	1.108	60.1	9.879	39.9	4.610	1.08	<1
2-(*R,R*)-DBCz	320	411	1.044	57.4	8.952	42.6	4.414	1.06	<1
3-(*S,S*)-DBCz	326	414	1.046	57.3	9.276	42.7	4.563	1.05	1.0
3-(*R,R*)-DBCz	326	414	1.018	55.8	9.050	44.2	4.567	1.02	1.0
3-(*S,S*)-BCz	302	418	0.905	72.0	8.531	28.0	3.040	1.17	<1
3-(*R,R*)-BCz	302	418	0.898	64.9	8.626	35.1	3.609	1.02	<1

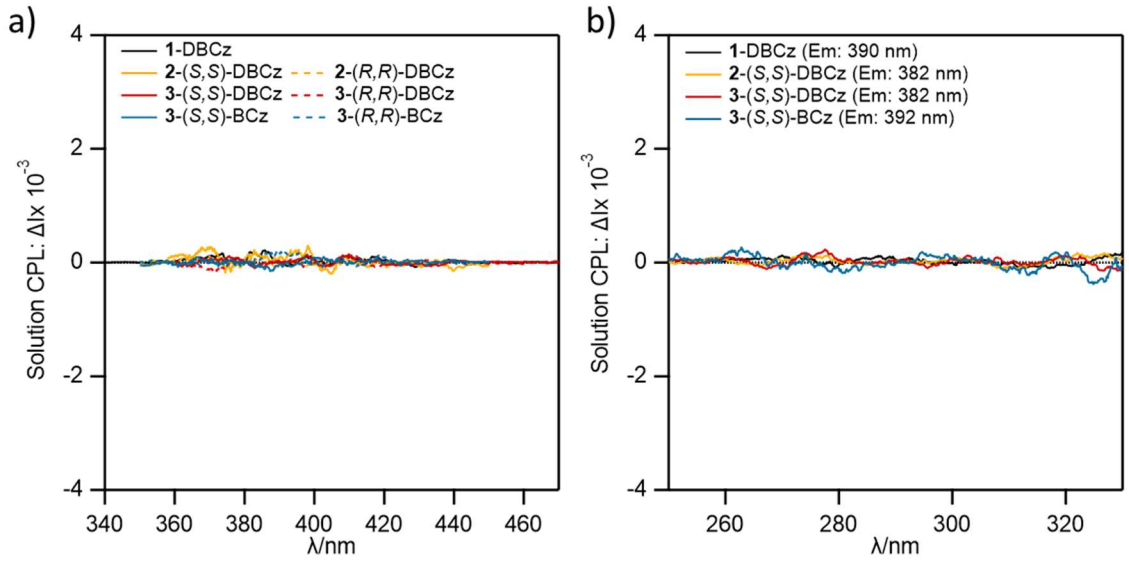

Figure S2.28. (a) CPL Spectra of **1**-DBCz (λ_{ex} = 276 nm), **2**-(*S,S*)-DBCz, **2**-(*R,R*)-DBCz (λ_{ex} = 276 nm), **3**-(*S,S*)-DBCz, **3**-(*R,R*)-DBCz (λ_{ex} = 267 nm), **3**-(*S,S*)-BCz, and **3**-(*R,R*)-BCz (λ_{ex}=264 nm) in CH_2Cl_2 solution; (b) Excitation CPL spectra of **1**-DBCz, **2**-(*S,S*)-DBCz, **3**-(*S,S*)-DBCz and **3**-(*S,S*)-BCz in CH_2Cl_2 solution.

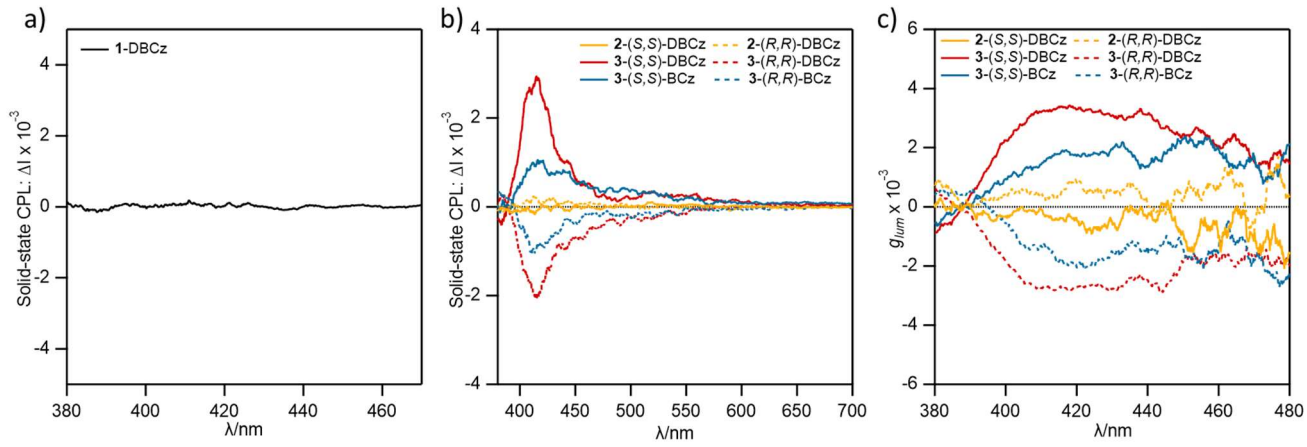

Figure S2.29. (a) CPL Spectra of **1**-DBCz in solid state (λ_{ex} = 300nm); (b) CPL spectra of **2**-(*S,S*)-DBCz, **2**-(*R,R*)-DBCz (λ_{ex} = 320nm), **3**-(*S,S*)-DBCz, **3**-(*R,R*)-DBCz (λ_{ex} = 326nm), and **3**-(*S,S*)-BCz, **2**-(*R,R*)-BCz (λ_{ex} = 302nm) in solid state, measured up to 700 nm; (c) g_{lum} plots of **2**-(*S,S*)-DBCz, **2**-(*R,R*)-DBCz (λ_{ex} = 320nm), **3**-(*S,S*)-DBCz, **3**-(*R,R*)-DBCz (λ_{ex} = 326nm), and **3**-(*S,S*)-BCz, **3**-(*R,R*)-BCz (λ_{ex} = 302nm) in solid state.

Table S2.10. Selected absorption dissymmetry factor values ($g_{abs} \times 10^{-3}$) at CD maxima and luminescence dissymmetry factor values ($g_{lum} \times 10^{-3}$) at emission maxima for NHC Au(I) azahelicene complexes in solution and solid state.

Complex	State	CD						CPL	
		nm	$g_{abs} \times 10^{-3}$	nm	$g_{abs} \times 10^{-3}$	nm	$g_{abs} \times 10^{-3}$	nm	$g_{lum} \times 10^{-3}$
2-(*S,S*)-DBCz	Solution	256	0.45	330	-0.14	388*	-0.04*	-	-
	Solid-state	257	-0.38	327	1.17	387	0.3	411	-0.32
2-(*R,R*)-DBCz	Solution	256	-0.47	330	0.18	385*	0.07*	-	-
	Solid-state	257	0.32	327	-1.3	387	-0.6	411	0.36
2-(*S,S*)-DBCz	Solution	275	-0.56	316	-0.12	385*	-0.07*	-	-
	Solid-state	275	-3.34	326	2.85	393	4.46	414	3.3
3-(*R,R*)-DBCz	Solution	275	0.58	317	0.09	385*	0.03*	-	-
	Solid-state	275	3.07	326	-3.22	393	-4.45	414	-2.8
3-(*S,S*)-BCz	Solution	267	-0.38	326	-0.26	388*	-0.10*	-	-
	Solid-state	275	0.22	295	2.45	388	1.73	418	1.8
3-(*R,R*)-BCz	Solution	267	0.42	326	0.26	388*	0.18*	-	-
	Solid-state	275	-0.35	296	-2.04	388	-1.99	418	-1.9
*– not CD maximum, g_{abs} value is given for comparison reason									

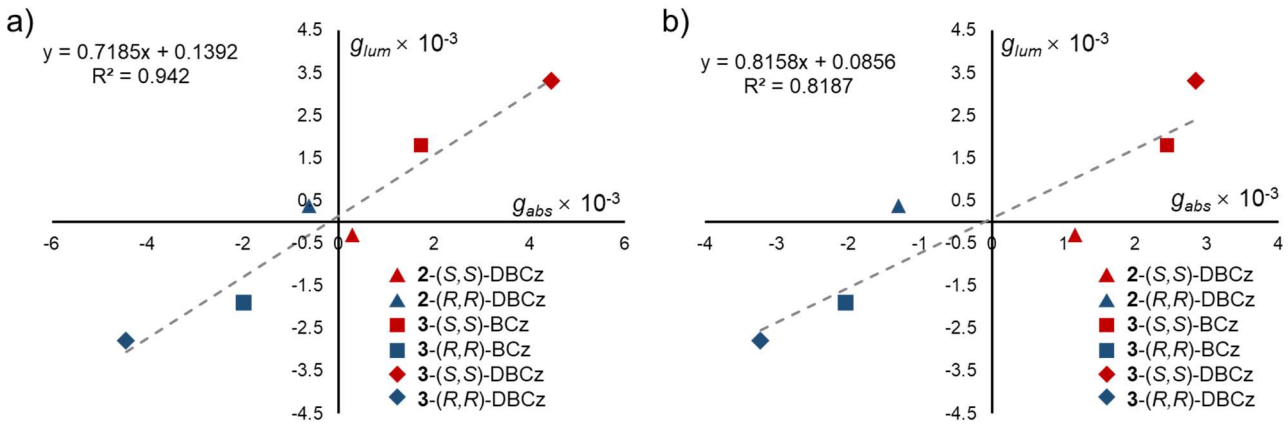

Figure S2.30. Relationship between the g_{abs} and g_{lum} values for the obtained NHC Au(I) azahelicene complexes in the crystalline state: g_{abs} maximum located (a) in the 385–395 nm range corresponding to the $S_0 \rightarrow S_1$ transition and (b) in the 300–330 nm range used for the excitation. This data was taken from **Table S2.10**.

4.5 References

1. Shen, Y.; Chen, C.-F., Helicenes: Synthesis and Applications. *Chem. Rev.* **2012**, *112*, 1463–1535.
2. Bedi, A.; Gidron, O., The Consequences of Twisting Nanocarbons: Lessons from Tethered Twisted Acenes. *Acc. Chem. Res.* **2019**, *52*, 2482–2490.
3. Rickhaus, M.; Mayor, M.; Juríček, M., Strain-induced helical chirality in polyaromatic systems. *Chem. Soc. Rev.* **2016**, *45*, 1542–1556.
4. Majewski, M. A.; Stępień, M., Bowls, Hoops, and Saddles: Synthetic Approaches to Curved Aromatic Molecules. *Angew. Chem., Int. Ed.* **2019**, *58*, 86–116.
5. Mori, T., Chiroptical Properties of Symmetric Double, Triple, and Multiple Helicenes. *Chem. Rev.* **2021**, *121* (4), 2373–2412.
6. Albano, G.; Pescitelli, G.; Di Bari, L., Chiroptical Properties in Thin Films of π-Conjugated Systems. *Chem. Rev.* **2020**, *120*, 10145–10243.
7. Sakamoto, D.; Gay Sánchez, I.; Rybáček, J.; Vacek, J.; Bednárová, L.; Pazderková, M.; Pohl, R.; Císařová, I.; Stará, I. G.; Starý, I., Cycloiridated Helicenes as Chiral Catalysts in the Asymmetric Transfer Hydrogenation of Imines. *ACS Catal.* **2022**, *12*, 10793–10800.
8. Yavari, K.; Aillard, P.; Zhang, Y.; Nuter, F.; Retailleau, P.; Voituriez, A.; Marinetti, A., Helicenes with Embedded Phosphole Units in Enantioselective Gold Catalysis. *Angew. Chem., Int. Ed.* **2014**, *53*, 861–865.
9. Demmer, C. S.; Voituriez, A.; Marinetti, A., Catalytic uses of helicenes displaying phosphorus functions. C. R. *Chim.* **2017**, *20*, 860–879.
10. Peurifoy, S. R.; Sisto, T. J.; Ng, F.; Steigerwald, M. L.; Chen, R.; Nuckolls, C., Dimensional Control in Contorted Aromatic Materials. *Chem. Rec.* **2019**, *19*, 1050–1061.
11. Isla, H.; Crassous, J., Helicene-based chiroptical switches. *C. R. Chim*. **2016**, *19*, 39–49.
12. Ravat, P.; Šolomek, T.; Juríček, M., Helicenes as Chiroptical Photoswitches. *ChemPhotoChem* **2019**, *3*, 180–186.
13. Rushworth, J. L.; Thawani, A. R.; Fajardo-Ruiz, E.; Meiring, J. C. M.; Heise, C.; White, A. J. P.; Akhmanova, A.; Brandt, J. R.; Thorn-Seshold, O.; Fuchter, M. J., [5]-Helistatins: Tubulin-Binding Helicenes with Antimitotic Activity. *JACS Au* **2022**, *2*, 2561–2570.
14. Summers, P. A.; Thomas, A. P.; Kench, T.; Vannier, J.-B.; Kuimova, M. K.; Vilar, R., Cationic helicenes as selective G4 DNA binders and optical probes for cellular imaging. *Chem. Sci.* **2021**, *12*, 14624–14634.
15. Janke, R. H.; Haufe, G.; Würthwein, E.-U.; Borkent, J. H., Racemization Barriers of Helicenes: A Computational Study1. *J. Am. Chem. Soc.* **1996**, *118*, 6031–6035.
16. Elm, J.; Lykkebo, J.; Sørensen, T. J.; Laursen, B. W.; Mikkelsen, K. V., Racemization Mechanisms and Electronic Circular Dichroism of [4]Heterohelicenium Dyes: A Theoretical Study. *J. Phys. Chem. A* **2011**, *115*, 12025–12033.
17. Watanabe, M.; Suzuki, H.; Tanaka, Y.; Ishida, T.; Oshikawa, T.; Tori-i, A., One-Pot Synthesis of Helical Aromatics: Stereoselectivity, Stability against Racemization, and Assignment of Absolute Configuration Assisted by Experimental and Theoretical Circular Dichroism. *J. Org. Chem.* **2004,** *69*, 7794–7801.

18. Chen, C.-T.; Tsai, C.-C.; Tsou, P.-K.; Huang, G.-T.; Yu, C.-H., Enantiodivergent Steglich rearrangement of O-carboxylazlactones catalyzed by a chirality switchable helicene containing a 4-aminopyridine unit. *Chem. Sci.* **2017**, *8*, 524–529.
19. Weiss, C.; Sharapa, D. I.; Hirsch, A., Coronenohelicenes with Dynamic Chirality. *Chem. – Eur. J.* **2020**, *26*, 14100–14108.
20. Mahlmeister, B.; Mahl, M.; Reichelt, H.; Shoyama, K.; Stolte, M.; Würthner, F., Helically Twisted Nanoribbons Based on Emissive Near-Infrared Responsive Quaterrylene Bisimides. *J. Am. Chem. Soc.* **2022**, *144*, 10507–10514.
21. Gingras, M., One hundred years of helicene chemistry. Part 1: non-stereoselective syntheses of carbohelicenes. *Chem. Soc. Rev.* **2013**, *42*, 968–1006.
22. Gingras, M.; Félix, G.; Peresutti, R., One hundred years of helicene chemistry. Part 2: stereoselective syntheses and chiral separations of carbohelicenes. *Chem. Soc. Rev.* **2013**, *42*, 1007–1050.
23. Dubey, R. K.; Melle-Franco, M.; Mateo-Alonso, A., Inducing Single-Handed Helicity in a Twisted Molecular Nanoribbon. *J. Am. Chem. Soc*. **2022**, *144*, 2765–2774.
24. Bao, S. T.; Jiang, H.; Schaack, C.; Louie, S.; Steigerwald, M. L.; Nuckolls, C.; Jin, Z., Remote Control of Dynamic Twistacene Chirality. *J. Am. Chem. Soc.* **2022**, *144*, 18772–18777.
25. Bao, S. T.; Louie, S.; Jiang, H.; Jiang, Q.; Sun, S.; Steigerwald, M. L.; Nuckolls, C.; Jin, Z., Near-Infrared, Organic Chiroptic Switch with High Dissymmetry Factors. *J. Am. Chem. Soc.* **2024**, *146*, 51–56.
26. Ouyang, G.; Rühe, J.; Zhang, Y.; Lin, M.-J.; Liu, M.; Würthner, F., Intramolecular Energy and Solvent-Dependent Chirality Transfer within a BINOL-Perylene Hetero-Cyclophane. *Angew. Chem., Int. Ed.* **2022**, *61*, e202206706.
27. Sapotta, M.; Spenst, P.; Saha-Möller, C. R.; Würthner, F., Guest-mediated chirality transfer in the host–guest complexes of an atropisomeric perylene bisimide cyclophane host. *Org. Chem. Front*. **2019**, *6*, 892–899.
28. Weh, M.; Kroeger, A. A.; Shoyama, K.; Grüne, M.; Karton, A.; Würthner, F., π-π Catalysis Made Asymmetric—Enantiomerization Catalysis Mediated by the Chiral π-System of a Perylene Bisimide Cyclophane. *Angew. Chem., Int. Ed*. **2023**, *62*, e202301301.
29. Weh, M.; Rühe, J.; Herbert, B.; Krause, A.-M.; Würthner, F., Deracemization of Carbohelicenes by a Chiral Perylene Bisimide Cyclophane Template Catalyst. *Angew. Chem., Int. Ed*. **2021**, *60*, 15323–15327.
30. Liu, J.; Su, H.; Meng, L.; Zhao, Y.; Deng, C.; Ng, J. C. Y.; Lu, P.; Faisal, M.; Lam, J. W. Y.; Huang, X.; Wu, H.; Wong, K. S.; Tang, B. Z., What makes efficient circularly polarised luminescence in the condensed phase: aggregation-induced circular dichroism and light emission. *Chem. Sci.* **2012**, *3*, 2737–2747.
31. Crassous, J.; Fuchter, M. J.; Freedman, D. E.; Kotov, N. A.; Moon, J.; Beard, M. C.; Feldmann, S., Materials for chiral light control. *Nat. Rev. Mat.* **2023**, *8*, 365–371.
32. He, J.; Fan, Y.; Lian, Z.; Guo, S.; Wang, Y.; Jiang, H., [2.2]Paracyclophane-Based Double Helices: Tunable Circularly Polarized Luminescence Driven by Self-Assembly. *Adv. Opt. Mat*. **2023**, 2302221.

33. Kumar, J.; Nakashima, T.; Tsumatori, H.; Kawai, T., Circularly Polarized Luminescence in Chiral Aggregates: Dependence of Morphology on Luminescence Dissymmetry. *J. Phys. Chem. Lett.* **2014**, *5 (2)*, 316–321.
34. Adamo, C.; Barone, V., Toward reliable density functional methods without adjustable parameters: The PBE0 model. *J. Chem. Phys.* **1999**, *110*, 6158–6170.
35. Grimme, S.; Antony, J.; Ehrlich, S.; Krieg, H., A consistent and accurate ab initio parametrization of density functional dispersion correction (DFT-D) for the 94 elements H-Pu. *J. Chem. Phys.* **2010**, *132*, 154104.
36. Grimme, S.; Ehrlich, S.; Goerigk, L., Effect of the damping function in dispersion corrected density functional theory. *J. Comput. Chem*. **2011**, *32*, 1456–1465.
37. Figgen, D.; Rauhut, G.; Dolg, M.; Stoll, H., Energy-consistent pseudopotentials for group 11 and 12 atoms: adjustment to multi-configuration Dirac–Hartree–Fock data. *Chem. Phys.* **2005**, *311*, 227–244.
38. Weigend, F.; Ahlrichs, R., Balanced basis sets of split valence, triple zeta valence and quadruple zeta valence quality for H to Rn: Design and assessment of accuracy. *Phys. Chem. Chem. Phys.* **2005**, *7*, 3297–3305.
39. Weigend, F., Accurate Coulomb-fitting basis sets for H to Rn. *Phys. Chem. Chem. Phys.* **2006**, *8*, 1057–1065.
40. Marenich, A. V.; Cramer, C. J.; Truhlar, D. G., Universal Solvation Model Based on Solute Electron Density and on a Continuum Model of the Solvent Defined by the Bulk Dielectric Constant and Atomic Surface Tensions. *J. Phys. Chem. B* **2009**, *113*, 6378–6396.
41. Heeb, J.-P.; Clayden, J.; Smith, M. D.; Armstrong, R. J., Interrogating the configurational stability of atropisomers. *Nat. Prot.* **2023**, *18*, 2745–2771.
42. Pammer, F.; Sun, Y.; May, C.; Wolmershäuser, G.; Kelm, H.; Krüger, H.-J.; Thiel, W. R., Dibenzo[c,g]fluorene: The Combination of Cyclopentadiene and 1,1′-Binaphthyl in One Ligand. *Angew. Chem., Int. Ed*. **2007**, *46*, 1270–1273.
43. Barroso, J.; Cabellos, J. L.; Pan, S.; Murillo, F.; Zarate, X.; Fernandez-Herrera, M. A.; Merino, G., Revisiting the racemization mechanism of helicenes. *Chem. Commun.* **2018**, *54*, 188–191.
44. Caronna, T.; Mele, A.; Famulari, A.; Mendola, D.; Fontana, F.; Juza, M.; Kamuf, M.; Zawatzky, K.; Trapp, O., A Combined Experimental and Theoretical Study on the Stereodynamics of Monoaza[5]helicenes: Solvent-Induced Increase of the Enantiomerization Barrier in 1-Aza-[5]helicene. *Chem. – Eur. J.* **2015**, *21*, 13919–13924.
45. Liu, Z.; Lu, T.; Chen, Q., An sp-hybridized all-carboatomic ring, cyclo[18]carbon: Electronic structure, electronic spectrum, and optical nonlinearity. *Carbon* **2020**, *165*, 461–467.
46. Goto, K.; Yamaguchi, R.; Hiroto, S.; Ueno, H.; Kawai, T.; Shinokubo, H., Intermolecular Oxidative Annulation of 2-Aminoanthracenes to Diazaacenes and Aza[7]helicenes. *Angew. Chem., Int. Ed.* **2012**, *51*, 10333–10336.
47. Pallova, L.; Abella, L.; Jean, M.; Vanthuyne, N.; Barthes, C.; Vendier, L.; Autschbach, J.; Crassous, J.; Bastin, S.; César, V., Helical Chiral N-Heterocyclic Carbene Ligands in Enantioselective Gold Catalysis. *Chem. – Eur. J.* **2022**, *28*, e202200166.

48. Yang, J.-G.; Li, K.; Wang, J.; Sun, S.; Chi, W.; Wang, C.; Chang, X.; Zou, C.; To, W.-P.; Li, M.-D.; Liu, X.; Lu, W.; Zhang, H.-X.; Che, C.-M.; Chen, Y., Controlling Metallophilic Interactions in Chiral Gold(I) Double Salts towards Excitation Wavelength-Tunable Circularly Polarized Luminescence. *Angew. Chem., Int. Ed.* **2020**, *59*, 6915–6922.
49. Liu, Y.-J.; Liu, Y.; Zang, S.-Q., Solvation-Mediated Self-Assembly from Crystals to Helices of Protic Acyclic Carbene AuI-Enantiomers with Chirality Amplification. *Angew. Chem., Int. Ed.* **2023**, *62*, e202311572.
50. Yu, F.-H.; Jin, R.; Chang, X.; Li, K.; Cui, G.; Chen, Y., Long-Persistent Circularly Polarized Luminescence from a Host-Guest System Regulated by the Multiple Roles of a Gold(I)-Carbene Motif. *Angew. Chem., Int. Ed.* **2023**, *62*, e202312927.
51. Cei, M.; Di Bari, L.; Zinna, F., Circularly polarized luminescence of helicenes: A data-informed insight. *Chirality* **2023**, *35*, 192–210.
52. Qiu, Z.; Ju, C.-W.; Frédéric, L.; Hu, Y.; Schollmeyer, D.; Pieters, G.; Müllen, K.; Narita, A., Amplification of Dissymmetry Factors in π-Extended [7]- and [9]Helicenes. *J. Am. Chem. Soc.* **2021**, *143*, 4661–4667.
53. Tian, X.; Shoyama, K.; Mahlmeister, B.; Brust, F.; Stolte, M.; Würthner, F., Naphthalimide-Annulated [n]Helicenes: Red Circularly Polarized Light Emitters. *J. Am. Chem. Soc*. **2023**, *145*, 9886–9894.
54. Hsueh, F.-C.; Tsai, C.-Y.; Lai, C.-C.; Liu, Y.-H.; Peng, S.-M.; Chiu, S.-H. Interlocking increases the persistence of N-heterocyclic carbenes in solution. *Chem. Commun.* **2020**, *56*, 4773–4776.
55. Zong, L.; Ban, X.; Kee, C. W.; Tan, C.-H. Catalytic enantioselective alkylation of sulfenate anions to chiral heterocyclic sulfoxides using halogenated pentanidium salts. *Angew. Chem. Int. Ed.* **2014**, *53*, 11849–11853.
56. Collado, A.; Gómez-Suárez, A.; Martin, A. R.; Slawin, A. M. Z.; Nolan, S. P. Straightforward Synthesis of [Au (NHC) X](NHC= N-Heterocyclic Carbene, X= Cl, Br, I) Complexes. *Chem. Commun.* **2013**, *49*, 5541–5543.
57. Tzouras, N.; Martynova, E.; Ma, X.; Scattolin, T.; Hupp, B.; Busen, H.; Saab, M.; Zhang, Z.; Falivene, L.; Pisanò, G.; Van Hecke, K.; Cavallo, L.; Cazin, C.; Steffen, A.; Nolan, S. Simple Synthetic Routes to Carbene-M-Amido (M= Cu, Ag, Au) Complexes for Luminescence and Photocatalysis Applications. *Chem.-Eur. J.* **2021**, *27*, 11904–11911.
58. Frisch, M. J.; Trucks, G. W.; Schlegel, H. B.; Scuseria, G. E.; Robb, M. A.; Cheeseman, J. R.; Scalmani, G.; Barone, V.; Petersson, G. A.; Nakatsuji, H.; Li, X.; Caricato, M.; Marenich, A.V.; Bloino, J.; Janesko, B.G.; Gomperts, R.; Mennucci, B.; Hratchian, H.P.; Ortiz, J.V.; Izmaylov, A.F.; Sonnenberg, J.L.; Williams-Young, D.; Ding, F.; Lipparini, F.; Egidi, F.; Goings, J.; Peng, B.; Petrone, A.; Henderson, T.; Ranasinghe, D.; Zakrzewski, V.G.; Gao, J.; Rega, N.; Zheng, G.; Liang, W.; Hada, M.; Ehara, M.; Toyota, K.; Fukuda, R.; Hasegawa, J.; Ishida, M.; Nakajima, T.; Honda, Y.; Kitao, O.; Nakai, H.; Vreven, T.; Throssell, K.; Montgomery, Jr., J.A.; Peralta, J.E.; Ogliaro, F.; Bearpark, M.J.; Heyd, J.J.; Brothers, E.N.; Kudin, K.N.; Staroverov, V.N.; Keith, T.A.; Kobayashi, R.; Normand, J.; Raghavachari, K.; Rendell, A.P.; Burant, J.C.; Iyengar, S.S.; Tomasi, J.; Cossi, M.; Millam, J.M.; Klene, M.; Adamo, C.; Cammi, R.; Ochterski, J.W.; Martin, R.L.; Morokuma, K.; Farkas, O.; Foresman, J.B.; Fox, D.J. *Gaussian 16, Revision A.03*; Gaussian, Inc.: Wallingford, CT, 2016.

59. Adamo, C.; Barone, V. Toward reliable density functional methods without adjustable parameters: The PBE0 model. *J. Chem. Phys.* **1999**, *110*, 6158–6170.
60. Grimme, S.; Antony, J.; Ehrlich, S.; Krieg, H. A consistent and accurate ab initio parametrization of density functional dispersion correction (DFT-D) for the 94 elements H-Pu. *J. Chem. Phys.* **2010**, *132,* 154104.
61. Grimme, S.; Ehrlich, S.; Goerigk, L. Effect of the damping function in dispersion corrected density functional theory. *J. Comput. Chem.* **2011**, *32*, 1456–1465.
62. Figgen, D.; Rauhut, G.; Dolg, M.; Stoll, H. Energy-consistent pseudopotentials for group 11 and 12 atoms: adjustment to multi-configuration Dirac–Hartree–Fock data. *Chem. Phys.* **2005**, *311*, 227–244.
63. Weigend, F.; Ahlrichs, R. Balanced basis sets of split valence, triple zeta valence and quadruple zeta valence quality for H to Rn: Design and assessment of accuracy. *Phys. Chem. Chem. Phys.* **2005**, *7*, 3297–3305.
64. Weigend, F. Accurate Coulomb-fitting basis sets for H to Rn. *Phys. Chem. Chem. Phys.* **2006**, *8*, 1057–1065.
65. Marenich, A. V.; Cramer, C. J.; Truhlar, D. G. Universal Solvation Model Based on Solute Electron Density and on a Continuum Model of the Solvent Defined by the Bulk Dielectric Constant and Atomic Surface Tensions. *J. Phys. Chem. B* **2009**, *113*, 6378–6396.
66. Bader, R. F. W. A quantum theory of molecular structure and its applications. *Chem. Rev.* **1991**, *91*, 893–928.
67. Lu, T.; Chen, Q. Independent gradient model based on Hirshfeld partition: A new method for visual study of interactions in chemical systems. *J. Comput. Chem.* **2022**, *43*, 539–555.
68. Liu, Z.; Lu, T.; Chen, Q. An sp-hybridized all-carboatomic ring, cyclo [18] carbon: Electronic structure, electronic spectrum, and optical nonlinearity. *Carbon* **2020**, *165*, 461–467.
69. Lu, T.; Chen, F. Multiwfn: A multifunctional wavefunction analyzer. *J. Comput. Chem.* **2012**, *33*, 580–592.
70. Humphrey, W.; Dalke, A.; Schulten, K. VMD: visual molecular dynamics. *J. Mol. Graphics* **1996**, *14*, 33–38.
71. Dolomanov, O.V.; Bourhis, L.J.; Gildea, R.J.; Howard, J.A.K; Puschmann, H. OLEX2: a complete structure solution, refinement and analysis program. *J. Appl. Crystallogr*. **2009**, *42*, 339–341.
72. Sheldrick, G. M. Crystal structure refinement with SHELXL. *Acta Crystallogr., Sect. A.* **2015**, *71*, 3–8.
73. Bourhis, L. J.; Dolomanov, O. V.; Gildea, R. J.; Howard J. A. K.; Puschmann, H. The anatomy of a comprehensive constrained, restrained refinement program for the modern computing environment–Olex2 dissected. *Acta Crystallogr., Sect. A*. **2015**, *71*, 59–75.
74. Macrae, C. F.; Sovago, I.; Cottrell, S. J.; Galek, P. T. A.; McCabe, P.; Pidcock, E.; Platings, M.; Shields, G. P.; Stevens, J. S.; Towler, M.; Wood, P. A. Mercury 4.0: From visualization to analysis, design and prediction. *J. Appl. Crystallogr.* **2020**, *53*, 226–235.
75. Castiglioni, E.; Biscarini, P.; Abbate, S. Experimental aspects of solid state circular dichroism. *Chirality* **2009**, *21* (1E), E28–E36.

76. Takaishi, K.; Yamamoto, T.; Hinoide, S.; Ema, T. Helical oligonaphthodioxepins showing intense circularly polarized luminescence (CPL) in solution and in the solid state. *Chem. - Eur. J.* **2017**, *23*, 9249–9252.

3. Crystallization-Induced Chirality Transfer in Conformationally Flexible Azahelicene Au(I) Complexes with Polarized Luminescence Activation

3.1 Introduction

The molecular rotational dynamics observed in amphidynamic crystals represent a promising tool for developing functional stimuli-responsive materials and molecular machines in the solid state.[1-6] These materials feature intricately designed structural units, such as gyroscope-like,[3,4,6-8] and dumbbell-shaped molecular scaffolds,[3,4,9,10] or porous frameworks.[11-13] These specific structural motifs play a crucial role in creating free local space that facilitates the rotational dynamics of distinct molecular fragments in the crystalline media. This, in turn, provides a platform for investigating the effects of molecular dynamics on physical properties at both the micro and macro levels in the solid state.[1-6]

Recently, Ito group introduced a novel platform for crystalline molecular rotors through the encapsulation of a central arylene-based rotator by bulky *N*-heterocyclic carbene (NHC) Au(I) or Cu(I) complexes as stators.[14-16] The concave-shaped NHC ligands should provide steric shielding for the rotator, creating local space near the rotator allowing its molecular rotation. In one of the reported examples based on this strategy, the crystalline cationic NHC Au(I) and Cu(I) complexes, possessing pyrazine as the central rotator, include the SbF_6^- counter-anions which are located along the sides of the pyrazine rotator in the crystal structure (**Figure. 3.1a**). [14] In another case, it was found that this local space near the pyrazine rotator could also be occupied by small organic molecules (such as tetrahydrofuran used in crystallization), which displayed correlated molecular dynamics with the pyrazine rotator.[15] Based on these

results, I anticipated that eliminating counter-anions from the crystal structure could affect the available local space near the rotator, altering its solid-state dynamics

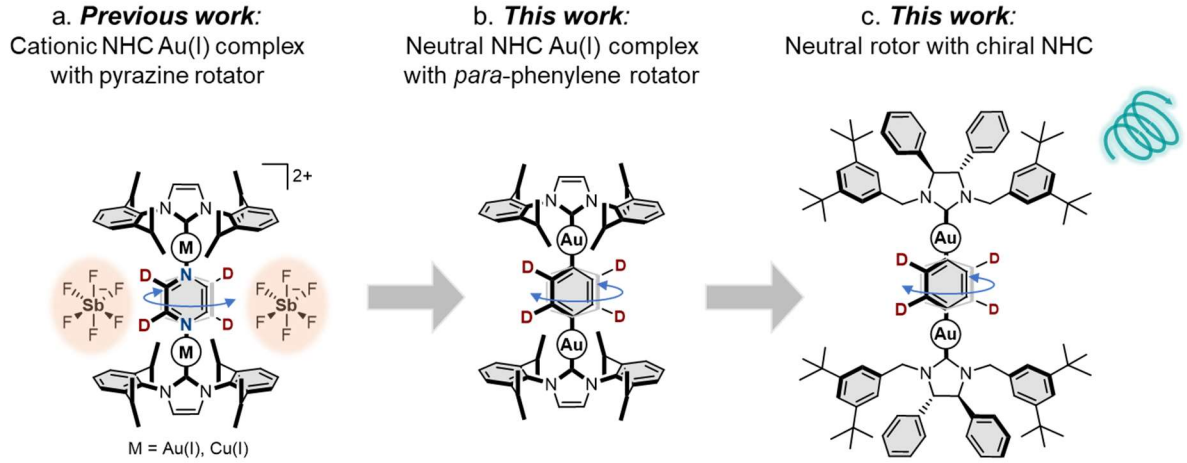

Figure3.1 Cationic (a) and neutral (b) binuclear NHC Au(I) complexes with pyrazine and *para*-phenylene rotator; c) chiral rotor to investigate the rotation and CPL properties.

To investigate this concept, I prepared a crystalline molecular rotor using a neutral binuclear 1,3-bis(2,6-diisopropylphenyl)imidazol-2-ylidene (IPr) Au(I) complex **4** with a *para*-phenylene rotator, which does not require the presence of counter-anions to balance the charge as in previously reported cationic analogs (Figure. 3.1b). Single-crystal X-ray diffraction (SCXRD) and Hirshfeld surface analysis revealed the presence of enough free local space around the *para*-phenylene moiety to allow its rotational dynamics. Variable-temperature solid-state ^{2}H NMR spin-echo indicated that the central *para*-phenylene rotator is undergoing a 180° 2-fold rotation, and its rotational dynamics were different compared to the previous pyrazine rotator, which is associated with a different crystal packing environment. Moreover, by utilizing this neutral rotor platform, I could introduce chirality by chiral NHC ligands and investigate the relationship between CPL and molecular rotation **(**Figure. 3.1c**)**.

3.2 Result and discussion

3.2.1 synthesis of neutral rotor

The target binuclear NHC Au(I) complex **4** and chiral binuclear NHC Au(I) complex **5** were obtained in a 90% and 92% yield through the reaction between corresponding NHC Au(I) chloride complexes (NHCAuCl, prepared according to literature procedure)[17] and 1,4-benzenediboronic acid bis(pinacol) ester-d_4, in the presence of potassium hydroxide as a base, in a toluene solution at 100 °C (Figure 3.2). The 1,4-benzenediboronic acid bis(pinacol) ester-d_4 was synthesized in two steps according to literature procedures.[18,19]

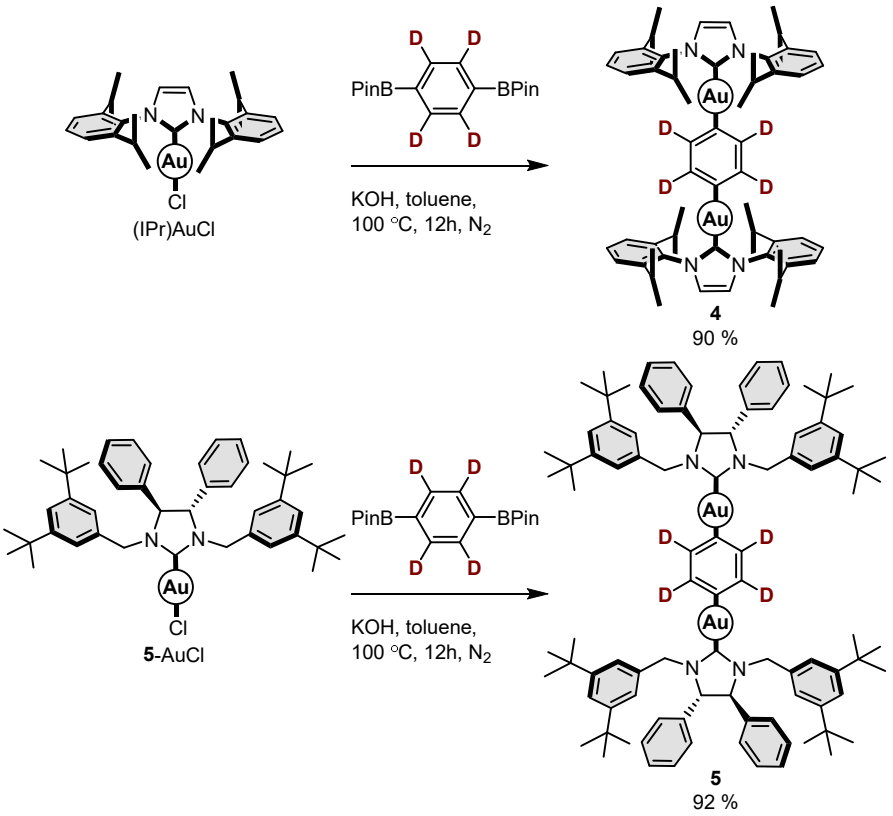

Figure 3.2 Synthesis of neutral rotor.

3.2.2 Single-crystal X-ray structures analysis

Neutral rotor **4** was crystallized via solvent diffusion of ethyl acetate layered over a dichloromethane solution of **4**. SCXRD analysis of rotor **4** was conducted at 293 K,[20;] the crystal structure view of **4** is shown in Figure 3.3, while the crystal data parameters are given in Table S1 in the Supporting Information. Complex **4** co-crystallizes with two molecules of ethyl acetate, which are located at the top side of the NHC ligands but do not enter in the cavity near the para-phenylene rotator (Figure 3.3a). The crystal structure belongs to the $P2_1/c$ space group, and the asymmetric unit contains half a molecule of **4** and one disordered molecule of ethyl acetate. The lengths of the Au–C bonds with the NHC ligand and the *para*-phenylene moiety in neutral complex **4** were both 2.038(3) Å at 293 K, which is slightly longer than the Au–C (1.941(17) Å) and Au–N (2.031(14) Å) bonds in the reported cationic NHC Au(I) rotor at 295 K.[14] This suggests less intramolecular steric hindrance for rotational motion in **4**. The twist angle between the NHC plane and the rotator planes in neutral complex **4** was found to be 49.74(12)°, in comparison to 21.1(10)° in the cationic Au(I) rotor at 295 K.[14]

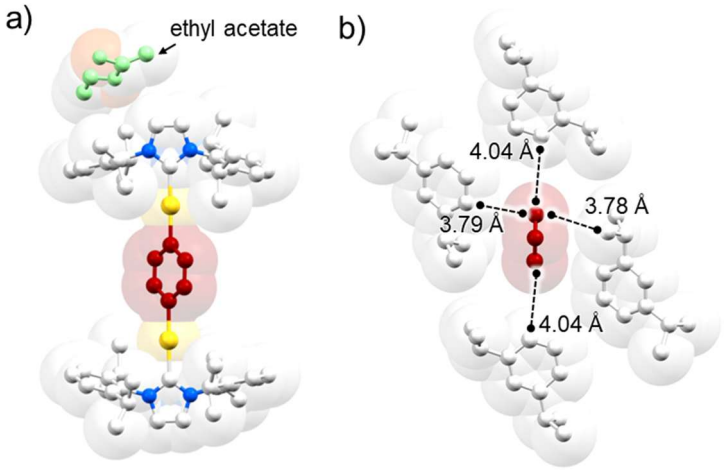

Figure 3.3 (a) Single crystal structure of rotor **4** at 293 K; (b) Short C−C contacts between the *para*-phenylene moiety and the nearby NHC ligands.

In contrast to the previous cationic NHC Au(I) rotor,[14] where SbF_6^- counter-anions were located along the pyrazine rotator (Figure 3.3b), in the neutral rotor **4**, the central *para*-phenylene rotator is surrounded by the NHC ligands of neighboring complex molecules (Figure 3.3b). The intermolecular C-C distances between the *para*-phenylene group and the NHC ligands varied from 3.78 Å to 4.04 Å, which are larger than the corresponding sum of the van der Waals radii (ΣvdWr) of the carbon atoms (3.4 Å).[21] Notably, in neutral rotor **4**, these short contacts are longer than the intermolecular contacts observed between the pyrazine rotator and SbF_6^- anions in the previous cationic rotor (Figure S3.2).

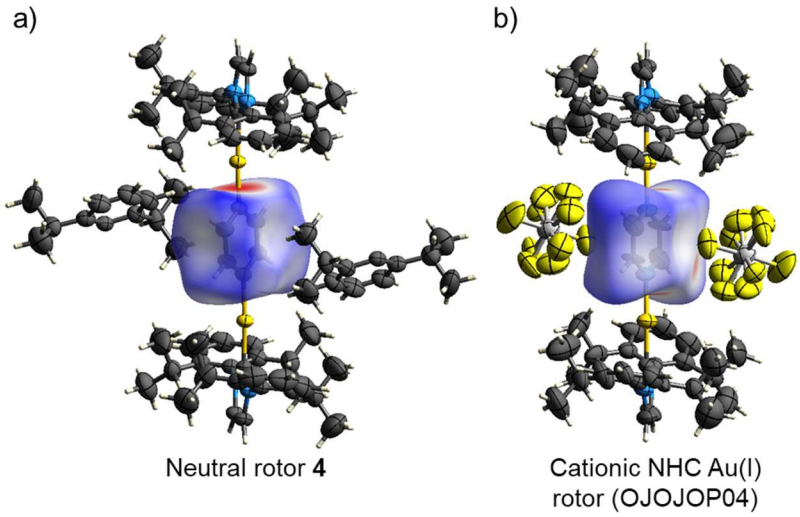

Figure 3.4 Hirshfeld surfaces for rotator moieties in the crystal structures of neutral rotor **4** (a) and the reported cationic NHC Au(I) rotor (CSD code: OJOJOP04) (b). Red areas on the HS indicate contacts shorter than the ΣvdWr, white areas denote intermolecular distances close to ΣvdWr, and blue areas indicate contacts longer than ΣvdWr.

The Hirshfeld surface (HS) analysis[22] depicted in Figure 3.4, was conducted to quantify and visualize the short contacts within the crystal structure of both neutral and cationic NHC Au(I) rotors. The HS of the *para*-phenylene rotator in **4** is mostly contributed by H–H (59.4 %) and C–H (25.8 %) interactions, while for the pyrazine rotator in the cationic NHC Au(I) rotor, besides H–H (39.5 %) and C–H (6.8 %), there is a contribution of H–F (14.9 %) and C–F (11.6 %) contacts. Additionally, the *para*-

phenylene rotator shows a slightly smaller contact area, which can be estimated by the HS area (S_{HS} = 120.76 Å^2) and a larger local volume (defined by the HS volume – V_{HS} = 102.49 Å^3) than the previously reported pyrazine rotor (S_{HS} = 120.76 Å^2, V_{HS} = 100.36 Å^3). These data are also in agreement with the observed packing coefficients of the two structures: 0.63 for the cationic NHC Au(I) rotor and 0.62 for **4**. These results suggest that even with different crystal packing, the structure of **4** should possess enough free local space to allow rotational motion of the *para*-phenylene moiety, as observed in the previously reported cationic NHC Au(I) rotors.

On the other hand, SCXRD analysis of chiral rotor **5** was also conducted at 293 K. The crystal structure view of **5** is shown in Figure 3.5a, belongs to the C2 chiral space group. The crystal data parameters are given in Table S1 in the Supporting Information, With a larger chiral NHC ligand exhibits a larger local space, with intermolecular C-C distances between the para-phenylene group and the NHC ligands varied from 3.81 Å to 4.26 Å (Figure 3.5b), which are larger than the corresponding sum of the van der Waals radii (ΣvdWr) of the carbon atoms (3.4 Å).[21]

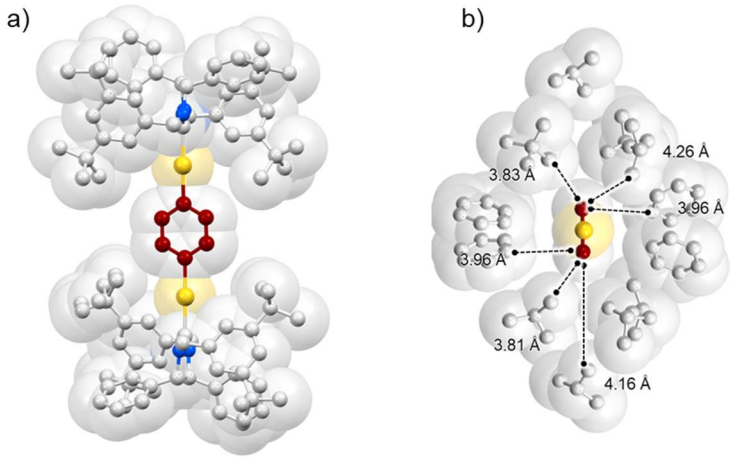

Figure 3.5 (a) Single crystal structure of chiral rotor **5** at 293 K; (b) Short C⋯C contacts between the *para*-phenylene moiety and the nearby NHC ligands.

3.2.2 Molecular dynamic studies by solid-state ^{2}H NMR spin-echo NMR

Variable temperature (VT) solid-state (SS) ^{2}H NMR spin-echo measurements were conducted on the crystalline sample of complex **4** to explore the solid-state dynamics of the *para*-phenylene rotator. This method is the classic approach to analyze the internal dynamics in the solid-state of deuterium-enriched moieties in the 10^3–10^8 Hz frequency range.[23] The composition of the sample before analysis was confirmed by PXRD (Figure S3.3). The experimentally obtained spectra (solid black lines), measured in the temperature range between 333 K and 273 K, are shown in Figure 3.6. Simulated line shapes[24] (dashed red lines) were generated using a quadrupolar coupling constant (QCC) of 176 kHz, a cone angle of 60° formed between the rotational axis and the C–D bond vector of the phenylene, a 10% static contribution, and a log-Gaussian distribution of the rotational jumping rates with a width σ = 2, featuring Brownian jumps of 180° (Figure 3.6a and Figure 3.6b).[6]

The simulated line shapes closely matched the experimental spectra, suggesting that complex **4** undergoes a 180° 2-fold flipping motion, indicating the rotation of the *para*-phenylene rotator in the crystalline media. The rotational frequencies (k_{rot}) were fitted as 850 kHz at 333 K, 550 kHz at 313 K, 350 kHz at 298 K, and 180 kHz at 273 K. The obtained k_{rot} values show a good correlation with temperature on the Arrhenius plot (Figure 3.6c), indicating an activation energy (E_a) of 4.7 kcal/mol and a pre-exponential factor (A) of 1.05×10^9 s^{-1}, which is typical for phenylene-type rotators.[6] The neutral rotor **4** exhibits a slower rotational frequency than the corresponding cationic Au(I) rotor (0.85 MHz at 333 K vs. 12.5 MHz at 325 K),[14] despite the *para*-phenylene rotator having slightly larger free local space and less dense crystal packing than the pyrazine one. I presume that the presence of SbF_6^- anions reduce the local volume but does not lead to the inhibition of rotation in comparison to the structure of **4**, due to the dynamic behavior of the SbF_6^- anion in the crystalline state. This is also manifested in the disorder of SbF_6^- in the crystal

structure.[14] A similar behavior was observed for the tetrahydrofuran molecule in the solvated crystal of the cationic NHC Au(I) rotor, which also displays relatively fast site exchange and does not hinder the rotation of the pyrazine moiety.[15] Conversely, the *para*-phenylene rotator in neutral rotor **4** is surrounded by immovable and static NHC ligands of neighboring molecules, which cannot adjust their position during the *para*-phenylene rotation. This results in a lower rotational frequency.

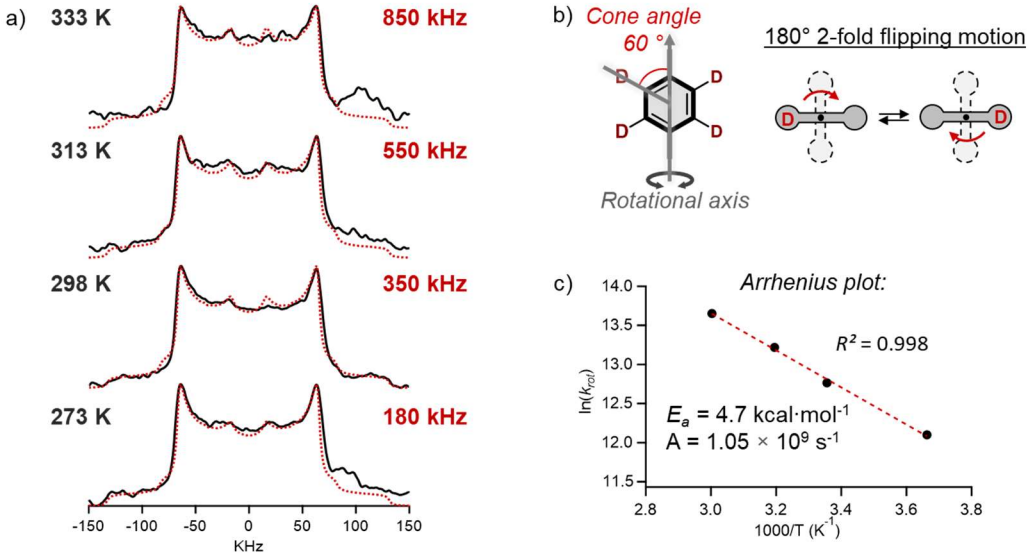

Figure 3.6 VT SS ^{2}H NMR spin–echo studies of rotor **4**. (a) Experimental (black) and simulated (red) spectra of rotor **4**; (b) Illustration of the 180° of 2-fold site-exchange rotation model for the central *para*-phenylene rotator; (c) Arrhenius plot with evaluated energy barrier (*E*a) and pre-exponential factor (A) of the rotation of the rotator.

VT solid-state (SS) ^{2}H NMR spin-echo measurements were performed on the crystalline sample of complex **5** to investigate the solid-state dynamics of the para-phenylene rotator. The experimentally obtained spectra (solid black lines), measured in the temperature range of 293 K to 183 K, are shown in Figure 3.7. From the line shape of the pattern, the *para*-phenylene rotator exhibits fast 2-fold rotation with a rotation frequency from a fast limit to 110 kHz. The obtained k_{rot} values show a good correlation with temperature on the Arrhenius plot (Figure 3.7c), indicating an

activation energy (E_a) of 5.9 kcal/mol and a pre-exponential factor (A) of 1.09×10^{11} s^{-1}, which is typical for phenylene-type rotators.[6]

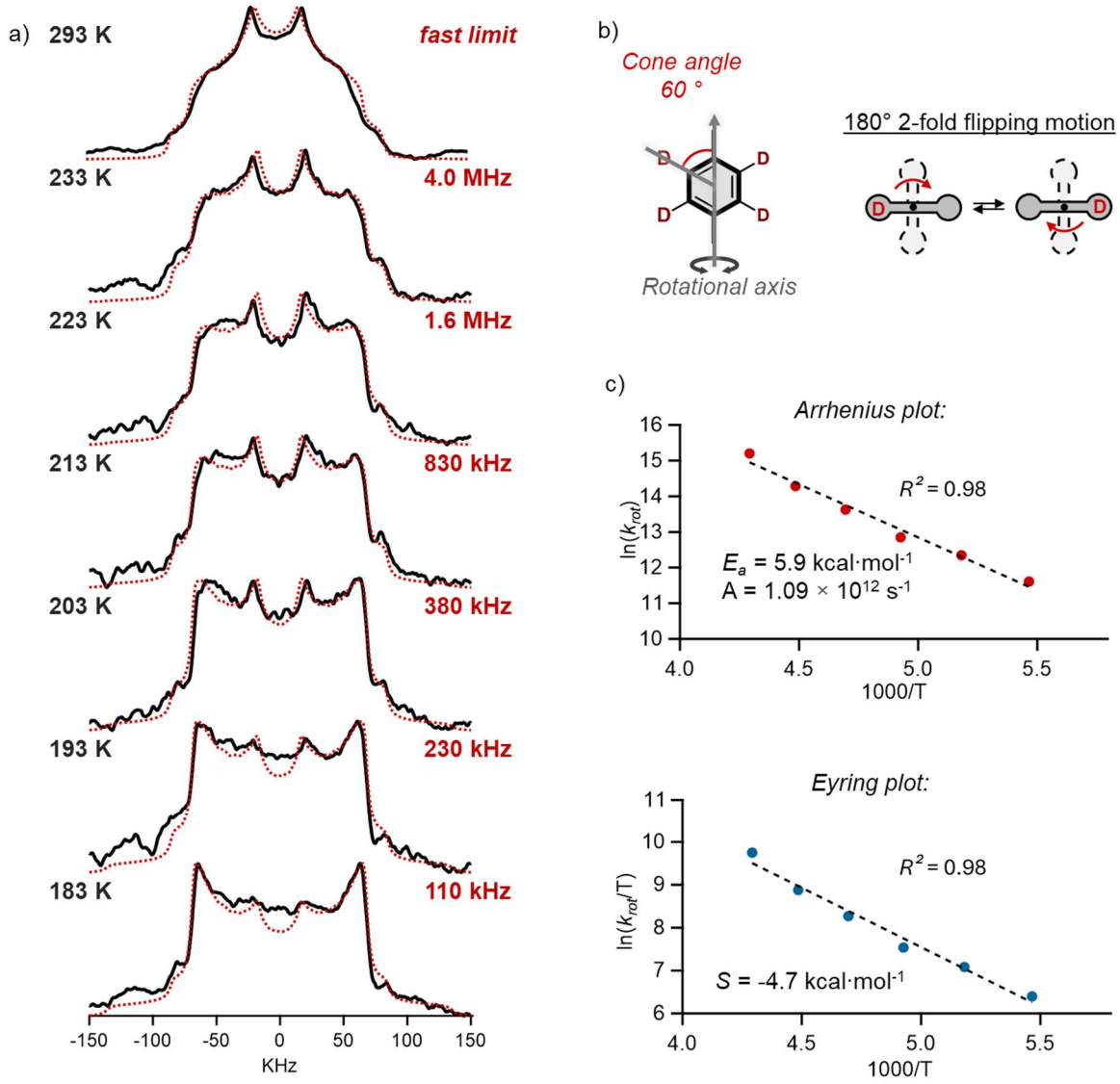

Figure 3.7 VT SS ^{2}H NMR spin–echo studies of rotor **5**. (a) Experimental (black) and simulated (red) spectra of rotor **5**; (b) Illustration of the 180° of 2-fold site-exchange rotation model for the central *para*-phenylene rotator; (c) Arrhenius and Eyring plot of the rotation.

3.2.3 Thermo-responsive CPL properties

The chiral rotor **5** displays clear mirrored CPL signals with a maximum at 415 nm under excitation at 305 nm. Similar to the general emission intensity of **5**, the CPL intensity (ΔI) also shows a strong dependence on temperature, increasing almost five-fold upon cooling from 253K to 193K (Figure 3.8a, 3.8b). While both the emission and CPL show a linear dependence on temperature, the complex **5** did not change by molecular rotation during the temperature change (Figure 3.8c). This is also indicated by no change in the CPL luminescence dissymmetry factor (g_{lum}) as the temperature rises (Figure 3.8d).

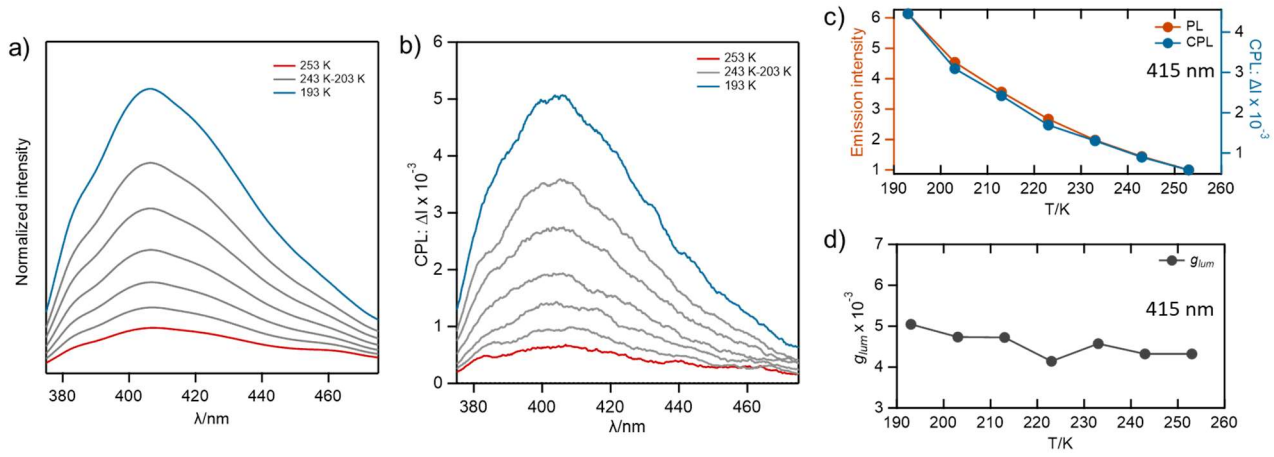

Figure 3.8 a) VT emission spectra of crystalline **5** in 193–253 K range; b) VT CPL spectra of crystalline **5** in 193–253 K range; c) Plots of CPL luminescence dissymmetry factor (g_{lum}) against temperature for crystalline **5** in 193–253 K.

3.3 Conclusion

In summary, this chapter describes a new crystalline neutral molecular rotor, designated as rotors **4** and **5**, constructed with a concave binuclear NHC stator that encapsulates the para-phenylene rotator along a C-Au-C rotational axis. The neutral crystalline rotor **4** exhibits slightly larger free local space and less dense crystal packing around the rotator moiety compared to the previously reported cationic NHC

Au(I) complex with a pyrazine rotator. However, due to the non-dynamic nature of the crystal packing environment, it generally displays slower rotational dynamics in the solid state. By using a bulkier chiral NHC ligand, **5** shows fast molecular rotation even at lower temperatures due to has a larger free local space for rotator. Also, **5** exhibits a clear CPL property in solid state. However, the fast molecular rotation of the central rotator did not change the symmetry, keeping the luminescence dissymmetry factor constant. This work adds new species to the family of crystalline encapsulated organometallic molecular rotors and highlights the importance of the crystal packing environment for solid-state molecular dynamics.

3.4 Experimental details and support information

3.4.1 general information

All commercially available reagents and solvents are reagent grade and were used without further purification unless otherwise noted. These reagents were purchased from TCI, Aldrich, Cica, and Wako. Solvents used for synthesis were further dried over with 4Å molecular sieves. Abbreviations for reagents are as follows: NHC (*N*-heterocyclic carbene), CH_2Cl_2 (dichloromethane), EtOAc (ethyl acetate), Hex (*n*-hexane).

NMR spectra were recorded on a JEOL JNM-ECZ400S (^{1}H: 400 MHz; ^{13}C: 100 MHz), using TMS or solvent residual signals as internal standards. NMR data are presented as follows: singlet (s), doublet (d), triplet (t), multiplet (m), coupling constant in Hertz (Hz) and integration. High resolution mass spectra (HRMS) were recorded at the Instrumental Analysis Division, Global Facility Center, Hokkaido University using a Thermo Scientific Exactive plus for ESI-HRMS. Detail of single-crystal (SCXRD), powder (PXRD) X-Ray diffraction experiments, and solid-state NMR (SSNMR) study are given below.

3.4.2 Synthesis

Synthesis of 1,4-benzenediboronic acid bis(pinacol) ester-d_4

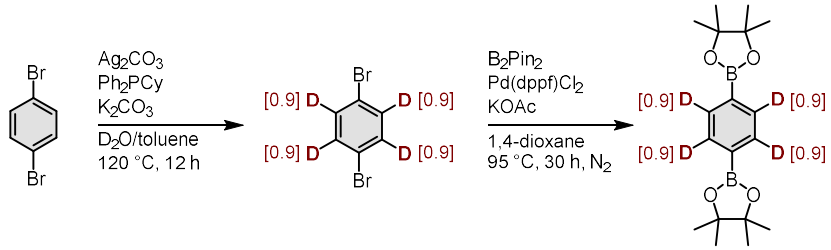

1,4-benzenediboronic acid bis(pinacol) ester-*d_4* was synthesized according to the literature procedure in two steps.

1,4-dibromobenzene-*d_4* [18]

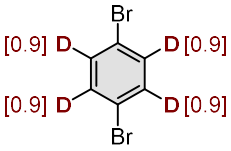

1,4-Dibromobenzene (1.0 equiv., 2.0 mmol), silver carbonate (0.2 equiv. 0.4 mmol), cyclohexyldiphenylphosphine (0.5 equiv., 1.0 mmol), potassium carbonate (1.0 equiv., 2.0 mmol), D_2O (20.0 equiv., 40.0 mmol), and toluene (0.2 mL) were added to an oven-dried reaction vessel (10 mL capacity). The reaction vessel was sealed with a septum and stirred in an oil bath at 120°C for 12 hours. Then, the reaction was quenched with saturated NH_4Cl solution. The product was extracted with CH_2Cl_2 (3.0 x 20 mL). The combined organic layer was washed with brine and dried over $MgSO_4$. The desired product was isolated by flash chromatography on silica gel (Hex). Yield: 73 %, 346 mg, white solid. ^{1}H NMR (400 MHz, $CDCl_3$, δ): 7. 36 (s, 4(D/H), deuterium ratio = 0.9, H-C_{Ar}). The deuterium ratio was confirmed by adding 1,2,3-trimethoxybenzene as the internal standard. The NMR spectra were confirmed with previous report.[18]

1,4-benzenediboronic acid bis(pinacol) ester-*d*$_4$[24]

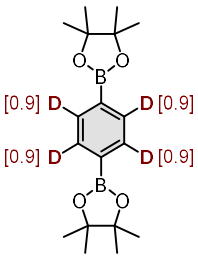

1,4-Dibromobenzene-*d*$_4$ (1.0 equiv. 1.0 mmol), bis(pinacolato)diboron (2.3 equiv., 2.3 mmol), [1,1'-Bis(diphenylphosphino)ferrocene] dichloropalladium (II) (0.05 equiv., 0.05 mmol), and potassium acetate (5.0 equiv., 5.0 mmol) were added to an oven-dried reaction vessel (10 mL capacity), the reaction vessel was sealed with a septum and connected to a vacuum/nitrogen manifold through a rubber tube. This process was repeated three times. 1,4-Dioxane (2.0 mL) was then added by a syringe under a nitrogen atmosphere. This mixture was stirred in an oil bath at 95°C for 30 hours. After cooling to room temperature, the reaction mixture was filtered through a pad of Celite and isolated by flash chromatography on silica gel (Hex/CH_2Cl_2= 2/1). Then, recrystallization from Hex was done to obtain a white solid and dried under vacuum. Yield: 72 %, 241mg, white solid. ^{1}H NMR (400 MHz, $CDCl_3$, δ): 1.35 (s, 24H, CH_3), 7.8 (s, 4(D/H), deuterium ratio = 0.9, H-C_{Ar}). the NMR spectra were confirmed with the previous report.[24]

*Synthesis of neutral rotor **4***

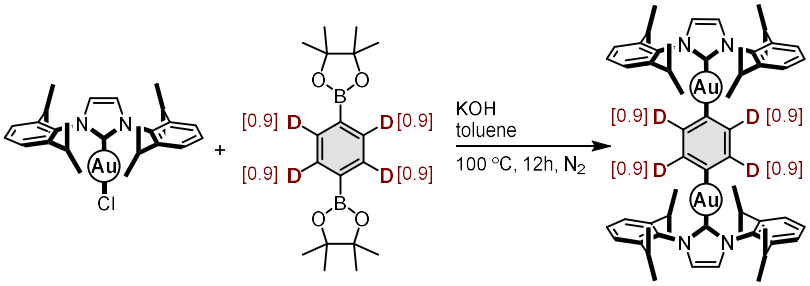

Neutral rotor **4** was synthesized according to the modified literature procedure.[25] IPrAuCl (1.0 equiv, 50 mg scale), 1,4-benzenediboronic acid bis(pinacol) ester-*d*$_4$ (0.6 equiv), and KOH (3.5 equiv.) were added to an oven-dried reaction vessel (10 mL capacity). The reaction vessel was sealed with a septum and connected to a vacuum/nitrogen manifold through a rubber tube. It was evacuated and then backfilled with nitrogen. This process was repeated three times. Toluene (1.5 mL) was

then added using a syringe under a nitrogen atmosphere. The mixture was stirred in an oil bath at 100°C for 12 hours. After cooling to room temperature, the reaction mixture was filtered through a pad of Celite to remove all insoluble precipitate. The solvents were evaporated under reduced pressure to yield the crude product (This Au(I) complex is not sable on silica gel, Al_2O_3, and JAIGEL-HR GPC preparative columns). Yield: 90 %, 45 mg, white solid. ^{1}H NMR (400 MHz, $CDCl_3$, δ): 1.18 (d, *J* = 6.8 Hz, 24H, CH_3), 1.31 (d, *J* = 6.8 Hz, 24H, CH_3), 2.59 (m, 8H, CH_2), 6.66 (s, 4(D/H), deuterium ratio = 0.9, H-$C_{rotator}$), 7.06 (s, 4H, H-imidazole), 7.19 (d, *J* = 7.8 Hz, 8H, H-C_{Ar}), 7.38 (t, *J* = 7.8 Hz, 4H, H-C_{Ar}). ^{13}C NMR (100 MHz, $CDCl_3$, δ): 24.00 (CH_3), 24.59 (CH_3), 28.83 (CH_2), 122.43 (C_{NHC}), 123.84 (C_{Ar}), 129.96 (C_{Ar}), 134.84 (C_{Ar}), 145.90 (C_{Ar}), 198.86 (C_{NHC}, C-Au). The *C*$_{ipso}$ and *C*$_{orto}$ signals of the deuterated *para*-phenylene rotator were not found due to low intensity. HRMS (ESI) m/z: $[M+H]^+$ calcd for $[C_{60}H_{73}D_4Au_2N_4]^+$: 1251.5725, Found: 1251.5691.

*Synthesis of neutral rotor**5***

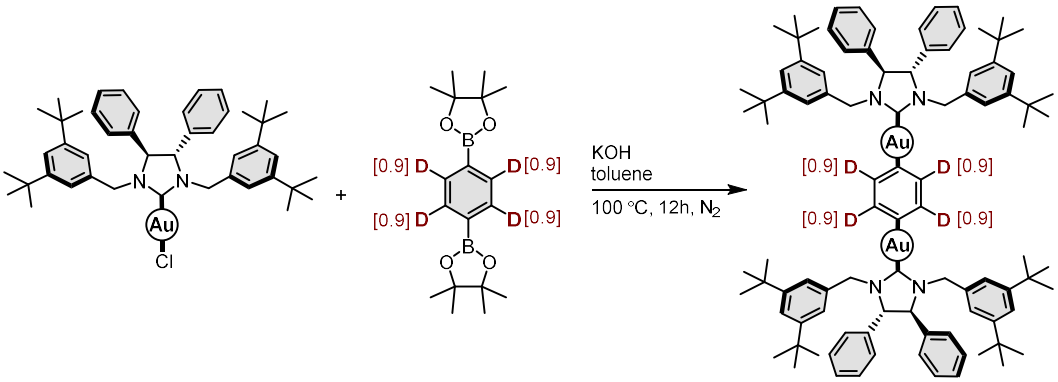

Neutral rotors were synthesized according to the modified literature procedure.[25] **3**-AuCl (1.0 equiv, 30 mg scale), 1,4-benzenediboronic acid bis(pinacol) ester-*d*$_4$ (0.6 equiv) and KOH (3.5 equiv.) were added to an oven-dried reaction vessel (10 mL capacity). The reaction vessel was sealed with a septum and connected to a vacuum/nitrogen manifold through a rubber tube. It was evacuated and then backfilled with nitrogen. This process was repeated three times. Toluene (1.0 mL) was then added using a syringe under a nitrogen atmosphere. The mixture was stirred in

an oil bath at 100°C for 12 hours. After cooling to room temperature, the reaction mixture was filtered through a pad of Celite to remove all insoluble precipitate. The solvents were evaporated under reduced pressure to yield the crude product. Yield: 92 %, 28 mg, white solid. ^{1}H NMR (400 MHz, $CDCl_3$, δ): 1.30 (m, 72H, CH_3), 2.36 (s, 8H, CH), 3.82 (d, *J* = 14.2 Hz, 4H, CH_2), 5.30 (s, 4H, H-NHC), 5.88 (d, *J* = 14.4 Hz, 4H, CH_2), 6.98 (d, 8H, *J* = 7.4 Hz), 7.14(m, 8H, H-C_{Ar}), 7.35(m, 16H, H-C_{Ar}).

Preparation of crystalline samples

4 was crystallized by dissolving the crude product (20 mg) in CH_2Cl_2 (1 mL) in a 10 mL flat-bottom vial and layering it with EtOAc (2 mL). The mixture was then left at room temperature under ambient conditions. Colorless needle-shaped crystals were obtained upon complete evaporation of the solvent after a few hours.

5 was crystallized by dissolving the crude product (20 mg) in CH_2Cl_2 (0.5 mL) in a 10 mL flat-bottom vial and layering it with 1,4-dioxane (2 mL). The mixture was then left at room temperature under ambient conditions. Colorless needle-shaped crystals were obtained upon complete evaporation of the solvent after a few days.

3.4.3 Single-crystal X-ray diffraction analysis

Single-crystal X-ray diffraction (SCXRD) analyses were carried out on a Rigaku XtaLAB Synergy diffractometer using graphite monochromated Cu-Kα radiation. The structures were solved with the SHELXT structure solution program using Intrinsic Phasing incorporated in the OLEX2 program package[26] and refined with the SHELXL package.[27] Hydrogen atoms were refined using the riding model.

The crystal data parameters are given in **Table S3.1**, while the crystal structure view of the complex is shown in **Figure S3.1**.

The Hirshfeld molecular surfaces were generated by the CrystalExplorer 21.5 program using the XRD structures of 1 and the cationic NHC Au(I) rotor (CSD code: OJOJOP04). The normalized contact distances, d_{norm},[21] based on the Bondi van der Waals radii,[20] were mapped onto the Hirshfeld surface of the phenylene and pyrazine rotators. In the color scale of **Figure 3.4**, negative values of d_{norm} are visualized in red, indicating contacts shorter than the sum of the van der Waals radii. White denotes intermolecular distances close to the van der Waals contacts, with d_{norm} equal to zero. In turn, contacts longer than the sum of the van der Waals radii, with positive d_{norm} values, are colored in blue.

Tables S1. Crystal data and structure refinement for Rotors**4**and **5**.

Identification code	Rotor_4_293K	Rotor_5_293K
CCDC No.	2353940	
Empirical formula	$C_{68}H_{92}Au_2N_4O_4$	C96H120Au2N4
Formula weight	1423.38	1723.89
Temperature/K	293	293(2)
Crystal system	monoclinic	monoclinic
Space group	P21/c	C2
a/Å	16.41210(10)	30.46318(13)
b/Å	13.18640(10)	15.75996(7)
c/Å	16.84340(10)	21.65294(7)
α/°	90	90
β/°	111.5720(10)	104.7975(4)
γ/°	90	90
Volume/Å^3	3389.87(4)	10050.77(7)
Z	2	4
ρ_{calc}g/cm^3	1.395	1.139
μ/mm^{-1}	8.371	5.699
F(000)	1436	3528
Crystal size/mm^3	0.3 × 0.1 × 0.01	0.2 × 0.1 × 0.01
Radiation	Cu Kα (λ = 1.54184)	Cu Kα (λ = 1.54184)
2Θ range for data collection/°	5.79 to 152.674	4.22 to 152.948
Index ranges	-20 ≤ h ≤ 20, -15 ≤ k ≤ 16, -20 ≤ l ≤ 20	-38 ⩽ h ⩽ 38, -19 ⩽ k ⩽ 19, -26 ⩽ l ⩽ 26
Reflections collected	32953	85823
Independent reflections	6891 [Rint = 0.0360, Rsigma = 0.0249]	19979 [Rint = 0.0270, Rsigma = 0.0239]
Data/restraints/parameters	6891/148/372	19979/2/974
Goodness-of-fit on F^2	1.066	1.049
Final R indexes [I>=2σ (I)]	R1 = 0.0252, wR2 = 0.0660	R1 = 0.0352, wR2 = 0.1040
Final R indexes [all data]	R1 = 0.0274, wR2 = 0.0673	R1 = 0.0369, wR2 = 0.1056
Largest diff. peak/hole / e Å^{-3}	0.84/-0.73	1.02/-0.42
Flack parameter		-0.027(3)

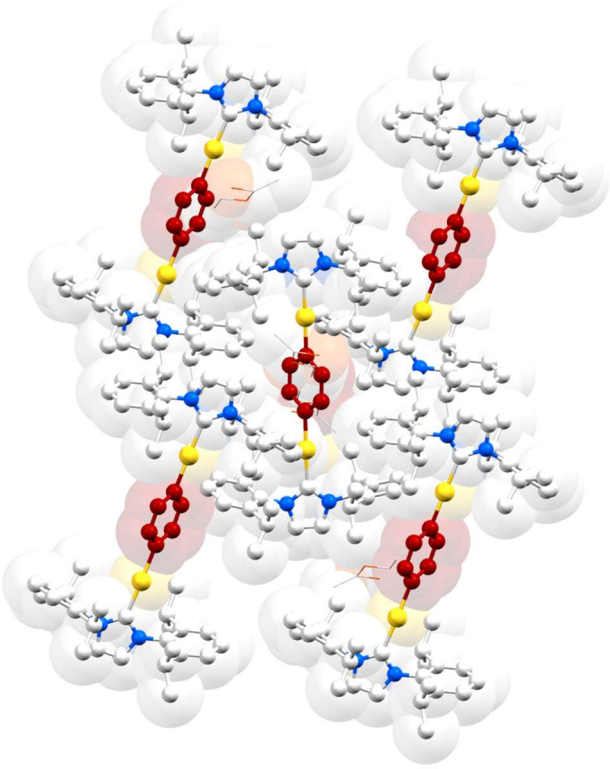

Figure S3.1 Crystal packing of rotor **4** at 293 K.

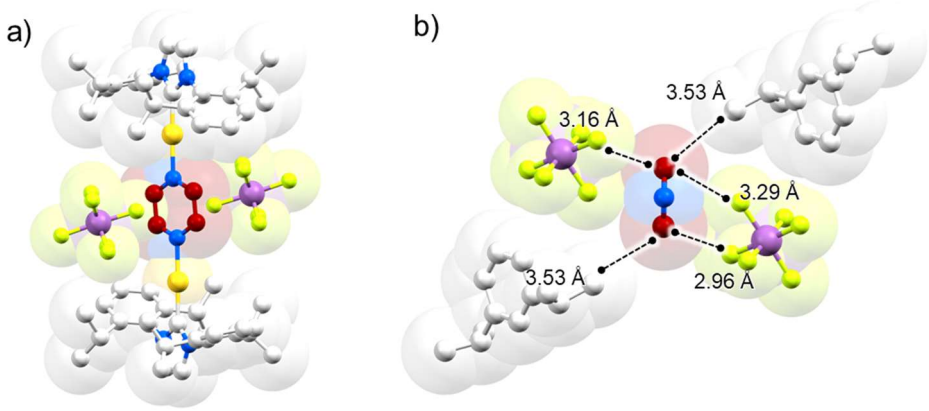

Figure S3.2. Single crystal structure of cationic NHC Au(I) rotor at 295 K (CSD code: OJOJOP04); (b) Short C-C contacts between the pyrazine groups and nearby NHC moieties or SbF_6^{-1} anion.

3.4.4 Powder-crystal X-ray diffraction analysis

Powder X-ray diffraction (PXRD) data of the ground crystalline samples were collected on a Rigaku SmartLab diffractometer with Cu-Kα radiation and D/teX Ultra detector covering a 5-50° (2θ) range at room temperature. Simulated powder patterns were generated with Mercury 2022.2.0[30] from the structures determined by the single-crystal X-ray diffraction analyses at 293 K. (**Figure S3.3**)

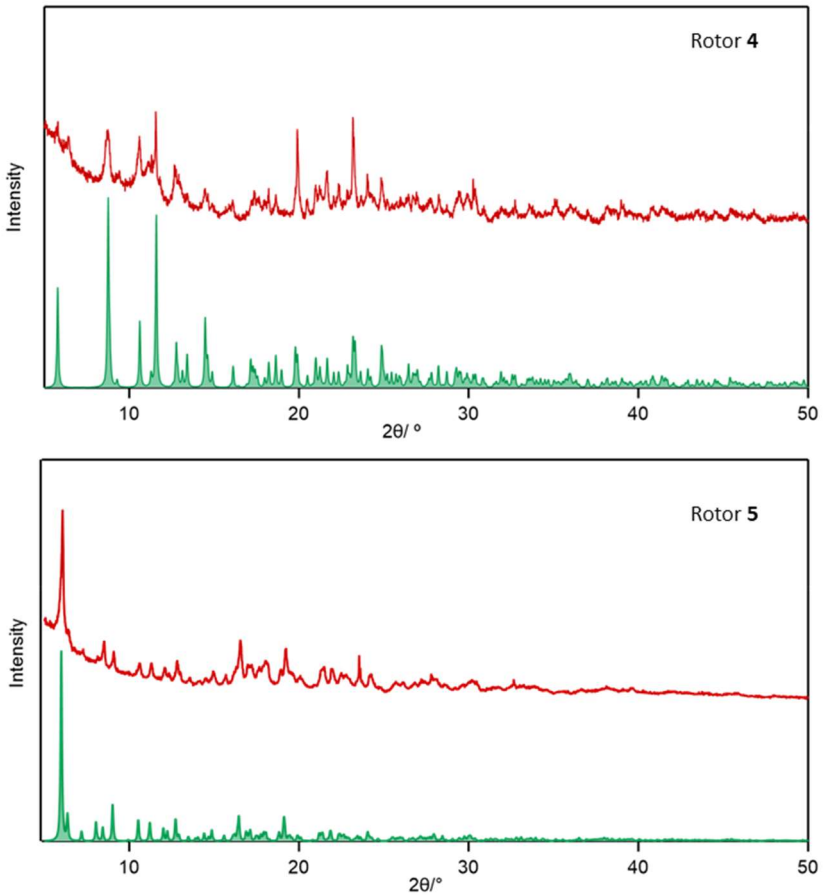

Figure S3.3 Experimental (red) and simulated (green) PXRD patterns of rotor **4** (upper) and **5** (lower) crystalline sample.

3.4.5 Solid-state NMR study

The solid-state ^{2}H NMR spin-echo experiments for rotor **4** were performed on a Bruker AVANCE NEO 500 MHz instrument at a ^{2}H frequency of 76.77 MHz (deuterium resonance frequency) and 90-degree pulse of 2.8 μs. A quadrupolar-echo sequence with phase recycling was used to suppress the undesired artifacts. An echo delay of 30 μs was used, and the recycle delay between pulses was 20 s. About 20 mg of crystal sample was placed in a ZrO_2 NMR sample tube for each experiment. 3500 scans were used to acquire each spectrum. All spectra in this work were obtained using a line broadening of 4.0 kHz in the data processing.

The solid-state ^{2}H NMR spin-echo experiments for rotor **5** were performed on a JEOL ECA300 instrument at 45.282 MHz (deuterium resonance frequency) with a 6.5 mm wide line probe and 90-degree pulse of 2.8 μs. A quadrupolar-echo sequence with phase recycling was used to suppress the undesired artifacts. An echo delay of 20 μs was used after the refocusing delay of 20 μs, and the recycle delay between pulses was 10s. An echo sequence (90-τ-90-τ-acquisition) was used with 20 μs and 2 ms of acquisition time. About 100 mg of the sample was placed in a short borosilicate glass NMR tube for each experiment. 512 scans or more were used to acquire each spectrum. All spectra in this work were obtained using a line broadening of 4.0 kHz in the data processing.

All simulation was performed utilizing the online program offered by H. W. Spiess [22]. The line shape simulation for rotor **4** was conducted with a delay time 30 μs and line broadening 4.0 kHz. A quadrupolar coupling constant (QCC) of 176 kHz, a cone angle of 60° formed between the rotational axis and C-D bond vector, a 10% static contribution, and a 2-fold 180° jumping log-Gaussian distribution with σ = 2 of the rotational jumping rates were used. The line shape simulation for rotor **5** was conducted with delay time 20 μs and line broadening 4.0 kHz. A quadrupolar coupling constant (QCC) of 181 kHz, a cone angle of 60° formed between the rotational axis

and C-D bond vector, and a 2-fold 180° jumping log-Gaussian distribution with $\sigma = 2.5$ of the rotational jumping rates were used.

3.5 References

1. Costil, R.; Holzheimer, M.; Crespi, S.; Simeth, N. A.; Feringa, B. L. Directing coupled motion with light: a key step toward machine-like function, *Chem. Rev.* **2021**, *121*, 13213–13237.
2. Ehnbom, A.; Gladysz, J. A. Gyroscopes and the Chemical Literature, 2002–2020: Approaches to a Nascent Family of Molecular Devices. *Chem. Rev.* **2021**, *121*, 3701–3750.
3. Howe, M. E.; Garcia-Garibay, M. A. The Roles of Intrinsic Barriers and Crystal Fluidity in Determining the Dynamics of Crystalline Molecular Rotors and Molecular Machines. *J. Org. Chem.* **2019**, *84*, 9835–9849.
4. Catalano, L.; Naumov, P. Exploiting rotational motion in molecular crystals. *CrystEngComm.* **2018**, *20*, 5872–5883.
5. Erbas-Cakmak, S.; Leigh, D. A.; McTernan, C. T.; Nussbaumer, A. L. Artificial molecular machines. *Chem. Rev.* **2015**, *115*, 10081–10206.
6. Vogelsberg, C. S.; Garcia-Garibay, M. A. Crystalline molecular machines: function, phase order, dimensionality, and composition. *Chem. Soc. Rev.* **2012**, *41*, 1892–1910.
7. Lang, G. M.; Shima, T.; Wang, L.; Cluff, K. J.; Skopek, K.; Hampel, F.; Blümel, J.; Gladysz, J. A. Gyroscope-like complexes based on dibridgehead diphosphine cages that are accessed by three-fold intramolecular ring-closing metatheses and encase Fe(CO)3, Fe(CO)2 (NO)+, and Fe(CO)3(H)+ rotators. *J. Am. Chem. Soc.* **2016**, *138*, 7649–7663.
8. Setaka, W.; Yamaguchi, K. Order-Disorder transition of dipolar rotor in a crystalline molecular gyrotop and its optical change. *J. Am. Chem. Soc.* **2013**, *135*, 14560–14563.
9. Jin, M.; Chung, T. S.; Seki, T.; Ito, H.; Garcia-Garibay, M. A. Phosphorescence Control Mediated by Molecular Rotation and Aurophilic Interactions in Amphidynamic Crystals of 1,4-Bis[tri-(p-fluorophenyl)phosphane-gold(I)-ethynyl]benzene. *J. Am. Chem. Soc.* **2017**, *139*, 18115–18121.
10. Jin, M.; Yamamoto, S.; Seki, T.; Ito, H.; Garcia-Garibay, M. A. Anisotropic Thermal Expansion as the Source of Macroscopic and Molecular Scale Motion in Phosphorescent Amphidynamic Crystals. *Angew. Chem. Int. Ed.* **2019**, *58*, 18003–18010.
11. Bracco, S.; Comotti, A.; Sozzani, P. Molecular rotors built in porous materials. *Acc. Chem. Res*. **2016**, *49*, 1701–1710.
12. Gonzalez-Nelson, A.; Coudert, F. X.; van der Veen, M. A. Rotational dynamics of linkers in metal-organic frameworks. *Nanomaterials* **2019**, *9*, 330.
13. Perego, J.; Bracco, S.; Negroni, M.; Bezuidenhout, C. X.; Prando, G.; Carretta, P.; Comotti, A.; Sozzani, P. Fast motion of molecular rotors in metal-organic framework struts at very low temperatures. *Nat. Chem.* **2020**, *12*, 845–851.
14. Jin, M.; Ando, R.; Jellen, M. J.; Garcia-Garibay, M. A.; Ito, H. Encapsulating N-heterocyclic carbene binuclear transition-metal complexes as a new platform for molecular rotation in crystalline solid-state. *J. Am. Chem. Soc.* **2021**, *143*, 1144–1153.
15. Jin, M.; Matsuura, S.; Yamamoto, H.; Mizuno, M.; Ito, H. Multidynamic Crystalline Molecular Rotors Comprising an N-Heterocyclic Carbene Binuclear Au(I) Complex Bearing Multiple Rotators. *Eur. J. Org. Chem.* **2023**, e202201468.

16. Ando, R.; Sato-Tomita, A.; Ito, H.; Jin, M. Giant Crystalline Molecular Rotors that Operate in the Solid State. *Angew. Chem. Int. Ed.* **2023**, *62*, e202309694.
17. Mikherdov, A. S.; Jin, M.; Ito, H. Exploring Au(I) involving halogen bonding with N-heterocyclic carbene Au(I) aryl complexes in crystalline media. *Chem. Sci*. **2023**,*14*, 4485–4494.
18. Hu, G. Q.; Bai, J. W.; Li, E. C.; Liu, K. H.; Sheng, F. F.; Zhang, H. H. Synthesis of Multideuterated (Hetero)aryl Bromides by Ag(I)-Catalysed H/D Exchange. *Org. Lett.* **2021**, *23*, 1554–1560.
19. Ishiyama, T.; Itoh, Y.; Kitano, T.; Miyaura, N. Synthesis of arylboronates via the palladium(0)-catalyzed cross-coupling reaction of tetra(alkoxo)diborons with aryl triflates. *Tetrahedron Lett.* **1997**, *38*, 3447 –3450.
20. Bondi, A. van der Waals Volumes and Radii. *J. Phys. Chem.* **1964**, 68, *3*, 441–451.
21. McKinnon, J. J.; Jayatilaka, D.; Spackman, M. A. Towards quantitative analysis of intermolecular interactions with Hirshfeld surfaces. *Chem. Commun*. **2007**, 3814–3816.
22. Hoatson, G.L.; Vold, R.L. *^{2}H-NMR Spectroscopy of Solids and Liquid Crystals. In: Blümich, B. (eds) Solid-State NMR III Organic Matter. NMR,* Springer, Berlin, Heidelberg, **1994**, Vol 32.
23. Macho, V.; Brombacher, L.; Spiess, H. W. The NMR-WEBLAB: An internet approach to NMR lineshape analysis. *Appl. Magn. Reson.* **2001**, *20*, 405–432. For the online program, visit: http://weblab.mpip-mainz.mpg.de/weblab
24. Hughes, A. R.; Brownbill, N. J.; Lalek, R. C.; Briggs, M. E.; Slater, A. G.; Cooper, A. I.; Blanc, F. Towards quantitative analysis of intermolecular interactions with Hirshfeld surfaces. *Chem. - Eur. J.* **2017**, *23*, 17217–17221.
25. Dupuy, S.; Crawford, L.; Bühl, M.; Slawin, A. M. Z.; Nolan, S. P. The Role of Metal Hydroxide Complexes in Late Transition Metal‐Mediated Transmetalation Reaction: The Case of Gold. *Adv. Synth. Catal.* **2012**, *354*, 2380–2386.
26. Dolomanov, O.V.; Bourhis, L.J.; Gildea, R.J.; Howard, J.A.K; Puschmann, H. OLEX2: a complete structure solution, refinement and analysis program. *J. Appl. Crystallogr*. **2009**, *42*, 339–341.
27. Sheldrick, G. M. Crystal structure refinement with SHELXL. *Acta Crystallogr., Sect. A.* **2015**, *71*, 3–8.
28. Macrae, C. F.; Sovago, I.; Cottrell, S. J.; Galek, P. T. A.; McCabe, P.; Pidcock, E.; Platings, M.; Shields, G. P.; Stevens, J. S.; Towler, M.; Wood, P. A. Mercury 4.0: From visualization to analysis, design and prediction. *J. Appl. Crystallogr.* **2020**, *53*, 226–235.

4. Symmetry Change Induced Circularly Polarized Luminescence Modulation through Molecular Rotation in Crystalline Chiral *N*-Heterocyclic Carbene Au(I) Complexes

4.1 Introduction

Amphidynamic crystals are solid-state materials known for their ability to allow molecular rotational motion within a well-organized crystal framework.[1-6] The presence of rotational dynamics in the free local space of crystalline media is a defining feature that sets amphidynamic crystals apart from more densely packed general "static" crystals (Figure 4.1a). The presence of rotational dynamics can impact both the crystal structure, including molecular orientation and symmetry, as well as bulk crystal properties such as thermal expansion,[7,8] phase transitions,[9] electromagnetic,[10,11] and photophysical properties.[12,13] These properties have allowed to post amphidynamic crystals as a promising direction in the fields of solid-state molecular machine and stimuli-responsive functional materials.[1-6,14]

The precise control of luminescent properties in solid-state materials has attracted much attention because of the potential for the development of functional materials such as sensors and external field-responsive devices.[15-19] Recently, several amphidynamic crystals with emission properties were demonstrated for controlling solid-state phosphorescence[13,20-23] and sensing the inclusion of organic vapors or solvents in solid-state porous materials.[24,25] The emission properties in the amphidynamic crystals were found to be strongly affected by internal rotational motion.[19] The presence of rotational motion in the crystals can cause reorientation and variation in the conjugation of the luminophore moieties, facilitating access to the conical intersection between excited and ground states, causing emission

quenching and excited state decay through a nonradiative relaxation pathway (Figure 4.1b).[26] Conversely, the restriction or inhibition of molecular rotation should enhance the photophysical performance, making this phenomenon akin to aggregation-induced emission (AIE).[27] While the presence of thermally-activated molecular motion is usually an unwanted feature for solid-state luminescent materials, in the case of amphidynamic crystals, their rational design allows for the fine-tuning and precise control of rotational motion. This results in emerging thermo-responsive luminescent properties, allowing control over luminescence intensity,[13,20-25] lifetime,[13] and color[20,23,25] through the rate and mode of thermally-activated rotational motion. On the other hand, I have encountered the question of whether the connection between molecular rotation and photophysical properties in crystalline media can be translated to solid-state chiroptical property, such as CPL.

The CPL is defined by the difference in intensity between left- and right-circularly polarized emission and the capability for it can evaluated by the luminescence dissymmetry factor. The control of ΔI_{CPL} and g_{lum} is one of key target in the development of functional CPL materials because of the potential in highly sensitive emission sensors response to the external stimuli.[28] There are many examples of modulation of the CPL (both ΔI_{CPL} and g_{lum}) achieved by utilizing dynamic fluid media, such as solution or polymer environment, while there are still limited examples in the well-organized and static crystalline phase.[29,30] The g_{lum} of molecules showing CPL is generally affected by the asymmetric geometry and orientation of the molecular structure. It is known that molecular rotation may lead to the alteration of symmetry in crystalline materials, which is high important for the chiroptical properties. Usually, the acceleration of molecular rotation in crystal with temperature elevation leads to the increase of the symmetry of the system which can be manifested in a dynamic disorder of molecular fragments or even crystal symmetry change and phase transition (Figure 4.1c).[31-36] Moreover, previously, Lui et al. reported the possibility of CPL quenching by molecular motion in the solid state on a similar basis to the

reported non-polarized emission in amphidynamic crystals.[37] Nevertheless, to the best of my knowledge, the current state of the solid-state CPL research lacks a connection between the features of rotational motion, effecting the crystal structure and symmetry, and chiroptical properties in the crystalline state.

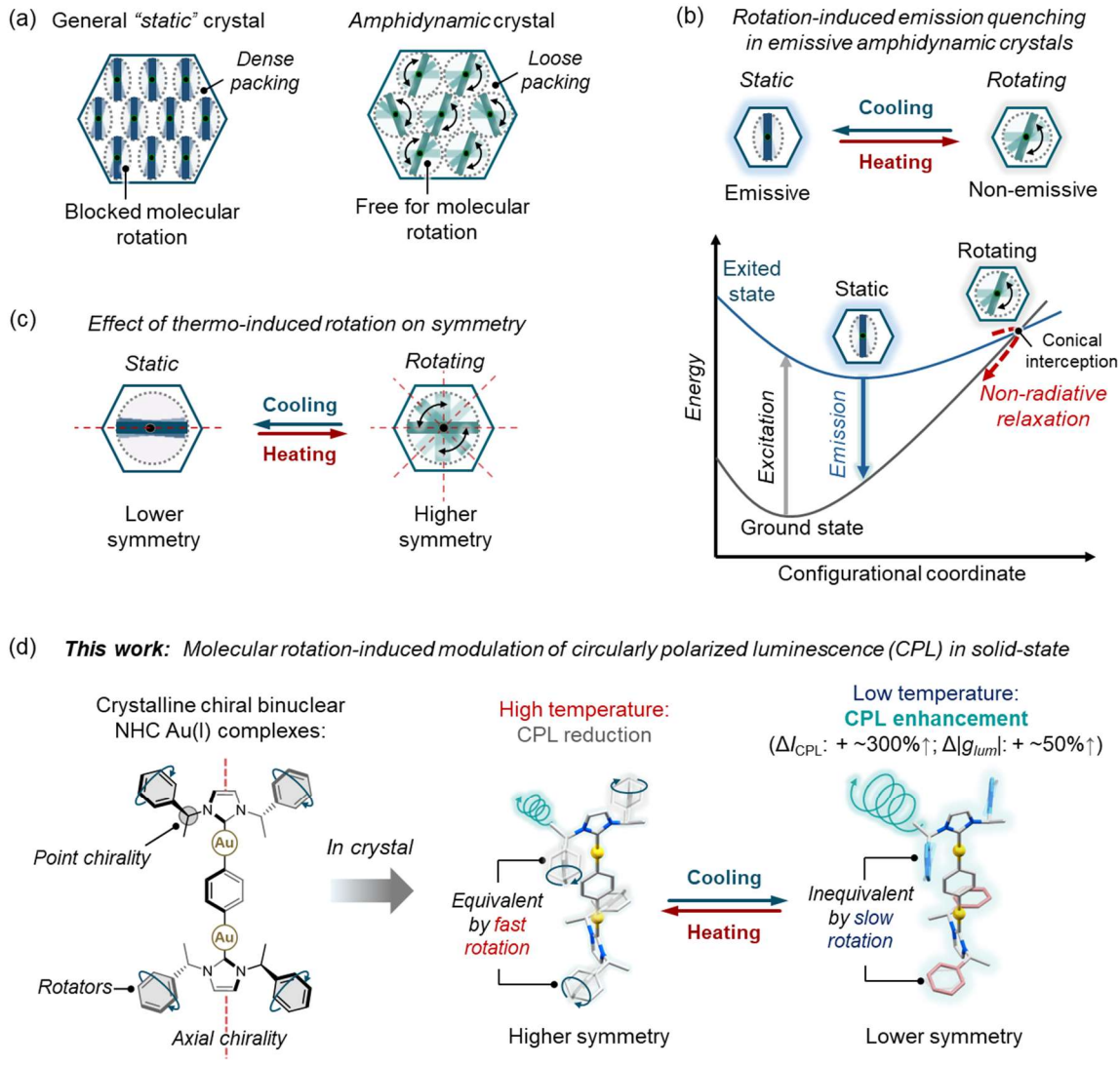

Figure 4.1. Illustration of amphidynamic crystal (a) and densely packed general "static" crystal (b); (c) Effect of a molecular rotation on the radiative processes in crystalline solid state; (d) Molecular rotation effect on crystal structure symmetry; (e) Molecular rotation modulation circularly polarized luminescence (CPL) of the binuclear chiral NHC Au(I) complexes through the symmetry alteration in the crystalline state.

Based on these premises, I envisioned introducing into a chiral luminophore species such as Au(I) complexes, moieties capable for rotational motion, anticipating the emergence of thermo-responsive CPL properties that can be controlled by molecular rotation in the crystal (Figure 4.1f). The binuclear Au(I) complexes, **6**-*R* and **6**-*S*, featuring chiral *N*-Heterocyclic carbene (NHC) ligands with phenylene rotator moieties at the chiral centers, were synthesized and studied. In the crystalline state, these complexes exhibit a distinct axially chiral conformation with C_2-symmetry, derived from non-equivalent orientations of phenyl moieties at the chiral centers of NHC ligands. In addition, variable-temperature solid-state ^{2}H NMR studies reveal that these non-equivalent phenyl moieties undergo fast rotational motion above 273 K. Such rotational motion may lead to the symmetrization of complexes with temperature elevation. Moreover, inherent chirality and the presence of thermally-activated rotational motion in the crystalline state result in the emergence of thermo-responsive CPL properties of the studied complexes, with CPL intensity (ΔI_{CPL}), lifetime, and luminescence dissymmetry factors (g_{lum}) showing a noticeable increase upon cooling from 333K to 213K ($|\Delta I_{CPL}|$: + ~300%; $|g_{lum}|$: + ~50%). This behavior is attributed not only to rotation-induced luminescence quenching but also to the rotation effect on the symmetry of the complexes, thereby affecting the g_{lum} values. This work demonstrates for the first time the correlation between molecular rotation and solid-state chiroptical properties, such as circularly polarized luminescence. Remarkably, the presence of molecular rotation can affect not only CPL intensity but also luminescence dissymmetry factors (g_{lum}) values, which usually require significant changes in the molecular [30] or supramolecular structure.[29,31,32]

4.2 Results and discussion

4.2.1 Synthesis and Characterization.

Chiral NHC Au(I) binuclear complexes **6**-*R*, **6**-*S* were synthesized in 73–76% yields through the transmetalation of {1,3-bis[(*R*)-1-phenylethyl]-imidazol-2-yl} Au (I) chloride or {1,3-bis[(*S*)-1-phenylethyl]-imidazol-2-yl} Au (I) chloride to 1,4-benzenediboronic acid bis(pinacol) ester in toluene at 70°C with potassium hydroxide as the base (Figure 4.2). The deuterated analog of **6**-*R* (**6**-*R*-d_4 and **6**-*R*-d_{20}) used in solid-state NMR studies were obtained by the same method. The complexes were characterized using ^{1}H and ^{13}C NMR spectroscopy, high-resolution mass-spectrometry (HRMS), C, H, and N elemental analysis, thermogravimetric analysis (TGA), differential scanning calorimetry (DSC), variable temperature (VT) single-crystal and powder X-ray diffraction (SCXRD and PXRD), circular dichroism (CD), photoluminescence, and circularly polarized luminescence (CPL) spectroscopies.

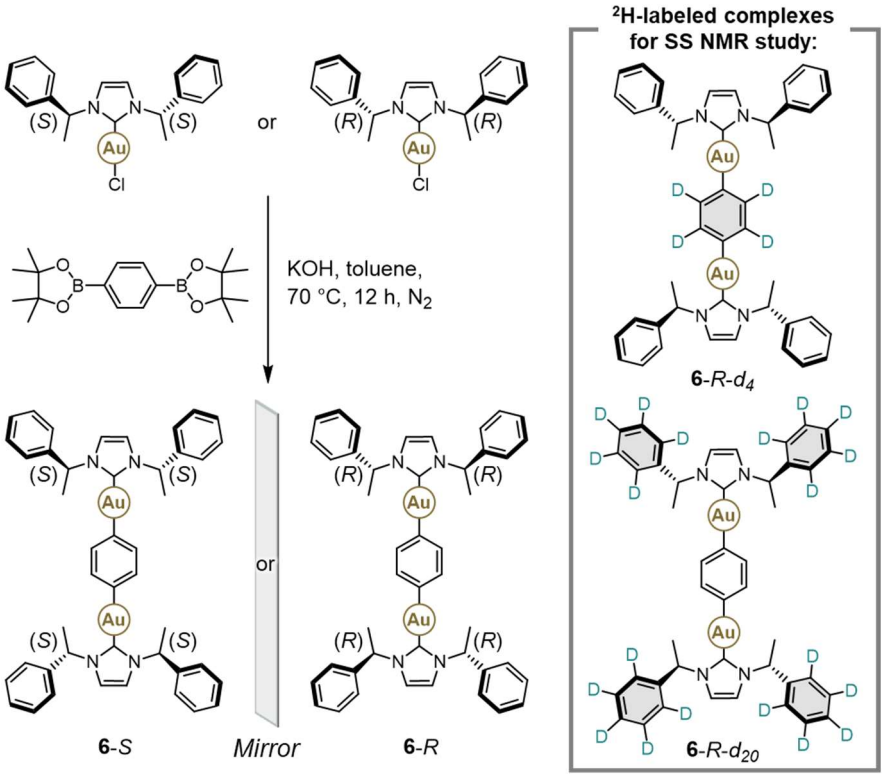

Figure 4.2 Synthesis and structures of Chiral NHC Au(I) binuclear complexes.

4.2.2 Single Crystal X-ray Diffraction

Crystallization of the complexes was conducted through vapor diffusion into dichloromethane/ethyl acetate solution in an *n*-hexane bath and yielded crystalline samples with no solvent inclusion, as confirmed by TGA and elemental analysis. The obtained single crystals were characterized by SCXRD, while the composition of the bulk crystalline samples was confirmed by PXRD at room temperature and elemental analysis. The crystal structures of the complexes are depicted in Figures 4.3 and 4.4, the crystallographic data parameters are given in Table S6-S4.4, while the complexes' geometrical parameters are listed in Table S4.5 in the Supporting Information.

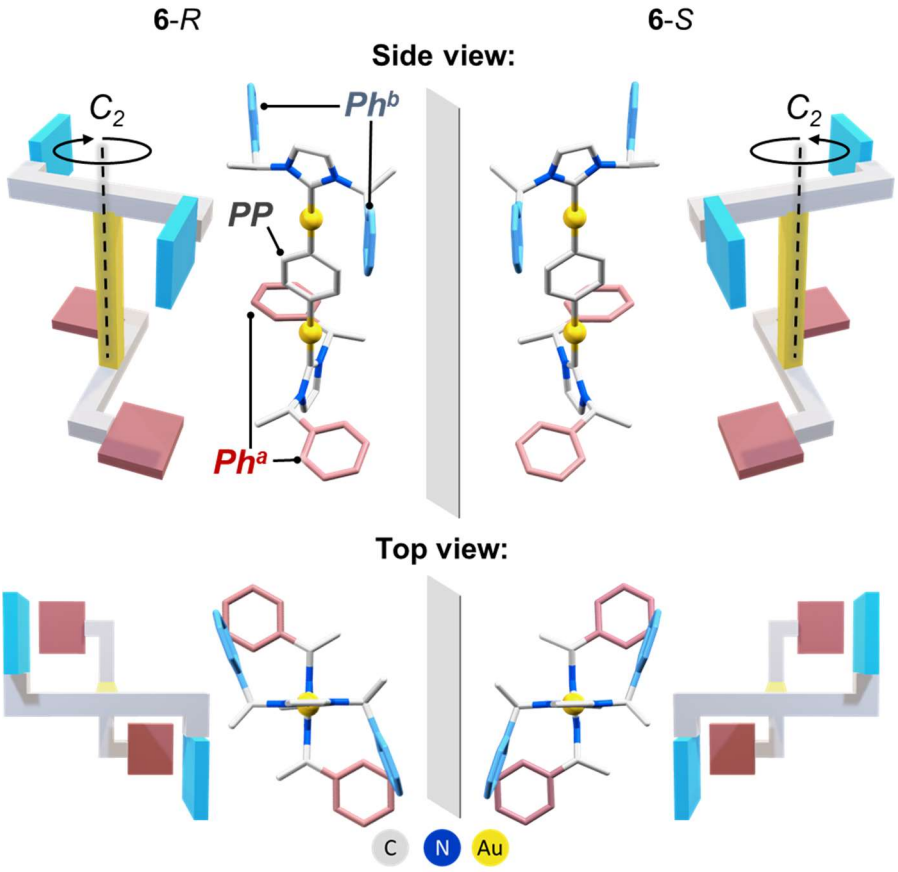

Figure 4.3. Crystal structure and the simplified conformation models of ***6**-R* and ***6**-S*.

6-*R* and **6**-*S* complexes possess crystal structures in the tetragonal enantiomorphic space group pair $P4_32_12$ and $P4_12_12$, respectively. The asymmetric unit includes only

half of the molecule of complex due to the presence of the 2-fold rotational axis passing through the two Au atoms (Figure 4.3). Notably, even though both Au atoms are bound with the same NHC ligands, in the crystal, these ligands are not equivalent due to the different orientations of the phenyl substituents at the NHC chiral centers: some are oriented vertically (Ph^a, indicated in red, Figure 4.3), while others are positioned horizontally (Ph^b, indicated in blue). At the same time, the *para*-phenylene bridging ligand (PP) is almost coplanar only with one of the NHC ligands while it is perpendicular to the other NHC ligands. The combination of inequivalent NHC ligands and 2-fold rotational symmetry in the crystal structure results in the emergence of a new stereogenic element as a C_2-symmetric axially chiral conformation, a simplified view of which is depicted in Figure 4.3.

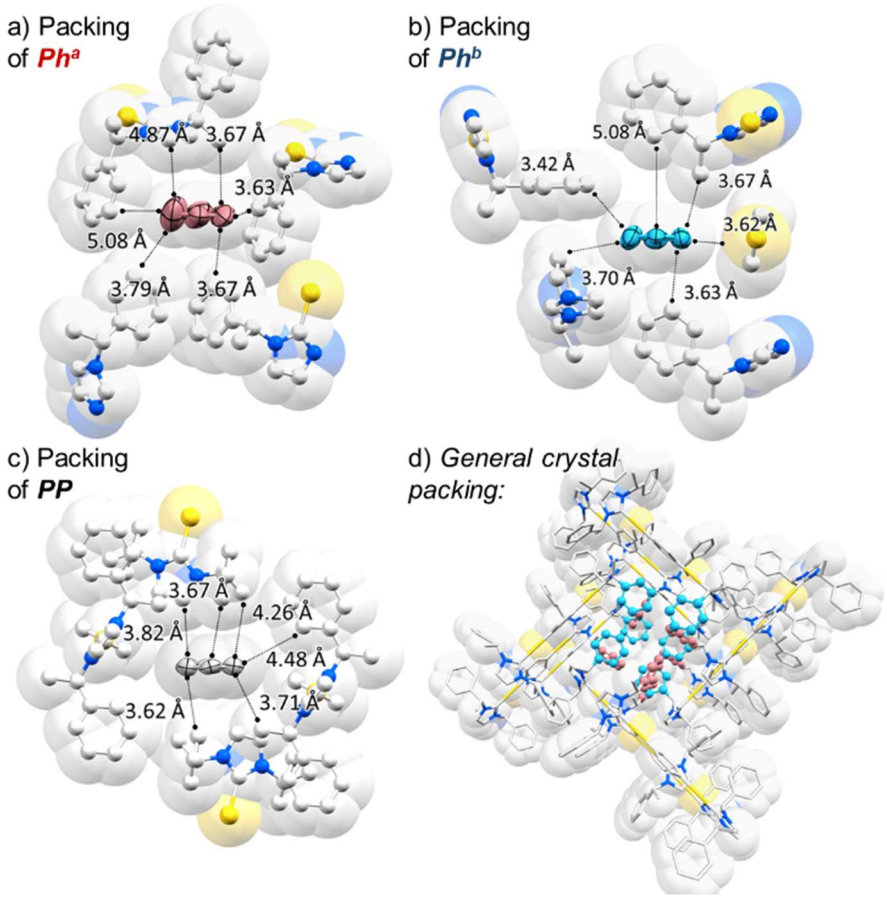

Figure 4.4. Crystal packing environment of Ph^a moieties (a), Ph^b moieties (b), PP moiety (c), as well as general packing (d) of **6**-*R* at 293K. In panels a-c, the dotted lines indicate short C-C intermolecular contacts.

Besides the different orientations of phenyl substituents at the NHC ligands (Ph^a and Ph^b), these inequivalent phenyl moieties also possess different crystal packing environments **(**Figure 4.4a and 4.4b). Notably, the Ph^a moieties experience less dense crystal packing than Ph^b, also displaying significantly larger thermal ellipsoids (estimated by average equivalent isotropic displacement parameters for phenyl C atoms – U_{eq}(Ph), $Å^2×10^3$: Ph^a – 190/233 vs Ph^b – 108/142 for **6**-*R*/**6**-*S* at 293K). The difference in the thermal ellipsoids of Ph^a and Ph^b suggests they may experience two different kinds of thermal motion. At the same time, the *PP* moiety displays an even tighter crystal packing with a larger number of short contacts with neighboring groups than Ph^a and Ph^b (Figure 4.4c). One the supramolecular level, molecules of **6**-*R*/**6**-*S* are forming helical "shaft" packing (*M*-helix for **6**-*R*, *P*-helix for **6**-*S*), with layered terminal Ph^a and Ph^b moieties pointing inwards (Figure 4.4d). Such organization of terminal phenyl groups in the crystal in the presence of their rotational motion may result into the emergence of the correlated motion.

Variable temperature SCXRD measurements in the 213–333K range (with a 20K step) indicate no significant crystal structure changes with temperature elevation, resulting in only an approximate 2% volume and density thermal expansion. These results align with the DSC data, which showed no noticeable exothermic or endothermic peaks during the heating/cooling cycle in the range of 213–333 K **(**Figure S4.3**)**. This indicates that the crystals of the complex of **6**-*R* and **6**-*S* do not undergo thermally-induced phase transitions in this temperature range.

4.2.3 Characterization of Rotational Dynamics by Variable Temperature Solid-State ^{2}H NMR.

To assess the solid-state dynamics in crystalline complexes, variable temperature (VT) solid-state (SS) ^{2}H NMR spin-echo spectroscopy was utilized. This technique is widely employed to analyze the internal dynamics of deuterium-enriched moieties in the 10^3–10^8 Hz regime.[38] VT SS ^{2}H NMR spin-echo measurements were conducted

on crystalline samples of two different isotopologues of **6**-*R* to extract dynamics information for different molecular fragments: **6**-*R*-d_4 with a deuterated bridging *para*-phenylene moiety (*PP*) and **6**-*R*-d_{20} with deuterated phenyl substituents (Ph^a and Ph^b) at the NHC ligands (Scheme 1).

VT SS ^{2}H NMR spin-echo measurements of crystalline **6**-*R*-d_4 in the 298–333K temperature range indicate a weak temperature-dependence of the signal line shape, which can be attributed to the close to static librations of the deuterated *PP* moiety (Figure 4.5). The presence of such a relatively slow flipping motion of the *PP* moiety can be explained by its tight packing within the crystal structure and by a larger number of short intermolecular contacts compared to the Ph^a and Ph^b moieties.

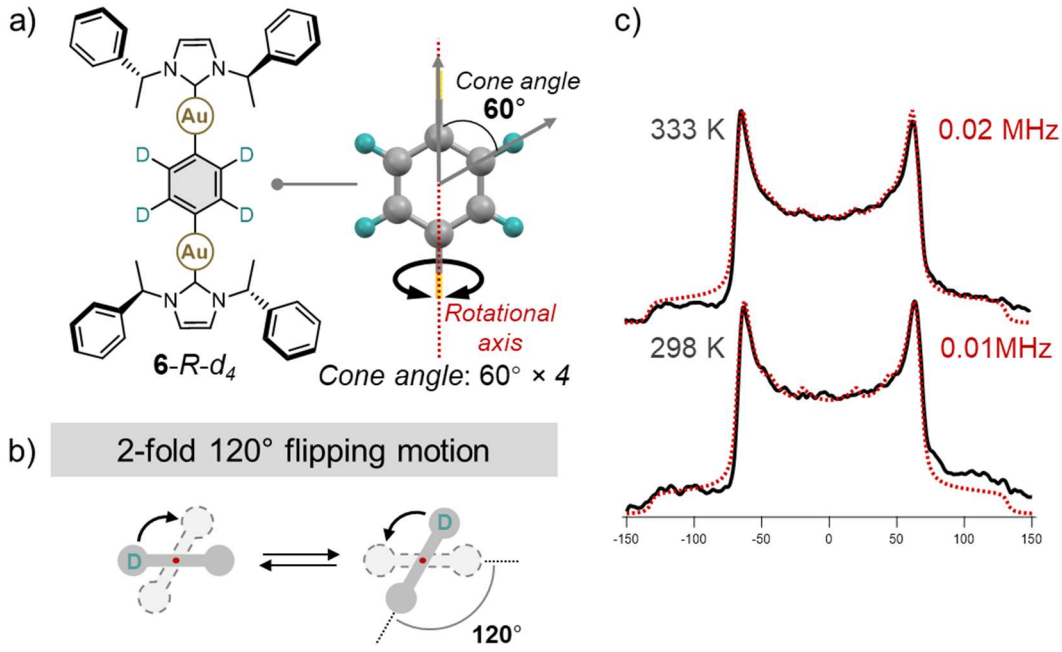

Figure 4.5 Variable-temperature solid-state ^{2}H NMR study of ***6***-*R*-d_4. (a) Cone angles experienced by the phenylene C–D bonds; (b) Illustration of the 2-fold 120° jump model for the PP moiety; (c) Line shape analysis of ^{2}H spin-echo SS NMR**.** measured under 298 K and 333 K.

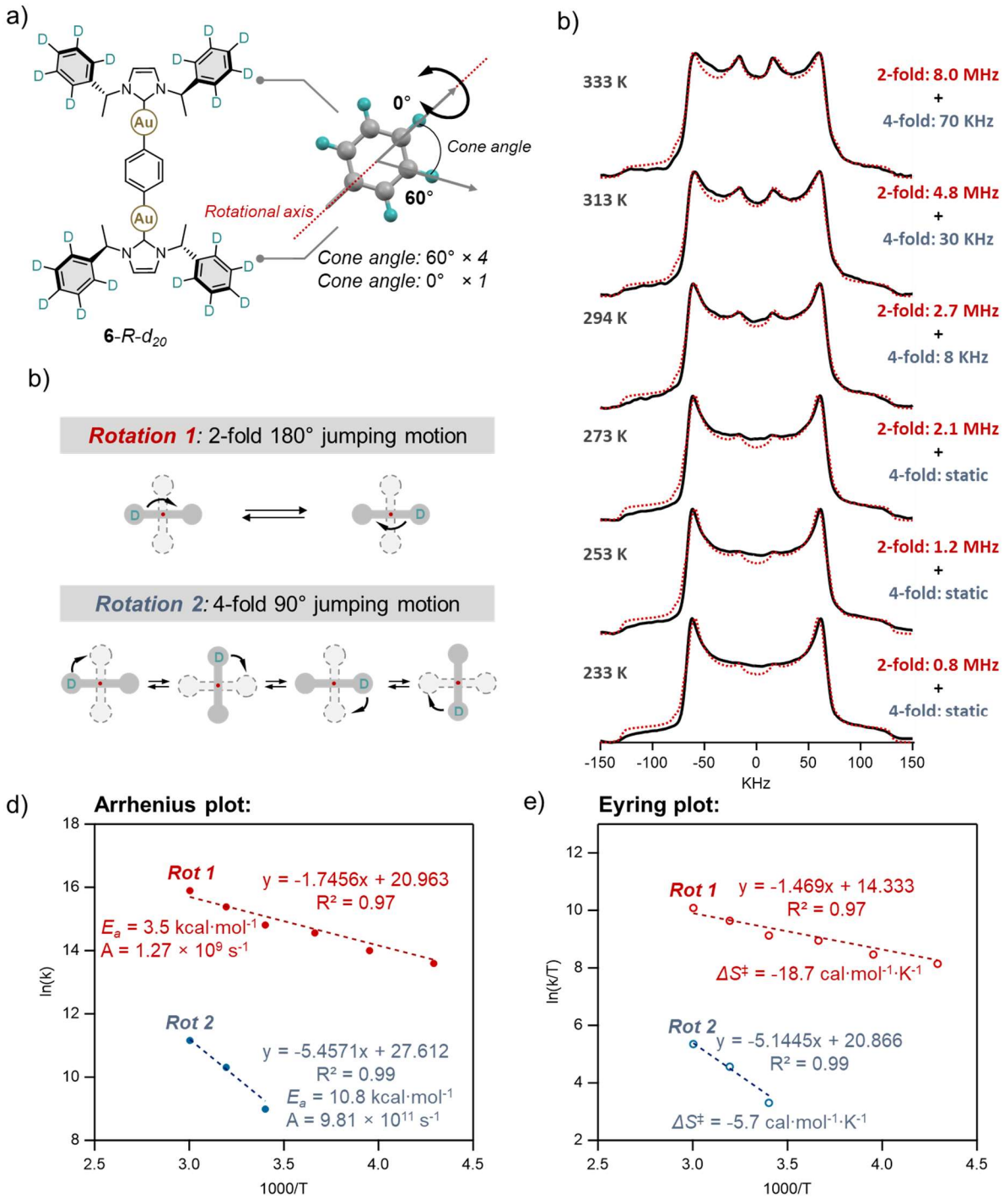

Figure 4.6. VT solid-state ^{2}H spin-echo NMR study of **6**-*R*-d_{20}. a) Experimental (black) and simulated (red) ^{2}H spin-echo NMR spectra of **6**-*R*-d_{20}; b) Structure of **6**-*R*-d_{20} and the cone angles experienced by the phenylene C–D bonds; c) Illustration of the 2-fold and 4-fold motion modes experiencing by the phenyl moieties; d-e) Arrhenius (d) and Eyring (e) plots for the **6**-*R*-d_{20} rotators dynamics in 233–333 K temperature range.

At the same time, experimental ^{2}H NMR line shapes obtained for **6**-*R*-d_{20} display more profound changes with temperature elevation (Figure 4.6a, black lines), suggesting the presence of more significantly thermally-activated dynamic processes involving the NHC phenyl moieties (Ph^a and Ph^b). It should be noted that in this case, the phenyl moieties contain two different types of deuterium atoms contributing to the ^{2}H NMR spectra (Figure 4.6b): two pairs of deuterium atoms at *ortho*- and *meta*-positions (cone angle = ±60°) and one deuterium at the *para*-position (cone angle = 0°, which should not affect the line shape with temperature change). Even though the obtained VT ^{2}H NMR spin-echo experimental patterns of **6**-*R*-d_{20} could not be accurately fitted using a single dynamic mode. This is due to Ph^a and Ph^b being non-equivalent in the crystal structure and experiencing different crystal packing, suggesting the presence of two types of thermal motion. Based on this premise, I used two types of motion in the^{2}H NMR simulations (Figure 4.6a, red lines): a faster 180° 2-fold jumping (rotation 1) and a slower 90° 4-fold motion (rotation 2; Figure 4.6c). Since the Ph^a is displaying generally larger thermal ellipsoids in SCXRD structures at all temperatures, I presume that it can exhibit a faster 180° 2-fold motion, while the slower 90° 4-fold jumping motion may be attributed to Ph^b. In the latter case, the crystal packing environment of Ph^b is also more suitable for the presence of 4-fold motion.

For the faster 2-fold motion, its rotational frequency (k_{rot1}) increases from 0.8 MHz at 233K to 8 MHz at 333K. At the same time, the frequency of the slower 4-fold motion (k_{rot2}) is only 70 kHz at 333K, while it falls below 1 kHz at 273K. The rotation frequencies of both types of motions in **6**-*R*-d_{20} fit well on Arrhenius and Eyring plots, allowing for the evaluation of their thermodynamic parameters (Figure 4.6d and F**i**gure 4.6e). The activation energy (E_a) of the fast 2-fold flip was found to be 3.5 kcal·mol^{-1}, while the pre-exponential factor (A) was 1.27 × 10^9 s^{-1}. Meanwhile, the E_a of the slower 4-fold motion was 10.8 kcal·mol^{-1}, with the A being 9.81 × 10^{11} s^{-1}. Utilizing the Eyring plot allowed us to determine the entropy of activation ($\Delta S^{\ddagger}$) of

rotational motions, which are negative in both cases: –18.7 cal·mol^{-1}·K^{-1} (Rotation 1) and –5.7 cal·mol^{-1}·K^{-1} (Rotation 2). The latter indicates the possibility of correlated rotational motion of the phenyl moieties in the crystal structure, which is also favorable due to their "shaft" packing in the crystal.

4.2.4 Thermo-responsive chiroptical and emission properties

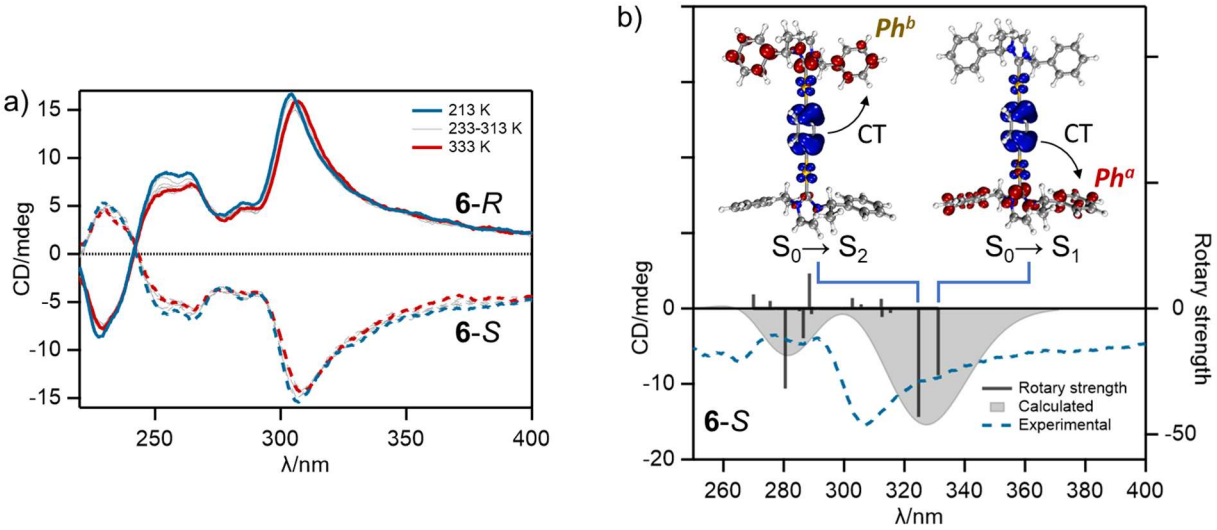

Figure 4.6. VT CD spectra of crystalline **6**-*S* (bottom) and **6**-*R* (top) in 233–333 K temperature range. b) Experimental and calculated CD spectra of **6**-*S* and rotatory strengths with the hole-electron distribution maps for the selected transitions (hole distribution is indicated in blue and electron distribution in red: isovalue of 0.002).

The absorption spectra of crystalline **6**-*R* and **6**-*S* exhibit two major peaks around 230 nm and 280 nm (Figures S4.8, and 4.9). The circular dichroism (CD) spectra in the crystalline state display a distinct mirror pattern for the crystals of both enantiomers, with a major CD response at approximately 310 nm (Figure 4.6a). At the same time, the variable temperature CD measurements of crystalline samples in 213K–333K range indicate a slight decrease in the CD signal upon heating (Figure 4.6a), which could possibly indicate some "loss" of chirality at the high temperature.[40] The conducted TD-DFT calculations (PBE0-D3(BJ)/def2SVP+MDF60 level)[41] for the solid-

state structure of **6**-*S* show good agreement with experimental CD data (Figure 4.6b). Notably, the major CD absorption peak (furtherly used for photoexcitation) corresponds to the $S_0 \longrightarrow S_1$ and $S_0 \longrightarrow S_2$ transitions, which are mainly attributed to ligand-to-ligand (LLCT) and metal-to-ligand (MLCT) charge transfers from the *para*-phenylene bridging ligand and the Au(I) atom to the NHC ligands, involving their phenyl substituents (Figure 4.6b).

6-*R* and **6**-*S* exhibit relatively weak photoluminescence in dichloromethane solution, with a broad band emission maximum at 392 nm (Figure S4.10) and a quantum yield (Φ_{PL}) of approximately 3%. Notably, the studied complexes do not display any CPL signal in solution. At the same time, their crystallization leads to a red shift of the emission maximum to 466 nm and a dramatic increase in Φ_{PL} to approximately 30% at room temperature. Such behavior is characteristic of aggregation-induced emission systems and relies on the restriction of intramolecular motion (RIM) model,[13] suggesting the suppression of motion-induced emission quenching in the solid state. Remarkable, that the obtained crystalline complexes also demonstrate thermo-responsive emission properties with approximately a 2.5-fold increase in luminescent intensity (I_{PL}, Figure 4.7a and Figure 4.7b) upon cooling from 333K to 213K. Previously, I observed the same behavior for relevant organogold(I) crystalline molecular rotors and associated it with the effect of phenylene or pyrazine moiety rotational motion on the excited state decay through a nonradiative relaxation pathway.[13,21]

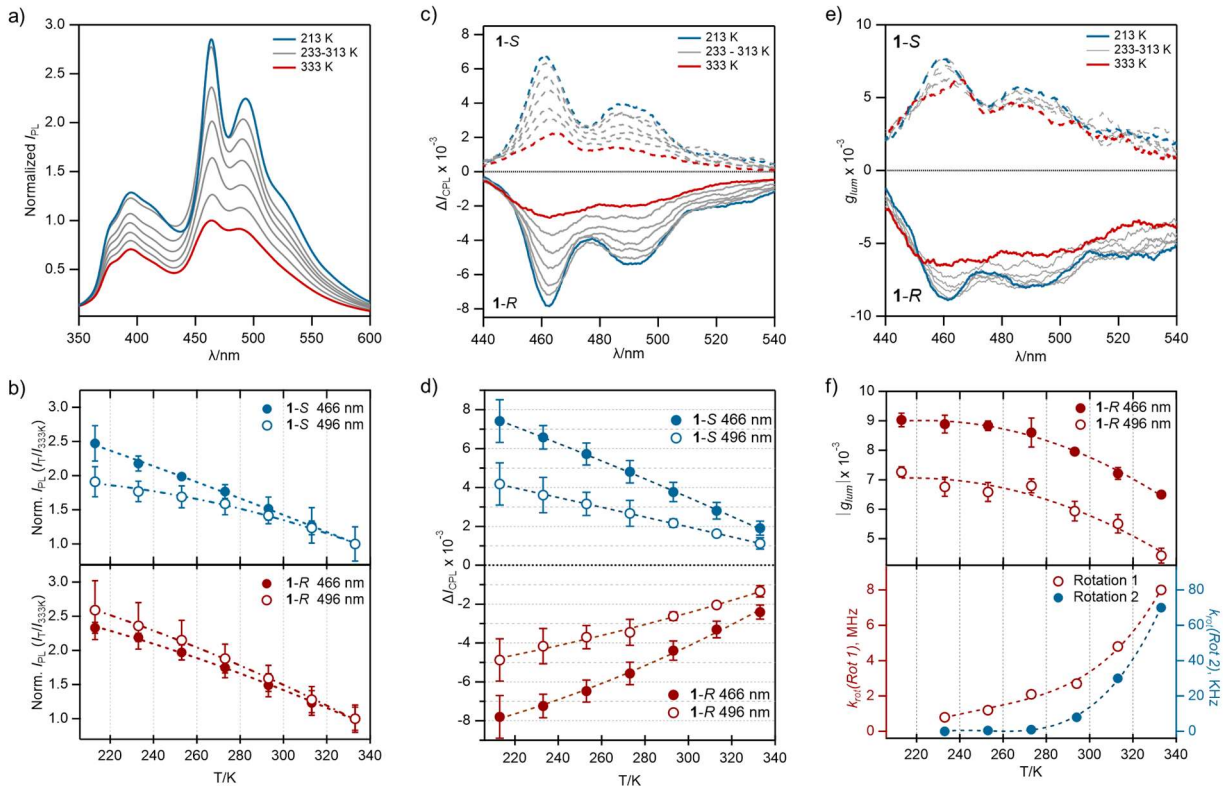

Figure 4.7. VT emission spectra of crystalline **6**-*R*; b) Plot of normalized emission intensity (Norm. I_{PL} = I_T/I_{333K}) at 466 and 496 nm maxima against the temperature for crystalline **6**-*S* (top) and **6**-*R* (bottom); c) VT CLP spectra of crystalline **6**-*S* (top) and **6**-*R* (bottom); d) Plots of CLP intensity ΔI_{CPL} at 466 and 496 nm maxima against temperature for crystalline **6**-*S* (top) and **6**-*R* (bottom); d) VT g_{lum} spectra of crystalline **6**-*S* (top) and **6**-*R* (bottom); g) Plots of g_{lum} at 466 and 496 nm of **6**-*R* (top) and rotation frequencies (k_{rot}) of **6**-*R*-d_{20} (bottom) against temperature. The norm. I_{PL} (b), ΔI_{CPL}(d) and g_{lum}(g) values are represented by an average of three independent measurements.

Unlike in solution media, the crystalline **6**-*R* and **6**-*S* display clear mirrored CPL signals with two maximums at 466 nm and 496 nm under excitation at 315 nm (Figure 4.7c). Notably, the CPL signal has the opposite sign compared to their CD signals. Similar to the general emission intensity (I_{PL}) of **6**-*R* and **6**-*S*, the CPL intensity (ΔI_{CPL}) also shows a strong dependence on temperature, increasing up to 4-fold upon cooling from 333K to 213K (Figure 4.7d). While both the I_{PL} and ΔI_{CPL} show increase with cooling, the ΔI_{CPL} rises faster with. This also suggests a change in the luminescence dissymmetry factors (g_{lum}) of crystalline **6**-*R* and **6**-*S*, which increase almost up to ~50% with cooling

(Figure 4.7e), from ±3–6 × 10^{-3} at 333K to ±7–9 × 10^{-3} at 213K (Table S4.9). The obtained $|g_{lum}|$ values of **6**-*R* and **6**-*S* complexes are comparable to those of the recently reported crystalline chiral aminocarbene Au(I) complexes (0.1–5.8 × 10^{-3}).[57-60] To ensure the reproducibility of the temperature effect on ΔI_{CPL} and g_{lum} values, measurements for each complex were conducted using three independently prepared crystalline samples. Moreover, the thermal reversibility of the effect was confirmed on the crystalline sample of **6**-*R* using three heating-cooling cycles from 333K to 213K (Figure S4.14).

4.2.4 Correlation between Chiroptical and Emission Properties and Rotational Dynamics.

While the change in CPL intensity with temperature is a fairly expected result of the thermo-responsive behavior of emissive organogold crystalline molecular rotors such as **6**-*R* and **6**-*S* (due to the general increase of emission intensity), the enhancement in luminescence dissymmetry factor values (g_{lum}) with cooling is a more surprising observation. Usually, alterations in the luminescence (or absorption) dissymmetry factors require significant changes and rearrangements in the molecular or supramolecular structure, which are more probable in less ordered and fluid media, such as solutions, dynamic aggregates, and polymer environments In the case of rigid crystalline media, significant changes in g_{lum} can be achieved through phase transitions (i.e., single-crystal-to-single-crystal or single-crystal-to-amorphous) or by changing the emission band or mechanism (e.g. from fluorescence to phosphorescence). [42, 43] However, for the crystalline **6**-*R* and **6**-*S*, no signs of any phase transitions or large structural changes were observed by VT SCXRD and DSC analyses in the studied temperature range. Additionally, we do not observe significant emission thermochromism that usually indicates a change in the emission mechanism/band. The emission and CPL intensity at both major peaks of 466 and 496 nm are rising simultaneously upon cooling, while there is almost no change in

the emission lifetime between 85K and 293K remains in the range of few hundreds μs, which can be attributed only to phosphorescence. Thus, we can assume that the thermally induced changes in g_{lum} cannot be associated neither with phase transition, nor with change of the emission mechanism, and should have another origin.

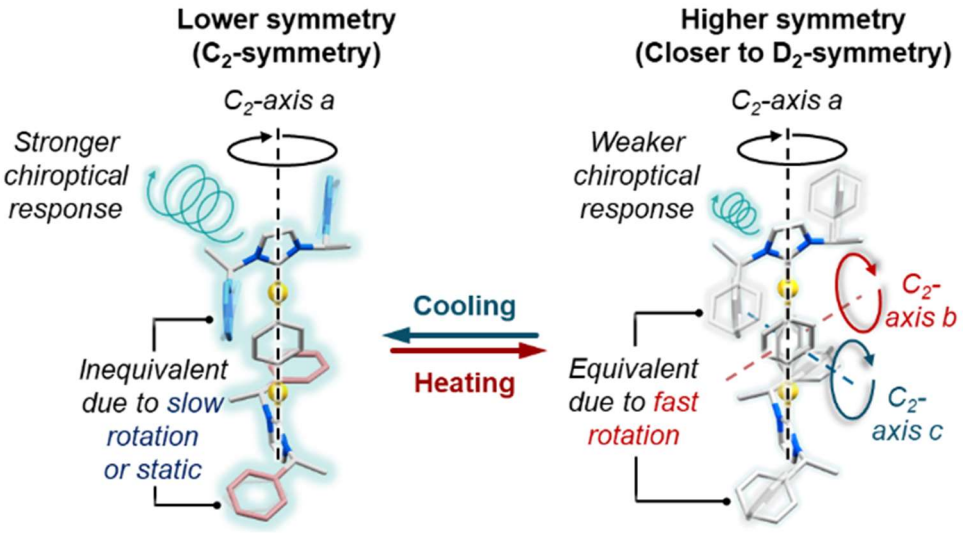

Figure 4.8. Illustration of the effect of internal molecular motion on complex symmetry.

Noteworthy that the g_{lum} values of **6**-*R* and **6**-*S* show clear nonlinear dependence on temperature, and they change less drastically below 273K (Figure 4.7f). Such stabilization of luminescence dissymmetry factor values below 273K correlates with the inhibition of one of rotational motions in phenylene moieties of NHC ligands observed by SS ^{2}H spin-echo NMR (Figure 6f, bottom). Therefore, we presume that the presence of rotational motion may also affect the dissymmetry factor values of **6**-*R* and **6**-*S*. In this case, the intramolecular rotational motion, especially the 4-fold 90° motion mode of the Ph moiety, can lead to the existence of temporary conformations where all Ph groups have the same orientation relative to their NHC ligands and are equivalent in the structure (Figure 4.8). This, in combination with some librational motion of the *PP* moiety, may result in the appearance of a symmetry of complex higher than C_2, approaching D_2 symmetry by the emergence of two additional perpendicular 2-fold axes of rotational symmetry (Figure S4.15). Such symmetry alteration may not strongly affect the general emission properties of the

complexes but should more significantly impact the chiroptical properties. This may explain the decrease in g_{lum} values with temperature elevation as well as some decrease in the CD signal (Figure S4.16). Conversely, the inhibition of one of internal motions below 273K should lead to the full domination of the lower symmetry C_2 conformation of **6**-*R* and **6**-*S* observed by SCXRD, resulting in a stronger chiroptical response. However, due to the presence of the second 2-fold type of rotational motion which is still quite fast below 273K, no full stabilization of luminescence and CPL intensities were observed in the studied temperature range.

4.3 Conclusion

In this chapter, I have demonstrated how thermally-activated molecular rotation can control chiroptical properties, such as circularly polarized luminescence (CPL), in the solid state, on the example of crystalline chiral binuclear NHC Au(I) complexes **6**-*R* and **6**-*S.* This enantiomeric pair of NHC Au(I) complexes exhibit distinct chiral conformations with C_2 symmetry and thermally-activated rotational motion of the phenyl groups in the crystalline state, as confirmed by SCXRD and solid-state ^{2}H NMR studies. The combination of these features results in the emergence of thermo-responsive emissive and CPL properties of the studied crystalline complexes.

Remarkably, the observed thermo-responsive behavior can be attributed not only to thermal motion-induced luminescence quenching, which affects general emission and CPL intensity and lifetime but also to the potential effect of phenyl rotation on the symmetry of the complexes. In this case, the combination of molecular rotational and librational motions within the complex structure may result in the appearance of temporary conformations with symmetry higher than C_2. Such rotation-induced symmetry alteration is capable of changing and control over luminescence dissymmetry factors (g_{lum}) values, which typically require significant modifications in

the molecular or supramolecular structure, but not just thermal motion in the solid state.

These findings demonstrate, for the first time, the correlation between molecular rotation and solid-state chiroptical properties, such as CPL. These insights into the control of CPL properties through molecular rotation are expected to be valuable for the development of new generations of stimuli-responsive chiroptical solid-state materials.

4.4 Experimental details and support information

4.4.1 General information

All commercially available reagents and solvents are reagent grade and were used without further purification unless otherwise noted. These reagents were purchased from TCI, Aldrich, Cica, and Wako. Solvents used for synthesis were further dried over with 4Å molecular sieves. Abbreviations for reagents are as follows: NHC (*N*-heterocyclic carbene), DCM (dichloromethane), EtOAc (ethyl acetate), Hex (*n*-hexane), THF (tetrahydrofuran).

NMR spectra were recorded on a JEOL JNM-ECZ400S (^{1}H: 400 MHz; ^{13}C: 100 MHz), using TMS or solvent residual signals as internal standards. NMR data are presented as follows: singlet (s), doublet (d), triplet (t), doublet of doublets (dd), multiplet (m), coupling constant in Hertz (Hz) and integration. High-resolution mass spectra (HRMS) and elemental analyses (Elem. Anal.) were recorded at the Instrumental Analysis Division, Global Facility Center, Hokkaido University. Using a Thermo Scientific Exactive plus for ESI-HRMS and an Exeter Analytical CE440 CHN analyzer for Elem. Anal. Details of the thermogravimetric analysis (TGA), differential scanning calorimetry (DSC), theoretical calculations, single-crystal (SCXRD), powder (PXRD) X-Ray diffraction experiments, solid-state NMR (SSNMR) study as well as the optical analyses (UV-Vis, circular dichroism (CD), photoluminescence (PL), and circularly polarized luminescence (CPL)) are given below. The raw data was plotted using Igor Pro version 9.0.1.2.

4.4.2 Synthesis and characterization

Synthesis of (R)-α-methylbenzylamine-d_5.

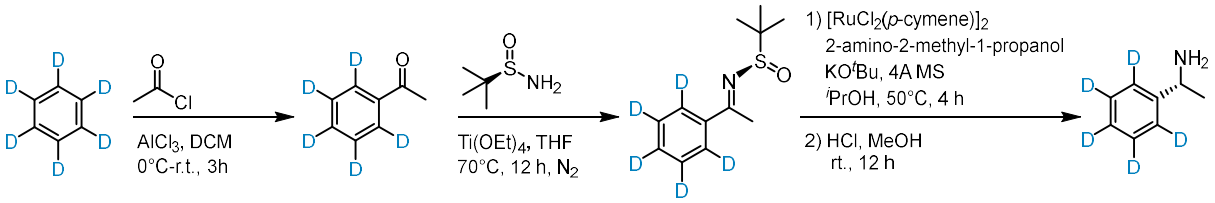

(R)-α-methylbenzylamine-d_5 was synthesized according to the modified literature procedure in three-steps.

Acetophenone-d_5

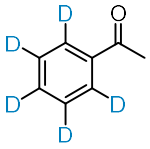

A Friedel-Crafts acylation was conducted by adding benzene-d_6 (1.0 equiv., 36.0 mmol) and aluminum chloride (3.0 equiv., 108.0 mmol) to a round-bottom flask (500 mL capacity). Subsequently, 150 mL of dry DCM was added, and the mixture was stirred at 0°C. Acetyl chloride (1.75 equiv., 63.0 mmol) was introduced dropwise via a syringe, and the resulting mixture was allowed to warm to room temperature. After 3 hours, the mixture was cooled to 0°C again and quenched with ice water. The organic layer was washed with 3M HCl (100 mL) and then dried over $MgSO_4$. The desired acetophenone-d_5 was isolated through flash chromatography on silica gel (Hex/EtOAc = 20/1). Yield: 44%, 2 g, pale yellow oil. ^{1}H NMR (400 MHz, $CDCl_3$, δ): 2.61 (s, 3H). The NMR spectra was confirmed with previous report.[42]

(*R*,E)-2-methyl-*N*-(1-phenylethylidene)propane-2-sulfinamide-d_5[43]

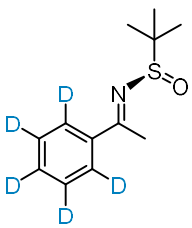

Acetophenone-d_5 (1.0 equiv., 8.0 mmol) and (*R*)-*tert*-butanesulfinamide (1.0 equiv., 8.0 mmol) were added to a round-bottom flask (100 mL capacity). The flask was sealed with a septum and connected to a vacuum/nitrogen Schlenk line. It was evacuated and backfilled with nitrogen three times. THF (32 mL) and titanium(IV) ethoxide (2.0

equiv., 16.0 mmol) were then added using a syringe under a nitrogen atmosphere and stirred at 70°C for 12 hours. Afterward, the reaction mixture was allowed to cool to room temperature, and EtOAc (10 mL) was added. Then the reaction was terminated by the addition of brine (20 mL). The resulting mixture was stirred for 30 minutes at room temperature, and the insoluble materials were removed by filtration through a pad of Celite. The combined organic phases were dried over $MgSO_4$, and the desired product was purified through flash column chromatography on silica gel (Hex/EtOAc = 5/1). Yield: 67%, 1.2 g, pale yellow oil. ^{1}H NMR (400 MHz, $CDCl_3$, δ): 1.32 (s, 9H), 2.76 (s, 3H). ^{13}C NMR (100 MHz, $CDCl_3$, δ): 19.80 (CH_3), 22.46 (CH_3), 57.37 (CH_3), 126.78 (t, C_{Ar}), 127.89 (t, C_{Ar}), 131.11 (t, C_{Ar}), 138.54 (C_{Ar}), 176.33 (C_{Ar}). HRMS (ESI) m/z: $[M+Na]^+$ calcd for $[C_{12}H_{12}D_5NOSNa]^+$: 251.1237, Found: 251.1232.

(*R*)-*α*-methylbenzylamine-*d*$_5$[44]

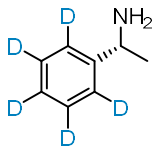

2-Amino-2-methyl-1-propanol (0.05 equiv., 0.1 mmol), $[RuCl_2(p\text{-cymene})]_2$ (0.025 equiv., 0.05 mmol), 4 Å molecular sieves (0.8 g), and ^{i}PrOH (2.5 mL) were combined in a round-bottom flask (50 mL capacity). The mixture was heated to 90°C for 20 minutes. During this heating period, the initially orange reaction mixture turned into a dark red color. The reaction was then cooled to 50°C, and (*R,E*)-2-methyl-*N*-(1-phenylethylidene)propane-2-sulfinamide-*d*$_5$ (1.0 equiv., 2.0 mmol, dissolved in ^{i}PrOH (12 mL)) and KO^{t}Bu (0.125 equiv., 0.25 mmol, dissolved in ^{i}PrOH (2.5 mL)) were successively added. After the completion of the reaction (monitored by TLC), the reaction mixture was passed through a small column of silica gel. The column was washed with EtOAc (10 mL), and the combined organic phases were evaporated and dissolved in a 1.5 M HCl in MeOH (8 mL, prepared by the dropwise addition of $SOCl_2$ to methanol at 0°C) and stirred for 12 hours at room temperature. Then, the solvent was evaporated, and a 2 M HCl aqueous solution (10 mL) was added and washed with EtOAc (3 × 20 mL). The aqueous layer was basified with a 1M NH_3/NH_4Cl buffer solution and extracted with DCM (3 × 20 mL). The combined organic phases were dried over $MgSO_4$, and the

target product was obtained after filtration and evaporation of the solvent. Yield: 90%, 227 mg, brown oil. ^{1}H NMR (400 MHz, $CDCl_3$, δ): 1.38-1.39 (d, *J* = 7.4 Hz, 3H, CH_3), 1.49 (s, 2H, NH_2), 1.10-1.14 (q, *J* = 6.6 Hz, 1H, CH). The NMR spectra were confirmed with the previous report.[45]

Synthesis of chiral imidazolium hexafluorophosphate salt.

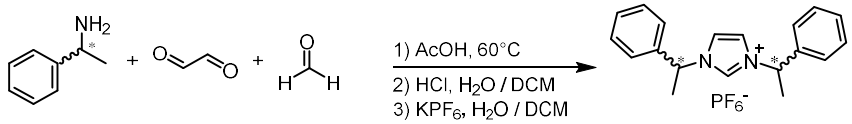

Imidazolium hexafluorophosphate salt was synthesized according to the modified literature procedure.[46] Glyoxal (0.5 equiv., 1.0 mmol, 40% in water), formaldehyde (0.5 equiv., 1.0 mmol, 37% in water), and acetic acid (10.0 equiv., 20.0 mmol) were added to an oven-dried reaction vessel (10 mL capacity), the reaction vessel was sealed with a septum and stirred in an oil bath at 60°C for 5 minutes. *α*-Methylbenzylamine (1.0 equiv., 2.0 mmol) was added by a syringe, and this mixture was continued stirred at 60°C for 1 hour. After cooling to room temperature, the reaction mixture was transferred to an Erlenmeyer flask (300 mL capacity), then added DCM (50 mL) and HCl (3M in water, 100 mL), and the resulting mixture was stirred at room temperature for 1 h. Then, the organic layer was separated. Water (100 mL) and potassium hexafluorophosphate (KPF_6, 1.0 equiv., 2.0 mmol) were added, and the resulting mixture was stirred at room temperature for 1 hour. After that, the organic layer was separated and dried over $MgSO_4$. The crude imidazolium salt was isolated by flash chromatography on silica gel (DCM/EtOAc = 1/1), and then recrystallization in EtOAc and Hex at -20°C to obtain a white solid, washed with Hex (three 3-mL portions) and dried under vacuum.

1,3-bis[(*R*)-1-phenylethyl]-1*H*-imidazol-3-ium hexafluorophosphate(V)

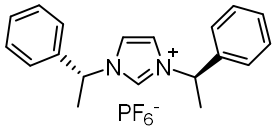

Yield: 88 %, 370 mg, white solid. ^{1}H NMR (400 MHz, $CDCl_3$, δ): 1.96 (d, *J* = 6.80 Hz, 6H, CH_3), 5.68 (q, *J* = 7.20 Hz, 2H, CH), 7.07 (d, *J* = 1.60 Hz, 2H, imidazole), 7.45-7.26 (m, 10H, H-C_{Ar}), 8.90 (s, 1H, imidazole). The NMR spectra was confirmed with previous report. [47]

1,3-bis[(*S*)-1-phenylethyl]-1*H*-imidazol-3-ium hexafluorophosphate(V)

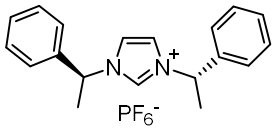

Yield: 92 %, 388 mg, white solid. ^{1}H NMR (400 MHz, $CDCl_3$, δ): 1.92 (d, *J* = 6.80 Hz, 6H, CH_3), 5.64 (q, *J* = 7.20 Hz, 2H, CH), 7.14 (d, *J* = 1.40 Hz, 2H, imidazole), 7.40-7.26 (m, 10H, H-C_{Ar}), 8.80 (s, 1H, imidazole). The NMR spectra was confirmed with previous report. [47]

1,3-bis[(*R*)-1-phenylethyl]-1*H*-imidazol-3-ium hexafluorophosphate(V)-*d*$_{10}$

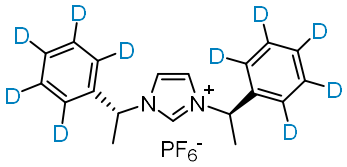

2.4 mmol scale reaction, yield: 80 %, 830 mg, white solid. ^{1}H NMR (400 MHz, $CDCl_3$, δ): 1.96 (d, *J* = 6.8 Hz, 6H, CH_3), 5.68 (q, *J* = 6.8 Hz, 2H, CH), 7.07 (d, *J* = 1.60 Hz, 2H, imidazole), 8.89 (s, 1H, imidazole). ^{13}C NMR (100 MHz, $CDCl_3$, δ): 20.67 (CH_3), 60.30 (CH), 120.83 (NHC, imidazole), 120.92(C_{Ar}), 126.52(t, C_{Ar}), 129.06 (t, C_{Ar}), 133.92 (m, C_{Ar}), 137.20 (imidazole). HRMS (ESI) m/z: $[M-PF_6^-]^+$ calcd for $[C_{19}H_{11}D_{10}N_2]^+$: 287.2327, Found: 287.2321.

Synthesis of Chiral NHC Au(I) chloride.

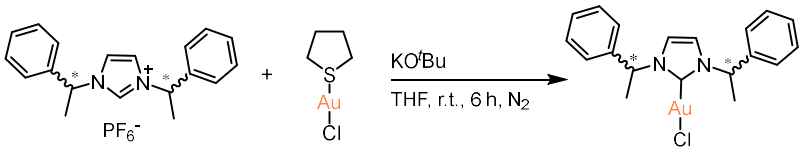

1,3-bis(1-phenylethyl)-1*H*-imidazol-3-ium hexafluorophosphate(V) (1.0 equiv., 0.237 mmol, 100 mg), and [Au(THT)Cl] (1.0 equiv., 0.237 mmol) were added to an oven-dried reaction vessel (10 mL capacity). The reaction vessel was sealed with a septum and connected to a vacuum/nitrogen manifold through a rubber tube. It was

evacuated and then backfilled with nitrogen. This process was repeated three times. Dry THF (3.0 mL) was then added by a syringe under a nitrogen atmosphere. After stirred at room temperature for 5 minutes, KO^{t}Bu (1.2 equiv. 0.28 mmol, 1M in THF) was add by a syringe, and this mixture was stirred at room temperature for 6 hours. After that, the reaction mixture was filtrated through a pad of Celite and isolated by flash chromatography on silica gel (Hex to DCM, be faster), and then recrystallization in DCM and Hex at room temperature to obtain a white solid, washed with Hex (three 3-mL portions) and dried under vacuum.

{1,3-bis[(*R*)-1-phenylethyl]-imidazol-2-yl} Au (I) chloride

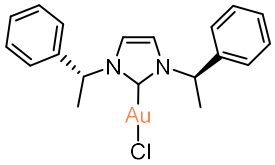

Yield: 77 %, 77 mg, white solid. ^{1}H NMR (400 MHz, $CDCl_3$, δ): 1.84 (d, *J* = 7.20 Hz, CH_3), 6.17 (q, *J* = 7.2 Hz, 2H, CH), 6.82 (s, 2H, NHC), 7.41-7.34 (m, 10H, H-C_{Ar}). The NMR spectra were confirmed with the previous report.[48]

{1,3-bis[(*S*)-1-phenylethyl]-imidazol-2-yl} Au (I) chloride

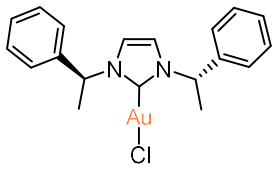

Yield: 72 %, 72 mg, white solid. ^{1}H NMR (400 MHz, $CDCl_3$, δ): 1.84 (d, *J* = 7.2 Hz, CH_3), 6.17 (q, *J* = 6.8 Hz, 2H, CH), 6.82 (s, 2H, NHC), 7.41-7.32 (m, 10H, H-C_{Ar}). The NMR spectra were confirmed with the previous report.[48]

({1,3-bis[(*R*)-1-phenylethyl]-imidazol-2-yl} Au (I) chloride-*d_{10}*.

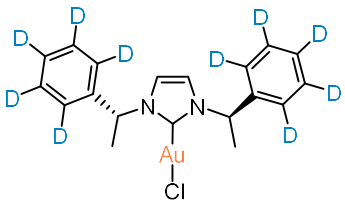

Yield: 52 %, 111 mg (0.46 mmol scale), white solid. ^{1}H NMR (400 MHz, $CDCl_3$, δ): 1.84 (d, *J* = 7.2 Hz, CH_3), 6.17 (q, *J* = 7.2 Hz, 2H, CH), 6.81 (s, 2H, NHC). ^{13}C NMR (100 MHz, $CDCl_3$, δ): 20.73 (CH_3), 59.98 (CH), 118.11 (C_{NHC}), 126.35 (t, C_{Ar}), 128.03 (t, C_{Ar}), 128.45 (t, C_{Ar}), 139.01 (C_{Ar}), 169.87(C_{NHC}). HRMS (ESI) m/z: $[M+Na]^+$ calcd for $[C_{19}H_{10}D_{10}AuClN_2Na]^+$: 541.1501, Found: 541.1492. Elem. Anal.

Calcd for $C_{19}H_{10}D_{10}AuClN_2$, C, 43.98; H/D, 5.82; N, 5.40. Found: C, 43.93; H, 3.82 (H+D = 1.88+3.35 = 5.23)[49]; N, 5.15.

*Synthesis of chiral rotor **6***

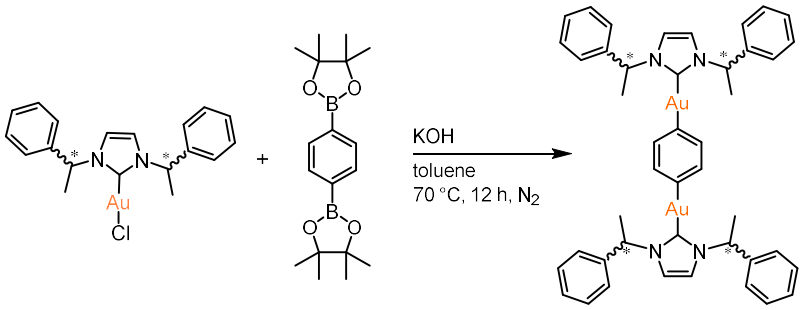

Chiral rotor **6** were synthesized according to the modified literature procedure.[50] [1,3-bis(1-phenylethyl)-imidazol-2-yl] Au (I) chloride (1.0 equiv., 0.10 mmol, 30 mg), 1,4-benzenediboronic acid bis(pinacol) ester (0.6 equiv., 0.06 mmol) and KOH (3.5 equiv., 0.35 mmol) were added to an oven-dried reaction vessel (10 mL capacity). The reaction vessel was sealed with a septum and connected to a vacuum/nitrogen manifold through a rubber tube. It was evacuated and then backfilled with nitrogen. This process was repeated three times. Toluene (1.0 mL) was then added using a syringe under a nitrogen atmosphere. The mixture was stirred in an oil bath at 70°C for 12 hours, during which some purple-black precipitate was produced. After cooling to room temperature, the reaction mixture was filtered through a pad of Celite to remove all insoluble precipitate. The solvents were evaporated under reduced pressure to yield the corresponding crude product.

*Preparation of crystalline samples of chiral rotor **6**.*

The crude product was dissolved in DCM (1.5 mL), filtered through Celite again, and then EtOAc (1.5 mL) was added. Recrystallization was performed under Hex

vapor diffusion conditions at room temperature. After several hours, colorless needle crystals were obtained.

6-*R*

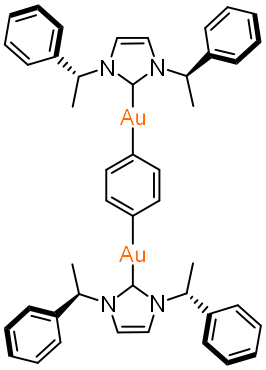

Yield: 73%, 22 mg, white solid. ^{1}H NMR (400 MHz, $CDCl_3$, δ): 1.84 (d, *J* = 7.2 Hz, 12H, CH_3), 6.41 (q, *J* = 7.2 Hz, 4H, CH), 6.79 (s, 4H, NHC), H-C_{Ar}), 7.30-7.38 (m, 12H, H-C_{Ar}), 7.47-7.49 (m, 12H, H-C_{Ar}). ^{13}C NMR (100 MHz, $CDCl_3$, δ): 20.69 (CH_3), 58.83 (CH), 117.32(C_{NHC}), 126.70 (C_{Ar}), 128.07 (C_{Ar}), 128.71 (C_{Ar}), 140.09 (C_{Ar}), 140.42 (C_{Ar}), 165.38(NHC), 193.72 (C_{NHC}, C-Au). HRMS (ESI) m/z: $[M+H]^+$ calcd for $[C_{44}H_{45}Au_2N_4]^+$: 1023.2970, Found: 1023.2960. Elem. Anal. Calcd for $C_{44}H_{44}Au_2N_4$, C, 51.67; H, 4.34; N, 5.48. Found: C, 51.33; H, 4.24; N, 5.30.

6-*S*

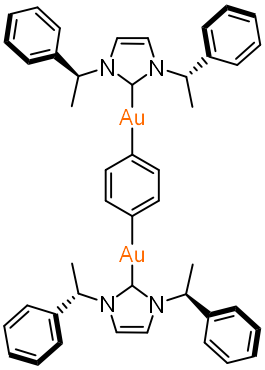

Yield: 76%, 23 mg, white solid. ^{1}H NMR (400 MHz, $CDCl_3$, δ): 1.84 (d, *J* = 7.2 Hz, 12H, CH_3), 6.41 (q, *J* = 6.8 Hz, 4H, CH), 6.79 (s, 4H, NHC), H-C_{Ar}), 7.30-7.38 (m, 12H, H-C_{Ar}), 7.47-7.49 (m, 12H, H-C_{Ar}). ^{13}C NMR (100 MHz, $CDCl_3$, δ): 20.70 (CH_3), 58.84 (CH), 117.32 (C_{NHC}), 126.70 (C_{Ar}), 128.07 (C_{Ar}), 128.71 (C_{Ar}), 140.09 (C_{Ar}), 140.42 (C_{Ar}), 165.38 (NHC), 193.78 (C_{NHC}, C-Au). HRMS (ESI) m/z: $[M+H]^+$ calcd for $[C_{44}H_{45}Au_2N_4]^+$: 1023.2970, Found: 1023.2960. Elem. Anal. Calcd for $C_{44}H_{44}Au_2N_4$, C, 51.67; H, 4.34; N, 5.48. Found: C, 51.14; H, 4.21; N, 5.28.

6-*R*-***d*₄**

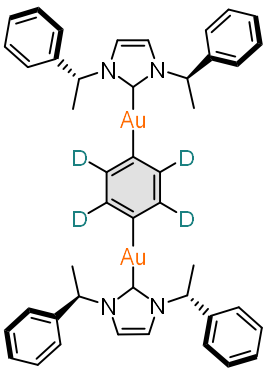

Yield: 70%, 20 mg, white solid. ^{1}H NMR (400 MHz, $CDCl_3$, δ): 1.84 (d, *J* = 7.6 Hz, 12H, CH_3), 6.41 (q, *J* = 7.6 Hz, 4H, CH), 6.79 (s, 4H, NHC), H-C_{Ar}), 7.28-7.28 (m, 12H, H-C_{Ar}), 7.49-7.47 (m, 8H, H-C_{Ar}), 7.50 (m, 4D/H). ^{13}C NMR (100 MHz, $CDCl_3$, δ): 20.70 (CH_3), 58.84 (CH), 117.32 (C_{NHC}), 126.70 (C_{Ar}), 128.07 (C_{Ar}), 128.72 (C_{Ar}), 139.84-140.25 (m, C-H/D), 140.42 (C_{Ar}), 165.02 (NHC), 193.78 (C_{NHC}, C-Au). HRMS (ESI) m/z: $[M+H]^+$ calcd for $[C_{44}H_{41}D_4Au_2N_4]^+$: 1027.3221, Found:

1027.3192. Elem. Anal. Calcd for $C_{44}H_{40}D_4Au_2N_4$, C, 51.47; H/D, 4.71; N, 5.46. Found: C, 51.37; H, 4.27 (H+D = 3.87+0.77 = 4.64)[49]; N, 5.25.

6-*R*-***d*$_{20}$**

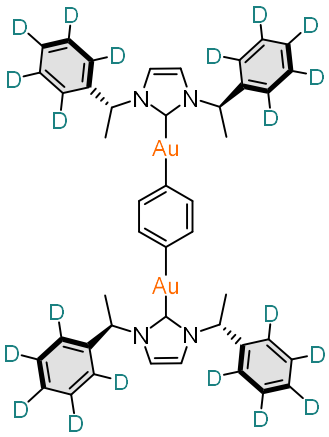

Yield: 73%, 23 mg, white solid. ^{1}H NMR (400 MHz, $CDCl_3$, δ): 1.84 (d, *J* = 7.2 Hz, 12H, CH_3), 6.41 (q, *J* = 6.8 Hz, 4H, CH), 6.79 (s, 4H, NHC), H-C_{Ar}), 7.49 (s, 4H, H-C_{Ar}). ^{13}C NMR (100 MHz, $CDCl_3$, δ): 20.71 (CH_3), 58.78 (CH), 117.32 (C_{NHC}), 140.09 (C_{Ar}), 165.39 (NHC), 193.77 (C_{NHC}, C-Au). HRMS (ESI) m/z: $[M+H]^+$ calcd for $[C_{44}H_{25}D_{20}Au_2N_4]^+$: 1043.4226, Found: 1043.4209. Elem. Anal. Calcd for $C_{44}H_{24}D_{20}Au_2N_4$, C, 50.67; H/D, 6.18; N, 5.37. Found: C, 50.71; H, 4.22 (H+D = 2.27+3.68 = 5.95)[49]; N, 5.17.

4.4.3 Single-Crystal X-ray Diffraction Analysis

Single-crystal X-ray diffraction (SCXRD) analyses were carried out on a Rigaku XtaLAB Synergy diffractometer using graphite monochromated Cu-Kα radiation. The structures were solved with the SHELXT structure solution program using Intrinsic Phasing incorporated in the OLEX2 program package[51] and refined with the SHELXL package[52] and olex2.refine refinement package[63] using Levenberg-Marquardt minimization. Hydrogen atoms were refined using the riding model.

The crystal data parameters are given in **Tables S4.1–S4.4**, geometrical parameters are given in **Table S4.5**, while the crystal structure views of complexes are shown in **Figures S4.1**

Table S4.1. Crystal and structure refinement data for chiral binuclear NHC Au(I) complexes.

Identification code	6-R_213K	6-R_233K	6-R_253K	6-R_273K
CCDC code				
Empirical formula	$C_{44}H_{44}Au_2N_4$	$C_{44}H_{44}Au_2N_4$	$C_{44}H_{44}Au_2N_4$	$C_{44}H_{44}Au_2N_4$
Formula weight	1022.8	1022.8	1022.8	1022.8
Temperature/K	213	233	253	273
Crystal system	tetragonal	tetragonal	tetragonal	tetragonal
Space group	$P4_32_12$	$P4_32_12$	$P4_32_12$	$P4_32_12$
a/Å	18.5675(2)	18.5700(4)	18.5890(1)	18.6000(1)
b/Å	18.5675(2)	18.5700(4)	18.5890(1)	18.6000(1)
c/Å	11.1978(2)	11.2226(5)	11.2385(2)	11.2575(2)
α/°	90	90	90	90
β/°	90	90	90	90
γ/°	90	90	90	90
Volume/Å^3	3860.46(9)	3870.1(2)	3883.47(8)	3894.64(8)
Z	4	4	4	4
ρ_{calc}g/cm^3	1.76	1.755	1.749	1.744
μ/mm^{-1}	14.345	14.31	14.26	14.219
F(000)	1951	1951	1951	1951
Crystal size/mm^3	0.2 × 0.02 × 0.02	0.2 × 0.02 × 0.02	0.2 × 0.02 × 0.02	0.2 × 0.02 × 0.02
Radiation	Cu Kα (λ = 1.54184)	Cu Kα (λ = 1.54184)	Cu Kα (λ = 1.54184)	Cu Kα (λ = 1.54184)
2Θ range for data collection/°	6.74 to 153.24	6.74 to 153.16	10.64 to 152.58	6.72 to 153.28
Index ranges	-18 ≤ h ≤ 23, -22 ≤ k ≤ 22, -13 ≤ l ≤ 13	-23 ≤ h ≤ 22, -23 ≤ k ≤ 19, -13 ≤ l ≤ 13	-22 ≤ h ≤ 23, -21 ≤ k ≤ 22, -13 ≤ l ≤ 13	-23 ≤ h ≤ 19, -22 ≤ k ≤ 22, -13 ≤ l ≤ 14
Reflections collected	42505	42404	40140	41927
Independent reflections	3991 [R_{int} = 0.0417, R_{sigma} = 0.0168]	3993 [R_{int} = 0.0421, R_{sigma} = 0.0171]	4001 [R_{int} = 0.0381, R_{sigma} = 0.0159]	4015 [R_{int} = 0.0367, R_{sigma} = 0.0159]
Data/restraints/parameters	3991/36/245	3993/120/233	4001/102/233	4015/102/249
Goodness-of-fit on F^2	1.096	1.033	0.991	1.057
Final R indexes [I>=2σ (I)]	R_1 = 0.0383, wR_2 = 0.0875	R_1 = 0.0409, wR_2 = 0.1069	R_1 = 0.0334, wR_2 = 0.0855	R_1 = 0.0304, wR_2 = 0.0749
Final R indexes [all data]	R_1 = 0.0471, wR_2 = 0.0921	R_1 = 0.0496, wR_2 = 0.1133	R_1 = 0.0392, wR_2 = 0.0896	R_1 = 0.0347, wR_2 = 0.0776
Largest diff. peak/hole / e Å^{-3}	0.76/-0.29	0.54/-0.43	0.45/-0.34	0.58/-0.27
Flack parameter	-0.012(5)	-0.006(6)	-0.027(5)	-0.028(5)

Table S4.2. Crystal and structure refinement data for chiral binuclear NHC Au(I) complexes.

Identification code	6-R_293K	6-R_313K	6-R_333K	6-S_213K
CCDC code				
Empirical formula	$C_{44}H_{44}Au_2N_4$	$C_{44}H_{44}Au_2N_4$	$C_{44}H_{44}Au_2N_4$	$C_{44}H_{44}Au_2N_4$
Formula weight	1022.8	1022.8	1022.8	1022.8
Temperature/K	293	313	333	213
Crystal system	tetragonal	tetragonal	tetragonal	tetragonal
Space group	$P4_32_12$	$P4_12_12$	$P4_32_12$	$P4_12_12$
a/Å	18.6082(1)	18.6427(3)	18.6331(2)	18.55247(15)
b/Å	18.6082(1)	18.6427(3)	18.6331(2)	18.55247(15)
c/Å	11.2810(1)	11.3023(4)	11.3266(2)	11.20668(16)
α/°	90	90	90	90
β/°	90	90	90	90
γ/°	90	90	90	90
Volume/Å^3	3906.22(5)	3928.12(17)	3932.51(9)	3857.27(7)
Z	4	4	4	4
ρ_{calc}g/cm^3	1.739	1.729	1.728	1.761
μ/mm^{-1}	14.177	14.098	14.082	14.357
F(000)	1951	1951	1951	1951
Crystal size/mm^3	0.2 × 0.02 × 0.02	0.2 × 0.02 × 0.02	0.2 × 0.02 × 0.02	0.2 × 0.02 × 0.02
Radiation	Cu Kα (λ = 1.54184)	Cu Kα (λ = 1.54184)	Cu Kα (λ = 1.54184)	Cu Kα (λ = 1.54184)
2Θ range for data collection/°	10.64 to 153.5	6.7 to 145.48	6.7 to 145.8	6.74 to 152.74
Index ranges	-18 ≤ h ≤ 23, -22 ≤ k ≤ 22, -14 ≤ l ≤ 13	-23 ≤ h ≤ 23, -22 ≤ k ≤ 22, -13 ≤ l ≤ 13	-23 ≤ h ≤ 22, -23 ≤ k ≤ 21, -13 ≤ l ≤ 13	-23 ≤ h ≤ 23, -23 ≤ k ≤ 23, -12 ≤ l ≤ 13
Reflections collected	45729	35795	35727	43083
Independent reflections	4038 [R_{int} = 0.0399, R_{sigma} = 0.0169]	3762 [R_{int} = 0.0472, R_{sigma} = 0.0208]	3742 [R_{int} = 0.0387, R_{sigma} = 0.0185]	3958 [R_{int} = 0.0540, R_{sigma} = 0.0177]
Data/restraints/parameters	4038/54/220	3762/91/233	3742/66/219	3958/103/217
Goodness-of-fit on F^2	1.053	1.021	1.034	1.028
Final R indexes [I>=2σ (I)]	R_1 = 0.0356, wR_2 = 0.0880	R_1 = 0.0347, wR_2 = 0.0899	R_1 = 0.0274, wR_2 = 0.0686	R_1 = 0.0629, wR_2 = 0.1375
Final R indexes [all data]	R_1 = 0.0395, wR_2 = 0.0905	R_1 = 0.0556, wR_2 = 0.1056	R_1 = 0.0340, wR_2 = 0.0725	R_1 = 0.0639, wR_2 = 0.1380
Largest diff. peak/hole / e Å^{-3}	0.96/-0.68	0.63/-0.35	0.45/-0.57	1.16/-1.29
Flack parameter	-0.021(5)	-0.015(6)	-0.034(6)	0.015(5)

Table S4.3. Crystal and structure refinement data for chiral binuclear NHC Au(I) complexes.

Identification code	6-S_233K	6-S_253K	6-S_273K	6-S_293K
CCDC code				
Empirical formula	$C_{44}H_{44}Au_2N_4$	$C_{44}H_{44}Au_2N_4$	$C_{44}H_{44}Au_2N_4$	$C_{44}H_{44}Au_2N_4$
Formula weight	1022.8	1022.8	1022.8	1022.8
Temperature/K	233	253	273	293
Crystal system	tetragonal	tetragonal	tetragonal	tetragonal
Space group	$P4_12_12$	$P4_12_12$	$P4_12_12$	$P4_12_12$
a/Å	18.5617(2)	18.5736(3)	18.6002(3)	18.6107(2)
b/Å	18.5617(2)	18.5736(3)	18.6002(3)	18.6107(2)
c/Å	11.2234(2)	11.2444(3)	11.2722(3)	11.2909(3)
α/°	90	90	90	90
β/°	90	90	90	90
γ/°	90	90	90	90
Volume/Å^3	3866.87(9)	3879.08(14)	3899.81(14)	3910.70(12)
Z	4	4	4	4
ρ_{calc}g/cm^3	1.757	1.751	1.742	1.737
μ/mm^{-1}	14.322	14.276	14.201	14.161
F(000)	1951	1951	1951	1951
Crystal size/mm^3	0.2 × 0.02 × 0.02	0.2 × 0.02 × 0.02	0.2 × 0.02 × 0.02	0.2 × 0.02 × 0.02
Radiation	Cu Kα (λ = 1.54184)	Cu Kα (λ = 1.54184)	Cu Kα (λ = 1.54184)	Cu Kα (λ = 1.54184)
2Θ range for data collection/°	6.74 to 152.94	6.74 to 152.64	6.72 to 152.68	6.72 to 153.4
Index ranges	-23 ≤ h ≤ 23, -23 ≤ k ≤ 23, -13 ≤ l ≤ 12	-23 ≤ h ≤ 23, -23 ≤ k ≤ 23, -13 ≤ l ≤ 13	-23 ≤ h ≤ 23, -23 ≤ k ≤ 23, -13 ≤ l ≤ 14	-23 ≤ h ≤ 23, -23 ≤ k ≤ 23, -14 ≤ l ≤ 13
Reflections collected	43196	40035	37351	42958
Independent reflections	3940 [R_{int} = 0.0507, R_{sigma} = 0.0186]	3988 [R_{int} = 0.0498, R_{sigma} = 0.0189]	3992 [R_{int} = 0.0475, R_{sigma} = 0.0189]	4033 [R_{int} = 0.0506, R_{sigma} = 0.0208]
Data/restraints/parameters	3940/90/233	3988/90/245	3992/90/233	4033/90/233
Goodness-of-fit on F^2	1.045	1.008	1.066	1.084
Final R indexes [I>=2σ (I)]	R_1 = 0.0480, wR_2 = 0.1190	R_1 = 0.0403, wR_2 = 0.1016	R_1 = 0.0367, wR_2 = 0.0889	R_1 = 0.0358, wR_2 = 0.0837
Final R indexes [all data]	R_1 = 0.0509, wR_2 = 0.1213	R_1 = 0.0450, wR_2 = 0.1053	R_1 = 0.0420, wR_2 = 0.0930	R_1 = 0.0421, wR_2 = 0.0873
Largest diff. peak/hole / e Å^{-3}	0.80/-0.76	0.87/-0.43	0.64/-0.37	0.53/-0.27
Flack parameter	0.018(6)	0.004(6)	-0.004(7)	-0.001(7)

Table S4.4. Crystal and structure refinement data for chiral binuclear NHC Au(I) complexes.

Identification code	6-S_313K	6-S_333K	6-R-d4_293K	6-R-d20_293K
CCDC code				
Empirical formula	$C_{44}H_{44}Au_2N_4$	$C_{44}H_{44}Au_2N_4$	$C_{44}H_{44}Au_2N_4$	$C_{44}H_{44}Au_2N_4$
Formula weight	1022.8	1022.8	1022.8	1022.8
Temperature/K	313	333	293	293
Crystal system	tetragonal	tetragonal	tetragonal	tetragonal
Space group	$P4_12_12$	$P4_12_12$	$P4_32_12$	$P4_32_12$
a/Å	18.6427(3)	18.6531(3)	18.6262(2)	18.63030(10)
b/Å	18.6427(3)	18.6531(3)	18.6262(2)	18.63030(10)
c/Å	11.3023(4)	11.3261(4)	11.3125(3)	11.30720(10)
α/°	90	90	90	90
β/°	90	90	90	90
γ/°	90	90	90	90
Volume/Å^3	3928.12(17)	3940.78(17)	3924.71(12)	3924.59(5)
Z	4	4	4	4
ρ_{calc}g/cm^3	1.729	1.724	1.731	1.731
μ/mm^{-1}	14.098	14.053	14.11	14.114
F(000)	1951	1951	1951	1976
Crystal size/mm^3	0.2 × 0.02 × 0.02	0.2 × 0.02 × 0.02	0.1 × 0.02 × 0.01	0.1 × 0.02 × 0.01
Radiation	Cu Kα (λ = 1.54184)	Cu Kα (λ = 1.54184)	Cu Kα (λ = 1.54184)	Cu Kα (λ = 1.54184)
2Θ range for data collection/°	6.7 to 145.48	6.7 to 145.72	6.72 to 152.92	6.71 to 152.864
Index ranges	-23 ≤ h ≤ 23, -22 ≤ k ≤ 22, -13 ≤ l ≤ 13	-22 ≤ h ≤ 23, -22 ≤ k ≤ 22, -13 ≤ l ≤ 13	-23 ≤ h ≤ 23, -20 ≤ k ≤ 19, -13 ≤ l ≤ 5	-23 ≤ h ≤ 23, -23 ≤ k ≤ 22, -14 ≤ l ≤ 14
Reflections collected	35795	35896	12559	26417
Independent reflections	3762 [R_{int} = 0.0472, R_{sigma} = 0.0208]	3805 [R_{int} = 0.0482, R_{sigma} = 0.0212]	3995 [R_{int} = 0.0296, R_{sigma} = 0.0279]	4069 [R_{int} = 0.0372, R_{sigma} = 0.0199]
Data/restraints/parameters	3762/91/233	3805/90/245	3995/42/233	4069/66/231
Goodness-of-fit on F^2	1.021	1.017	1.037	1.048
Final R indexes [I>=2σ (I)]	R_1 = 0.0347, wR_2 = 0.0899	R_1 = 0.0328, wR_2 = 0.0853	R_1 = 0.0320, wR_2 = 0.0778	R_1 = 0.0292, wR_2 = 0.0700
Final R indexes [all data]	R_1 = 0.0556, wR_2 = 0.1056	R_1 = 0.0519, wR_2 = 0.1003	R_1 = 0.0363, wR_2 = 0.0800	R_1 = 0.0330, wR_2 = 0.0721
Largest diff. peak/hole / e Å^{-3}	0.63/-0.35	0.59/-0.36	0.88/-0.34	0.84/-0.51
Flack parameter	-0.015(6)	-0.025(7)	-0.022(10)	-0.024(8)

Table S4.5. Selected geometrical parameters in crystal structures of chiral binuclear NHC Au(I) complexes at 333 K to 213 K: Au-C bond length with NHC and para-phenylene ligands, twist (θ) and fold (χ) angles between the planes of phenyl (Ph^a and Ph^b) and NHC fragments or para-phenylene (PP) and NHC fragments.

T/K	d(Au-C_{NHC})	d(Au-C_{PP})	φ_{Pha}	χ_{Pha}	φ_{Phb}	χ_{Phb}	φ_{PPa}	φ_{PPb}
6-*R*								
333	2.007(8)/2.029(6)	2.017(6)/2.035(6)	106.3(6)	118.4(10)	171.7(4)	108.4(5)	94.8(8)	2.2(5)
313	2.022(8)/2.047(6)	2.038(6)/2.026(6)	108.0(6)	118.4(9)	171.9(4)	109.0(4)	96.3(8)	2.8(5)
293	2.051(10)/2.048(8)	2.037(9)/2.041(8)	105.3(10)	116.2(15)	171.9(5)	109.3(6)	98.1(11)	3.2(6)
273	2.049(6)/2.054(4)	2.054(6)/2.050(4)	105.3(7)	117.3(10)	172(4)	108.5(4)	96.3(8)	1.9(5)
253	2.057(6)/2.058(6)	2.049(8)/2.051(6)	106.8(7)	117.0(11)	171.7(4)	108.4(5)	97.0(9)	1.8(6)
233	2.032(9)/2.066(6)	2.052(9)/2.055(6)	108.5(8)	118.9(14)	171.8(5)	107.9(6)	95.1(11)	1.8(7)
213	2.004(8)/2.041(6)	2.042(8)/2.053(6)	102.2(10)	118.8(15)	172.3(5)	109.5(6)	95.4(11)	2.3(6)
6-*S*								
333	2.025(9)/2.034(8)	2.048(8)/2.031(8)	108.0(8)	117.0(22)	172.5(5)	108.1(6)	97.3(10)	2.8(7)
313	1.997(11)/2.017(8)	2.047(9)/2.035(8)	105.8(10)	117.3(15)	173.0(5)	107.9(7)	97.6(12)	2.7(8)
293	2.016(8)/2.041(6)	2.058(6)/2.042(6)	104.7(8)	117.3(13)	172.9(4)	108.1(5)	96.8(10)	2.1(6)
273	2.035(9)/2.052(6)	2.055(8)/2.055(8)	105.8(9)	117.5(14)	172.4(5)	107.9(6)	96.6(11)	1.7(6)
253	2.056(9)/2.049(8)	2.053(9)/2.054(8)	107.6(9)	118.0(15)	171.2(5)	108.8(6)	96.5(12)	2.3(7)
233	2.064(11)/2.055(8)	2.057(9)/2.061(8)	109.9(10)	118.6(16)	170.9(6)	107.0(7)	96.6(13)	1.8(8)
213	2.050(15)/2.041(9)	2.051(17)/2.070(11)	108.7(10)	119.0(2)	171.2(7)	107.6(9)	94.8(16)	1.9(11)

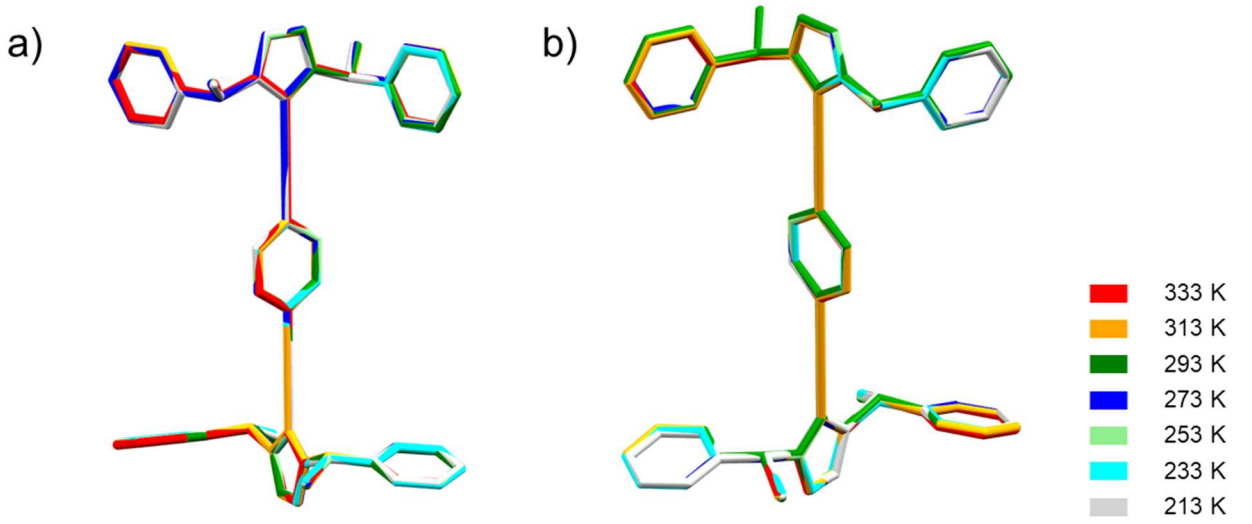

Figure S4.1. Superposition of the crystal structure of **6**-*R* (a) and **6**-*S* (b) obtained at 333 K to 213 K.

Table S4.6. Unit cell and crystal parameters of for chiral binuclear NHC Au(I) complexes at 333 K to 213 K.

T / K	a/b, Å	c, Å	Volume, Å^3	ρ, g/cm^3	Packing coefficient
6-*R*					
333	18.6331	11.3266	3932.51	1.728	0.632
313	18.6154	11.3009	3916.14	1.735	0.637
293	18.6082	11.2810	3906.22	1.739	0.638
273	18.6000	11.2575	3894.64	1.744	0.638
253	18.5890	11.2385	3883.47	1.749	0.643
233	18.5700	11.2226	3870.1	1.755	0.644
213	18.5675	11.1978	3860.46	1.76	0.643
6-*S*					
333	18.6531	11.3261	3940.78	1.724	0.629
313	18.6427	11.3023	3928.12	1.729	0.634
293	18.6107	11.2909	3910.7	1.737	0.636
273	18.6002	11.2722	3899.81	1.742	0.639
253	18.5736	11.2444	3879.08	1.751	0.642
233	18.5617	11.2234	3866.87	1.757	0.646
213	18.5525	11.2067	3857.27	1.761	0.647

4.4.4 Powder X-Ray Diffraction Analysis

Powder X-ray diffraction (PXRD) data of the grinded crystalline samples were collected on a Rigaku SmartLab diffractometer with Cu-Kα radiation and D/teX Ultra detector covering a 5-50° (2θ) range at room temperature. Simulated powder patterns were generated with Mercury 2022.2.0 (Build 353591)[54] from the structures determined by the single-crystal X-ray diffraction analyses at 293K (**Figures S4.2**)

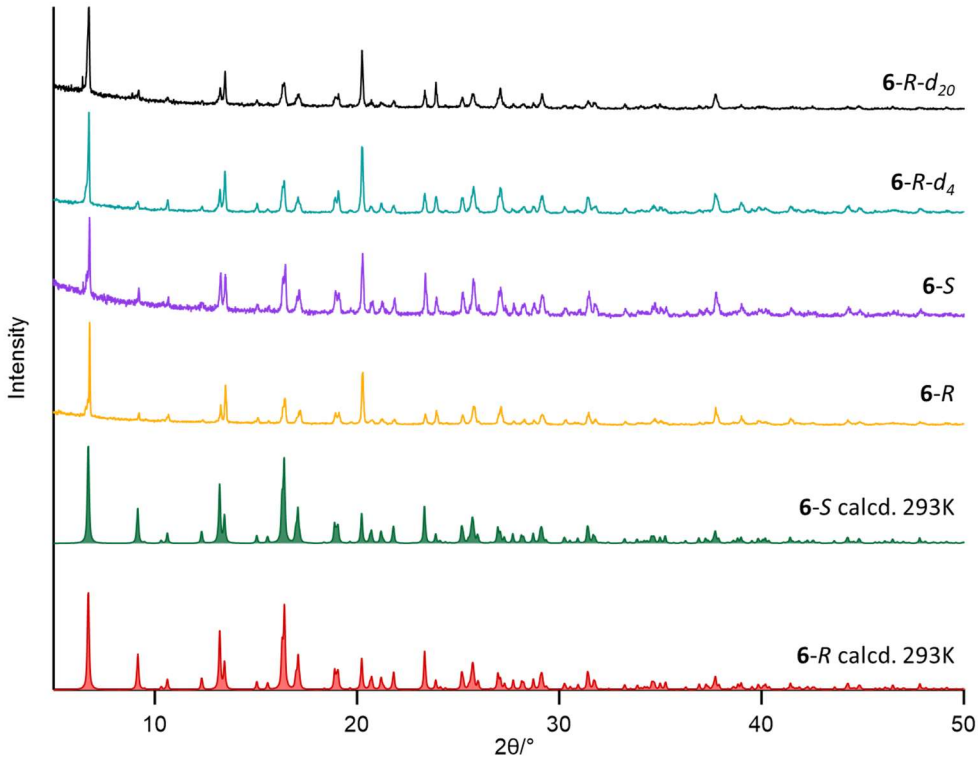

Figure S4.2 Experimental and simulated PXRD patterns.

4.4.5 TGA and DSC data

TGA profiles of the crystalline samples were recorded on a Rigaku TG-DTA8122/S using a heating rate of 20 °C/min. DSC profiles of the crystalline samples were measured on a HITACHI DSC7020 using a heating rate of 5 °C/min. The TGA results indicated that weight loss due to the decomposition of the complexes occurs only above ~260°C (**Figure S4.1a**). Concurrently, the DSC measurements showed no significant peaks, indicating that the crystals have no thermally triggered phase transitions (**Figure S4.1b**).

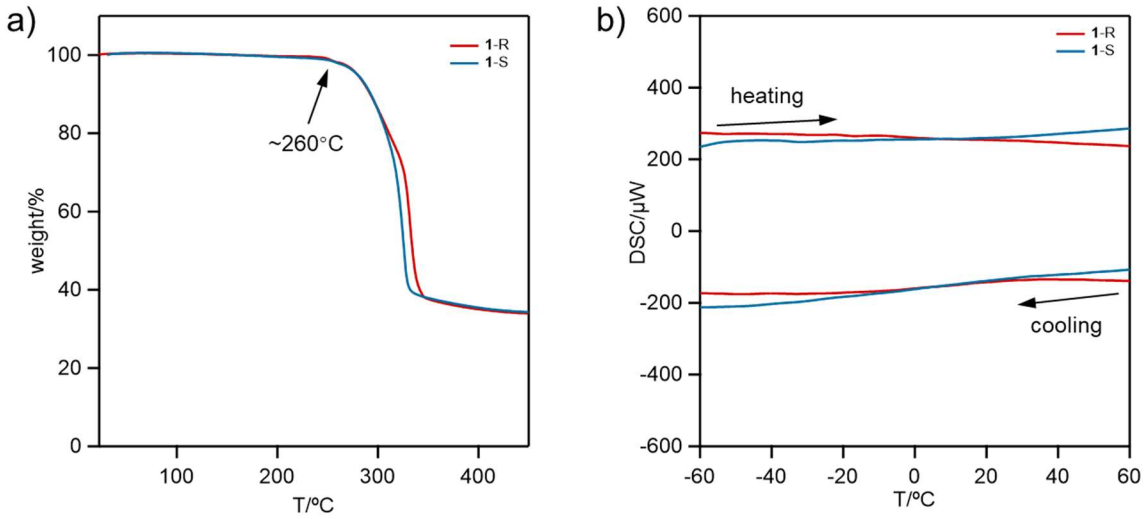

Figure S4.3. a) TGA profiles of crystalline sample of **6**-*R* and **6**-*S*; b) DSC profiles of crystalline sample of **6**-*R* and **6**-*S*.

4.4.6 Solid-state NMR Study

The solid-state ^{2}H NMR (SS ^{2}H NMR) spin-echo experiments in this work were performed on a Bruker AVANCE NEO 500 MHz instrument at a ^{2}H frequency of 76.77 MHz (deuterium resonance frequency) and 90-degree pulse of 2.8 µs. For suppression of the undesired artifacts, a quadrupolar-echo sequence with phase recycling was used. An echo delay of 30 µs was used, and the recycle delay between pulses was 20 s. About 20 mg of crystal sample was placed in a ZrO_2 NMR sample tube for each experiment. 800 scans were used to acquire each spectrum. All spectra in this work were obtained using a line broadening of 4.0 kHz in the data processing. All simulation was performed utilizing the online program offered by H. W. Spiess.[55]

The crystalline sample of **6**-*R*-d_4 was measured at 295 and 333K using long recycle delays between pulses (d_1) of 20 sec (**Figure S4.4**). The obtained spectra do not show significant changes of line-shape with the temperature elevation, but still do not quite fit for the static motion (**Figure S4.4a**). The reasonable matching was found for model with a low frequency (10–20 kHz) 2-fold 120° flipping motion (**Figure S4.4b**) and using a quadrupolar coupling constant (QCC) of 176 kHz, an asymmetry factor (η_0) of 0.05, a cone angle of 60° formed between the rotational axis and C-D bond vector, and log-Gaussian distribution with 3.0 decades full width at half maximum (FWHM) of the flipping rates (**Figure S4.4c**).

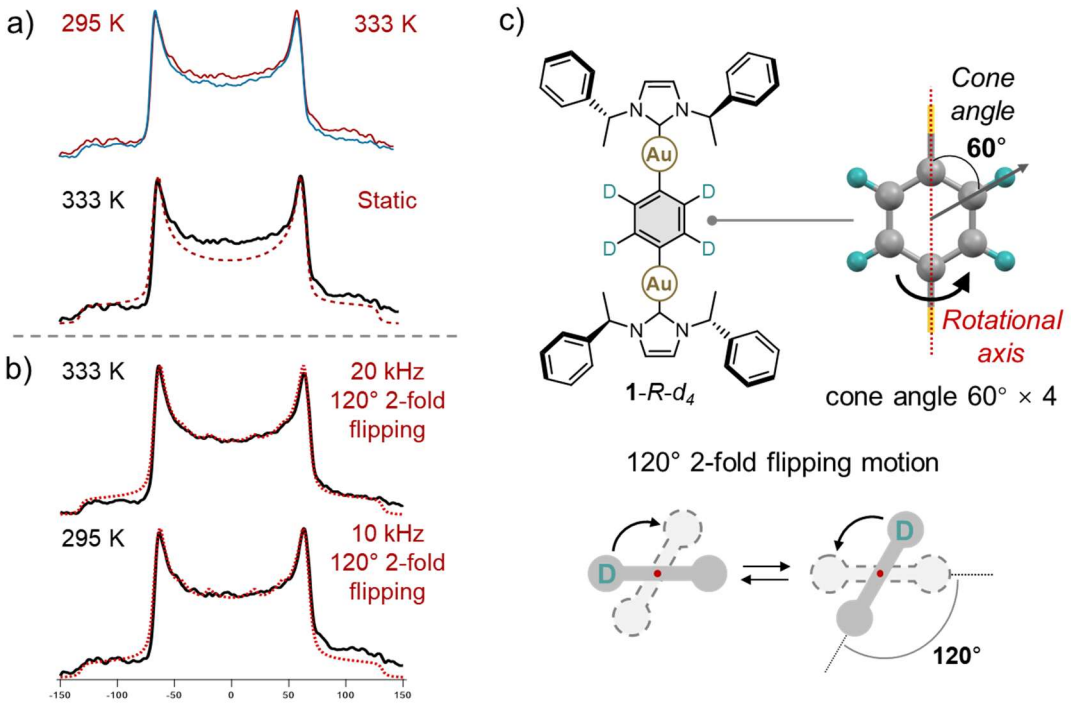

Figure S4.4. Variable-temperature solid-state ^{2}H spin-echo NMR study of **6**-*R*-d_4: a) Comparison between ^{2}H spin-echo NMR spectra of **6**-*R*-$d_4$at different temperatures and the simulated static motion; b) Experimental (black) and simulated (red) ^{2}H spin-echo NMR spectra of **6**-*R*-d_4; c) Structure of **6**-*R*-$d_4$and the cone angles experienced by the C−D bonds of *PP*-d_4 and illustration of the 120° 2-fold flipping motion experiencing by the *PP*-d_4 moiety.

The experimental SS ^{2}H NMR spin-echo spectra of **6**-*R*-d_{20} obtained using different recycle delays between pulses (d_1) indicate a strong dependence of the ^{2}H NMR line shape on the delay time (**Figure S4.5**). This suggests the presence of deuterium atoms with noticeably different spin-lattice relaxation times (T_1), caused by the presence of both mobile and static deuterium atoms or even a combination of noticeably different types/rates of motions of deuterated Ph moieties. The SCXRD data also indicate that the Ph moieties (Ph^a and Ph^b) are non-equivalent in the crystal structure and experience different crystal packing, suggesting the presence of two types of thermal motion. Notably, there is a significant difference between the spectra recorded with delay times of 1 sec and 5 sec, while there is little difference between the spectra recorded with delay times of 5 sec and 20 sec. Therefore, we may

consider the spectra recorded with a delay time of 1 sec as partially relaxed, while those recorded with a d1 of 20 sec are fully relaxed.

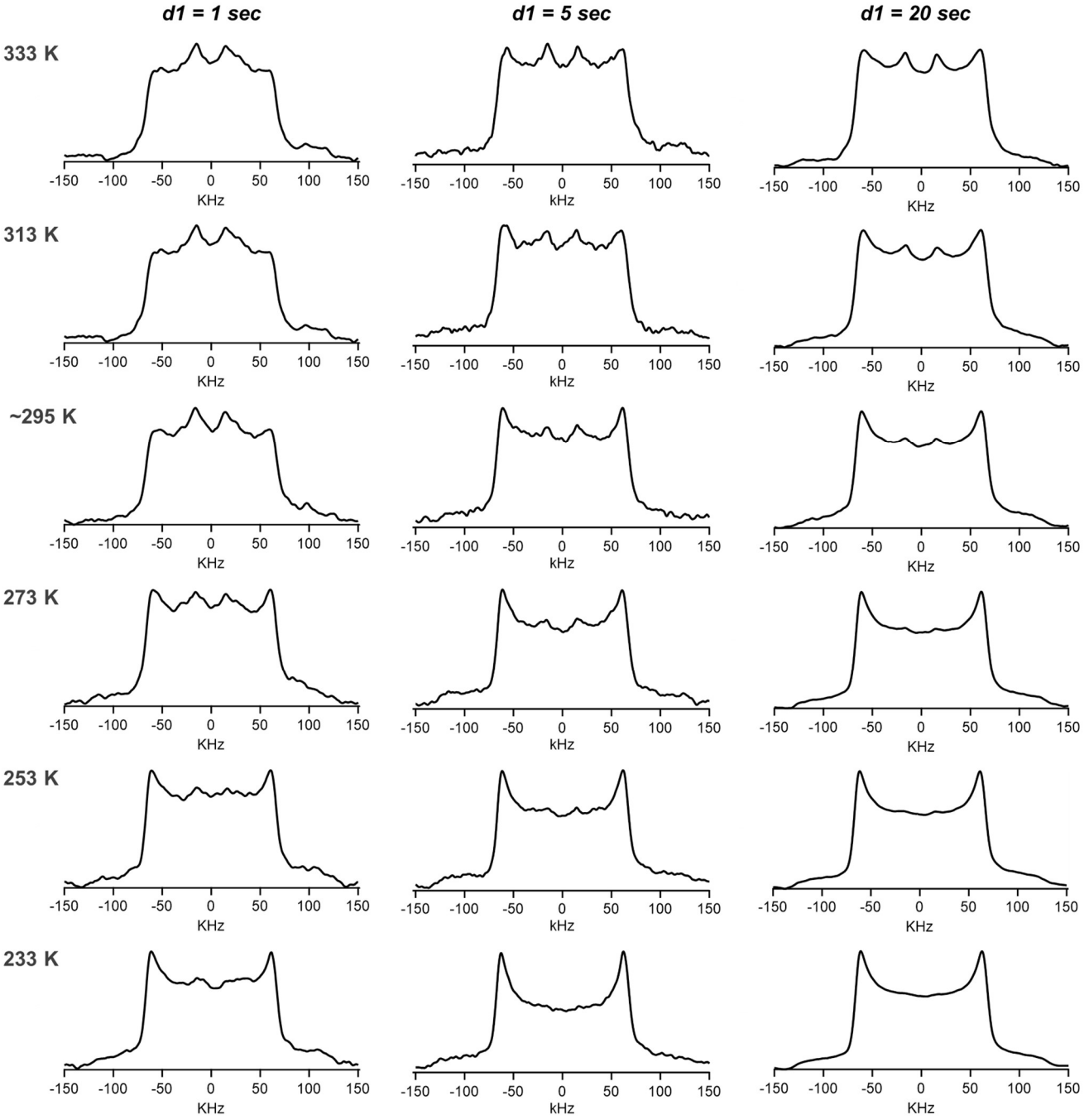

Figure S4.5. Experimental variable-temperature solid-state ^{2}H spin-echo NMR spectra of **6**-*R*-d_{20} recorded using recycle delays between pulses (d_1) of 1, 5, and 20 sec.

It should be noted that in this case, the Ph-d_5 moieties contain two different types of deuterium atoms contributing to the ^{2}H NMR spectra in course of the jumping motion along the 1,4-rotational axis: two pairs of deuterium atoms at *ortho*- and *meta*- positions (cone angle = ±60°) and one deuterium atom at the *para*-position (cone angle = 0°; **Figure S4.6**). In the second case, para-deuterium atom should appear as static and not affect the line shape with temperature change. However, the experimental VT ^{2}H NMR spin-echo patterns obtained with a delay time of 20 sec could not be adequately fitted using a single dynamics mode for all Ph-d_5 moieties – only by combination the patterns with cone angles ±60° x 4 and 0° x 1 with the unified motion frequency. Similarly, accounting for half of the Ph-d_5 moieties as mobile and the other half as static also did not lead to patterns matching the experimental data. Based on these premises, we used two types of motion in the ^{2}H NMR simulations: a faster 180° 2-fold jumping and a slower 90° 4-fold motion. For 2-fold motion simulation, a quadrupolar coupling constant (QCC) of 171 kHz, and 180° Brownian jump were used. For 4-fold motion simulation, a QCC of 173 kHz, an asymmetry factor (η_0) of 0.1 and 90° Brownian jump, and 4:1:4:1 population were used. At temperatures below 293K the 4-fold motion was simulated as static (rigid = 100%). Additionally, the simulations of both 2-fold and 4-fold motions required to apply a log-Gaussian distribution with 3.0 decades full width at half maximum (FWHM) of the rotational jumping rates. The obtained simulated models fit well the experimental patterns (**Figure S4.6**) as well as their rotation frequencies of both types of motions in **6**-*R*-d_{20} correlate well with temperature on Arrhenius and Eyring plots.

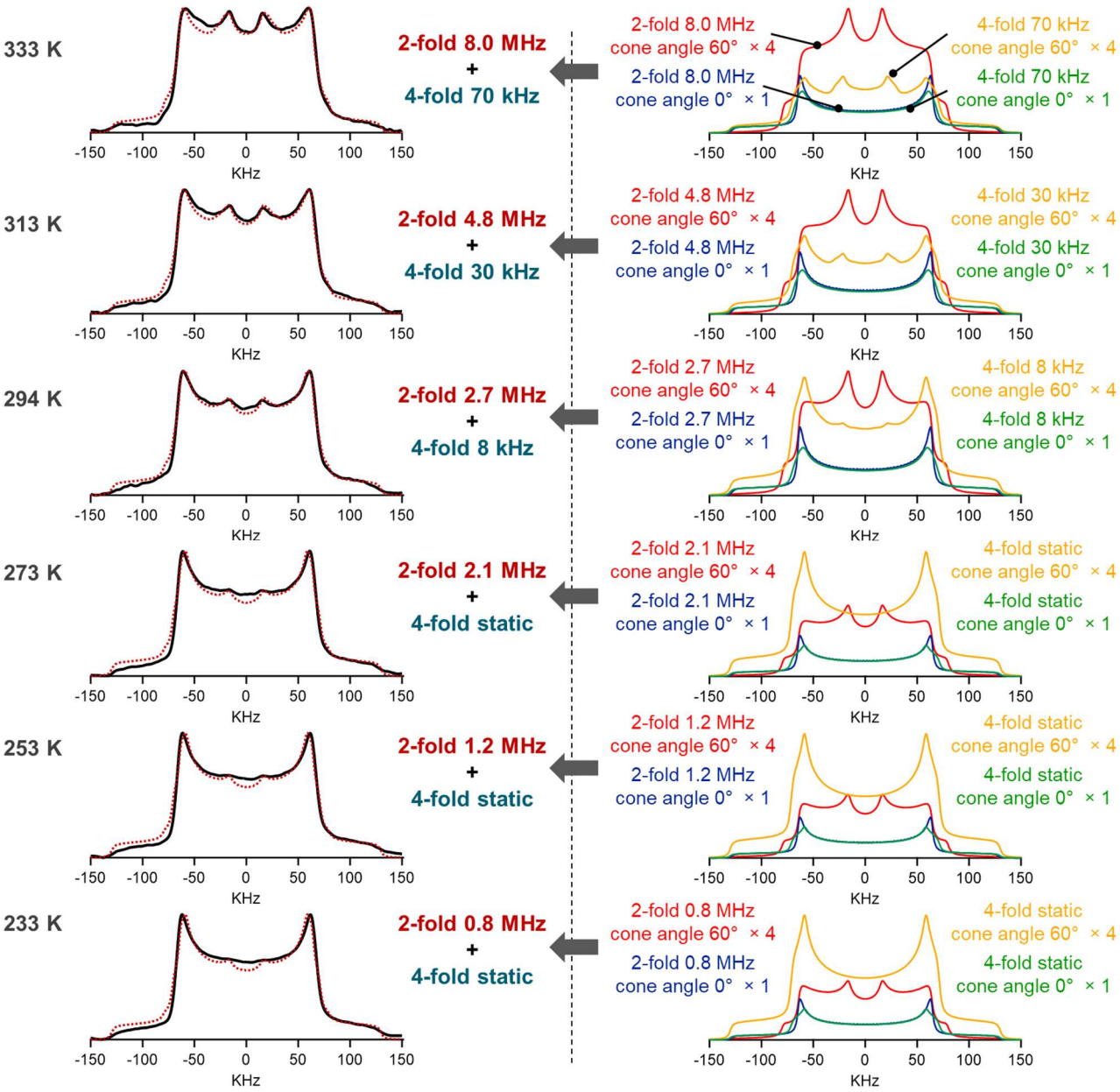

Figure S4.6. Line shape analysis of ^{2}H spin-echo SS NMR of crystal **6**-*R*-d_{20} measured in 233 - 333 K range using recycle delays between pulses (d_1) of 20 sec and their simulation models.

Previously, in a ^{2}H NMR study of the motion of *Ph*-d_5 substituents in polystyrene in the glassy state by H. W. Spiess, it was indicated that the separate observation of mobile and rigid fractions of Ph-d_5 may be possible through T_1 discrimination. This discrimination is feasible if the mobile moieties are spatially distinct from the rigid ones.

Considering the dependence of the ^{2}H NMR spectrum line shape on d_1 time, as well as the presence of static 4-fold motion of Ph groups below 293 K in the simulated model, we attempted to simulate the line shapes for ^{2}H NMR spectra obtained with d_1 = 1 sec. In this case, we applied the same parameters and motion frequencies as for the 2-fold motion model used in the simulations of spectra with d_1 = 20 sec. These parameters included deuterium atoms with four 60° and one 0° cone angles, a quadrupolar coupling constant (QCC) of 171 kHz, and a 180° Brownian jump, using a log-Gaussian distribution with 3.0 decades FWHM of the rotational jumping rates. However, we did not account for the slow or static 4-fold motion, considering it silent at lower temperatures and short d_1.

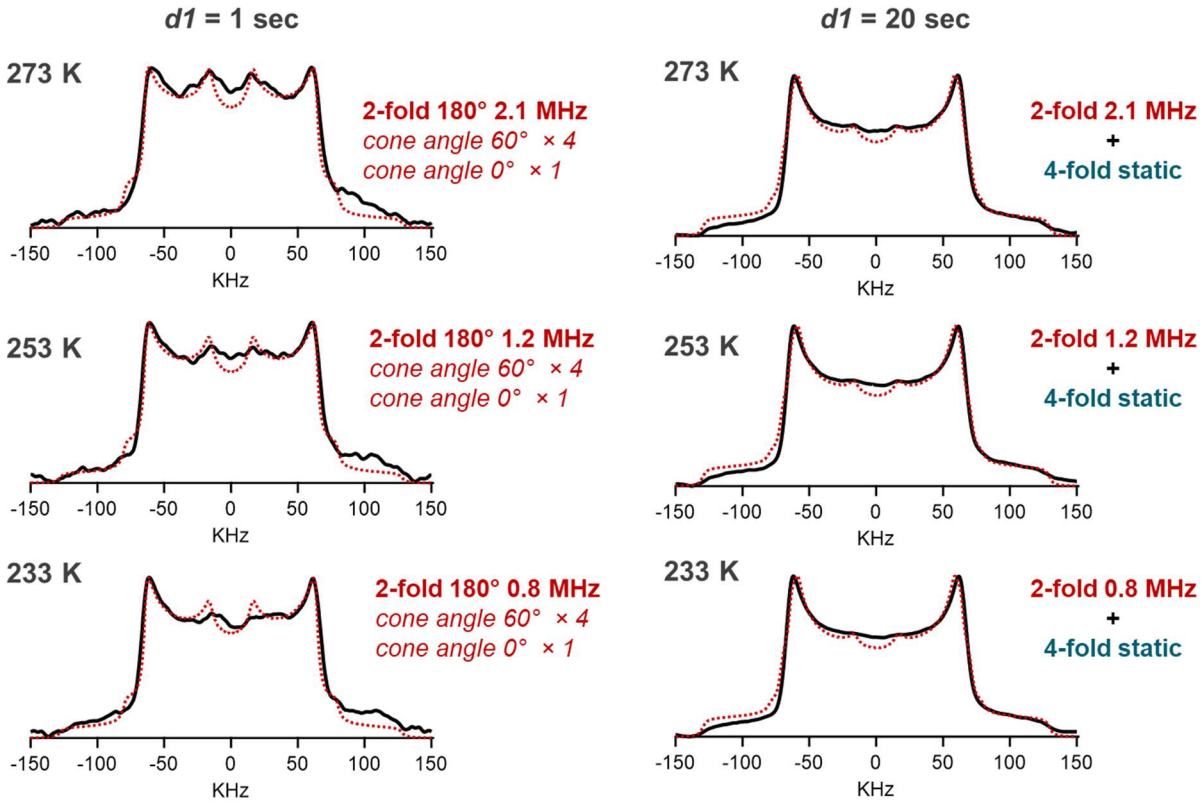

Figure S4.7. Line shape analysis of ^{2}H spin-echo SS NMR of crystal **6**-*R*-d_{20} measured in 233 –273 K range using recycle delays between pulses (d_1) of 1 and 20 sec, and their simulation models.

The obtained simulated line shapes adequately fit the experimental patterns observed in the 233 – 273 K temperature range, where half of the Ph-d_5 groups are

considered static according to the simulation model for ^{2}H NMR spectra with d_1 = 20 sec (**Figure S4.7**). However, applying the same model to simulate ^{2}H NMR spectra with d_1 = 1 sec above 273 K does not work due to significant underestimation of the rotation frequency. This may indicate the rapid onset of an additional type of motion, such as the 4-fold motion used in the simulations of ^{2}H NMR spectra with d1 = 20 sec, at higher temperatures.

4.4.7 Chiroptical and Photophysical Study

UV-Vis Absorption (Abs) and Circular Dichroism (CD)

UV-Vis absorption (Abs) and diffuse reflection spectra were measured on a JASCO V-770 at room temperature. Circular dichroism (CD) spectra were measured on a JASCO J-1500 Circular Dichroism Spectrophotometer. A 10 mm cell was used for solution samples. For solid-state measurements, diffuse reflection was conducted with crystalline samples, and CD measurements were performed using the Nujol mull method.[56] For CD measurements, both solution and solid samples were record with a 2-second D.I.T., a 1.0 nm bandwidth, a scanning speed of 200 nm/min, and 2 accumulations with Auto HT voltage settings. Variable-temperature (VT) CD spectra were obtained using a UNISOKU CoolSpeK CD: USP-203CD-B as a cryosystem, which employs liquid nitrogen for cooling. All data underwent background subtraction, and the absorption dissymmetry factor (g_{abs}) was calculated using JASCO Spectra Manager software.

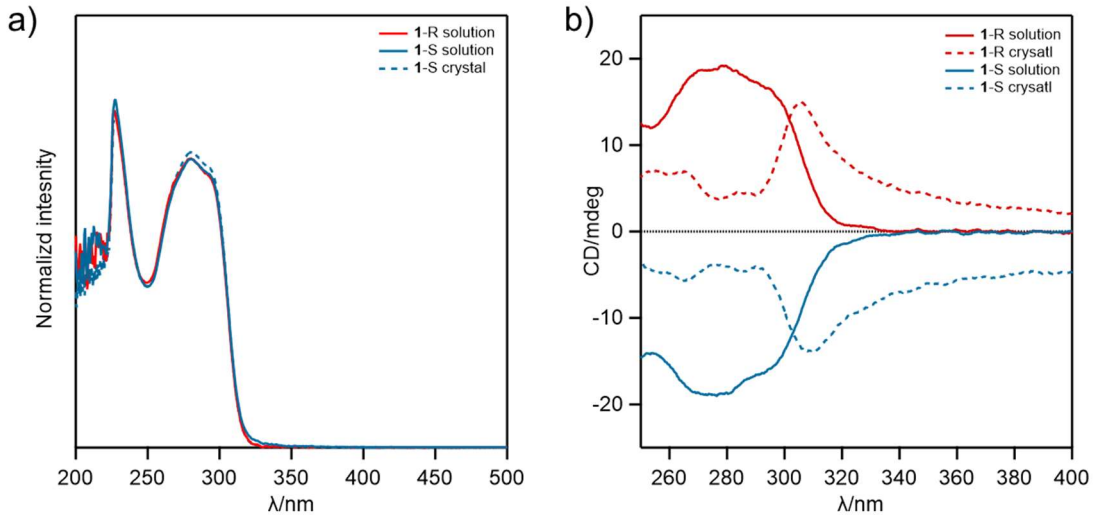

Figure S4.8. a) UV-vis absorption spectra of **6**-*R* and **6**-*S* in CH_2Cl_2 solution (2.5 x 10^{-5} mol/L) and diffuse reflection **6**-*R* in solid state (crystal) at room temperature; b) CD spectra of **6**-*R* and **6**-*S* in CH_2Cl_2 solution (2.5 x 10^{-5} mol/L) and in solid state (Nujol mull method, 5 % *w*/*w* in paraffin oil) at room temperature.

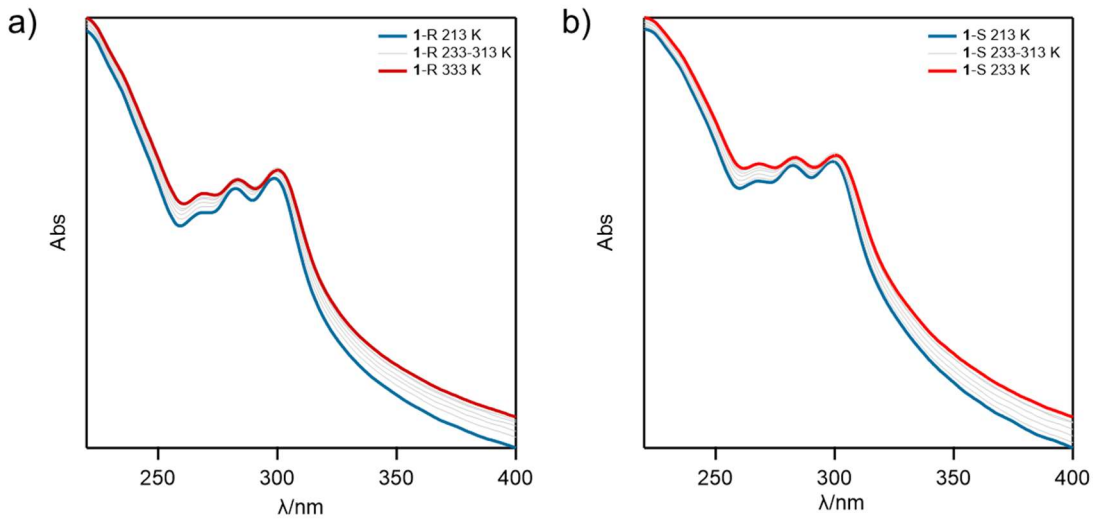

Figure S4.9 VT-Abs spectra of (a) **6**-*R* and (b) **6**-*S in* solid state (Nujol mull method, 5 % *w*/*w* in paraffin oil, measured by JASCO J-1500) from 213 K to 333 K.

Table S4.7 Selected VT-CD data for **6**-*R* and **6**-*S*.

	6-*R*			**6**-*S*		
T/K	CD at 280nm, mdeg	$CD_{max,}$ nm	$CD_{max,}$ mdeg	CD at 280nm, mdeg	$CD_{max,}$ nm	$CD_{max,}$ mdeg
213	8.15	304.3	16.66	-5.93	307.0	-15.42
233	7.43	304.3	16.13	-5.60	307.1	-14.94
253	7.09	305.3	15.27	-5.38	306.8	-15.00
273	6.74	305.1	15.46	-5.27	307.5	-14.30
293	6.70	305.4	15.00	-4.84	310.6	-13.88
313	6.61	306.1	15.85	-5.04	307.6	-14.31
333	6.62	307.3	15.92	-5.11	308.7	-14.44

Photoluminescence (PL) and Circularly Polarized Luminescence (CPL)

Photoluminescence emission and excitation measurement were recorded on an Edinburgh Instruments FLS1000 Photoluminescence Spectrometer. A 10 mm cell was used for solution samples. Solid-state measurements were conducted with crystalline samples. 1.5 nm excitation/emission bandwidth and 0.1 dwell time were set, the data were accumulated 5 times. Emission decay traces were obtained using an Edinburgh Instruments FLS1000 Photoluminescence Spectrometer with a micro halogen lamp (μF). The Variable-temperature (VT) photoluminescence emission and lifetime spectra were obtained using a Thermal Block Company: SYS-K12309SB as

cryosystem, which employs liquid nitrogen for cooling and conducts measurements under vacuum.

The emission QY were recorded on a Hamamatsu Quantaurus-QY absolute PL quantum yield spectrometer with an integrating sphere with five independent measurements. A 10 mm cell was used for solution samples. Solid-state measurements were conducted with crystalline samples. In the CH_2Cl_2 solution (2.5 x 10^{-5} mol/L), the QY of 6-R and 6-S were 2.9%, while in crystalline state, the QY of **6**-*R* and **6**-*S* were 29.9 ± 0.3% and 30.1 ± 0.2%, respectively.

Circularly Polarized Luminescence (CPL) data were recorded on a JASCO CPL-300 Circularly Polarized Luminescence Spectrophotometer at room temperature. For the solution sample, the cell was 10 mm in size. 2 sec D.I.T. with 15.0 nm excitation/emission bandwidth and 200 nm/min scanning speed was set, and the data were accumulated 10 times. For the crystalline sample, the measurements were performed using the Nujol mull method.[17,18] 4 sec D.I.T. with 10.0 nm Ex bandwidth, 10.0 nm Em bandwidth,100 nm/min scanning speed, and 800–900 V HT voltage was set, the data were accumulated 20 times. The variable-temperature (VT) CPL was obtained using a UNISOKU CoolSpeK CD: USP-203CD-B as a cryosystem, which employs liquid nitrogen for cooling. Additionally, all the VT-CPL were measure three times independently, and the measurement parameters for VT measurements remained unchanged for a single sample. The luminescent dissymmetry factor (g_{lum}) was calculated by JASCO Spectra Manager software.

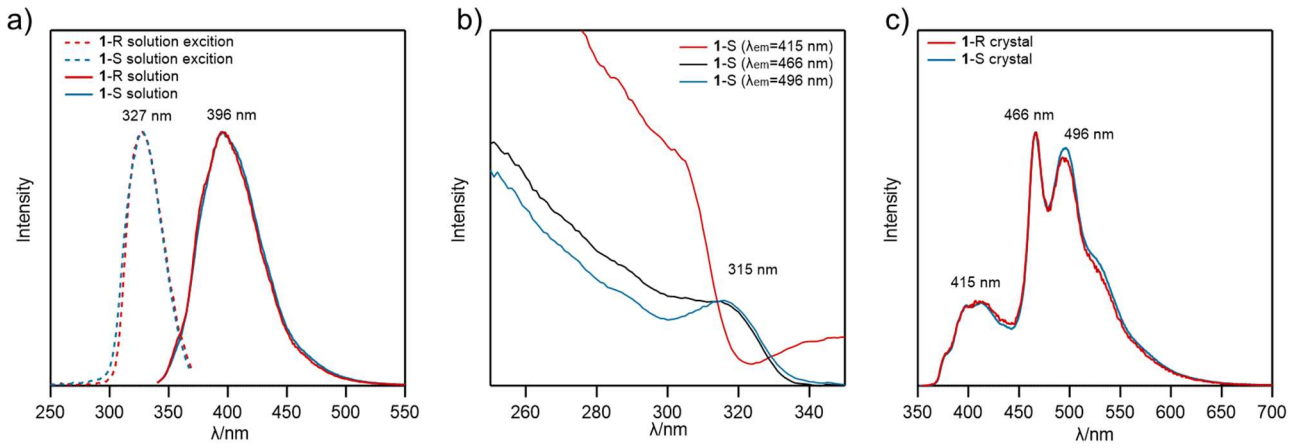

Figure S4.10. a) Normalized excitation (λ_{em} = 396 nm) and emission (λ_{ex} = 327 nm) spectra **6**-*R* and **6**-*S* in CH_2Cl_2 solution (2.5 x 10^{-5} mol/L) at room temperature; b) Normalized excitation spectra of **6**-*R* and **6**-*S* in solid state; c) Normalized emission (λ_{ex} = 315 nm) of 6-R and 6-S in solid state.

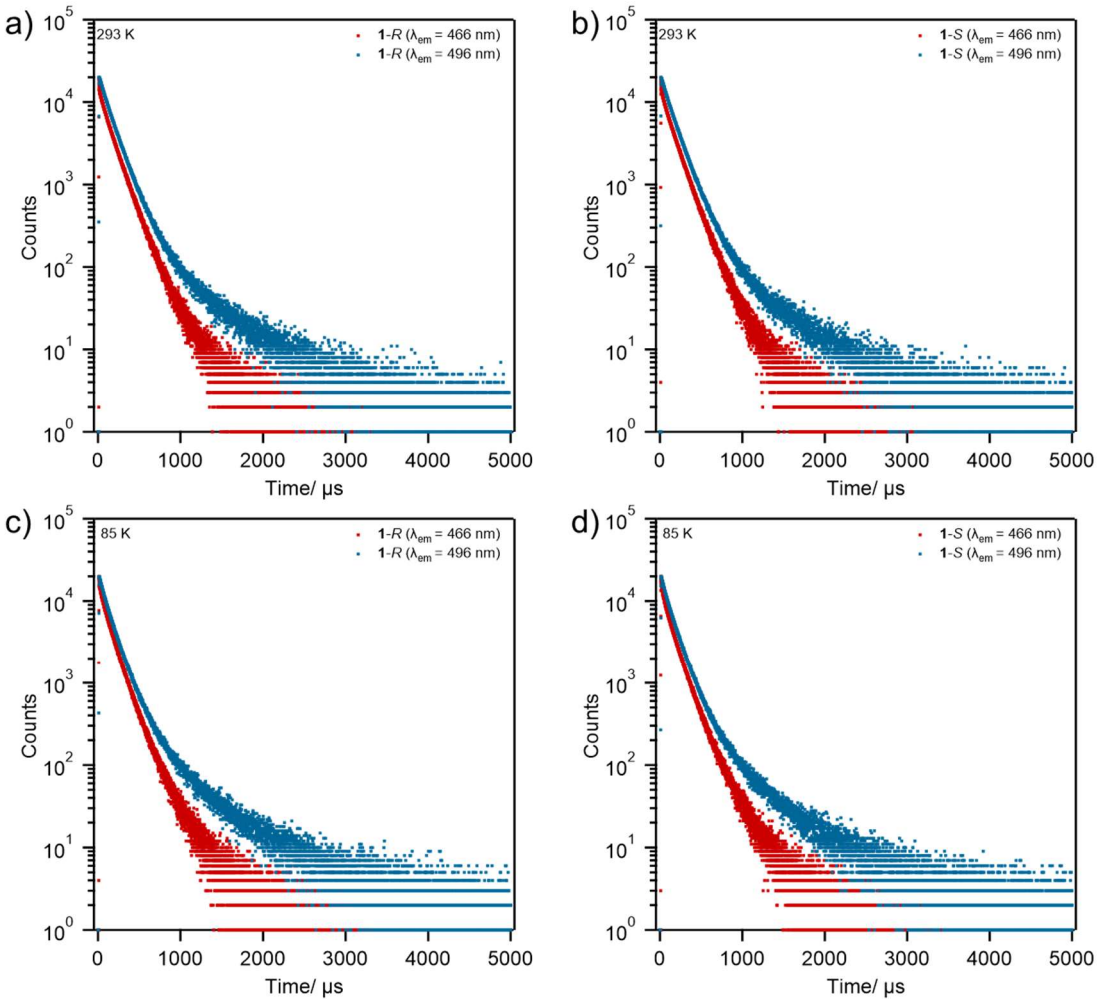

Figure S4.11.Photoluminescence decay profiles of **6**-*R* (a, c) and **6**-*S* (c, d)in crystalline solid state (λ_{ex} = 315nm) at 293 K and 85 K.

Table S4.8. VT photoluminescence lifetime in crystalline solid state.

T,K	t_1,μs	r_1,%	t_2,μs	r_2,%	t_3,μs	r_3,%	t_{av},μs	χ^2	A
	6-*R* (466 nm)								
85	13.3	3.1	116.9	75.1	237.9	21.8	140.2	1.04	0.79
293	13.2	1.9	129.5	80.9	250.7	17.2	148.2	1.19	0.68
	6-*R* (496 nm)								
85	87.0	26.8	165.5	62.7	619.4	8.3	180.1	1.01	1.11
293	86.6	19.9	161.5	73.6	613.3	6.5	175.9	1.04	0.97
	6-*S* (466 nm)								
85	15.8	4.5	120.4	75.5	253.9	20.0	142.4	0.99	0.71
293	15.8	2.0	129.4	78.0	240.0	20.0	149.3	1.02	0.75
	6-*S* (496 nm)								
85	87.0	28.9	166.8	62.5	600.0	8.6	180.8	1.05	1.07
293	87.9	20.3	163.9	73.9	620.0	5.9	175.2	1.00	0.93

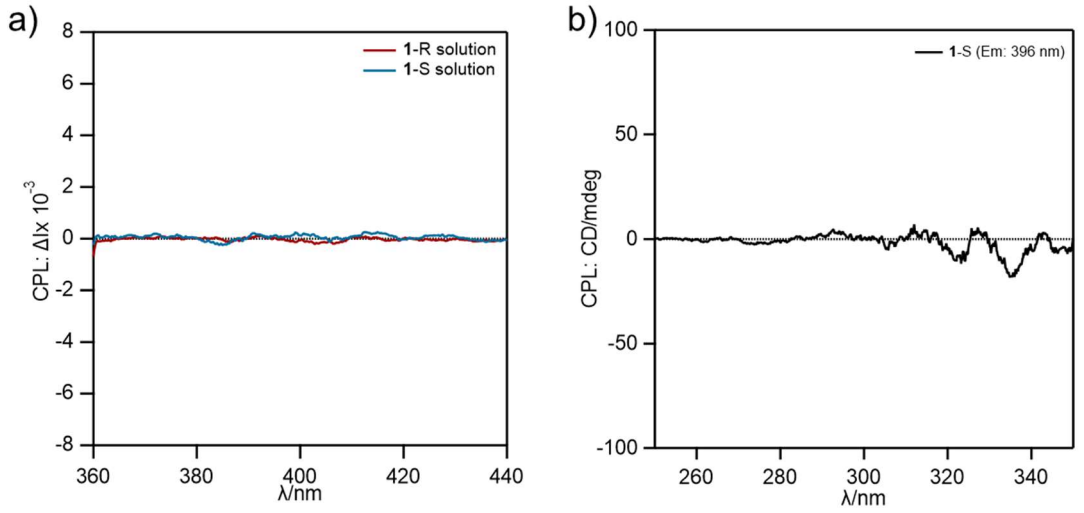

Figure S4.12 (a) CPL spectra (λ_{ex} = 327 nm) of **6**-*R* and **6**-*S* in CH_2Cl_2 solution (2.5 x 10^{-5} mol/L) at room temperature; (b) CPL excitation (λ_{em} = 396 nm) spectra of **6**-*S*in CH_2Cl_2 solution (2.5 x 10^{-5} mol/L) at room temperature.

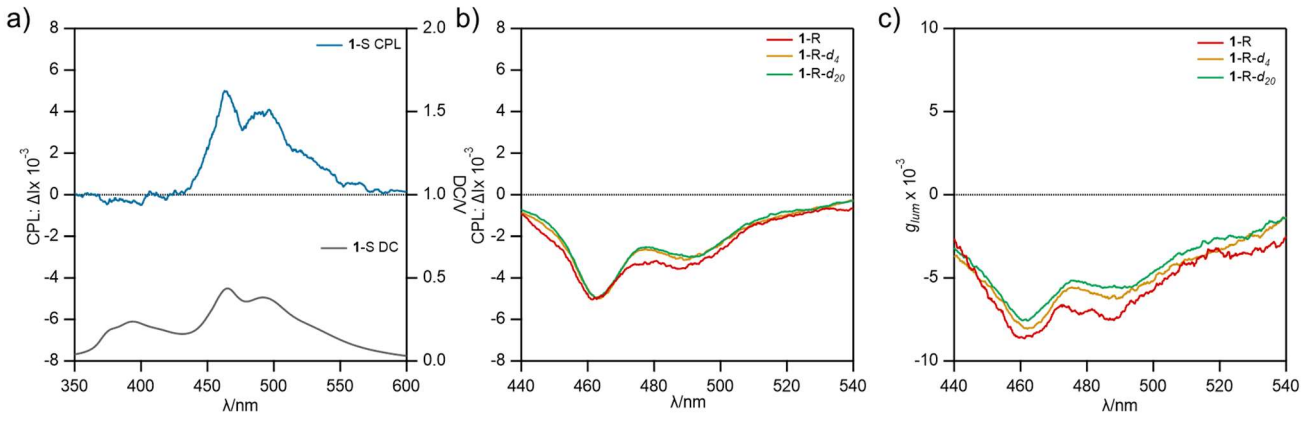

Figure S4.13 (a) CPL and emission spectra (DC) of **6**-*S* in solid state (Nujol mull method, 20 % w/w in paraffin oil) at room temperature (λex = 315 nm), range from 350 nm to 600 nm. (b) CPL spectra and (c) g_{lum} of **6**-*R*, **6**-*R*-d_4 and **6**-*R*-d_{20} in solid state (Nujol mull method, 20 % *w*/*w* in paraffin oil) at room temperature (λ_{ex} = 315 nm).

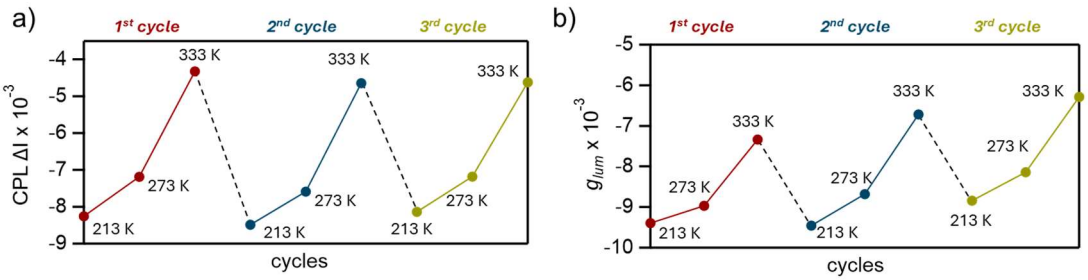

Figure S4.14 The thermal reversibility of **6**-*R* in solid state (Nujol mull method, 20 % *w*/*w* in paraffin oil): (a) CPL intensity and (b) the g_{lum} at 466 nm (λ_{ex} = 315 nm).

4.4.8 Calculations

All geometry optimization and single-point calculations were performed using the Gaussian 16 (revision C.01) program package.[57] For the experimental geometry of **6**-*S* taken from the XRD structure at 293K, only the positions of H atoms were optimized by the DFT calculations using the PBE[58]-D3[59](BJ)[60] functional and mixed basis set (relativistic pseudopotentials ECP60MDF with corresponding Stuttgart–Köln basis sets for the Au[24] atom and def2-SVP basis set[61,62] for other atoms), while the positions of all other atoms were fixed to preserve the XRD geometry. No symmetry restrictions were applied during the geometry optimization procedure. In all cases, frequency analyses were carried out to ensure that the optimized geometries belong to minima on the potential energy surface (no imaginary frequencies were found for the stationary state structures). To simulate the effect of internal molecular rotation on the symmetry of the complex, the Ph^b moieties in the experimental geometry of **6**-*S* were rotated by ca. 66° around the C_{ipso}-C_{para} axis, adjusting to the same position as Ph^a relative to the NHC ligand, while the *PP* moiety was rotated by ca. 35°. After that, only the positions of H atoms were optimized giving “rotated” structure of **6**-*S* (**Figure S4.15**). The analysis of the symmetry of complexes was conducted using ChemCraft 1.8 software[63]. The Cartesian atomic coordinates for model structures are given as XYZ-files in the Supplementary Files.

For the simulation of ECD spectra (**Figure S4.16**) and analysis of the exited states the TD-DFT calculation of the first singlet 25 excited states for the experimental and “rotated” geometries of **6**-*S* were carried on using the same level of theory as for the optimization. To study the nature of single-electron excitation transitions and associated with them charge transfers, the hole-electron distribution analysis was using Multiwfn 3.8 software[64] and visualized by VMD software.[65] The latter method describes where the excited electron leaves as "hole" and arrives as "electron".

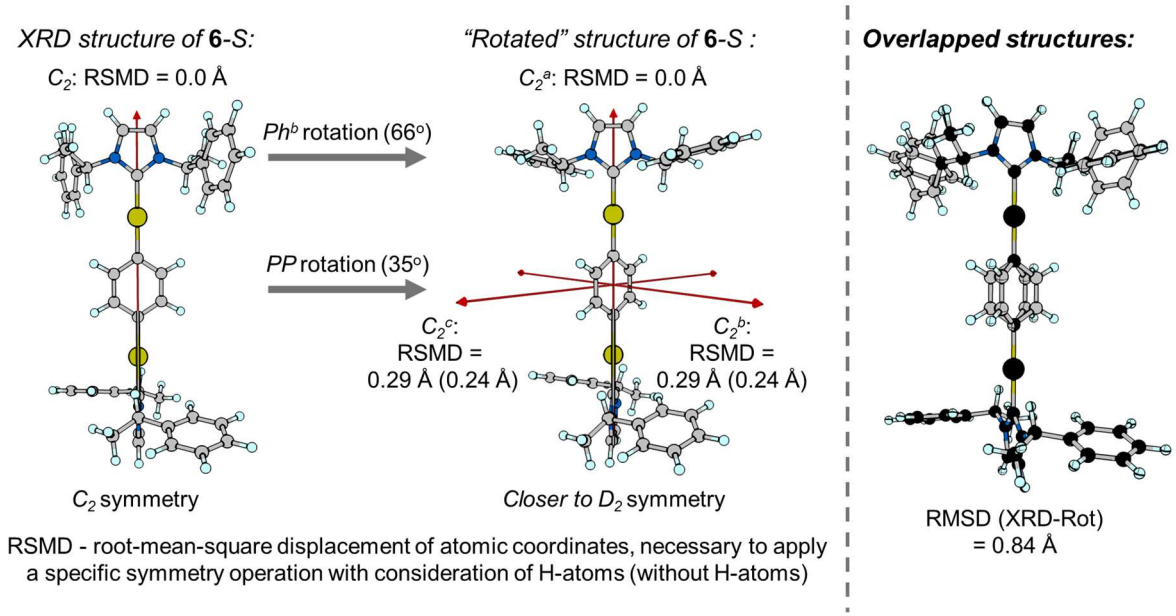

Figure S4.15. Analysis of the symmetry of different conformation of **6**-*S*.

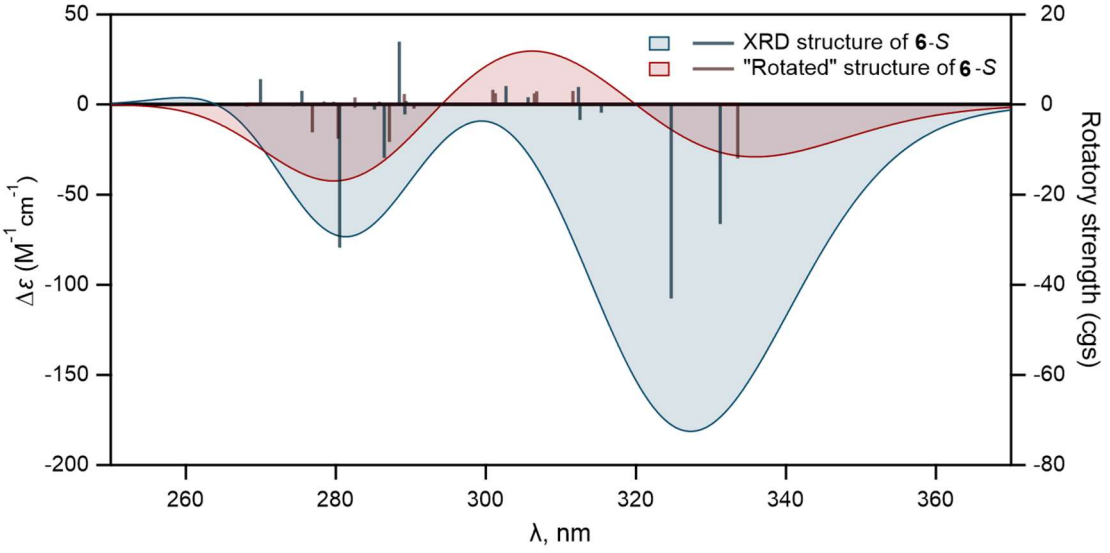

Figure S4.16. Calculated ECD spectra and rotatory strengths for the experimental and "rotated" geometries of **6**-*S*.

4.5 References

1. Vogelsberg, C. S.; Garcia-Garibay, M. A. Crystalline molecular machines: function, phase order, dimensionality, and composition. *Chem. Soc. Rev.* **2012**, *41*, 1892–1910.
2. Catalano, L.; Naumov, P. Exploiting rotational motion in molecular crystals. *CrystEngComm.* **2018**, *20*, 5872–5883.
3. Howe, M. E.; Garcia-Garibay, M. A. The Roles of Intrinsic Barriers and Crystal Fluidity in Determining the Dynamics of Crystalline Molecular Rotors and Molecular Machines. *J. Org. Chem.* **2019**, *84*, 9835–9849.
4. Comotti, A.; Bracco, S.; Sozzani, P. Molecular Rotors Built in Porous Materials. *Acc. Chem. Res.* **2016**, *49*, 1701–1710.
5. Costil, R.; Holzheimer, M.; Crespi, S.; Simeth, N. A.; Feringa, B. L. Directing coupled motion with light: a key step toward machine-like function, *Chem. Rev.* **2021**, *121*, 13213–13237.
6. Ehnbom, A.; Gladysz, J. A. Gyroscopes and the Chemical Literature, 2002–2020: Approaches to a Nascent Family of Molecular Devices. *Chem. Rev.* **2021**, *121*, 3701–3750.
7. Setaka, W.; Yamaguchi, K. A Molecular Balloon: Expansion of a Molecular Gyrotop Cage Due to Rotation of the Phenylene Rotor. *J. Am. Chem. Soc.* **2012**, *134*, 12458–12461.
8. Yao, Z. S.; Mito, M.; Kamachi, T.; Shiota, Y.; Yoshizawa, K.; Azuma, N.; Miyazaki, Y.; Takahashi, K.; Zhang, K.; Nakanishi, T.; Kang, S.; Kanegawa, S.; Sato, O. Molecular motor-driven abrupt anisotropic shape change in a single crystal of a Ni complex. *Nat. Chem.* **2014**, *6*, 1079–1083.
9. Jin, M.; Kitsu, R.; Hammyo, N.; Sato-Tomita, A.; Mizuno, M.; Mikherdov, A. S.; Tsitsvero, M.; Lyalin, A.; Taketsugu, T.; Ito, H. A Steric-Repulsion-Driven Clutch Stack of Triaryltriazines: Correlated Molecular Rotations and a Thermoresponsive Gearshift in the Crystalline Solid. *J. Am. Chem. Soc*. **2023**, *145*, 27512–27520.
10. Akutagawa, T.; Koshinaka, H.; Sato, D.; Takeda, S.; Noro, S.; Takahashi, H.; Kumai, R.; Tokura, Y.; Nakamura, T. Ferroelectricity and polarity control in solid-state flip-flop supramolecular rotators. *Nat. Mater.* **2009**, *8*, 342–347.
11. Miao, L.-P.; Ding, N.; Wang, N.; Shi, C.; Ye, H.-Y.; Li, L.; Yao, Y.-F.; Dong, S.; Zhang, Y. Direct observation of geometric and sliding ferroelectricity in an amphidynamic crystal. *Nat. Mater.* **2022**, *21*, 1158–1164.
12. Setaka, W.; Yamaguchi, K. Thermal modulation of birefringence observed in a crystalline molecular gyrotop *Proc. Natl. Acad. Sci. U. S. A.* **2012**, *109*, 9271–9275.
13. Jin, M.; Chung, T. S.; Seki, T.; Ito, H.; Garcia-Garibay, M. A. Phosphorescence Control Mediated by Molecular Rotation and Aurophilic Interactions in Amphidynamic Crystals of 1,4-Bis[tri-(p-fluorophenyl)phosphane-gold(I)-ethynyl]benzene. *J. Am. Chem. Soc.* **2017**, *139*, 18115–18121.
14. Balzani, V.; Credi, A.; Raymo, F.; Stoddart, J. F. Artificial Molecular Machines. *Angew. Chem., Int. Ed.* **2000**, *39*, 3348–3391.
15. Friend, R. H.; Gymer, R. W.; Holmes, A. B.; Burroughes, J. H.; Marks, R. N. Electroluminescence in conjugated polymers. *Nature* **1999**, *397*, 121–128.

16. Sagara, Y.; Yamane, S.; Mitani, M.; Weder, C.; Kato, T. Mechanoresponsive Luminescence: Mechanoresponsive Luminescent Molecular Assemblies: An Emerging Class of Materials. *Adv. Mater.* **2016**, *28*, 977–977.
17. Gierschner, J.; Shi, J.; Milián-Medina, B.; Roca-Sanjuán, D.; Varghese, S.; Park, S. Y. Luminescence in Crystalline Organic Materials: From Molecules to Molecular Solids. *Adv. Opt. Mater.* **2021**, 9, 2002251.
18. Gao, R.; Kodaimati, M. S.; Yan, D. Recent Advances in Persistent Luminescence Based on Molecular Hybrid Materials. *Chem. Soc. Rev.* **2021**, *50*, 5564–5589.
19. Jin, M.; Ito, H. Solid-state luminescence of Au(I) complexes with external stimuli-responsive properties. *J. Photochem. Photobiol., C* **2022**, *51*, 100478.
20. Jin, M.; Yamamoto, S.; Seki, T.; Ito, H.; Garcia-Garibay, M. A. Anisotropic Thermal Expansion as the Source of Macroscopic and Molecular Scale Motion in Phosphorescent Amphidynamic Crystals. *Angew. Chem., Int. Ed.* **2019**, *58*, 18003–18010.
21. Jin, M.; Ando, R.; Jellen, M. J.; Garcia-Garibay, M. A.; Ito, H. Encapsulating N-Heterocyclic Carbene Binuclear Transition-Metal Complexes as a New Platform for Molecular Rotation in Crystalline Solid-State. *J. Am. Chem. Soc.* **2021**, *143* (2), 1144–1153.
22. Zhang, J.; He, B.; Wu, W.; Alam, P.; Zhang, H.; Gong, J.; Song, F.; Wang, Z.; Sung, H. H. Y.; Williams, I. D.; Wang, Z.; Lam, J. W. Y.; Tang, B. Z. Molecular Motions in AIEgen Crystals: Turning on Photoluminescence by Force-Induced Filament Sliding. *J. Am. Chem. Soc.* **2020**, *142* (34), 14608–14618.
23. Yang, Y.-H; Chen, Y.-S.; Chuang, W.-T.; Yang, J.-S. Bifurcated Polymorphic Transition and Thermochromic Fluorescence of a Molecular Crystal Involving Three-Dimensional Supramolecular Gear Rotation. *J. Am. Chem. Soc*. **2024**, *146*, 8131–8141.
24. Dong, J.; Qiao, Z.; Pan, Y.; Peh, S. B.; Yuan, Y. D.; Wang, Y.; Zhai, L.; Yuan, H.; Cheng, Y.; Liang, H.Encapsulation and protection of ultrathin two-dimensional porous organic nanosheets within biocompatible metal-organic frameworks for live-cell imaging. *Chem. Mater.* **2019**, *31*, 4897–4912.
25. Hsu, Y.-F.; Wu, T.-W.; Kang, Y.-H.; Wu, C.-Y.; Liu, Y.-H.; Peng, S.-M.; Kong, K. V.; Yang, J.-S. Porous Supramolecular Assembly of Pentiptycene-Containing Gold(I) Complexes: Persistent Excited-State Aurophilicity and Inclusion-Induced Emission Enhancement. *Inorg. Chem.* **2022**, *61,* 11981–11991.
26. Li, Q.; Blancafort, L. A conical intersection model to explain aggregation-induced emission in diphenyl dibenzofulvene. *Chem. Commun*. **2013**, *49*, 5966–5968.
27. Mei, J.; Leung, N. L. C.; Kwok, R. T. K.; Lam, J. W. Y.; Tang, B. Z. Aggregation-Induced Emission: Together We Shine, United We Soar!. *Chem. Rev*. **2015**, *115*, 11718–11940.
28. Deng, Y.; Wang, M.; Zhuang, Y.; Liu, S.; Huang, W.; Zhao, Q. Circularly polarized luminescence from organic micro-/nano-structures. *Light Sci. Appl.* **2021**, *10,* 76.
29. Takaishi, K.; Iwachido, K.; Ema, T. Solvent-Induced Sign Inversion of Circularly Polarized Luminescence: Control of Excimer Chirality by Hydrogen Bonding. *J. Am. Chem. Soc.* **2020**, *142*, 1774–1779.

30. David, A. H. G.; Casares, R.; Cuerva, J. M.; Campaña, A. G.; Blanco, V. A [2]Rotaxane-Based Circularly Polarized Luminescence Switch. *J. Am. Chem. Soc.* **2019**, *141*, 18064–18074.
31. Wang, C.; Liu, L.; Wang, J.; Yan, Y. Electrochemically Switchable Circularly Polarized Photoluminescence within Self-Assembled Conducting Polymer Helical Microfibers. *J. Am. Chem. Soc.* **2022**, *144*, 19714–19718.
32. Han, J.; Shi, Y.; Jin, X.; Yang, X.; Duan, P. Regulating the excited state chirality to fabricate high-performance-solid-state circularly polarized luminescence materials. *Chem. Sci.* **2022**, *13*, 6074–6080.
33. Sickinger, A.; Grasser, M.; Baguenard, B.; Bensalah-Ledoux, A.; Guy, L.; Bui, A. T.; Guyot, Y.; Dorcet, V.; Pintillart, F.; Cador, O.; Guy, S. Maury, O., Guennic, B. L.; Riobé. Temperature-dependent NIR-CPL spectra of chiral Yb(III) complexes. *ChemRxiv.* **2023**, DOI: 10.26434/chemrxiv-2023-8z10s This content is a preprint and has not been peer-reviewed.
34. Yao, Z. S.; Wu, S. Q.; Kitagawa, Y.; Su, S. Q.; Huang, Y. G.; Li, G. L.; Ni, Z. H.; Nojiri, H.; Shiota, Y.; Yoshizawa, K.; Kang, S.; Kanegawa, S.; Sato, O. Anisotropic Change in the Magnetic Susceptibility of a Dynamic Single Crystal of a Cobalt(II) Complex. *Angew. Chem., Int. Ed.* **2017**, *56*, 717–721.
35. Tanaka, H.; Ikenosako, M.; Kato, Y.; Fujiki, M.; Inoue, Y.; Mori, T. Symmetry-Based Rational Design for Boosting Chiroptical Responses. *Commun. Chem.* **2018**, *1*, 38.
36. Hernández-Morales, E. A.; Colin-Molina,A.; Arcudia, J.; Hernández, F. J.; Rodríguez, M.; Toscano, R. A.; Crespo-Otero, R.; Merino, G. Molina, B. R. Indolocarbazole as a Platform for Concatenated Crystalline Rotors. *Cryst. Growth Des.* **2023**, *23*, 9, 6785–6794.
37. Shang, W., Wang, Y., Zhu, X., Liang, T., Du, C., Xiang, J., Liu, M. Helical Cage Rotors Switched on by Brake Molecule with Variable Fluorescence and Circularly Polarized Luminescence. . *J. Am. Chem. Soc.* **2023**, *145*, 27639–27649.
38. Hansen, M. R.; Graf, R.; Spiess, H. W. Solid-State NMR in Macromolecular Systems: Insights on How Molecular Entities Move. *Acc. Chem. Res.* **2013**, *46*, 1996–2007.
39. Rodríguez-Molina, B.; Farfán, N.; Romero, M.; Méndez-Stivalet, J. M.; Santillan, R.; Garcia-Garibay, M. A. Anisochronous Dynamics in a Crystalline Array of Steroidal Molecular Rotors: Evidence of Correlated Motion within 1D Helical Domains. *J. Am. Chem. Soc.* **2011**, *133*, 7280–7283.
40. Pei, X.-L.; Zhao, P.; Ube, H.; Lei, Z.; Nagata, K.; Ehara, M.; Shionoya, M. Asymmetric Twisting of C-Centered Octahedral Gold(I) Clusters by Chiral N-Heterocyclic Carbene Ligation. *J. Am. Chem. Soc.* **2022**, *144* (5), 2156–2163.
41. Jiang, P.; Mikherdov, A.S.; Ito, H.; Jin, M. Crystallization-Induced Chirality Transfer in Conformationally Flexible Azahelicene Au(I) Complexes with Circularly Polarized Luminescence Activation. *J. Am. Chem. Soc.* **2024**, 146, 18, 12463–12472.
42. Tu, G.; Yuan, C.; Li, Y.; Zhang, J.; Zhao, Y. A. A Ligand-Enabled Palladium-Catalyzed Highly para-Selective Difluoromethylation of Aromatic Ketones. *Angew. Chem., Int. Ed.* **2018**, *57*, 15597–15601.

43. Feng, M.; Mosiagin, I.; Kaiser, D.; Maryasin, B.; Maulide, N. Deployment of sulfinimines in charge-accelerated sulfonium rearrangement enables a surrogate asymmetric Mannich reaction. *J. Am. Chem. Soc.* **2022**, *144*, 13044–13049.
44. Guijarro, D.; Oscar, P.; Yus, M. Achiral β-amino alcohols as efficient ligands for the ruthenium-catalysed asymmetric transfer hydrogenation of sulfinylimines. *Tetrahedron Lett.* **2011**, *52*, 789–791
45. Tachrim, Z. P.; Hashinoki, M.; Wang, Z. Wen, Z. Zihan, Z. Hashimoto, M. Mild and selective hydrogen-deuterium exchange for aromatic hydrogen of amines. *J Label Compd Radiopharm*. **2023**, *66*, 321–331.
46. Queval, P.; Jahier, C.; Rouen, M.; Artur, I.; Legeay, J.-C.; Falivene, L.; Toupet, L.; Crévisy, C.; Cavallo, L.; Baslé O.; Mauduit, M. Atropisomeric N-Heterocyclic Carbene-Palladium (II) Complexes: Influence of the Backbone Substitution. *Angew. Chem. Int. Ed.* **2013**, *125*, 14353–14357.
47. Consorti, C. S.; Suarez, P. A. Z.; de Souza, R. F.; Burrow, R. A.; Farrar, D. H.; Lough, A. J.; Loh, W.; da Silva, L. H. M.; Dupont, J. *Identification of 1, 3-dialkylimidazolium salt supramolecular aggregates in solution. J. Phys. Chem. B* **2005**, *109*, 4341–4349.
48. Price, G. A.; Brisdon, A. K.; Randall, S.; Lewis, E.; Whittaker, D. M.; Pritchard, R. G.; Muryn, C. A.; Flower, K. R.; Quayle, P. Some insights into the gold-catalysed A3-coupling reaction. *J. Organomet. Chem.* **2017**, *846*, 251–262.
49. Method for calculating H% in elemental analysis of deuterated compounds:

$$H\% = H\%_{(exp)} \times \frac{h}{h + d \times 1.028}$$

$$D\% = H\%_{(exp)} \times \frac{d \times 1.028}{h + d \times 1.028} \times 1.944$$

where *h* and *d* are the numbers of atom for H and D.
50. Dupuy, S.; Crawford, L.; Bühl, M.; Slawin, A. M. Z.; Nolan, S. P. The Role of Metal Hydroxide Complexes in Late Transition Metal-Mediated Transmetalation Reaction: The Case of Gold. *Adv. Synth. Catal.* **2012**, *354*, 2380–2386.
51. Dolomanov, O.V.; Bourhis, L.J.; Gildea, R.J.; Howard, J.A.K; Puschmann, H. OLEX2: a complete structure solution, refinement and analysis program. *J. Appl. Crystallogr*. **2009**, *42*, 339–341.
52. Sheldrick, G. M. Crystal structure refinement with SHELXL. *Acta Crystallogr., Sect. A.* **2015**, *71*, 3–8.
53. Bourhis, L. J.; Dolomanov, O. V.; Gildea, R. J.; Howard J. A. K.; Puschmann, H. The anatomy of a comprehensive constrained, restrained refinement program for the modern computing environment–Olex2 dissected. *Acta Crystallogr., Sect. A*. **2015**, *71*, 59–75.
54. Macrae, C. F.; Sovago, I.; Cottrell, S. J.; Galek, P. T. A.; McCabe, P.; Pidcock, E.; Platings, M.; Shields, G. P.; Stevens, J. S.; Towler, M.; Wood, P. A. Mercury 4.0: From visualization to analysis, design and prediction. *J. Appl. Crystallogr.* **2020**, *53*, 226–235.
55. Macho, V.; Brombacher, L.; Spiess, H. W. The NMR-WEBLAB: An internet approach to NMR lineshape analysis. *Appl. Magn. Reson.* **2001**, *20*, 405–432. For the online program, visit: http://weblab.mpip-mainz.mpg.de/weblab

56. Castiglioni, E.; Biscarini, P.; Abbate, S. Experimental aspects of solid state circular dichroism. *Chirality* **2009**, *21* (1E), E28–E36.
57. Frisch, M. J.; Trucks, G. W.; Schlegel, H. B.; Scuseria, G. E.; Robb, M. A.; Cheeseman, J. R.; Scalmani, G.; Barone, V.; Petersson, G. A.; Nakatsuji, H.; Li, X.; Caricato, M.; Marenich, A.V.; Bloino, J.; Janesko, B.G.; Gomperts, R.; Mennucci, B.; Hratchian, H.P.; Ortiz, J.V.; Izmaylov, A.F.; Sonnenberg, J.L.; Williams-Young, D.; Ding, F.; Lipparini, F.; Egidi, F.; Goings, J.; Peng, B.; Petrone, A.; Henderson, T.; Ranasinghe, D.; Zakrzewski, V.G.; Gao, J.; Rega, N.; Zheng, G.; Liang, W.; Hada, M.; Ehara, M.; Toyota, K.; Fukuda, R.; Hasegawa, J.; Ishida, M.; Nakajima, T.; Honda, Y.; Kitao, O.; Nakai, H.; Vreven, T.; Throssell, K.; Montgomery, Jr., J.A.; Peralta, J.E.; Ogliaro, F.; Bearpark, M.J.; Heyd, J.J.; Brothers, E.N.; Kudin, K.N.; Staroverov, V.N.; Keith, T.A.; Kobayashi, R.; Normand, J.; Raghavachari, K.; Rendell, A.P.; Burant, J.C.; Iyengar, S.S.; Tomasi, J.; Cossi, M.; Millam, J.M.; Klene, M.; Adamo, C.; Cammi, R.; Ochterski, J.W.; Martin, R.L.; Morokuma, K.; Farkas, O.; Foresman, J.B.; Fox, D.J. *Gaussian 16, Revision A.03*; Gaussian, Inc.: Wallingford, CT, 2016.
58. Adamo, C.; Barone, V. Toward reliable density functional methods without adjustable parameters: The PBE0 model. *J. Chem. Phys.* **1999**, *110*, 6158–6170.
59. Grimme, S.; Antony, J.; Ehrlich, S.; Krieg, H. A consistent and accurate ab initio parametrization of density functional dispersion correction (DFT-D) for the 94 elements H-Pu. *J. Chem. Phys.* **2010**, *132,* 154104.
60. Grimme, S.; Ehrlich, S.; Goerigk, L. Effect of the damping function in dispersion corrected density functional theory. *J. Comput. Chem.* **2011**, *32*, 1456–1465.
61. Figgen, D.; Rauhut, G.; Dolg, M.; Stoll, H. Energy-consistent pseudopotentials for group 11 and 12 atoms: adjustment to multi-configuration Dirac–Hartree–Fock data. *Chem. Phys.* **2005**, *311*, 227–244.
62. Weigend, F.; Ahlrichs, R. Balanced basis sets of split valence, triple zeta valence and quadruple zeta valence quality for H to Rn: Design and assessment of accuracy. *Phys. Chem. Chem. Phys.* **2005**, *7*, 3297–3305.
63. Weigend, F. Accurate Coulomb-fitting basis sets for H to Rn. *Phys. Chem. Chem. Phys.* **2006**, *8*, 1057–1065.
64. Chemcraft - graphical software for visualization of quantum chemistry computations. Version 1.8, build 682. Visit: https://www.chemcraftprog.com

65. Liu, Z.; Lu, T.; Chen, Q. An sp-hybridized all-carboatomic ring, cyclo[18]carbon: Electronic structure, electronic spectrum, and optical nonlinearity. *Carbon* **2020**, *165*, 461–467.
66. Lu, T.; Chen, F. Multiwfn: A multifunctional wavefunction analyzer. *J. Comput. Chem.* **2012**, *33*, 580–592.
67. Humphrey, W.; Dalke, A.; Schulten, K. VMD: visual molecular dynamics. *J. Mol. Graphics* **1996**, *14*, 33–38.

5. Summary of Thesis

My Ph.D. study focuses on designing and synthesizing novel CPL-active materials based on chiral NHC Au(I) complexes and controlling CPL through the modulation of molecular dynamics.

Chapter 2 details the development of a method to stabilize dynamic chirality in flexible azahelicene species via crystallization-induced intermolecular chirality transfer in Au(I) complexes with chiral NHC ligands. Using shape-tailored chiral NHC ligands, the crystallization of azahelicene Au(I) complexes suppresses dynamic chirality and stabilizes homochirality through the intermolecular interaction between chiral NHC and dibenzocarbazole ligands. For Au(I) benzocarbazole complexes, this interaction induces chirality in the initially achiral benzocarbazole ligand, significantly enhancing CPL properties.

Chapter 3 introduces a platform for amphidynamic crystals featuring a concave binuclear NHC stator and para-phenylene as the rotator. Utilizing this rotor with chiral NHC, I prepared a CPL-active rotor to demonstrate how molecular rotation affects CPL properties by altering molecular symmetry. However, with this central rotation, the symmetry of the crystal does not change dramatically, and CPL only changes in intensity but maintains the dissymmetry factor.

Chapter 4 describes the synthesis of a pair of CPL-active arm rotors. The phenyl rotator moieties of this arm undergo fast rotational motion at high temperatures, potentially leading to the symmetrization of the entire crystal. In this case, the rotation not only changes the intensity but also controls the dissymmetry factor of CPL.

This Ph.D. thesis provides several pathways for designing controllable solid-state CPL-active materials, which can serve as smart materials and molecular machines in the solid state.

List of Publications

Chapter 2:

Crystallization-Induced Chirality Transfer in Conformationally Flexible Azahelicene Au(I) Complexes with Circularly Polarized Luminescence Activation

Jiang, P.;[#] Mikherdov, A.S.;[#] Ito, H.*; Jin, M.* *J. Am. Chem. Soc.* **2024**, *146*, 18, 12463–12472. https://doi.org/10.1021/jacs.4c00345.

Chapter 3:

Solid-state Dynamics of Binuclear *N*-Heterocyclic Carbene Au(I) Rotor with para-Phenylene Rotator

Jiang, P.; Mikherdov, A.S.; Ito, H.*; Jin, M.* *Chem. Lett.* **2024**, accepted. https://doi.org/10.1093/chemle/upae139

Molecular Rotation in Neutral Crystalline Chiral Binuclear *N*-Heterocyclic Carbene Au(I) Complexes and Control of Circularly Polarized Luminescence

Jiang, P.;[#] Mikherdov, A.S.;[#] Ito, H.*; Jin, M.* *manuscript under preparation.*

Chapter 4:

Circularly Polarized Luminescence Control through Molecular Rotation in Crystalline Chiral Binuclear *N*-Heterocyclic Carbene Au(I) Complexes

Jiang, P.;[#] Mikherdov, A.S.;[#] Ito, H.*; Jin, M.* *manuscript under preparation.*

Acknowledgement

The research outlined in this thesis was conducted under the supervision of Professor Hajime Ito and Associate Professor Mingoo Jin at the Division of Applied Chemistry, Graduate School of Engineering, Hokkaido University, and the Institute for Chemical Reaction Design and Discovery (WPI-ICReDD), Hokkaido University, from 2021 to 2024. I extend my deepest gratitude to Professor Hajime Ito for his unwavering guidance, generous support, and insightful feedback throughout the research journey. I am also thankful to professor Mingoo Jin, associate professor Tatsuo Ishiyama, visiting professor Tsuneo Imamoto, associate professor Koji Kubota, assistant professor Ryota Isshiki, and Dr. Mikherdov S. Alexander for their invaluable advice, enlightening suggestions, and continuous encouragement. Additionally, I express my gratitude to Dr. Pan Gao, Dr. Yunpeng Gao, Dr. Xihong Wang, Dr. Chi Feng and other members of Ito's group and WPI-ICReDD for their excellent collaboration and fostering a conducive working environment. Furthermore, I wish to acknowledge my family, especially my wife Tingyu Fu, and all my friends at Sapporo for their enduring understanding, support, and motivation. Lastly, I am grateful for the financial support provided by the China Scholarship Council for my PhD studies (CSC 202108430010).

Pingyu Jiang

July 2024

Hokkaido University